NANOMECHANICAL PROPERTIES, THERMAL STABILITY, AND CORROSION RESISTANCE OF ALUMINIUM AND NITROGEN DOPED DIAMOND-LIKE CARBON FILM

ACTING.SUB-LT. PRAPHAPHON SILAWONG

A Thesis Submitted in Partial Fulfillment of the Requirements for the

Degree of Doctor of Philosophy in Materials Engineering

Suranaree University of Technology

Academic Year 2021

สมบัติเชิงกลระดับนาโน เสถียรภาพทางความร้อน และความต้านทานการ
กัดกร่อนของชั้นเคลือบคล้ายเพชรด้วยการเจืออะลูมิเนียมและไนโตรเจน

ว่าที่ร้อยตรีหญิง ประภาพร ศิลาวงศ์

NANOMECHANICAL PROPERTIES, THERMAL STABILITY, AND CORROSION RESISTANCE OF ALUMINIUM AND NITROGEN DOPED DIAMOND-LIKE CARBON FILM

Suranaree University of Technology has approved this thesis submitted in partial fulfillment of the requirements for the Degree of Doctor of Philosophy.

Thesis Examining Committee

_____
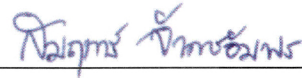
(Prof. Dr. Somrerk Chandra-ambhorn)

Chairperson

_____
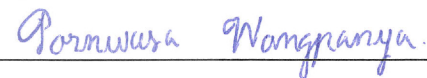
(Assoc. Prof. Dr.-Ing Pornwasa Wongpanya)

Member (Thesis Advisor)

_____

(Dr. Pat Photongkam)

Member (Thesis Co-Advisor)

_____

(Asst. Prof. Dr. Usanee Kitkamthorn)

Member

_____
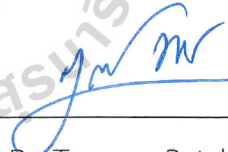
(Asst. Prof. Dr. Tapany Patcharawit)

Member

_____

(Asst. Prof. Dr. Panya Buahombura)

Member

_____   _____

(Assoc. Prof. Dr. Chatchai Jothityangkoon)   (Assoc. Prof. Dr. Pornsiri Jongkol)

Vice Rector for Academic Affairs   Dean of Institute of Engineering

and Quality Assurance

ประภาพร ศิลาวงศ์ : สมบัติเชิงกลระดับนาโน เสถียรภาพทางความร้อน และความต้านทาน
การกัดกร่อนของชั้นเคลือบคล้ายเพชรด้วยการเจืออะลูมิเนียมและไนโตรเจน
(NANOMECHANICAL PROPERTIES, THERMAL STABILITY, AND CORROSION
RESISTANCE OF ALUMINIUM AND NITROGEN DOPED DIAMOND-LIKE CARBON FILM)
อาจารย์ที่ปรึกษา : รองศาสตราจารย์ ดร.พรวสา วงศ์ปัญญา, 145 หน้า.

คำสำคัญ: FCVA/AL-N CO-DOPED DLC/ NEXAFS/XPS /สมบัติเชิงกลระดับนาโน/ความแข็งแรงใน
การยึดเกาะ/เสถียรภาพทางความร้อน/ความต้านทานการกัดกร่อน

ในทางวิศวกรรมมักใช้เหล็กกล้าอัลลอยด์ต่ำ AISI4140 เนื่องจากมีคุณสมบัติทางกลที่
โดดเด่น รวมทั้งมีความต้านทานแรงดึงสูง ทนต่อความล้า ความแกร่ง และทนต่อแรงกระแทก แต่มีความ
ต้านทานการสึกหรอต่ำ จึงจำเป็นต้องมีการปรับปรุงพื้นผิวเพื่อให้สอดคล้องกับการใช้งานสำหรับใน
สภาพแวดล้อมที่มีการกัดกร่อนและการทำงานที่อุณหภูมิสูง ฟิล์มคาร์บอนคล้ายเพชร (Diamond-like
carbond, DLC) ช่วยเพิ่มความแข็ง โมดูลัสความยืดหยุ่น การยึดเกาะ ความทนทานต่อการเสียดสี ทน
ความร้อน และทนต่อการกัดกร่อน สำหรับการศึกษานี้ฟิล์ม DLC ได้ถูกผลิตขึ้นโดยเทคนิคการเคลือบ
ฟิลเตอร์คาร์โธดิกอาร์ก (Filtered cathodic vacuum arc, FCVA) เทคนิคนี้สามารถสร้างชั้นฟิล์ม
คาร์บอนอสัณฐานเตตระฮีดรัลที่ปราศจากไฮโดรเจน (hydrogen-free tetrahedral amorphous
carbon, ta-C) ที่มีอัตราส่วนพันธะคาร์บอน sp^3/sp^2 สูง ในทางกลับกันฟิล์ม ta-C มีความเค้นภายใน
อย่างมาก ซึ่งทำให้ชั้นฟิล์มยึดเกาะกับพื้นผิวโลหะได้ไม่ดี ด้วยเหตุนี้จึงเพิ่มความแข็งแรงในการยึดเกาะ
ขึ้นโดยการเจือธาตุผสมลงในฟิล์ม DLC เพื่อลดความเค้นภายในชั้นฟิล์ม ในงานวิจัยนี้ฟิล์ม DLC ที่
พัฒนาขึ้นนั้น ถูกเจือด้วยอะลูมิเนียม (Al) และไนโตรเจน (N) และสังเคราะห์ฟิล์มโดยใช้เทคนิค FCVA
เพื่อเคลือบชั้นฟิล์ม ta-C, ta-C:N, ta-C:Al และฟิล์ม ta-C:Al:N ตามลำดับ ลงบนผิวเหล็ก AISI 4140
โครงสร้างและองค์ประกอบทางเคมีของฟิล์ม DLC ที่ถูกสังเคราะห์ขึ้นได้รับการตรวจสอบโดยใช้รามาน
สเปกโตรสโกปี (Raman spectroscopy), เอ็กซ์เรย์โฟโต้อิเล็กตรอนสเปกโตสโกปี (X-ray
photoelectron spectroscopy, XPS) และการดูดกลืนรังสีเอกซ์โครงสร้างใกล้ขอบ (Near Edge X-
Ray Absorption Fine Structures, NEXAFS) จากนั้น จึงตรวจวัดคุณสมบัติทางกลและแรงยึดเกาะของ
ฟิล์ม พฤติกรรมการเกิดออกซิเดชันของฟิล์ม DLC ถูกวิเคราะห์โดยใช้เทคนิค NEXAFS ที่ให้ความร้อนใน
แหล่งกำเนิด ตามด้วยพฤติกรรมการกัดกร่อนของฟิล์มทั้งหมด ชิ้นงานถูกประเมินโดยใช้โพเทนชิโอสแตต
ในสารละลายของโซเดียมคลอไรด์ 3.5 โดยน้ำหนัก สุดท้ายตรวจสอบบริเวณที่กัดกร่อนและผลิตภัณฑ์
การกัดกร่อนจากการทดสอบการกัดกร่อนโดยใช้กล้องจุลทรรศน์อิเล็กตรอนแบบส่องกราดเอ็กซ์เรย์
(X-ray photoemission electron microscopy, XPEEM) และ NEXAFS ตามลำดับ และศึกษาผลิตภัณฑ์
การกัดกร่อนโดยใช้เทคนิค XPS ผลการวิจัยพบว่าชั้นฟิล์ม DLC ที่เจือด้วย Al และ N ที่มีโครงสร้าง sp^3

C-N และ Al_2O_3 มีคุณสมบัติทางกลที่คล้ายคลึงกับของ DLC ที่ไม่เจือธาตุผสม (ความแข็ง = 49.04 ± 1.33 GPa, โมดูลัสยืดหยุ่น (E) = 251.09 ± 6.57GPa, ค่าเปอร์เซ็นต์การคืนรูป (%ER) = 58.43 ± 1.73) และยังมีการยึดเกาะของฟิล์มที่ดีขึ้น (ความต้านทานรอยขีดข่วน, CPRs = 12187.06 mN^2), ความคงตัวทางความร้อน (ทนต่ออุณหภูมิได้ถึง 600 °C) และความต้านทานการกัดกร่อนโดยการเพิ่มค่า E_{corr} จาก -443.31 ถึง -382.93 mV (เมื่อเปรียบเทียบกับ DLC บริสุทธิ์) ด้วยเหตุนี้ชิ้นงานทดสอบ ta-C:Al:N จึงเหมาะสำหรับใช้งานที่ต้องการความต้านทานการกัดกร่อนและทนความร้อน

สาขาวิชาวิศวกรรมวัสดุ

ปีการศึกษา 2564

ลายมือชื่อนักศึกษา _____

ลายมือชื่ออาจารย์ที่ปรึกษา _Pornwasa Wongpanya_

ลายมือชื่ออาจารย์ที่ปรึกษาร่วม _Pat Photongkam_

PRAPHAPHON SILAWONG : NANOMECHANICAL PROPERTIES, THERMAL STABILITY, AND CORROSION RESISTANCE OF ALUMINIUM AND NITROGEN DOPED DIAMOND-LIKE CARBON FILM. THESIS ADVISOR : ASSOC. PROF. PORNWASA WONGPANYA, Dr.-Ing., 145 PP.

Keyword: FCVA/Al-N Co-Doped DLC/NEXAFS/XPS/Nanomechanical/Adhesion Strength/ Thermal Stability/Corrosion Resistance

In engineering, AISI4140 low alloy steel is commonly utilized. It has outstanding mechanical qualities, including high tensile strength, fatigue resistance, toughness, and impact resistance, but low wear resistance. Surface enhancement is required for corrosive environments and operations at high temperatures to satisfy its application. Diamond-like carbon (DLC) film enhances hardness, modulus of elasticity, adhesion, abrasion resistance, heat resistance, and corrosion resistance. As a result, DLC films were produced by filtered cathodic vacuum arc (FCVA) for this investigation. This technique is capable of fabricating a hydrogen-free tetrahedral amorphous carbon (ta-C) film layer with a high sp^3/sp^2 carbon bond ratio. On the other hand, the ta-C film has a significant internal stress, which contributes to the coating's poor adherence to the metal surface. As a consequence, the adhesion strength is enhanced by the incorporation of doping elements into the DLC film to relieve internal stress. In this work, the developed DLC film was doped with aluminum (Al) and nitrogen (N) and synthesized by using the FCVA technique to coat AISI 4140 steel and produce ta-C, ta-C:N, ta-C:Al, and ta-C:Al:N films, respectively. The structure and chemical composition of the produced DLC films were investigated using Raman spectroscopy, X-ray photoelectron spectroscopy (XPS), and near edge X-ray absorption fine structures (NEXAFS). Following that, the mechanical characteristics and adhesive strengths of the films were determined. The oxidation behavior of the DLC films was determined using in situ heating NEXAFS, followed by the corrosion behavior of the whole film. They were evaluated using a potentiostat in a solution of 3.5 wt% sodium chloride (NaCl). Finally, the corroded regions and corrosion products from the corrosion test were evaluated using X-ray photoemission electron microscopy (XPEEM) and

NEXAFS, respectively, and the corrosion products were studied using XPS. The results indicated that Al and N–doped DLC film (ta–C:Al:N) with sp^3 C–N and Al_2O_3 structures had similar mechanical properties to that of non–doped DLC (ta–C) (hardness = 49.04 ± 1.33 GPa, elastic modulus (E) = 251.09 ± 6.57GPa, elastic recovery (%ER) = 58.43 ± 1.73), and also had improved film adhesion (scratch propagation resistance, CPRs = 12187.06 mN^2), thermal stability (temperature resistance up to 600°C), and corrosion resistance by raising the E_{corr} value from –443.31 to –382.93 mV (in comparison to pure DLC). As a result, ta–C:Al:N specimens are suitable for use in applications requiring corrosion resistance and thermal resistance.
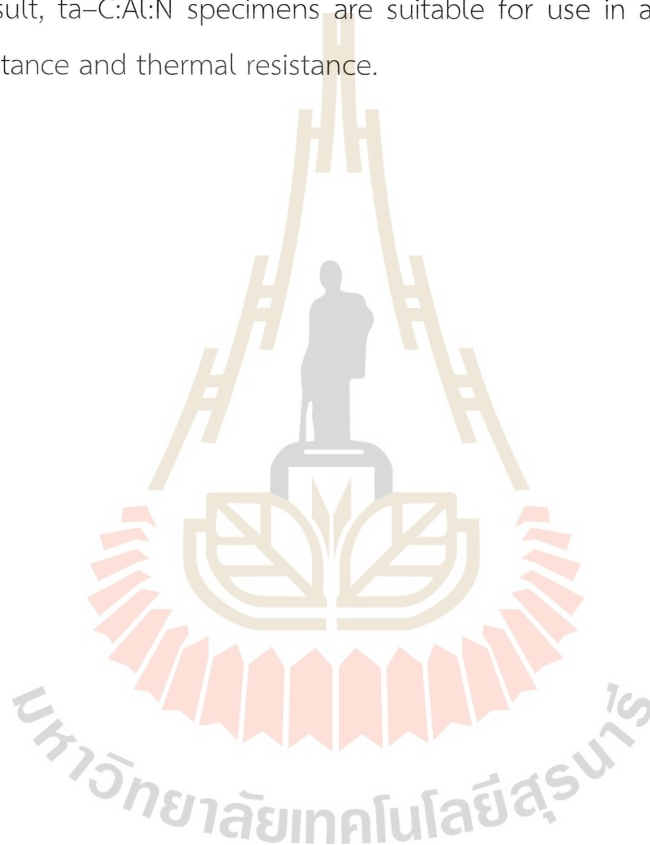
School of <u>Materials Engineering</u>

Academic Year <u>2021</u>

Student's Signature _____

Advisor's Signature _Pornwasa Wongpanya_

Co–Advisor's Signature _Pat Photongkam_

ACKNOWLEDGMENTS

Finally, I want to express my heartfelt gratitude to my wonderful family for their unending love and unwavering support during the writing of my thesis and my life in general. The Ph.D. thesis would not have been finished or made feasible without the kindness and care of everyone who has stood by my side.

Praphaphon Silawong

TABLE OF CONTENTS

Page

TABLE OF CONTENTS (Continued)

TABLE OF CONTENTS (Continued)

LIST OF TABLES

LIST OF TABLES (Continued)

LIST OF FIGURES

LIST OF FIGURES (Continued)

LIST OF FIGURES (Continued)

LIST OF FIGURES (Continued)

LIST OF FIGURES (Continued)

LIST OF FIGURES (Continued)

LIST OF ABREVIATIONS

a-C	=	Amorphous carbon
a-C:H	=	Hydrogenated amorphous carbon
BE	=	Binding energy
CR	=	Corrosion rate
E	=	Elastic modulus
E_{corr}	=	Corrosion potential
%ER	=	Elastic recovery
FCVA	=	Filtered cathodic vacuum arc
FOV	=	Field of view
FWHM	=	Full width at half-maximum
H/E	=	Plastic index parameter
HOPG	=	Highly oriented pyrolytic graphite
$h\nu$	=	Photon energy
i_{corr}	=	Corrosion current density
I_D/I_G ratio	=	The intensity ratio of the D and G bands
KE	=	Kinetic energy
kV	=	Kilo voltage
L_a	=	Cluster size of the sp^2 sites
L_c	=	Critical load
NEXAFS	=	Near edge X-ray absorption fine structure
OCP	=	Open circuit potential
P	=	Porosity
P_i	=	Protection efficiency
R_p	=	Polarization resistance
ta-C	=	Tetrahedral amorphous carbon
ta-C:H	=	Tetrahedral hydrogenated amorphous carbon
UHV	=	Ultra high vacuum

LIST OF ABREVIATIONS (Continued)

V_{bias} = Negative direct current bias voltage

X-PEEM = X-ray photoemission electron microscopy

XPS = X-ray photoelectron spectroscopy

XRR = X-ray reflectivity

θ_c = Critical angle

ρ = Density

σ = Compressive internal stress or Residual internal stress
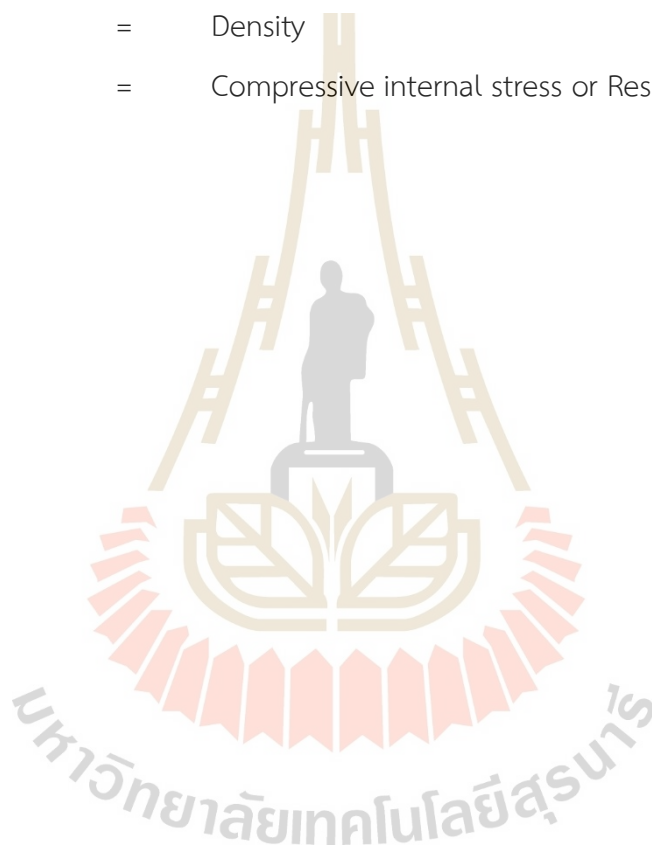
CHAPTER 1

INTRODUCTION

1.1 Rationale of the study

AISI 4140 steel is a low–alloy steel widely used in engineering applications. The main feature of AISI 4140 is that it contains low compositions of chromium (Cr) and molybdenum (Mo) which results in high hardness and fabrication ability. It has excellent mechanical properties (i.e., tensile strength and abrasion wear resistance) that can be enhanced by heat treatment processes such as quenching and tempering, and surface treatment (i.e., carburizing) for suitable application. AISI 4140 is used in automotive parts (i.e., gear, transmission, crank shaft, piston, and piston–ring) operating in environments of humidity, lubrication, temperature, and friction as consequences of corrosion and degradation of materials. Surface technologies, such as the carbonitriding and nitriding processes, have been used widely to prevent the steel surface from oxidation and corrosion (Grill, 1999; Mahmud *et al.*, 2015).

Diamond–like carbon (DLC) is an amorphous carbon with a structural combination of diamond (sp^3 bonding) and graphite (sp^2 bonding). It has recently been applied to automotive industries due to its unique properties, for example it has high hardness, a low friction coefficient, and is chemically inert. The DLC coating has been challenging because high internal stress can exist in the films when a thickness layer is required. Moreover, decreasing the sp^3/sp^2 ratio of DLC film at high temperature has an effect of low hardness. Therefore, the incorporation of elements in the DLC structure has been employed to enhance the adhesion efficiency and mechanical properties (Grill, 1999; Yang *et al.*, 2012).

In this research, the improvement of the oxidation and corrosion properties of the AISI 4140 through the DLC doping method with aluminium and nitrogen will be studied and discussed. Also, the mechanical properties and tribology will be investigated.

1.2   Aims of thesis

The purpose of this thesis was to synthesize DLC (ta–C), N–doped DLC (ta–C:N), Al–doped DLC (ta–C:Al), and co–doped (Al, N) DLC (ta–C:Al:N) films on an AISI 4140 low alloy steel substrate using a pulsed two–FCVA deposition method for improving the DLC films' oxidation and corrosion resistance. In addition, the structural bonding, nanomechanical properties, adhesion strength, and corrosion properties were examined, using a number of effective analytical approaches in order to gain a better understanding of the films' properties. The purpose was separated into three major areas:

1.2.1   To determine the optimal conditions for the deposition of ta–C, ta–C:N, ta–C:Al, and ta–C:Al:N films using the pulsed two–FCVA method.

1.2.2   To examine the thermal stability (oxidation resistance) of ta–C, ta–C:N, ta–C:Al, and ta–C:Al:N films at room temperature (RT) and the annealing temperature range to 700°C.

1.2.3   To get a better understanding of the mechanisms that contribute to the enhancement of the nanomechanical characteristics, corrosion resistance, and adhesion strength of ta–C, ta–C:N, ta–C:Al, and ta–C:Al:N films.

1.3   The scope of the study

1.3.1   The ta–C, ta–C:N, ta–C:Al, and ta–C:Al:N depositions were performed on a Si (100) wafer and an AISI 4140 low alloy steel substrate.

1.3.2   The ta–C, ta–C:N, ta–C:Al, and ta–C:Al:N films were synthesized using the developed pulsed two–FCVA deposition method with a separate cathodic arc source.

1.3.3   The doping elements were Al and N.

1.3.4   The following factors were used to determine the critical deposition parameters: base vacuum pressure, negative direct current bias voltage of the substrate, deposition time, arc voltage, pulse repetition or frequency rate, and duty cycle.

1.3.5   The following methodology was used to determine the identity of the ta–C, ta–C:N, ta–C:Al, and ta–C:Al:N films:

(a) for the microstructure, chemical composition, and bonding configuration, Raman spectroscopy, X–ray photoelectron spectroscopy (XPS), and near edge X–ray absorption fine structure spectroscopy (NEXAFS) were used.

(b) morphological evaluation of the surface used scanning electron microscopy (SEM) and atomic force microscopy (AFM).

(c) X–ray reflectometry (XRR) was used to determine density.

(d) nanomechanical properties was as determined by nanoindentation testing.

(e) adhesion strength was as determined by the nanoscratch testing.

(f) corrosion resistance was determined using a potentiostat analyzer.

(g) thermal stability was measured with X–ray photoemission electron microscopy (X–PEEM) in conjunction with in–situ NEXAFS.

1.4   The research places

1.4.1   Suranaree University of Technology's (SUT) Center for Scientific and Technological Equipment, Nakhon Ratchasima, Thailand.

1.4.2   Synchrotron Light Research Institute (SLRI), Nakhon Ratchasima, Thailand:

(a) Research Department Beamline 3.2Ub PEEM,

(b) Building and Utilities Division, Mechanical System Development and Utilities Department,

(c) Electrical and Electronics Division, Technical and Engineering Department.

1.5   Expected results

1.5.1   The ability to synthesize and analyze ta–C, ta–C:N, ta–C:Al, and ta–C:Al:N films deposited using the pulsed two–FCVA method.

1.5.2   Knowledge of ta–C, ta–C:N, ta–C:Al, and ta–C:Al:N films' microstructures, bonding configurations, nanomechanical properties, adhesion strengths, thermal stability, and corrosion resistance.

1.5.3   Al and N co–doping is a feasible method for increasing DLC's thermal stability, oxidation resistance, and corrosion resistance.

1.5.4   Gain experience of research in line with the principles of research practice, the solution of problems during research, and practice collaboration, together with contact and coordination in order to accomplish the research.

1.5.5   The study findings are published in international publications and are available in the SCOPUS or ISI databases.

1.6   Outline of the thesis

This thesis is split into five chapters, each of which is concerned with the deposition and characterization of the structure and properties of ta–C, ta–C:N, ta–C:Al, and ta–C:Al:N films produced by pulsed two–FCVA deposition.

The introduction to this thesis is stated above in this Chapter 1, including the rationale of the study, aims of this thesis, scope of the study, research places, expected results, and thesis outline.

The literature reviews in Chapter 2 provide a basic principle and brief review of AISI 4140 low alloy steel, diamond–like carbon (DLC) films, incorporation of alloying elements in DLC films, deposition methods for DLC films, applications of DLC films, nanomechanical properties and adhesion strength of non–doped DLC, doped DLC, and co–doped DLC films, thermal stability of DLC films, electrochemical corrosion, and a review of the literature.

The experimental procedures that have been implemented are described in Chapter 3 and include the preparation of the DLC films, the structural bonding configuration, elemental analysis, film thickness, density, nanomechanical properties and adhesion strength, and electrochemical corrosion analysis of the DLC films.

Chapter 4 offers a detailed description of the findings as well as a commentary of this study, which is divided into two major sections: (i) the structure, bonding configuration, thickness, and morphology of FCVA–synthesized ta–C, ta–C:N, ta–C:Al, and ta–C:Al:N films; and (ii) the nanomechanical properties and adhesion strength, thermal stability, and corrosion resistance of Al and N co–doped DLC films deposited on AISI 4140.

Finally, in Chapter 5, the thesis's findings and suggestions for further research are explored.

CHAPTER 2

RITERATURE REVIEWS

2.1   AISI 4140 low alloy steel

Due to its high strength and ductility, American Iron and Steel Institute (AISI) 4140 alloy steel is a chromium and molybdenum low alloy steel that is one of the most often used materials for gears, blades, and other industrial uses. Being subjected to difficult working conditions such as high temperatures, corrosion, oxidation, tribology, it suffers from severe mechanical failure modes including micro–pitting and scuffing which shorten the service life of essential components by causing full failure (Liu *et al.*, 2017; Khani Sanij *et al.*, 2012; Li *et al.*, 2014). Additionally, it is possible to enhance the mechanical characteristics, wear, and corrosion resistance of AISI 4140 steel by applying heat treatment and traditional surface treatments including quenching and tempering, carburizing, nitriding, nitrocarburizing, and plasma nitriding (Li *et al.*, 2014; Sayuti *et al.*, 2014; Kovaci *et al.*, 2018). For AISI 4140 steel, the chemical composition is mostly carbon (C) in the range of 0.39 – 0.48 wt%, chromium (Cr) 0.80 – 1.10 wt%, and molybdenum (Mo) 0.15 – 0.25 wt%, as listed in **Table 2.1**. Furthermore, **Table 2.2** and **Table 2.3** exhibit the mechanical and physical qualities, respectively.

Table 2.1 Chemical composition of AISI 4140 (modified from Suryo *et al.*, 2018)

Chemical composition (wt%)							
C	Si	Mn	P	S	Cr	Mo	Fe
0.39 – 0.48	0.20 – 0.35	0.75 – 1.00	≤0.035	≤0.04	0.80 – 1.10	0.15 – 0.25	balance

Table 2.2 Mechanical properties of AISI 4140 (modified from [Online], Available: https://www.theworldmaterial.com/astm–sae–aisi–4140–steel/)

Conditions	Normalized at 870 °C	Annealed at 815 °C	Water quenched from 845°C & tempered at 540 °C
Mechanical Properties			
Tensile strength (MPa)	1020	655	1075
Yield strength (MPa)	655	414	986
Elongation in 50 mm, %	17.7	25.7	15.5
Reduction in area, %	46.8	56.9	56.9
Hardness (HB)	302	197	311
Density (g cm^{-3})		7.85* (Liu *et al.*, 2017)	

Table 2.3 Physical properties of AISI 4140 (modified from [Online], Available: https://www.theworldmaterial.com/astm–sae–aisi–4140–steel/)

Physical Properties	Temperature (°C)				
	20	100	200	400	600
Electrical resistivity value (μΩ m)	0.22	0.26	0.33	0.48	0.65
Thermal conductivity value (W/m·K)		42.7	42.3	37.7	33.1
	Temperature (°C)				
	20–100		20–200	20–400	20–600
Coefficients of linear thermal expansion value (10^{-6}/K)	12.2		12.6	13.6	14.5
Specific heat value (J/Kg·K)			473	519	561

2.2   Diamond–like carbon (DLC) films

Since the 1990s, diamond–like carbon (DLC) has been gaining in popularity in industry (Vetter, 2014), because the DLC has excellent mechanical, tribological, and chemical properties, e.g., high hardness, elastic modulus, wear, oxidation and corrosion resistance, and a low friction coefficient (Donnet, 1998; Robertson, 2002; Bootkul *et al.*, 2014; Dai *et al.*, 2017; Zhou *et al.*, 2019). These properties depend on the structure of the carbon inside the DLC. The DLC structure can be modified by the deposition processes or methods and the incorporation elements, such as gas doping (i.e., hydrogen and nitrogen) and metal doping (i.e., silicon, titanium, aluminium, tungsten, chromium, and copper).

2.2.1   Structure bonding of DLC films

The DLC is an amorphous carbon structure with a proportion of diamond (sp^3 bonding) and graphite (sp^2 bonding) (Robertson, 2002; Aperador *et al.*, 2013; Ruden *et al.*, 2013; Lei *et al.*, 2019). In terms of being diamond–like, the proportion of sp^3 bonding can be manipulated to give different mechanical properties of DLC films. **Figure 2.1** shows the various structures of carbon–based materials, such as graphite, diamond, and amorphous carbon films (Robertson, 2002).

a) Graphite structure   b) Diamond structure

c) Diamond like carbon structure
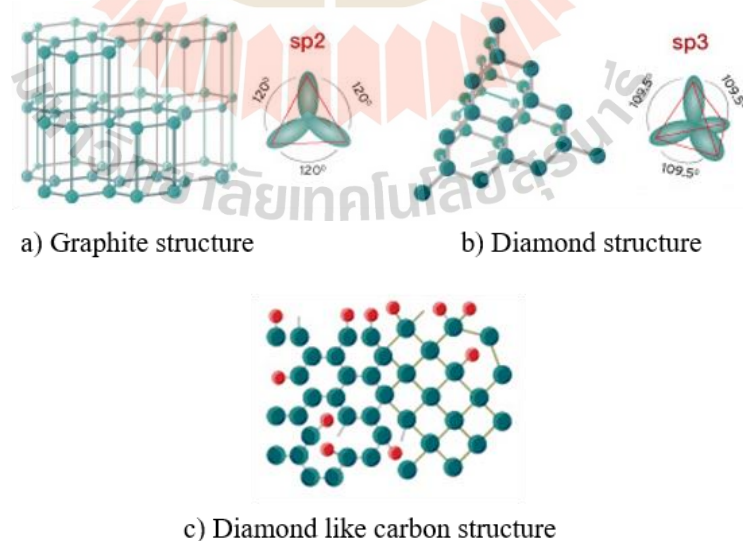
Figure 2.1 The structure of graphite, diamond, and DLC [Online], Available: [http://www.pvdadvancedtech.com/dlc/] Dec 30, 2021

There are 4 main categories of the DLC film depending on the hydrogen content, which are hydrogen–free amorphous carbon (*a*–C), hydrogenated amorphous carbon (*a*–C:H), hydrogen–free tetrahedral amorphous carbon (*ta*–C), and hydrogenated tetrahedral amorphous carbon (*ta*–C: H), respectively, (Grill, 1999). **Figure 2.2** shows the ternary phase diagram of sp^2, sp^3 and H components of various amorphous carbon (Robertson, 2002). In the lower left corner is the sp^2 bond showing the graphitic carbon and glassy carbon phases. The central area is both sp^2 and sp^3 bonded carbon demonstrated by the a–C: H or *ta*–C: H area (Grill, 1999; Robertson, 2002). The lower right corner shows the limits of hydrocarbon polymers and that no films can form in those regions. **Table 2.4** shows the main properties of the DLC film (Grill, 1999).
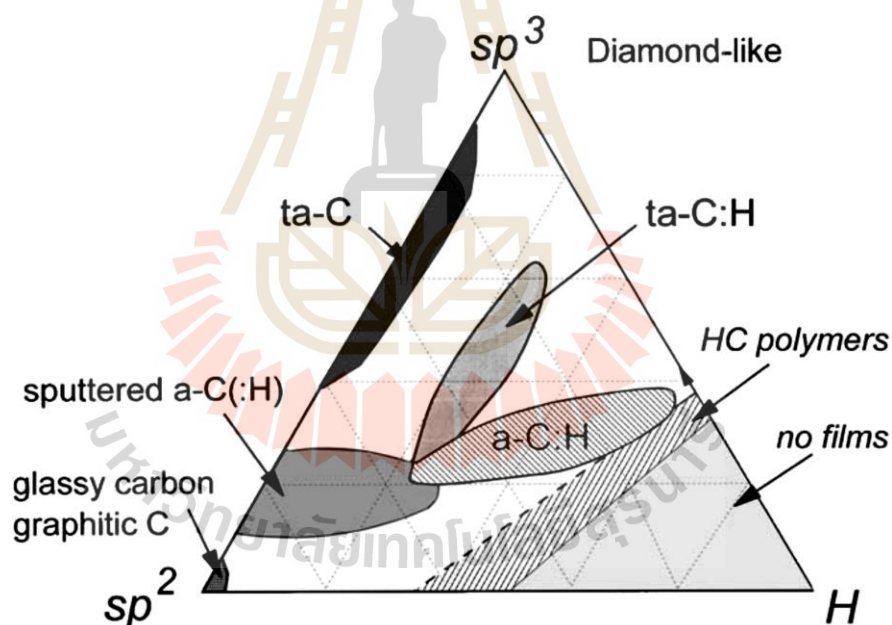
Figure 2.2 Ternary phase diagram of sp^2, sp^3 and H components of various amorphous carbon (Robertson, 2002).

2.2.2 Structure and mechanical properties of DLC films

The maximum hardness the DLC film is the tetrahedral–bonded hydrogen–free coating (ta–C), which is generated when carbon from graphite or hydrocarbon gas is evaporated or ionized in a vacuum and deposited on the substrate.

When the DLC film is deposited on the specimen's surface, it is organized with amorphous carbon atoms, and thus the term amorphous carbon. Amorphous carbon is made of carbon links between graphite (sp^2 bonds) and diamond (sp^3 bonds), with the ratio of diamond to graphite determined by the film's structure. Arc voltage, bias voltage, carbon ion energy, ion density, and temperature are critical parameters for creating a high–quality DLC film. The larger the sp^3 percentage of the diamond carbon bond (DLC) or sp^3 fraction, the more diamond–like the DLC film's characteristics. The DLC layer's distinguishing characteristics are its hardness, Young's modulus of elasticity (Young's modulus), and strong chemical inertness (Grill, 1999; Ferrari *et al.*, 2000; Robertson, 2002; Anders, 2008; Vetter, 2014).

Table 2.4 The comparison of the main properties of various amorphous carbon materials (Grill, 1999)

Materials	sp^3 (%)	H (%)	Density (g.cm^{-3})	Energy gap (eV)	Hardness (GPa)
Diamond	100	0	3.515	55	100
Graphite	0	0	2.267	0	–
Glassy C	0	0	1.3–1.55	0.01	3
Evaporated C	0	0	1.9	0.4–0.7	3
Sputtered C	5	0	2.2	0.5	–
ta–C	80–88	0	3.1	2.5	80
a–C:H Hard	40	30–40	1.6–2.2	1.1–1.7	10–20
a–C:H soft	60	40–50	1.2–1.6	1.7–4	<10
ta–C:H	70	30	2.4	2.0–2.5	50

2.3   Doping element in DLC films

Although the DLC film is very hard, durable, and chemically inert, the adhesion between the DLC layer and the substrate is often an issue. This is because when the film's thickness rises or as the DLC film grows, increased compressive forces inside the film arise, causing the film to peel away from the substrate material (Wang *et al.*, 2007;

Zhang *et al.*, 2013; Bootkul *et al.*, 2014). Thus, in order to maximize the performance of the DLC film without peeling and to decrease the stress inside the film layer. It also improves the adhesion between the film layer and the substrate material, which is why it is used for improvement and is common today, such as by including a combination of materials into the DLC film layer or by forming an interlayer between the film layer and the substrate material. Additionally, mixed components are used to combine 2 or more kinds and to provide additional features as required for the application (Sun *et al.*, 2016; Xu *et al.*, 2020; Dai *et al.*, 2016, 2017). Three types of doping agents are employed in DLC films:

Firstly, non–metallic doping elements that make bonds with carbon (C) in DLC films, such as nitrogen (N), oxygen (O), and fluorine (F), respectively (Hauert *et al.*, 1995; Bootkul *et al.*, 2014; Safaie *et al.*, 2017; Ryu *et. al.*, 2020).

Secondly, a class of metal alloys that react with carbon in the DLC film to form metal carbides; examples include titanium (Ti), chromium (Cr), tungsten (W), molybdenum (Mo), and iron (Fe) (Liu *et al.*, 2018; Zhang *et al.*, 2015; Cui *et al.*, 2019; Constantinou *et. al.*, 2017; Ray *et al.*, 2016).

Finally, a class of metal alloys that do not react with the carbon in the DLC film includes carbide compounds such as aluminium (Al), gold (Au), silver (Ag), copper (Cu), nickel (Ni), and cobalt (Co) (Ding *et al.* 2021; Zou *et al.*, 2012; Wang *et al.*, 2012). These are available as a pure metal contained inside a film or as a cluster of nanocrystals. The incorporation of the alloying elements of metal atoms into the DLC structure enhances the adhesion strength and reduced compressive stress. Additionally, it may aid in the enhancement of mechanical, tribological, and corrosion resistance, thermal stability, electrical and optical properties, and biocompatibility. It enables the use of film in a broader range of applications. However, since doping may result in an increase in the content of sp^2 in the carbon network structure (Bootkul *et al.*, 2014), the doping concentrations must be considered to prevent impairing the increased DLC film's properties.

2.4   Deposition methods for DLC films

DLC films can be synthesized by various techniques. In 1971, the first DLC thin

film was deposited by Aisenberg and Chabot using the ion beam deposition technique. Subsequently, the DLC deposition was developed by the chemical vapor deposition (CVD) and physical vapor deposition (PVD) methods, respectively. For the synthesis of DLC films, plasma enhanced chemical vapor deposition (PECVD) is the most commonly used method for the laboratory scale, but it has limited industrial applications. The sputtering method is preferred for industrial processes because of the ability and simplicity to adjust the process. Finally, the cathodic arc method can generate a high–density plasma ion, but it is limited in its applications because of the unstable cathode spot and insufficient filtering for the macroparticle elimination in the process. Currently, methods such as sputtering and cathodic arc coating have been evolved into the high–power impulse magnetron sputtering (HiPIMS) and filtered cathodic vacuum arc (FCVA) processes, respectively, to enable the generation of high–density and uniform plasma ions throughout the coating. Additionally, a magnetic filtered coil is included to filter and decrease the number of macroscopic particles that fall onto the film layer during coating, so that it is really possible to produce a high–quality diamond–like carbon film and to eliminate film defects.

2.4.1 Sputtering

Sputtering is a popular coating technique. The coated target is bombarded with ion energy created by the plasma in a glow discharge, causing sputtering of the coated target atoms which condense and form a thin layer on the coating surface. This procedure is carried out under argon gas conditions to promote the co–reaction of sputtering and acetylene gas. Furthermore, the specimen must be heated to roughly 200°C at a base pressure of approximately 10^{-1} Pa, to allow the ionization process to proceed easily. The procedure is capable of uniformly coating the workpiece. However, the consequence of significant surface heating is that there is a modest rate of film deposition and ionization in the plasma. At present, it is created by arranging magnets in such a manner that the initial pole is positioned in the middle of the workpiece. The second pole generates a magnetic ring around the workpiece's outside border, trapping electrons and increasing the likelihood of atomic collisions and electron ionization. This results in concentrated plasma in the coated target region and greater ion bombardment of the coated target. This results in a faster sputtering

rate and a faster surface coating deposition rate (Kelly and Arnell, 2000; Hainsworth and Uhure, 2007). This technique is known as magnetron sputtering and is shown in **Figure 2.3**.
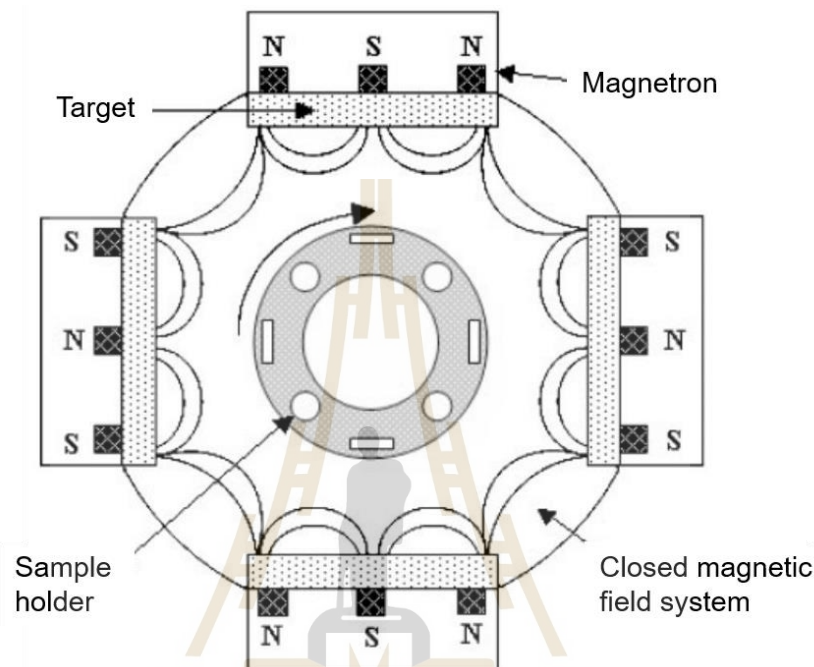
Figure 2.3 Schematic of the plasma in magnetron sputtering process (Hainsworth and Uhure, 2007)

2.4.2 Plasma enhanced chemical vapor deposition (PECVD)

To induce electron production between cyclotron resonance, inductively coupled or capacitively coupled areas, most PECVDs use radio frequency (RF) plasma at the ambient temperature. The capacitive parallel plate design is the most frequently used parallel plate configuration in which ion densities and the temperature distinguish the features of the plasma employed in the PECVD process. To reduce the reflected energy, the plasma has a radio frequency generator and a matching box. For traditional film coatings, the RF power ranges from 200 W to 20 kW, with RF electrodes utilized to form the plasma. Deposition variables such as temperature, deposition duration, pressure, inert gas flow rate, and the RF power

employed for the PECVD process all impact the deposition rate of the thin film created at 13.56 MHz. In plasma production, the surface might be positioned immediately between the parallel plates or at the plasma zone tip. The monomer inlet and argon gas is required for plasma formation and to prevent the effects of bombardment in the plasma zone. Additionally, it is connected to a vacuum pump which allows low-pressure film deposition within the standard PECVD coating chamber, which is shown in **Figure. 2.4** (Vasudev *et al.*, 2013; Pauschitz *et al.*, 2003; Woehrl *et al.*, 2014).
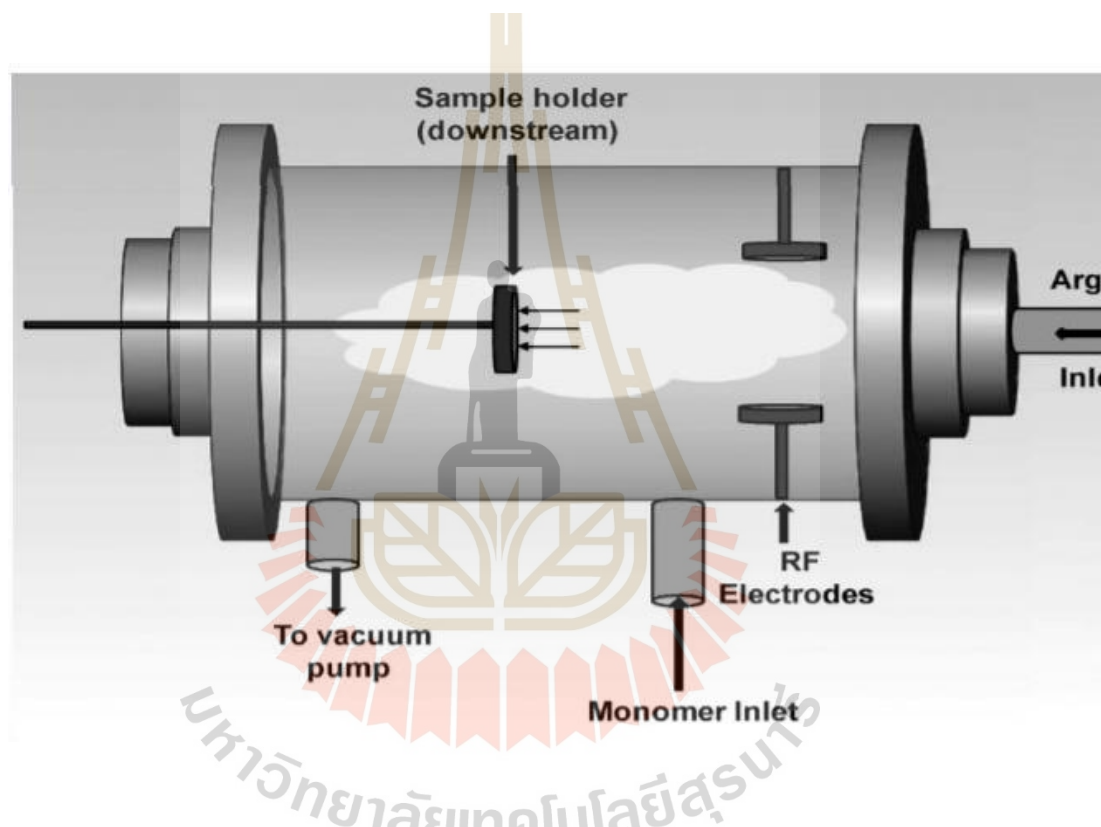
Figure 2.4 Schematic representation of a standard chamber used in the PECVD process (Vasudev *et al.*, 2013)

2.4.3 High power impulse magnetron sputtering (HiPIMS)

HiPIMS is a technology that uses a sputtering mechanism to generate vapor plasma at a base pressure of 10^{-4} Pa while being vacuumed by rotary vane pumps and turbomolecular pumps to maintain a constant amount of plasma discharge during the coating time. It uses up to a kW/cm^2 of electrical power, a kHz pulse frequency, and a microsecond duty cycle. A control approach may also be used to

alter the plasma density. High amounts of ionization are produced via power, frequency, and duty cycle, comparable to arc evaporation methods. As a result, ionization during coating is high, and the coating layer is thick. To reduce the number of flaws in the film, surfaces with intricate forms may be coated using this method. On the workpiece's surface, a low amount of heat is applied. HiPIMS is more suitable for creating usable films at lower temperatures than other technologies because, during lamination, an ion bombardment is delivered to the workpiece's surface to deposit the film. The schematic of the HiPIMS process is shown in **Figure 2.5** (Tucker, 2016; Gómez *et al.*, 2021).
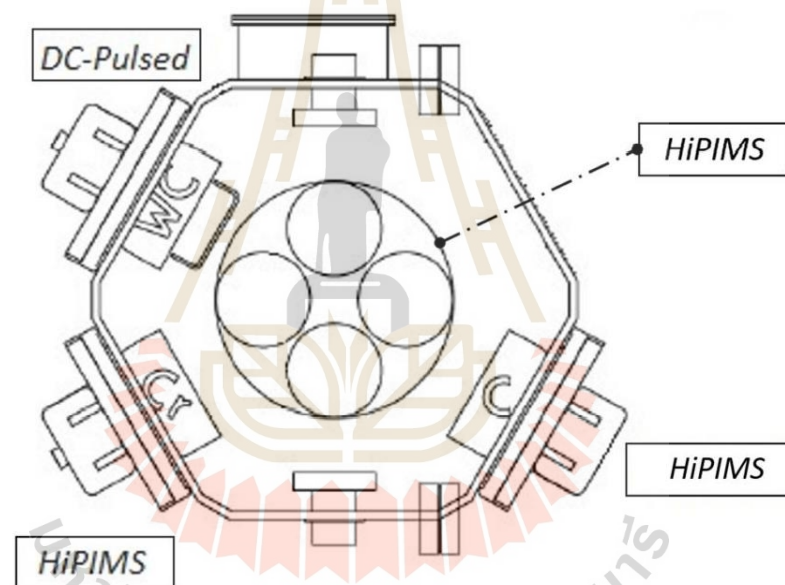
Figure 2.5 A horizontal cross–section of the HiPIMS chamber (Gómez *et al.*, 2021)

2.4.4 Filtered cathodic vacuum arc (FCVA)

The filtered cathodic vacuum arc (FCVA) is the most common technique used to synthesize the DLC film since it produces an excellent DLC film with sp^3 carbon bonds of more than 80% in the DLC film's structure, but it will produce the so–called macroparticles during the deposition. A 90–degree bending magnetic coil is used as a filter to control the plasma's direction. Subsequently, the macroparticles are trapped inside the coil and the remaining ions are controllable within the coil before expanding

rapidly toward the substrate which can remove more than 99% of the macroparticles. **Figure 2.6** shows the schematic diagram of the FCVA machine. It uses a high–frequency power DC voltage, a negative bias voltage at the substrate, a solid graphite used as the cathode, and a counter anode connected to the ground potential. The DLC film can thus be deposited in gas plasma by active ions moving through a magnetic coil and deposited on the substrate. **Figure 2.6** also shows the design of the FCVA system for doping of Al to the DLC film. As a result, carbon and aluminium ions can be simultaneously deposited on the substrate. The amount of the doping can be controlled by adjusting the arcing frequency ratio of the 2 cathodes. Nitrogen doping can be performed by introducing the nitrogen gas into a deposition chamber during the coating process (Anders, 2008; Marques *et al.*, 2003; Wei and Yen, 2007; Lu and Chung, 2008).
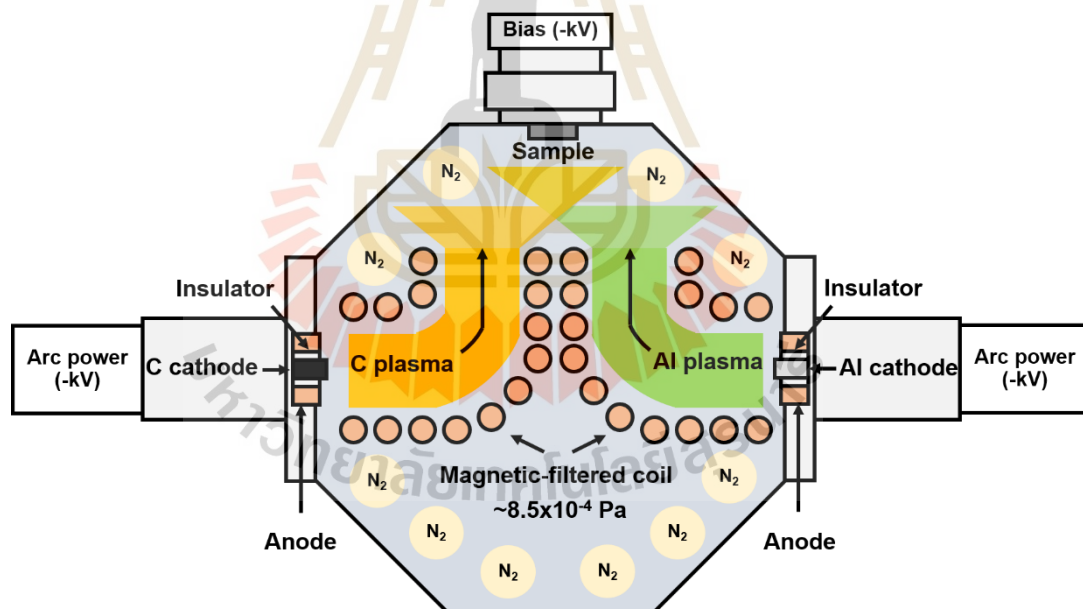
Figure 2.6 Schematic of developed FCVA technique for metal doping (Wongpanya *et al.*, 2022)

2.5   Applications of DLC films

The DLC coating techniques are becoming more prevalent nowadays due to its high hardness, wear resistance, and corrosion resistance, as well as its excellent thermal stability. As a result, the techniques are well–suited for automotive applications such as bearings and pistons for motors and pumps, as well as driving components such as gears and shafts. The diamond–like carbon coating on the drive shafts results in a 1% improvement in fuel efficiency and a 1% reduction in CO_2 emissions (Hainsworth and Uhure, 2007). Due to its strong electrical resistance, excellent thermal conductivity, and dielectric properties, DLC film may be used in a variety of applications in the electronics sector, including hard disk heads. Additionally, the use of elemental alloys such as Ti doping to increase the DLC characteristics may improve biocompatibility while maintaining strong corrosion resistance. Notably, it is non–toxic to the body (Wongpanya, Pintitraratibodee, Thumanu, & Euaruksakul, 2021; Liu *et al.*, 2018). This enables the use of DLC's tribological features in the medical field. Currently, it is employed as a coating on materials used in artificial joints – knees and hips – implants, and artificial heart valves. Depending on the DLC, this coating has excellent wear resistance, corrosion resistance, and thermal stability. DLC film is gaining popularity and is being utilized in an increasing number of other applications, including home appliances, razor blades, jewellery, and wristwatches. As can be seen, the DLC covering has been a huge success for many decades in addressing many real engineering difficulties. There is a competitive opportunity to further enhance the characteristics of DLC to meet the expectations of additional future applications (Hainsworth and Uhure, 2007; Konkhonthot *et al.*, 2018). Some examples of the application of DLC films are shown in brief in **Figure 2.7**.

Figure 2.7 Examples of the DLC coating application: automotive parts, engineering parts, hard disk drive parts, medical parts, razor blades and a watch (Hainsworth and Uhure, 2007; [Online], Available: http://nptel.ac.in /courses/115103038/28; [Online], Available: http://www.indiamart.com /devraj– engineering/job–work.html; [Online], Available: http://www. caperay. com/blog/ index.php /2013/i-guarantee–this–device–wont–fail/; [Online], Available: http://www.intechopen. com/books/ arthroplasty– update/the–evolution–of–modern–total–knee–prostheses; [Online], Available: https://watchessiam.com/2019/10/30/panerai–luminor –titanium –dlc–bucherer –blue–pam01021/)

2.6 The nanomechanical and adhesion strength of DLC films

2.6.1 Nanoindentation testing

Nanoindentation is commonly used for determining the mechanical properties (i.e., hardness, elastic modulus, creep, and residual stress) of thin–film and nanocomposite materials. The result of the nanoindentation shows the load and contact stiffness as a function of the displacement of the indenter onto the samples, as shown in **Figure 2.8**. The Oliver and Pharr equation model is used to determine the

elastic modulus of the thin films from the linear portion of the force–displacement unloading curve that can be shown in the following Equation (2.1) (Oliver and Pharr, 2004):

$$S = \frac{dP}{dh} = \frac{2\sqrt{A}}{\sqrt{\pi}} \times E_r \qquad (2.1)$$

where E_r is the reduced modulus (GPa), S is the contact stiffness (N/m), and A is the contact area (m). Then, the reduced modulus E_r can be computed from the following Equation (2.2):

$$\frac{1}{E_r} = \frac{1-v_i^2}{E_i} + \frac{1-v_s^2}{E_s} \qquad (2.2)$$

where E_i and V_i are Young's modulus and Poisson's ratio of the indenter. And then, E_s and V_s are Young's modulus and Poisson's ratio of the specimen, respectively.

Finally, the hardness can be calculated using the relative of the following Equation (2.3),

$$H = \frac{P_{max}}{A} \qquad (2.3)$$

where H is the hardness (H_v), P_{max} is the peak of indentation load (N), and A is the projected area of the hardness impression (m).
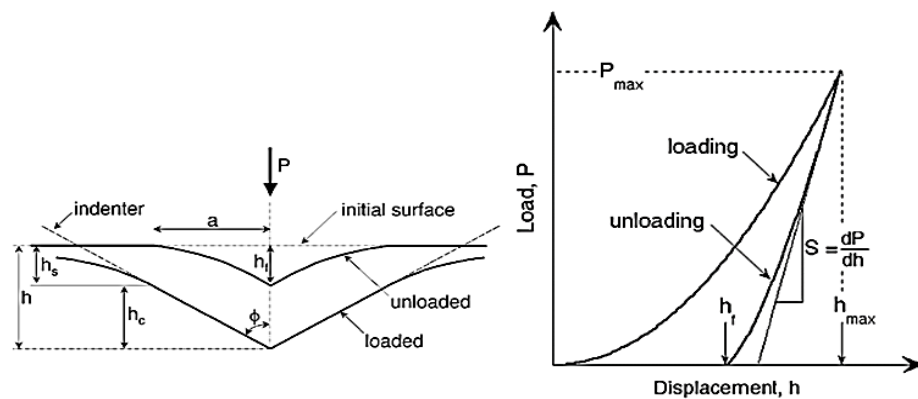
Figure 2.8 Schematic of the load and displacement curve, and deformation surface (Oliver and Pharr, 2004)

2.6.2 Adhesion testing

Adhesion strength is a very important property of the coating films which shows the critical strength between the interface of the coating film and the substrate (Marjanovic *et al.*, 2006; Moerlooze *et al.*, 2011). In the field of science, the adhesion strength is a major concern for designing engineering parts, automotive parts, tools, medical equipment, etc. The adhesion test is widely used to investigate the adhesion strength between the coating and the substrate because it is easy to prepare a sample test and it is reliable. Various methods have been efficiently used to evaluate the cohesive strength of DLC film, such as the pull–off test, tape test, chisel test, bend test, and scratch test (Marjanovic *et al.*, 2006). A scratch tester is used to measure the mechanism of the adhesion strength to obtain constant normal loads on a coating film until film damage has occurred in testing and it exhibits the critical load (L_c) of the film. In addition, the constant load confirmation of the film damage during the scratch test is also simulated by the acoustic emission (AE) and electrical surface resistance (ESR) techniques, respectively (Moerlooze *et al.*, 2011).
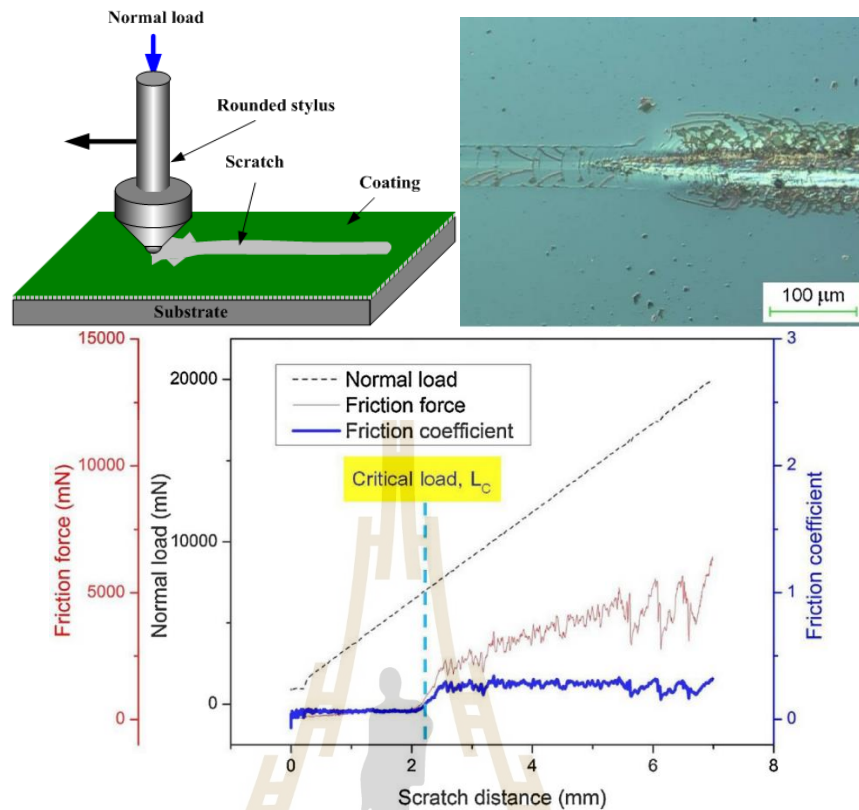
Figure 2.9 The schematic of a scratch tester, the result of the scratch test, and a microscope image of the damaged features at the critical (L_c) (Bootkul et al., 2014; Tay et al., 2000)

For adhesion testing, the resistance to crack initiation will be considered from L_{c1}. This means that the greater the L_{c1}, the more difficult it is to create a fracture in the film. Furthermore, the toughness of the film should be proportional to the difference between the higher and lower critical loads ($L_{c2} - L_{c1}$), as well as proportional to the lower critical load L_{c1} (Zhang *et al.*, 2004). Thus, scratch crack propagation resistance, or CPRs, is often employed to assess the adhesion strength as shown in Equation (2.4) below:

$$CPRs = L_{c1} (L_{c2} - L_{c1}) \tag{2.4}$$

2.7   Thermal stability of DLC films by in–situ NEXAFS

High–temperature oxidation of metals is a corrosion process, involving the reaction between a metal and the atmospheric oxygen at a high temperature. It results in an oxide layer formed on the surface of the oxidized metal. The oxide layer may protect an underlying metal or may also thicken into a non–protective layer with various defects, such as a cavity, micro–crack, and porosity. The oxide layer degrades the underlying material's properties, particularly the strength, corrosion resistance, and conductivity. These degradations are a problem for engineering parts such as heat exchangers, valves, pistons, and cutting tools. Rapid deterioration is observed for steel automotive parts exposed to high temperatures during service. The in–situ NEXAFS methodology (Maruyama *et al.*, 2015; Lapteva *et al.*, 2019) was utilized to evaluate the structural changes of the DLC film layer while heated by rapid thermal annealing (RTA), which is a heating method, for the thermal stability investigation in this work. RTA uses filaments to heat the specimen in a high vacuum system in the main analysis chamber until the test temperature is attained, and then the heating period is measured. At the end of the time, the temperature was lowered to 300°C, and the local bonding structure was assessed to determine its thermal stability based on the increasing quantity of the graphite structure (sp^2 fraction), known as graphitization, in the DLC film layer (Konkhunthot *et. al.*, 2019; Zhang *et al.*, 2002).

Photoemission electron microscopy (PEEM) is an imaging technique which utilizes photo–emitted electrons to generate an image of a surface. It can be used to analyze the elemental components and chemical structures at a particular area at microscale size. **Figure 2.10** shows the SPELEEM schematic. The microscope consists of multiple lenses and an energy analyzer between the projector lens and the multichannel plate screen (MCP). Secondary electrons, Auger electrons, and photoelectrons can be selected with the energy analyzer to form the image (i.e., low pass filtering).
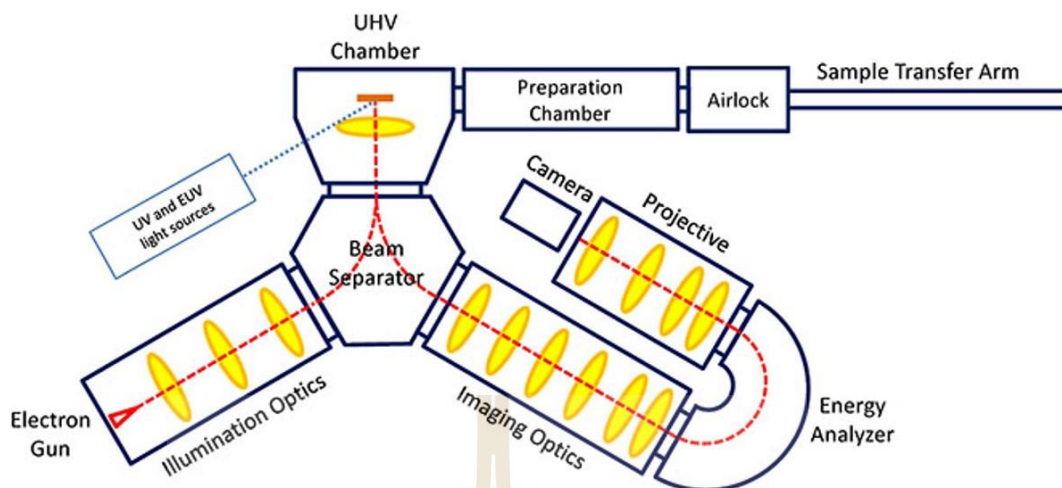
Figure 2.10 chematic of spectroscopic photoemission and low electron microscope (SPELEEM) [Online], Available: https://groups.oist.jp/fsu/leem–peem
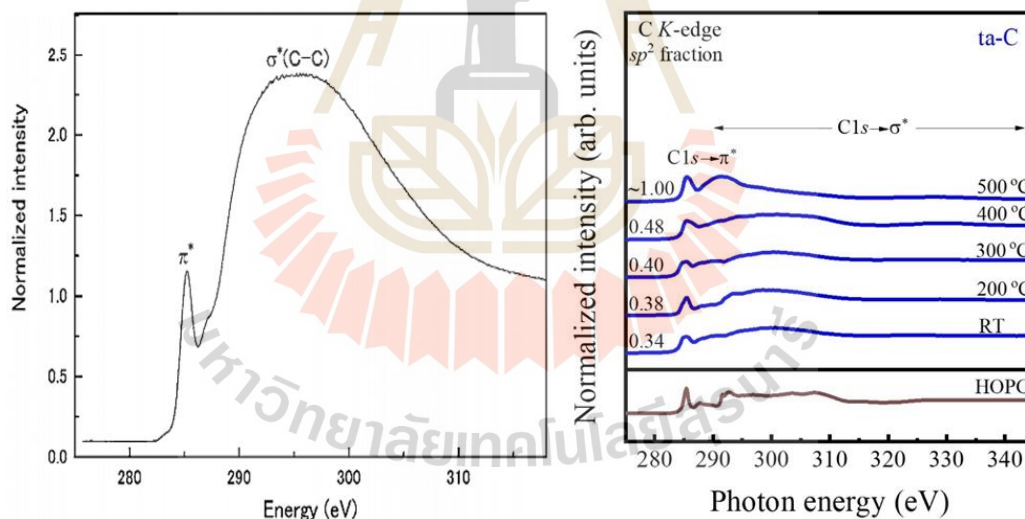
Figure 2.11 C *K*–edge NEXAFS spectrum of DLC film from X–ray absorption technique and C *K*–edge NEXAFS spectra obtained at room temperature (RT) and thermally annealed to graphitization temperature for ta–C (Saikubo *et al.*, 2006; Wongpanya, Silawong, & Photongkam, 2021).

In metallurgy, the PEEM is used to observe the formation of a microstructure and to characterize the chemical compositions on a material's surface in real–time. The technique has the capability for X–ray absorption spectroscopic imaging, especially in the soft X–ray region. It can be used to analyze the structure of the C, Al and, N in the DLC film (Euaruksakul *et al.*, 2013). **Figure 2.11** shows the C *K*–edge NEXAFS spectrum, obtained from the PEEM and C *K*–edge NEXAFS spectra obtained at room temperature (RT) and thermally annealed to the graphitization temperature for ta–C for the local bonding of carbon elements from the NEXAFS analysis in this study, as illustrated in **Table 2.5**.

Table 2.5 The local bonding of carbon elements obtained from the NEXAFS analysis.

Type of bonding	Energy band (eV)	Reference
π^* (C=C sp^2)	285.4	Konkhunthot *et. al.*, 2019
π^* (C=N sp^2)	285.9	Zhang, 2003
π^* (C=OH)	286.1	Sainio, 2021
π^* (C–O)	286.5	Gandhiraman, 2014
σ^* (C–H)	287.5	Sainio, 2016, McChan, 2005
σ^* (C–N sp^3)	287.7	Zhang, 2003
π^* (C=O)	288.5	Gandhiraman, 2014 Sainio, 2016
σ^* (C–C sp^3)	289.8	Sainio, 2016
σ^* (C=C sp^2)	292.8	Sainio, 2016
σ^* (C–O)	297.5	Gandhiraman, 2014
σ^* (C≡C sp^1)	303.8	Ohmagari, 2009

2.8 Electrochemical corrosion of DLC films

2.8.1 Electrochemical corrosion

Corrosion is the degradation and destruction of a metal that has reacted with the environment. The corrosion product is mostly formed as an oxide film on the

surface that is affected by the decrease of mechanical properties, conductivities, and the reflection of material. Delamination of oxide film can be generated by an initial crack on the surface and develop finally into a fracture. Therefore, corrosion testing is important to study the corrosion behavior of materials. Currently, the potentiostat analyzer is widely used to evaluate the corrosion rate of materials. The concept of a potentiostat analyzer is that the corrosion current and potential occurring from an electrochemical reaction will be measured between the specimen and the reference electrode, and the specimen and the counter electrode, respectively.

The relationship between a potential and current density is plotted and is called a polarization curve. The polarization curve is used to determine the corrosion rate. **Figure 2.12** shows the schematic of a potentiostat analyzer.

There are three electrodes used to conduct the corrosion test:

1. An Ag/AgCl (3.3M KCL) used as a reference electrode;
2. A platinum or graphite rod used as a counter electrode;
3. A specimen used as a working electrode.
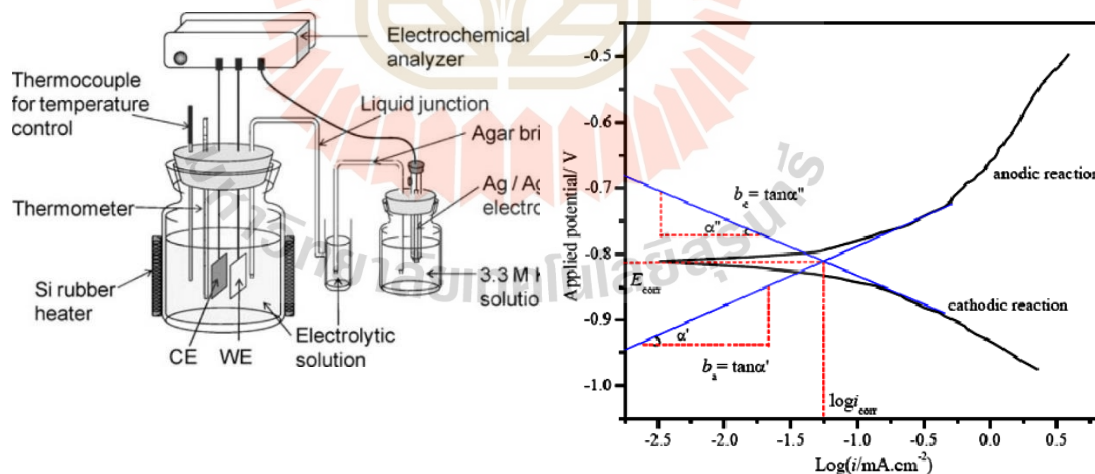
Figure 2.12 The schematic of a potentiostat analyzer and polarization curve [Online], Available: http://jes.ecsdl.org/content/159/4/D181.abstract., (Bhandari *et al.*, 2012)

In the DLC films, the corrosion resistance has been evaluated by potentiostat analyzer in sodium chloride (NaCl) solution (Bhandari *et al.*, 2012; Khun *et al.*, 2009). **Figure 2.13** shows an example of the polarization curve of the DLC film and an SEM image of the corrosive area after corrosion testing.
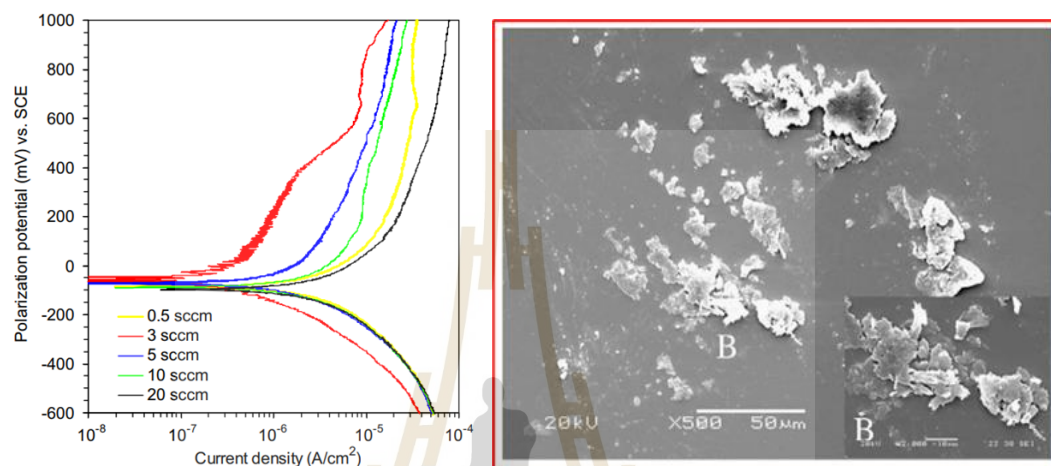
Figure 2.13 The polarization curve of ta–C:N and SEM image after potentiodynamic polarization test (Khun *et al.*, 2009).

2.8.2 Electrochemical analytical method and Interpretation of result data

Using Faraday's law and the Tafel extrapolation technique, significant corrosion parameters such as the corrosion potential (E_{corr}), the corrosion current density (i_{corr}), the polarization resistance (R_p), and the anodic and cathodic Tafel constants (b_a and b_c, respectively) were extracted from the acquired polarization curves as illustrated in **Figure 2.14**.
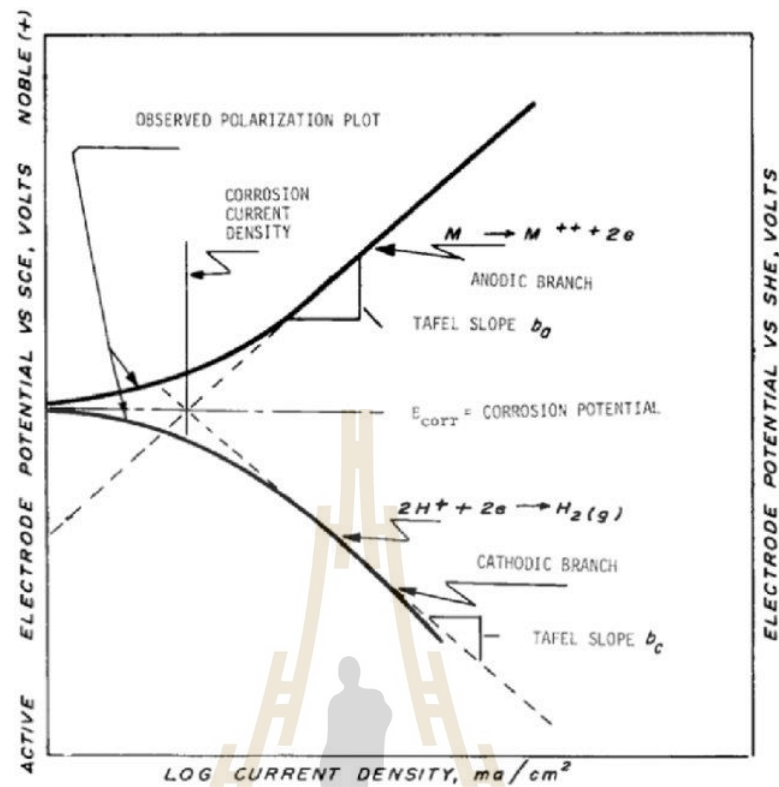
Figure 2.14 The polarization curve of E_{corr} and i_{corr} from polarization test [ASTM standard G3–89, 2006]

The corrosion rate (CR) was calculated using i_{corr}, whereas R_p was calculated using Equations (2.5) – (2.6) according to ASTM G102–89 and ASTM G59–97, respectively (ASTM Standard G102–89, 2015; ASTM Standard G59–97, 2014).

$$CR = \frac{0.00327 \times i_{corr} \times EW}{\rho}$$ (2.5)

where i_{corr} is the corrosion current density (μA cm^{-2}), EW is the alloy equivalent weight (derived from using Equation (7) and is each sample's density (g cm^{-3}), in which the XRR method was used in conjunction with XRD to determine this: 7.85, 2.52, 2.22, 2.17, and 2.32 g cm^{-3} for AISI 4140, ta–C, ta–C:N, ta–C:Al, and ta–C:Al:N, respectively.

$$EW = \frac{1}{\sum \frac{f_i n_i}{W_i}}$$

(2.6)

where f_i is the mass fraction of the ith element in the sample, n_i is the number of electrons transferred during corrosion of the ith element in the sample, and W_i is the ith element's atomic weight.

$$R_p = \frac{(b_a \times b_c)}{(2.303 \times (b_a + b_c) \times i_{corr})}$$

(2.7)

where R_p denotes the polarization resistance in Ω cm^2, i_{corr} denotes the corrosion current density in A cm^{-2}, and b_c and b_a denote the cathode and anode Tafel slopes in V dec^{-1}, respectively (ASTM Standard G59–97, 2014).

In addition, Equations (2.8) – (2.9) (Konkhunthot et $al.$, 2019; Matthes et $al.$, 1991; Yu et $al.$, 2003) may be used to calculate the porosity (P) and protective efficiency (P_i) of each DLC film, which are crucial indicators of the films' corrosion resistance.

$$P = \frac{R_P^0}{R_p} \times 10^{-|\Delta E_{corr}/b_a|}$$

(2.8)

where R_P^0 and R_p are the substrate's and the DLC's polarization resistances, respectively, ΔE_{corr} is the substrate's and the DLC's corrosion potential difference, and b_a is the substrate's anodic Tafel slope.

$$P_i = 100\left(1 - \frac{i_{corr}}{i_{corr}^0}\right)$$

(2.9)

The corrosion current density of the substrate and the DLC film, respectively, are i_{corr}^0 and i_{corr}.

This thesis will investigate the influence of Al–N dopants on the structure, mechanical properties, adhesion strength, thermal stability, and corrosion resistance, respectively. The DLC films were deposited utilizing 2 pulsed FCVA deposition processes to produce the DLC films of the ta–C type. In the system, there is a magnetic field coil that can be used to eliminate the macroparticles that produce surface defects in each of the DLC films. To investigate the link between the films' structures, mechanical characteristics, adhesion strengths, thermal stability, and corrosion resistance capabilities, AISI 4140 steel was coated with DLC films. It was utilized to analyze a film's structure and thermal stability using in–situ Near edge x–ray absorption fine structure (in–situ NEXAFS) spectroscopy. The ta–C, ta–C:N, ta–C:Al, and ta–C:Al:N films were investigated at room temperature (RT) and during utilizing radiant heating and electron beam bombardment. The cross section was evaluated using heat annealing to 700°C, field emission scanning electron microscopy (FE–SEM), and focused ion beam etching in conjunction with scanning electron microscopy (FIB–SEM). DLC Raman spectroscopy was used to determine the critical structural parameters such as the I_D/I_G ratio, peak D and G, full width at half maximum (FWHM (G)), compressive residual stress (CRS), and cluster size of the sp^2 sites or graphite (L_a), while X–ray photoelectron spectroscopy (XPS) was used to determine the impurities content and sp^3/sp^2 ratio. Nanoindentation was used to determine a film layer's adhesion capability. Finally, the DLC film's corrosion resistance was examined using a potentiostat analyzer, and the specimen's surface was evaluated after corrosion tests using XPS, NEXAFS, and SEM, respectively.

CHAPTER 3
EXPERIMENTAL PROCEDURES

3.1   Preparation of DLC films by FCVA

The workpieces were separated into 2 groups for this investigation. The first set were investigated for the coating's nanomechanical characteristics, thermal stability, and thickness layer. The first set (set I) of the specimens used were coated with ta–C, ta–C:N, ta–C:Al, and ta–C:Al:N film. All films were coated on AISI 4140 steel samples. After 30 minutes for the coating time, the specimens were evaluated for the film layer structure in preparation for mechanical property testing, the thermal stability, and the thickness of the film layer, respectively.

For the second set (set II) of workpieces, all 4 kinds of film were coated, and the workpieces named identically to the first set, but the thickness was uniform throughout. All film layers were coated on Si (100) specimens to determine the film density and thickness, as well as on AISI 4140 steel to determine the corrosion resistance and film adhesion strength, and to analyze the complete film layer's structure. The procedure chart of the thesis activities for the research and the coating parameters for the FCVA deposition of ta–C, ta–C:N, ta–C:Al, and ta–C:Al:N are as shown in **Figure 3.1** and **Table 3.1**, respectively.
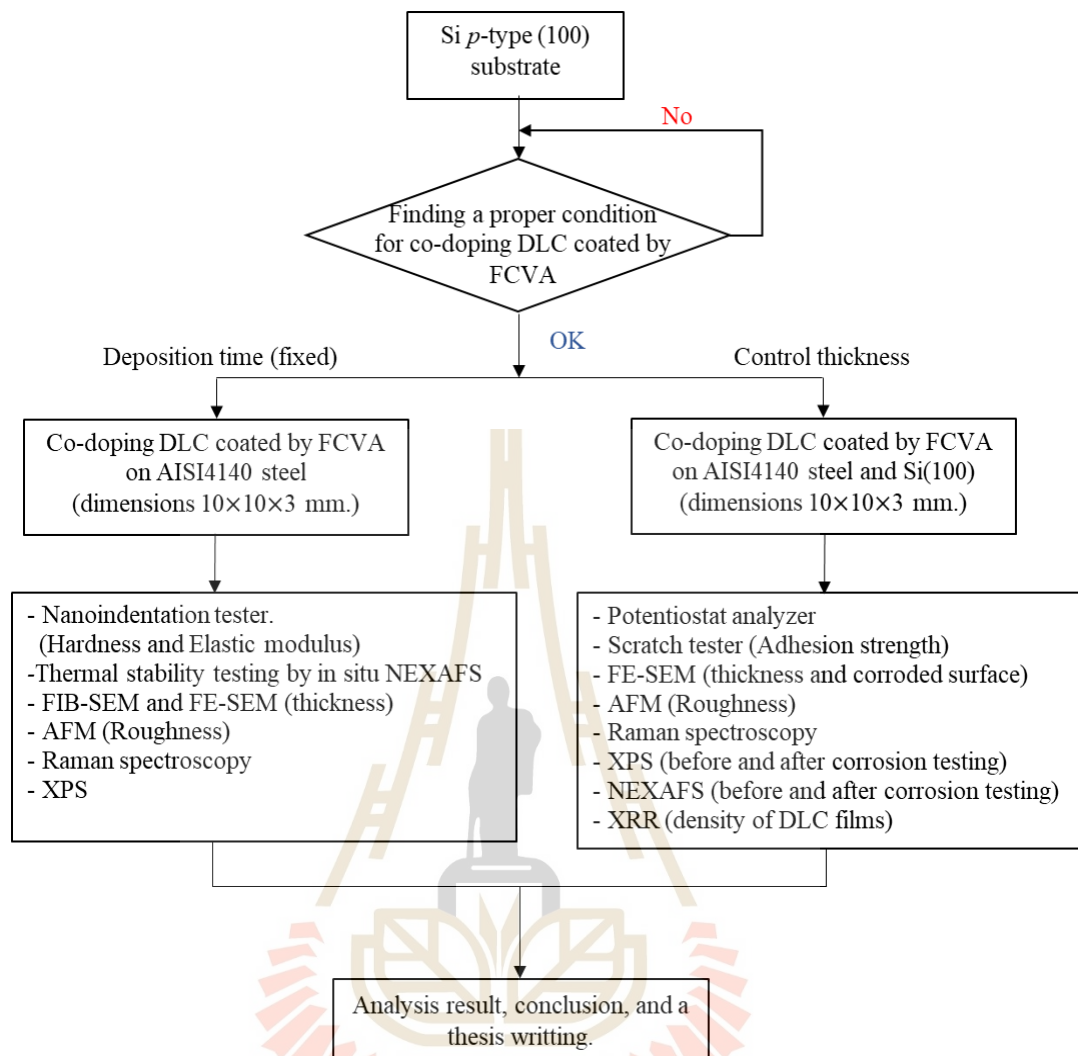
Figure 3.1 The procedure chart of project activities for research on the topic of nanomechanical properties, thermal stability, and corrosion resistance of aluminium and nitrogen doped diamond–like carbon film

Table 3.1 Coating parameters for FCVA deposition of ta–C, ta–C:N, ta–C:Al, and ta–C:Al:N. (modified from Wongpanya, Silawong, & Photongkam, 2021; Wongpanya *et al.*, 2022)

Coating parameters	Deposited time	Control thickness
Coating materials (Targets)	Graphite (99.99% C) and Aluminium (99.99% Al)	
Arc potential applied to cathodes (V_{arc})	400 and 800 V for Al and C	
Base pressure	8.5×10^{-4} Pa	
Base pressure for N doping	3.0×10^{-2} Pa	
UHP N_2 flow rate	2.5 SCCM* for ta–C:N and ta–C:Al:N	
Bias voltage applied to cathodes (V_{bias})	–1000 V	
Duty cycle	0.003%	
Frequency	6.0 Hz	
Coating time	30 min	19, 15, 30, and 22 min for ta–C, ta–C:N, ta–C:Al, and ta–C:Al:N, respectively

*SCCM denotes standard cubic centimeters per minute at standard temperature and pressure (STP)

    3.1.1   The DLC film samples were coated on AISI 4140 steel and Si (100) which were cut into $10 \, mm^2$ pieces. All the samples were ground using silicon carbide paper of successively finer grits up to 1500 grit, and then ultrasonically cleaned with acetone and ethanol for 20 minutes to remove surface contamination before being dried with N_2 gas (99.99% pure).

    3.1.2   To deposit the non–doped, doped, and co–doped DLC coatings, the pre–cleaned substrates were put into an FCVA chamber, which was then evacuated to a regulated base pressure of 8.5×10^{-4} Pa.

    3.1.3   On each cathodic source, a graphite cathode and an aluminium cathode (99.00%C and 99.99%Al) with an 8–mm rod were fitted independently. During the DLC deposition, targets and ceramic insulators were put between the anode and cathode and a conduction line was marked with a graphite pencil to commence the spot arc and create the plasma arc discharge. Magnetic filter coils with 90–degree bends were used to filter the plasma produced by the source during the DLC deposition, and the

distance between the magnetic filter coil output and the substrate was 30 mm, as shown in **Figure 3.2**.

      3.1.4   In order to maintain the balance between the cathode consumption and arc stability during deposition, a bias voltage (V_{bias}) of −1000V was used to drive the arc current with pulse repetition rates of 6.0 Hz and a duty cycle of 0.003% for both the graphite and aluminium cathodes, as shown in **Table 3.1**.

      3.1.5   To eliminate any surface contaminations, both the aluminium and graphite cathodes were arced for 5 minutes at V_{bias} of −1500 V (Konkhunthot *et al.*, 2018, 2019). To eliminate any surface oxides and provide an active surface for DLC films, the substrate was blasted with carbon ions at a V_{bias} of −1500 V, which was greater than the bias employed in the deposition procedure.

      3.1.6   After the vacuum pressure was reduced to 8.5×10^{-4} Pa, the film coating process began. Before N doping, ultrahigh purity (UHP) N_2 gas was constantly circulated into the chamber, raising the vacuum pressure from the base pressure to 3×10^{-2} Pa; there was a wait of 5 minutes to ensure that the N_2 gas was flowing stably within the chamber (Bootkul *et al.*, 2014).

      3.1.7   On the jig, the sample was deposited (a cross region between C and Al) and V_{bias} was applied immediately.

      3.1.8   Non–doped DLC (ta–C), nitrogen–doped DLC (ta–C:N), aluminium–doped DLC (ta–C:Al), and aluminium and nitrogen co–doped DLC (ta–C:Al:N) films can all be produced via FCVA deposition, as listed in **Table 3.1**.
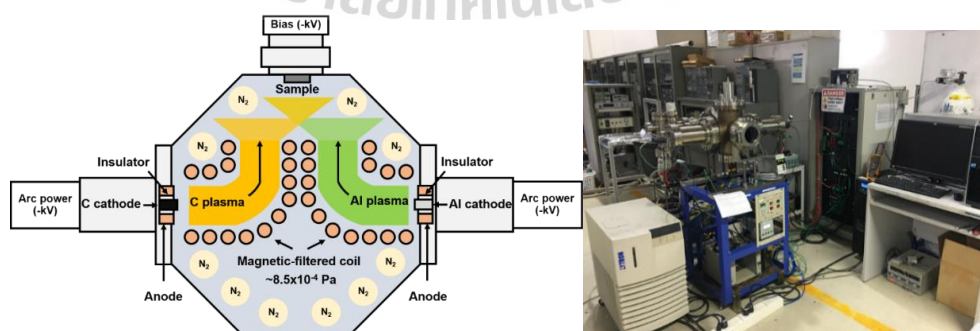
Figure 3.2 Schematic of developed FCVA technique for synthesis films (Wongpanya *et al.*, 2022)

3.2 Structural bonding configuration, elemental analysis, film thickness and surface morphology

3.2.1 Raman spectroscopy

Raman spectroscopy, a popular technique, is a non–destructive method to characterize the structure of carbon–based materials. As light is scattered on a surface, there are 2 main types of scattering, an elastic process (Rayleigh scattering) and an inelastic process (Raman scattering). The Raman scattering occurs by atomic vibration in the excited state within the energy shell in accordance with the Boltzmann's law based on Raman spectroscopy. The scattered photon is generated mostly into low energy (Stokes scattering) and high energy (anti–Stokes scattering) more than an absorbed photon, as shown in **Figure 3.3**.
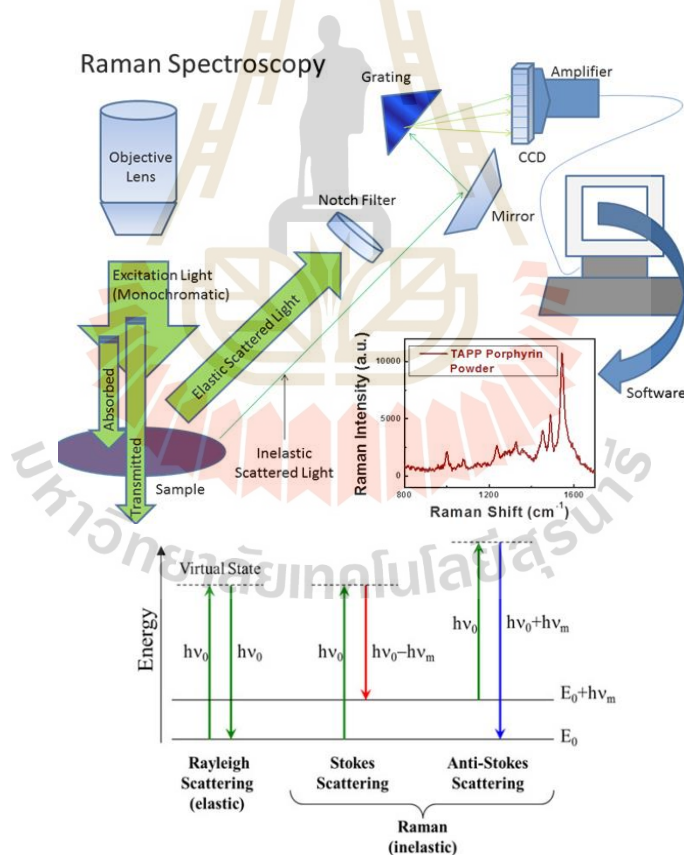
Figure 3.3 Schematic of Raman spectroscopy [Online], Available: http://bwtek.com/
Raman–theory–of–Raman–scattering/; [Online], Available : https:// www3.
nd.edu/~kamatlab/facilities_spectroscopy.html

Figure 3.4 shows Raman spectra of HOPG, glassy carbon and DLC film. The Raman shift is commonly used to explain the microstructure of the amorphous carbon via the Raman parameters, for example, the intensity ratio of the D and G bands (I_D/I_G ratio), the position of the D and G bands (Raman shift or wavenumber in-unit cm^{-1}), and the full width at half maximum (FWHM) of the D and G bands, respectively. The Raman results show the relationship between the atom and molecular vibration, which can describe the domain size and internal stress sensitivity of an amorphous thin film (Chu and Li, 2006).
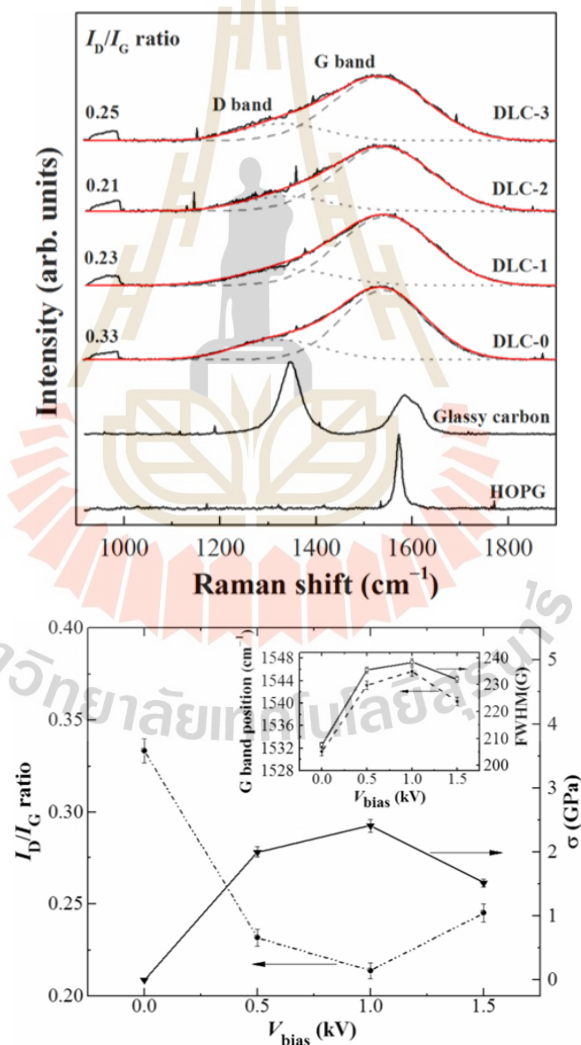
Figure 3.4 The Raman spectra of DLC films and the relationship of I_D/I_G ratio, FWHM (G) as a function of the various V_{bias} (Konkhunthot *et al.*, 2018)

A dispersive Raman microscope (SENTERRA, Bruker Optik GmbH, Ettlingen, Germany) working in backscattering mode was utilized to explore the bonding structures of the ta–C, ta–C:N, ta–C:Al, and ta–C:Al:N films. An Ar⁺ laser (λ = 532 nm; power: 25 mW) was employed as the excitation source. For the scanned Raman range (800–2000 cm⁻¹), the focused–spot size and spectral resolution were 3 µm² and 3 cm⁻¹, respectively. OriginPro software, Version 2018 (OriginLab Corporation, Northampton, MA, USA) was used to fit the Raman spectra to three Gaussian line forms. Peaks at around 1360 and 1540 cm⁻¹ showed the sites of the D (disordered) and G (graphite) bands, respectively, and the full width at half maximum (FWHM) was used to determine the D–G band intensity ratio (I_D/I_G) from the fitted Raman spectra (Bootkul *et al.*, 2014; Libassi *et al.*, 2000; Srisang *et al.*, 2012; Ferrari, 2002; Konkhunthot *et al.*, 2013).

3.2.2 X–ray photoelectron spectroscopy (XPS)

XPS is a qualitative and quantitative analysis used to study the chemical composition and chemical structure on the surface. Figure 3.5 shows the basic principle of the XPS. Since the photon energy activates the electron in the inner shell under the surface of a material, the energy analyzer measures the kinetic energy distribution of photo–emitted electrons. Therefore, the binding energy is calculated using the law of energy conservation as shown in Equation (3.1) (Panwar *et al.*, 2008; Gunther *et al.*, 2002):

$$E_B = h\nu - E_{kin} - \phi_{analyzer} \tag{3.1}$$

where E_B is the electron binding energy, E_{kin} is the electron kinetic energy, $h\nu$ is the photon energy, and $\phi_{analyzer}$ is the work function of the energy analyzer.

This binding energy is useful to identify elements. The results of XPS are a spectrum line; an example of the XPS spectrum is shown in **Figure 3.5**. The binding energy also varies according to the chemical state (i.e., oxidation number) and chemical structure (bonding) of the elements.
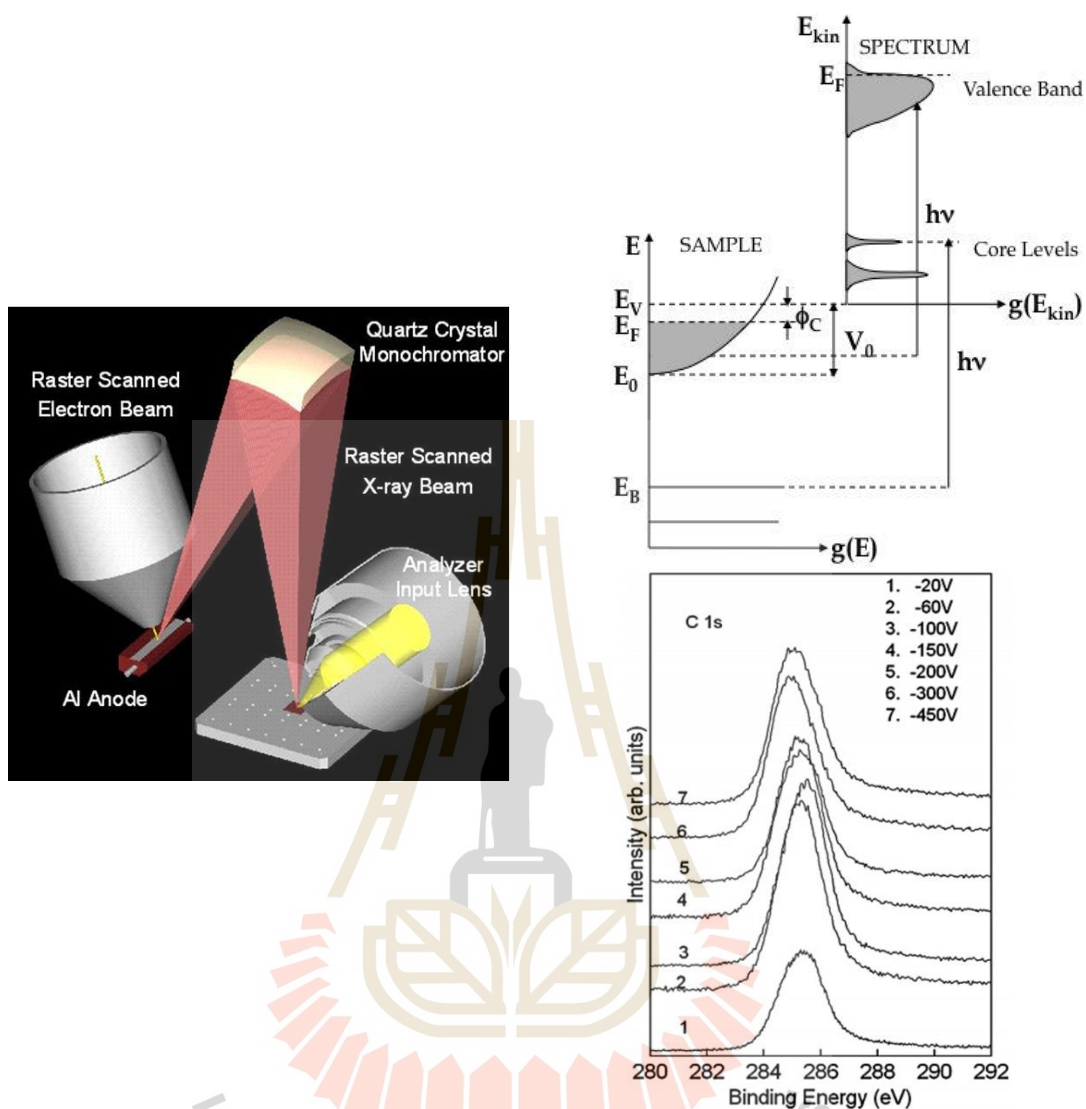
Figure 3.5 Schematic of X–ray photoelectron spectroscopy (XPS) [Online], Available : http : //www.phi.com/images/products/quantera/scanning–xray.jpg 18/13; [Online], Available : https://www.uj.ac.za/ faculties/ science/physics/ research/ Pages/Electronic–Structure–studies–at–UJ–Physics.aspx. ; and the C 1s XPS spectra of ta–C films at different negative substrate bias voltages (Panwar *et al.,* 2008)

In this study, the elemental composition of the DLC films was determined by XPS (PHI5000; VersaProbe™, ULVAC–PHI INC, Chigasaki, Japan) at the SUT–NANOTEC–SLRI joint research facility, beamline 5.3: SUT–NANOTEC–SLRI XPS, SLRI,

Nakhon Ratchasima, Thailand. To remove any natural oxides, the sample surfaces were sputtered with Ar$^+$ ions accelerated at 1000 V for 1 minute before examination. At a 100 µm spot, the pass energy and scanning step were 46.95 and 0.1 eV, respectively. The film bonding states were quantified using XPS spectra with CasaXPS software, and elemental atomic concentrations were computed using MultiPak Spectrum ESCA software.

3.2.3 X–ray Photoemission electron microscopy (X–PEEM) and near edge X–ray absorption fine structure (NEXAFS) spectroscopy

The thermal stabilities of ta–C, ta–C:N, ta–C:Al, and ta–C:Al:N were examined sequentially in a UHV system employing in–situ high–temperature NEXAFS spectroscopy from room temperature (RT) to 700°C at 10°C for 1 min, with the films held for 20 minutes at each annealing temperature. At each step, the films were cooled to 300°C, and the local bonding configuration was measured using in–situ NEXAFS spectroscopy combined with spectroscopic photoemission and low–energy electron microscopy (SPELEEM) (ELMITEC Elektronenmikroskopie GmbH, Clausthal–Zelllerfeld, Germany) at beamline 3.2Ub: PEEM, SLRI, Nakhon Ratchasima, Thailand. The beamline's monochromatic photon energy ranged from 40 to 1040 eV, and the synchrotron radiation was applied at 17 degrees incident to the films' surfaces under UHV (3×10^{-8} Pa). By setting the bias to 20 kV, which is equivalent to the hemispherical energy analyzer's pass energy, NEXAFS spectra were obtained in partial–electron–yield (PEY) mode. As a result, the NEXAFS intensity was limited to low–energy electrons (around the photoelectron threshold). Photons in the range 270–350 eV were used to analyze the NEXAFS C K–edge spectra, which were scanned in 0.1 eV increments. The NEXAFS intensity (in the same photon–energy range) of a flashed–Si wafer and a highly oriented pyrolytic graphite (HOPG) as the reference material were used to standardize the absorption signals of all the DLC films. To determine the sp^2–bonding percentage of the films, the normalized C K–edge spectra were deconvoluted using IGOR Pro 6.3 software. Based on the change in the sp^2–bonding percentage, the thermal stability of non–doped, doped, and co–doped DLC films was examined, and correlations between thermal stability and other film parameters were found.

3.2.4 Scanning electron microscopy (FE–SEM and FIB–SEM)

The scanning electron microscope (SEM) utilizes an electron beam to image a specimen's surface. It provides information about the sample's surface and near surface at a high magnification and resolution. **Figure 3.6** shows the schematic of the SEM. The electrons are accelerated from the electron gun to the bottom of the column with the range of the potential accelerating voltage between 0 to 50 kV. The condenser lenses are used for controlling the electron beam's moving direction, while the apertures are used for controlling the emitted electrons' beam size through the column to the sample. When the electrons penetrate the surface, interactions occur leading to an emission of electrons or photons from the surface. Emitted electrons are collected with a detector and interpreted as an image. The incident electrons or primary electrons lead to the secondary effects, classified into 3 types: secondary electron (SE), backscattering electrons (BSE), and relaxation of excited atoms (REA). However, all SEMs have facilities for detecting only the SE and BSE. The SE is mostly used in the SEM system. When a primary electron penetrates the sample surface, it can attack an electron of an atom at the surface leading to its emission. The BSE occurs when the primary electron goes back and leaves the surface without collision. Most of the BSEs carry higher energies than the SE. The BSE is used for surface imaging and elemental analysis. The images obtained from SE and BSE modes are different. The SE provides topographic information and higher resolution images while the BSE gives the contrast information (Toya *et al.*, 1986; Zhang and M. Fujii, 2015; [Online], Available : https://cellularphysiology.wikispaces.com).

FIB–SEM (AURIGA, Carl Zeiss AG, Oberkochen, Germany) at 50000 magnification and FE–SEM at 5–kV acceleration were also used to quantify the thicknesses of the DLC film cross sections in this study.
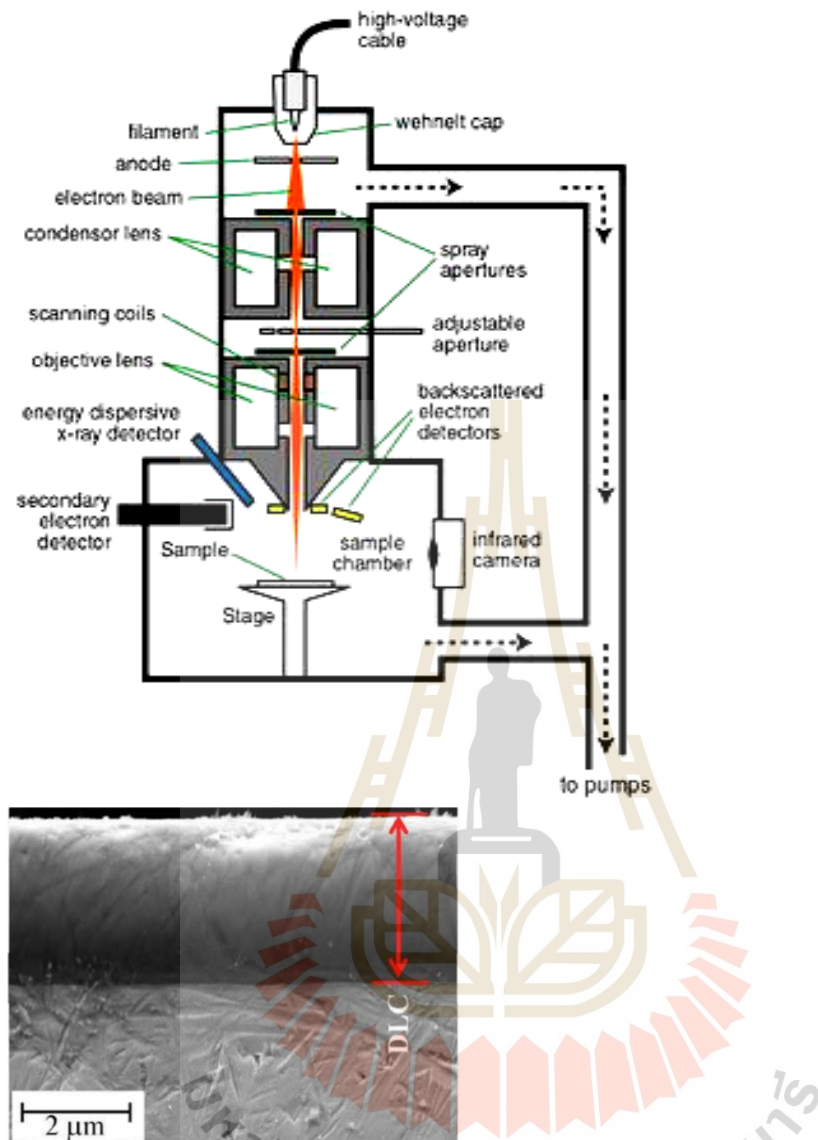
Figure 3.6 Schematic and cross–section image resulting from Scanning Electron Microscope (SEM) [Online], Available : https://cellularphysiology. wikispaces.com; (Zhang and Fujii, 2015)

3.2.5 Atomic force microscopy (AFM)

Atomic force microscopy (AFM) is a versatile technique for analyzing surface properties. It provides topographic imaging of a surface at the nano– and microscales. The important area is the study of force and friction force with the piconewton force resolution. The basic principle is to use a probe tip to map the

surface of the material, controlled by a piezoelectric scanner unit. The probe tip will bend along the surface as it changes, and the changes can be measured by a photodetector resulting in images that correspond to the surface conditions in each area, as shown in **Figure 3.7** (Sharifahmadian *et al.*, 2019; [Online],Available:https://pharm.virginia.edu/facilities/atomic–force–microscope–afm/; [Online],Available:http://www.parkafm.com/index.php/products/small–sample–afm/ park–nx10/technical–info).

The surface roughness of the AISI 4140 substrate and all DLC layers was determined using an atomic force microscope (AFM) (AFM XE–120, Park Systems Corporation, Suwon, South Korea) in non–contact mode with a 5×5 μm area and a scan rate of 0.3 Hz.
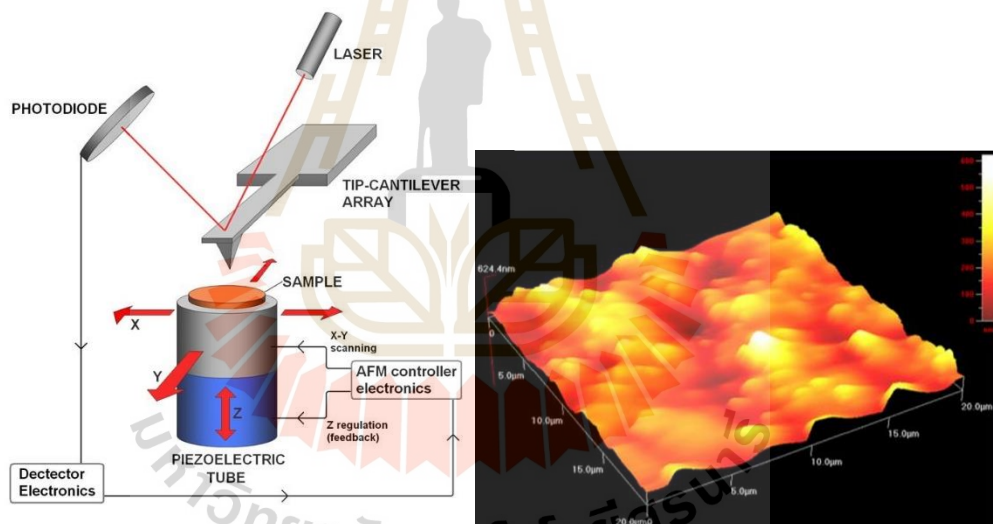
Figure 3.7 Schematic and surface image resulting from Atomic Force Microscopy (AFM) [Online], Available : https://pharm.virginia.edu/facilities/atomic–force–microscope–afm/; (Sharifahmadian *et al.*, 2019)

3.2.6 X–ray reflectometry (XRR)

To determine the density of DLC film, X–ray reflectivity (XRR) and a high–resolution X–ray diffractometer (XRD D8 ADVANCE, Bruker Optik GmbH, Ettlingen, Germany) were used with a Cu *K* radiation source at a wavelength of 1.541 Å, a voltage

of 40 kV, and a current of 40 mA (Konkhunthot *et al.*, 2018; Libassi *et al.*, 2000). The incidence angle was varied in the range of 0.0–3.0° with a scanning step of 0.005° for the XRR measurements of each DLC film. The entire reflection happened at a critical angle (θ_c), dependent on the electrical density of the material, when X–rays were incident on each surface of the DLC films at grazing angles of incidence. The square of the modulus of the Fourier transform of the electron density is proportional to the reflection intensity of each DLC film; hence, the profile of the electron density can be calculated from the observed intensity pattern (Konkhunthot *et al.*, 2018; Libassi *et al.*, 2000). According to Parratt's idea (Parratt, 1954), the XRR profiles were simulated using the Leptos 7.1 program. The θ_c and interference fringe give the average electron density from XRR data (reflectivity profiles); hence, Equation (3.2) may be used to measure the thickness of the DLC films at a low angle (Konkhunthot *et al.*, 2018; Ferrari *et al.*, 2000; Kishimoto *et al.*, 2008).

$$\rho = \left[\frac{\pi\theta_c^2}{N_A r_e \lambda^2}\right]\left[\frac{X_C(M_C - M_H) + M_H}{X_C(Z_C - Z_H) + Z_H}\right], \tag{3.2}$$

where θ_c and r_e are the critical angles and the classical electron radius, respectively, N_A is Avogadro's number, λ is the experiment's applied wavelength, X_C and X_H are the relative atomic fractions of C and H, respectively, (note that the atomic fraction of X_H is a form of $1 - X_C$), Z_C and Z_H are the atomic numbers of C and H, respectively, and M_C and M_H are the molar of C and H element, respectively.

3.3 Nanomechanical and Adhesion strength performance analysis

3.3.1 Nanoindentation tests

The ASTM Standard (E2546–07, 2007) was used to analyze the DLC–films' hardness and elastic moduli using nanoindentation testing with a NanoTest Vantage (Micro Materials Limited, Wrexham, UK) equipped with a Berkovich indenter under maximum stress. Nanoindentation is a method for mechanically measuring amorphous carbon thin films that uses a pendulum–based approach to detect depth–sensing. The specimens were measured 10 times and a six–point average value was

chosen for the report's statistical reliability. To eliminate the substrate effect, each sample was measured using the Berkovich type of indenter, and the maximum penetration depth for the films was in the range of 10 – 15% of the films' thickness (Konkhunthot *et al.*, 2019). Furthermore, each film's maximum penetration depth was consistent with the ASTM Standard (E2546–07, 2007). As a result, the nanomechanical characteristics in this investigation met worldwide standards, despite the fact that their thickness varied. With a dwell period of 10 seconds, loading and unloading curves were observed at a rate of 0.1 mN s^{-1}.

3.3.2 Nanoscratch tests

Adhesion testing was carried out while the platform was moving, with friction and acoustic emission measured throughout the scratch test. The nanoscratch tests were carried out at a relative humidity of roughly 50% at a temperature of 27 ± 0.5℃. A conical diamond tip (90° angle, 5 μm of final radius) was used to measure 3 consecutive scratches on each DLC film. A pre–scratching method is required to reduce the influence of surface roughness, topography, slope, and instrument bending (Beake *et al.*, 2006; Hassan *et al.*, 2015). Three sequential scans at 12.30 μm s^{-1} over a 5000 μm scan length were performed in the scratch process: (i) a preliminary topography scan at 0.50 mN with a constant load, (ii) a scratch scan at 1.0 mN s^{-1} applied load, ramped after 10 μm to a maximum load of 400 mN, and (iii) a final subsequent topography scan at 0.50 mN with the constant load over the scratch area. Furthermore, a very low speed was maintained to minimize the heat side effect, which causes the DLC film to degrade between testing. Finally, an SEM microscope and a digital capture system were used to see the scratch tracks, which were then evaluated and integrated with the findings of the nanoscratch test.

3.4 Electrochemical corrosion analysis

3.4.1 Potentiodynamic polarization technique

The tests were carried out at 27 ± 0.5℃ in a 3.5 wt% NaCl solution (pH ~6.6) using an Autolab PGSTAT 128N (Metrohm AG, Herisau, Switzerland) equipped with a graphite counter electrode (CE), an Ag/AgCl (3M, KCl) reference electrode (RE), and AISI 4140 steel with non–doped and co–doped DLC coatings as the working electrodes

(WE) (Konkhunthot *et al.,* 2019). The samples were immersed in the solution for 20 minutes before beginning the corrosion tests at a scan rate of 1 mV s^{-1} (Wongpanya, Pintitraratibodee, Thumanu, & Euaruksakul, 2021; Wachesk *et al.,* 2016) to maintain the steady–state or open–circuit potential (OCP). A fixed exposure area of 0.19625 cm^2 was also used in the scan, which ranged from −150 mV below the OCP (the cathodic region) to +300 mV above the OCP (the anodic region) (Konkhunthot *et al.,* 2019).
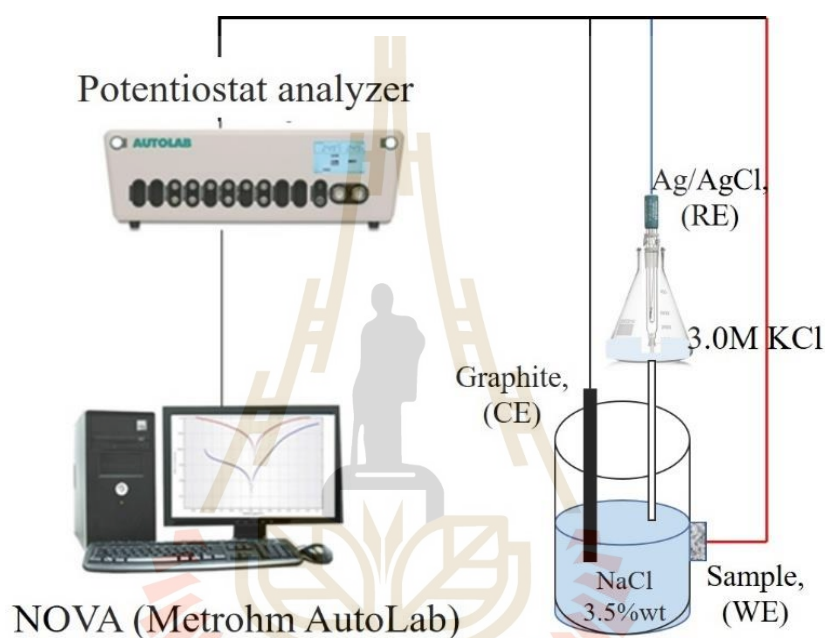
Figure 3.8 The schematic of a potentiostat analyzer by Autolab PGSTAT 128N
(Metrohm AG®, Switzerland)

CHAPTER 4

RESULTS AND DISCUSSION

4.1 The structural bonding configuration, thickness, and morphology of non–doped N–doped, Al–doped, and Al–N co–doped films synthesis by FCVA

4.1.1 Raman analysis

Raman spectroscopy is a non–destructive technology that is widely used. It is often used to examine the bonding structure of amorphous carbon film, or DLC. It offers data in the form of D and G peaks, FWHM, I_D/I_G ratios with L_a, and compressive stress (σ) (Ferrari, 2002; Hauert *et al.*, 1995).
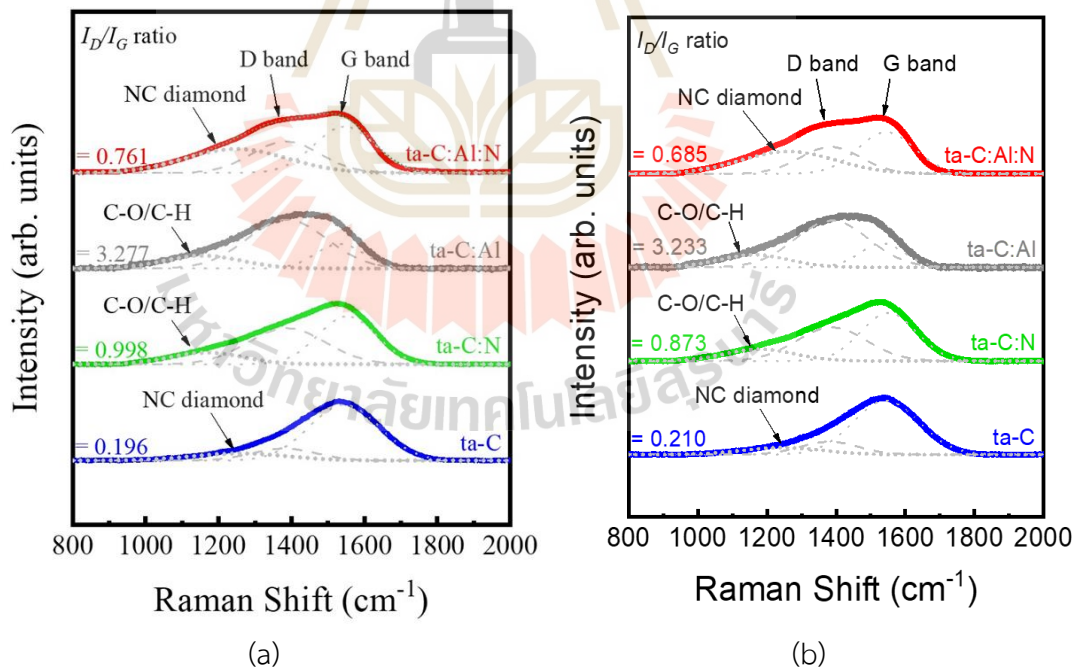
Figure. 4.1 Raman spectra of ta–C, ta–C:N, ta–C:Al, and ta–C:Al:N ((a) Set sample I and (b) Set sample II) (modified from Wongpanya, Silawong, & Photongkam, 2021; Wongpanya *et al.*, 2022)

Table 4.1 The Raman analysis parameters: D and G peaks, FWHM (D), FWHM (G), I_D/I_G ratios with L_a, and of ta–C, ta–C:N, ta–C:Al, and ta–C:Al:N (set I) and (set II) (modified from Wongpanya, Silawong, & Photongkam, 2021; Wongpanya *et al.*, 2022)

Sample	Raman analysis						
	G Peak (cm⁻¹)	D Peak (cm⁻¹)	FWHM of G peak (cm⁻¹)	FWHM of D peak (cm⁻¹)	I_D/I_G ratio	L_a (nm)	σ (GPa)
ta–C_(I)	1544.54	1379.77	226.91	205.44	0.196	5.965	0.000
ta–C:N_(I)	1552.49	1386.85	189.17	250.05	0.998	13.469	1.339
ta–C:Al_(I)	1532.33	1387.15	156.16	257.53	3.277	24.409	−2.056
ta–C:Al:N_(I)	1545.14	1384.34	195.66	219.15	0.761	11.765	0.102
ta–C_(II)	1544.18	1379.58	223.94	196.61	0.210	6.185	0.000
ta–C:N_(II)	1551.26	1389.18	189.52	236.43	0.873	12.601	1.193
ta–C:Al_(II)	1532.97	1387.53	151.65	249.93	3.233	24.246	−1.886
ta–C:Al:N_(II)	1544.93	1383.84	193.93	205.09	0.685	11.159	0.127

The findings of the Raman measurements are shown as spectra, as shown in Figure 4.1 (a) and (b), and all the DLC films were Raman measured in the 800–2000 cm⁻¹ range of the wavenumber in this investigation. The Raman spectra on the main Gaussian curve were split in half; peak D, with a wavelength of 1360 cm⁻¹, corresponds to the disordered structure of 6 aromatic rings, also known as the aromatic rings' respiration or vibrational mode, and the G peaks, which correspond to vibrations in the carbon chain and aromatic ring, are at a wavelength of 1540 cm⁻¹. The other wavenumber is a band centered between 1140 and 1260 cm⁻¹ that involves sp^2 and sp^3 bonds in a trans–polyacetylene (trans–PA) DLC film which is related to an atom of trans–PA DLC (Nakazawa *et al.*, 2007; Piazza *et al.*, 2003). Hydrogen is connected to an sp^2–site carbon atom in the chain. A nanocrystalline (NC) diamond structure is also indicated by the peak at 1260 cm⁻¹ (Singha *et al.*, 2006), which might reflect the

quantity of the mixed carbon sp^3–hybridized and H in the DLC film (Piazza *et al.*, 2003; Pu *et al.*, 2015; Liu *et al.*, 2005; Rao *et al.*, 2020). The major findings from the Raman analysis are shown in Table 4.1. All the DLC films display the data of peaks D and G, the FWHM of peaks D and G, I_D/I_G ratios with L_a, and σ; evidently, the G peaks of the ta–C, ta–C:N, ta–C:Al, and ta–C:Al:N films of both sample sets (set I and II) were found at 1544.50–1544.18, 1552.49–1551.26, 1532.33–1532.97, and 1554.49–1551.26 cm^{-1} respectively. A higher wavenumber is moved for the transition of the G peaks of the ta–C:N and ta–C:Al:N film layers, whereas the ta–C:Al films are shifted to the G peak at a lower wavenumber compared to the G peak position of the ta–C film. In previous research (Liu *et al.*, 2005; Rao *et al.*, 2020), G–peak shifting has been linked to L_a changes in DLC films, and important Raman parameters such as the G and D peaks, I_D/I_G, and the FWHM (G) are calculated from the area under the Gaussian peak curve G and D, while L_a and σ are estimated using the following Equations (4.1) and (4.2) in below (Konkhunthot *et al.*, 2018; Zarei Moghadam *et al.*, 2019; Tunmee *et al.*, 2016; Ferrari and Robertson, 2001; Lifshitz *et al.*,1989):

$$\frac{I_D}{I_G} = C^{'}(\lambda)L_a^2, \tag{4.1}$$

where $C^{'}$(514 nm) ≈ 0.0055.

$$\sigma = 2G\left[\frac{1+v}{1-v}\right]\left[\frac{\Delta\omega}{\omega_0}\right]; \tag{4.2}$$

where G is the shear modulus (70 GPa), 0.3 v is the Poisson ratio, $\Delta\omega$ is the change in the G–peak Raman wavenumber, and ω_0 is the DLC sample's Raman wavenumber (stress–free) as a reference material.

The I_D/I_G ratio may be considerably increased by doping with N, Al, or Al–N. The doping also resulted in a significant decrease in the FWHM (G). Because L_a, estimated using Equation (4.1), was similar to that obtained in earlier research (Konkhunthot *et al.*, 2018; Ferrari, 2002, Tunmee *et al.*, 2016), the drop in G correlated to bigger graphite clusters at sp^2–hybridized carbon sites. According to the Raman

analysis, the addition of N or Al or Al–N into the DLC film resulted in a shift towards the sp^2 hybridized carbon structure and carbon content, and there is less sp^3–hybridized carbon in the pure DLC film.

Internal stresses of materials may also be quantified using Raman analysis methods. This is because the vibration frequency of atoms is directly connected to stress. Furthermore, Raman spectroscopy yields a number of waves proportionate to the frequency of oscillations, which is shown by the location of the wavenumber that has changed. As a result, the Raman approach may be used to measure the internal compressive stress (σ) of the DLC film (Miki *et al.*, 2015; Narayan *et al.*, 2005; Lubwama *et al.*, 2013). As a result, the inter–atomic force constant associated with inter–atomic spacing, which affects the atoms' vibration frequency, shifts. The bond length rises as the tensile load of the DLC film increases, for example, the vibration frequency and the force constant are both lowered, and when the material is compressed a force is exerted in the opposite direction (Miki *et al.*, 2015; Narayan *et al.*, 2005; Lubwama *et al.*, 2013). The Raman spectra clearly reveal that simply adding N or Al–N to the DLC film causes the peak G to transition to a higher wavenumber. The peak of G in the Al–doped element has shifted to a low wavenumber at 1532.33–1532.97 cm^{-1}, whereas the peak of G in the ta–C:N and ta–C:Al:N is shown in the ranges of 1552.49–1551.26 cm^{-1} and 1545.14–1544.93 cm^{-1}, respectively. The computed values of σ in ta–C:N, ta–C:Al, and ta–C:Al:N for the set I DLC films were 1.339, −2.056, and 0.102 GPa, respectively, while for the set II DLC films they were 1.193, −1.886, and 0.127 GPa, respectively.

Residual stress is formed and accumulates inside the DLC coating throughout a film's growth process. High residual stresses are often associated with high hardness films, and are the primary cause of disintegration and distortion of a film's flexible surface. This is due to the fact that significant residual stress in the film might cause it to distort (Xu *et al.*, 2012, 2013). Furthermore, when a DLC film's layer thickness increased, so did the residual stress inside the film. The film begins to stabilize at a particular thickness before the residual stress inside the film is enhanced at the maximum thickness before the film begins to start to crack (Sheeja *et al.*, 2002). To avoid the film peeling, residual stress in the film must be controlled. The reduction

of residual stress in DLC may be achieved by including an elemental combination within the film or by forming a film base layer between the specimen and the film (Xu *et al.*, 2013). For this investigation, the addition of alloying elements to the film layer, such as nitrogen, aluminium, and co–doping, results in residual stress values determined from Equation (4.2) Two of the ta–C:N, ta–C:Al, and ta–C:Al:N specimens exhibited the internal stress (σ) and the L_a values that are close to one another.

The identicality was clearly shown by the peak G and computed σ value based on the difference between the higher and lower wavenumbers with increasing and decreasing the compressive stress in the DLC films (Miki *et al.*, 2015; Narayan *et al.*, 2005; Lubwama *et al.*, 2013). The structure bonding was created by increasing the compressive stress (σ) in ta–C:N and ta C:Al:N. The lower the compressive stress in ta–C:Al, where the conversion of the carbon bond from sp^3 to sp^2 is especially essential, the less the carbon transition from sp^3 to sp^2–hybridized carbon (Xu *et al.*, 2018; Narayan *et al.*, 2005). The increased amount of graphite at the disorganized of sp^2–hybridized carbon in the DLC structure and combined with the low Al/Al_2O_3 content in the ta–C:Al film may be affecting the peak G of the ta–C:Al film shifted towards the low wavenumber. Furthermore, the Al crystal structure is face–centered cubic (FCC), preventing carbide formation in the DLC layer and allowing nanocrystals to develop in the DLC matrix (Chen *et al.*, 2005).

4.1.2 Structural and chemical state of DLC film

XPS analysis was used to quantify the elemental composition, the chemical bond type, the sp^3/sp^2 ratio, and the relative fraction of sp^3 of all the DLC films. It was evident that the elemental doped DLC film layer had a reduced C atom concentration which decreased from 90.01–90.65 at.% for ta–C to 79.23–79.57 at.%, 78.20–78.23 at.% and 58.83–58.76 at.%) for ta–C:N, ta–C:Al, and ta–C:Al:N, respectively, as indicated in **Table 4.2**, and the sp^3 C—C content of the DLC film, as shown in **Figure 4.2**. The N content was approximately 11.21–11.46 at.% and 14.12–13.99 at.% in ta–C:N and ta–C:Al:N, respectively, while the Al content was approximately 4.77–5.05 at.% and 7.18–7.59 at.% in ta–C:Al and ta–C:Al:N, respectively; the O content increases with the increasing Al content, possibly because the O has adsorbed or adhered to the Al on the film's surface to form an oxide layer upon the film when exposed to air (Zhou

et al., 2019). From the chemical composition in **Table 4.2**, it is shown that the number of compounds in each film is quite comparable. This provides both sets of films with structural and mechanical properties, thermal stability, corrosion resistance, and other characteristics of the same or comparable film layers.

Table 4.2 The ta–C, ta–C:N, ta–C:Al, and ta–C:Al:N elemental compositions (at.%) quantitively measured using XPS (modified from Wongpanya, Silawong, & Photongkam, 2021; Wongpanya *et al.*, 2022)

Sample	Atomic Concentration* (at.%)			
	C 1s	N 1s	O 1s	Al 2p
ta–C_(I)	90.01	–	9.99	–
ta–C:N_(I)	79.23	11.21	9.56	–
ta–C:Al_(I)	78.20	–	17.03	4.77
ta–C:Al:N_(I)	58.83	14.12	19.87	7.18
ta–C_(II)	90.65	–	9.35	–
ta–C:N_(II)	79.57	11.46	8.97	–
ta–C:Al_(II)	78.23	–	16.72	5.05
ta–C:Al:N_(II)	58.76	13.99	19.67	7.59

*Atomic concentration was calculated using MultiPak Spectrum ESCA software

The chemical compositions and bonding states of the undoped, doped, and co–doped DLC films were examined using XPS, and the requisite C 1s, N 1s, and Al 2p peaks were identified across the spectrum as shown in **Figures 4.2–4.4**, respectively. As seen in **Figures 4.2**, the XPS spectra of C 1s were divided into distinct Gaussian Lorentzian peaks using Shirley backgrounds to measure the fraction of sp^3 C–C bonds in the DLC films (Modabberasl *et al.*, 2015; Yan *et al.*, 2004).

Figure 4.2 shows the acquired peaks for the C 1s spectra deconvoluted for ta–C, ta–C:N, ta–C:Al, and ta–C:Al:N, corresponding to the C–C bonds at 283.5 and 284.19 eV, the C=C bond is sp^2–hybridized and the C–C bond is sp^3–hybridized, while the other peak in the 286–288 eV binding energy range is of the C–OH, C–O, or C=O bonds, indicating the films' bond structure with hydrogen atoms and oxygen

contamination in the environment (Wu *et al.*, 2007; Konkhunthot *et al.*, 2018; Mabuchi *et al.*, 2013; Zarei Moghadam *et al.*, 2019; Tunmee *et al.*, 2016; Honglertkongsakul *et al.*, 2010; Maruno *et al.*, 2018).
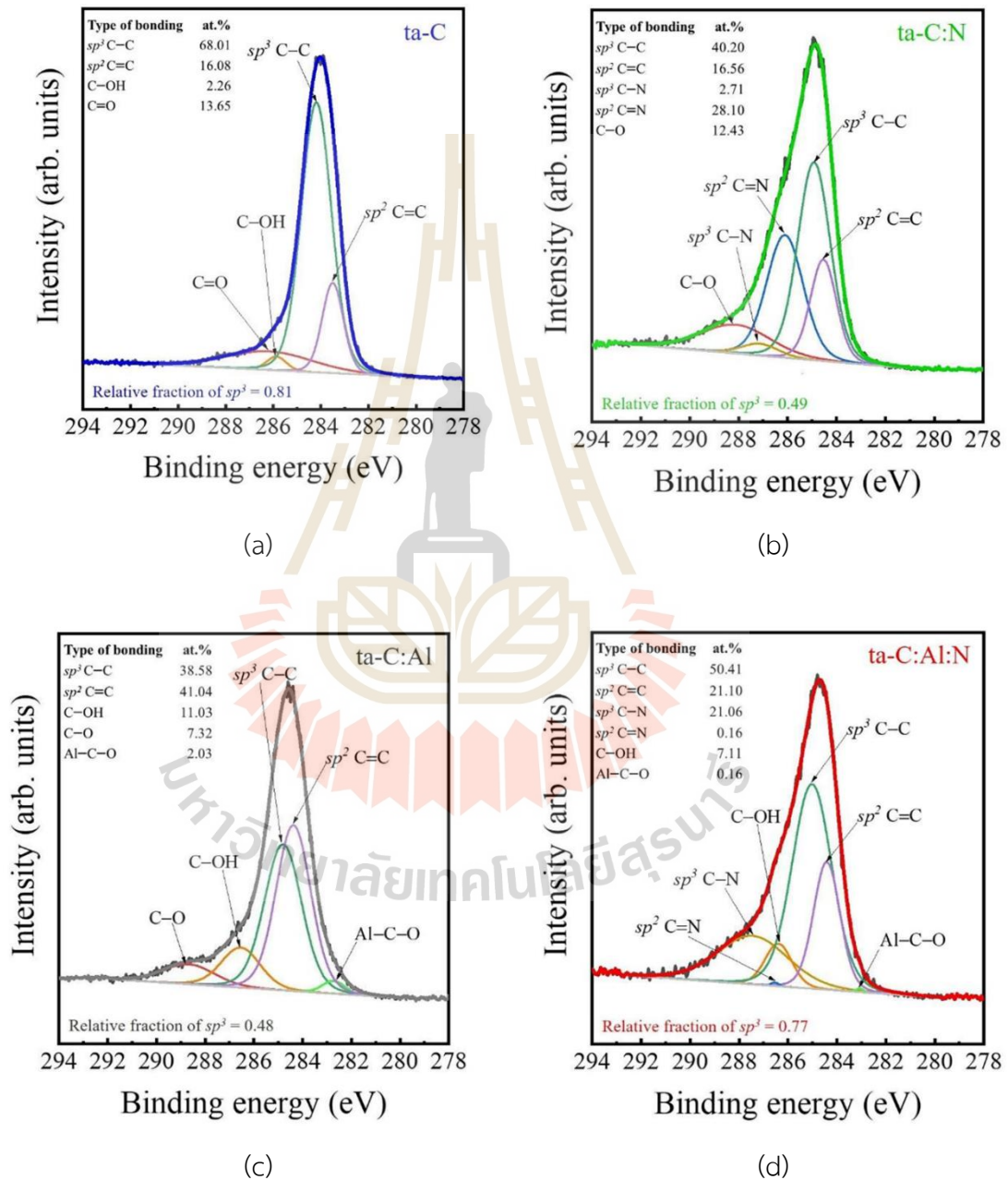
Figure 4.2 The C 1*s* XPS spectra and corresponding deconvoluted Gaussian peaks of
(a) ta–C, (b) ta–C:N, (c) ta–C:Al, and (d) ta–C:Al:N. (Wongpanya, Silawong,
& Photongkam, 2021)

Because the double bond is somewhat shorter than the single bond, the divided C 1s peak produced for the (sp^3 C–C) and (sp^2 C=C) bonds shifts significantly. In the C=C sp^2–hybridized bond, the charge density surrounding the C atom shifts closer to the carbon nucleus, and the valence electrons compress. In the deconvoluted spectra for ta–C:N, ta–C:Al, and ta–C:Al:N, the binding energy of the C 1s axis level (Wu $et\ al.$, 2007) decreases. The sp^2 C=C bonds (at 284.54, 284.38, and 284.42 eV for ta–C:N, ta–C:Al, and ta–C:Al:N, respectively) and sp^3 C–C bonds (at 284.92, 284.80, and 285.02 eV for ta–C:N, ta–C:Al, and ta–C:Al:N, respectively) were converted to higher binding energies than may be found in practically all other work (Wu $et\ al.$, 2007; Zhou $et\ al.$, 2019; Bouabibsa $et\ al.$, 2018).

Due to the DLC film being doped with Al or N, the percentage of the bond (sp^3 C–C) in the DLC film fell substantially from 68.01 at.% for ta–C to 40.20 and 38.58 at.% for ta–C:N and ta–C:Al, respectively. The Al and N co–doping, on the other hand, resulted in a minor reduction in the percentage of the bond (sp^3 C–C) compared to the single doped films, from 68.01 to 50.41 at.% for ta–C and ta–C:Al:N, respectively. These data reveal that as the alloy content rises, the relative fraction of the bond (sp^3 C–C) drops. Furthermore, the decrease in the relative fraction of sp^3 C–C bond in the ta–C:N, ta–C:Al, and ta–C:Al:N films corresponds to a decrease in the hardness (H) in the doped DLC films. It can be seen that the deconvoluted peak into C 1s spectra of ta–C:N and ta–C:Al:N, in the range of 285.50–286.54 eV and 285.20–287.45 eV, corresponds to sp^2–hybridized C=N and sp^3–hybridized C–N, respectively. There are no peaks in the spectrum at 286.70 eV, corresponding to the sp hybridized C≡N bond (i.e., nitrile group) (Hauert $et\ al.$, 1995; Mabuchi $et\ al.$, 2013; Yan $et\ al.$, 2004; Shi, 2006). Various bonds are produced when the DLC film is doped with N during the DLC coating process. Significantly with nearby carbon atoms, pyridine (sp^2–hybridized C=N bond), urotropine (sp^3–hybridized C–N bond), and nitrile groups generate an amorphous structure. As a consequence, the $sp^3/(sp^2 + sp^3)$ ratio for ta–C lowers to 0.49, 0.48, and 0.77, respectively, for ta–C:N, ta–C:Al, and ta–C:Al:N in **Figure 4.2**. The C 1s spectra indicated that as the quantity of N and Al grew, the proportions of sp^3 hybridized C atoms dropped, resulting in lower H values. In addition, the lower

relative proportions of the sp^3–bound C and N atoms corresponded to bigger and larger sp^2–bonded (L_a) clusters and higher I_D/I_G, as illustrated in the Raman results (Ferrari and Robertson, 2000).
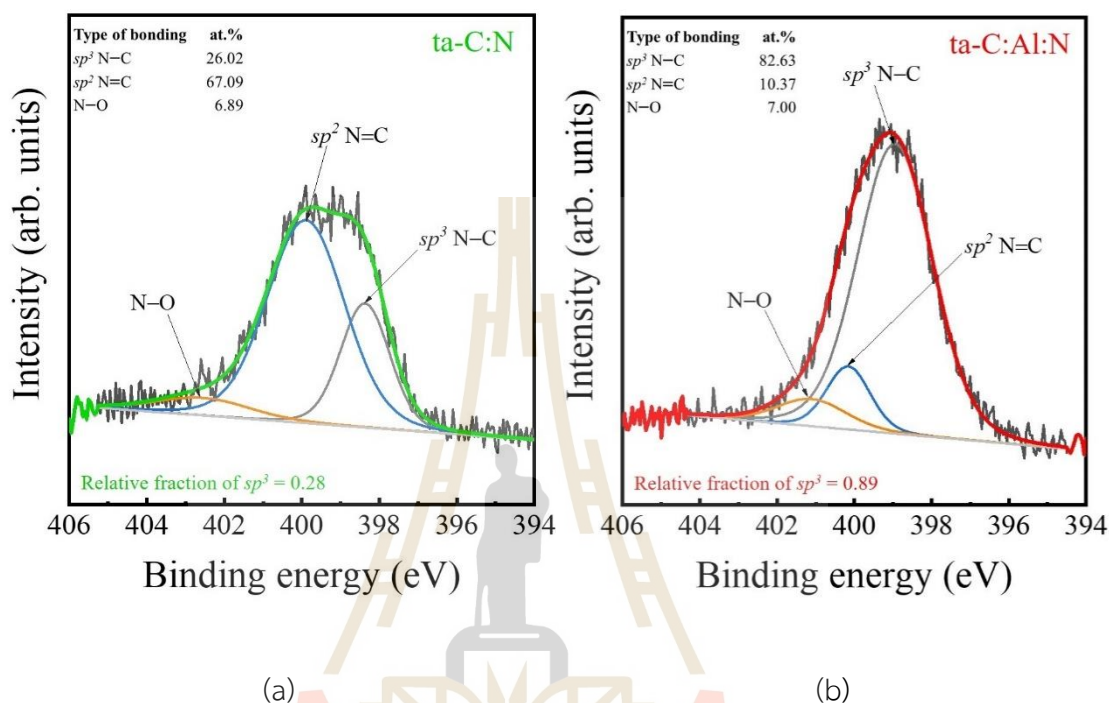
Figure 4.3 The N 1s XPS spectra and corresponding deconvoluted Gaussian peaks of (a) ta–C:N, and (b) ta–C:Al:N (Wongpanya, Silawong, & Photongkam, 2021)

Similarly, **Figure 4.3** depicts the separated N 1s spectra for ta–C:N and ta C:Al:N, emphasizing the 3 peaks for sp^3–hybridized C–N bonds, sp^2–hybridized C=N bonds, and N–O bonds are all 397.50–399.40 eV compliant with the literature (Zhou *et al.*, 2019; Mabuchi *et al.*, 2013; Yan *et al.*, 2004). These peaks are associated with pyridine containing organic nitrogen, which expresses the sp^2 C=N–hybridized and has C 1s and N 1s peaks at 285.50 and 400.16 eV, respectively, and urotropine, which contains sp^3 C–N bonds and has C 1s and N 1s peaks at 286.9 and 399.40 eV, respectively (Yan *et al.*, 2004). In ta–C:N and ta–C:Al:N, the majority of the N atoms are connected to the sp^2–hybridized and sp^3–hybridized carbon atoms, i.e., C=N and C–N bonds. As shown in **Figure 4.3**, the relative sp^3 C—N bonded atoms changed from 0.28

to 0.89: (sp^3 C–N)/(sp^3 C–N + sp^2 C=N). Because the addition of N reduced the number of suspended bonds in the aromatic ring, more sp^2–hybridized C=N bonds in the DLC films, especially ta–C:N, reduced the relative amounts of the sp^3 C—N bond (Mabuchi *et al.*, 2013). The Al–O–C bond is weak in the C 1s spectra of ta–C:Al and ta–C:Al:N, at 282.2 eV, likely due to contamination and oxygen exposure from the air.

(a)   (b)
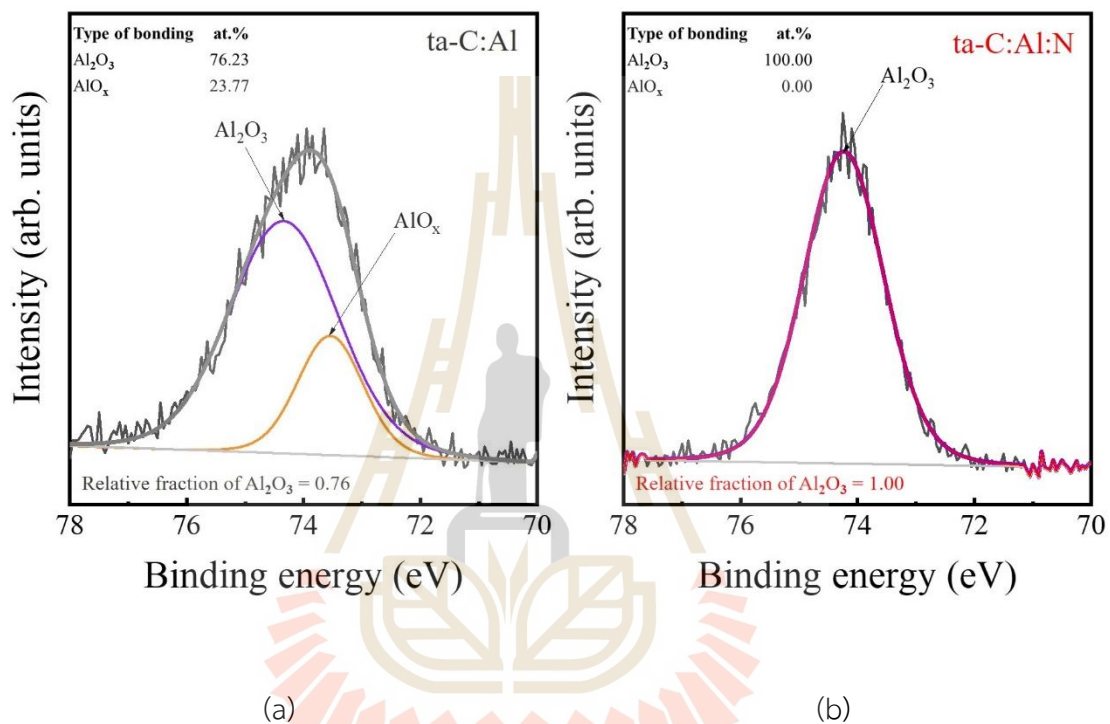
Figure 4.4 The Al 2p XPS spectra and corresponding deconvoluted Gaussian peaks
of (a) ta–C:Al, and (b) ta–C:Al:N (Wongpanya, Silawong, & Photongkam,
2021)

Figure 4.4 shows the peaks in the Al 2p deconvoluted spectra of ta–C:Al and ta–C:Al:N. AlO_x and Al_2O_3 have peaks at 73.54 and 74.24 eV, respectively. While the spectra for ta–C:Al:N contains just 1 peak of 74.24 eV, the relative percentages for Al_2O_3: Al_2O_3/($Al2O_3$+AlO_x) for ta–C:Al and ta C:Al:N are 0.76 and 1.00, respectively, as shown in Figure 4.4. Aluminium oxide (Al_2O_3) (Edlmayr *et al.*, 2010), the most stable aluminium oxide, is clearly present in ta–C:Al:N, whereas aluminium

suboxide (AlO_x) coexists with Al_2O_3 in ta–C:Al:N (Zhou *et al.*, 2019; Dai and Wang, 2011; Ozensoy *et al.*, 2005). Al_2O_3 possesses outstanding qualities, including wear resistance (Dingemans *et al.*, 2010; Eklund *et al.*, 2009), thermal stability, and corrosion resistance; the doped DLC with Al only, on the other hand, reduces compressive stress (σ) and hardness (H), both of which are key qualities for tribological applications such as adhesion and wear resistance. This is owing to far fewer sp^3 C–C bonds, as previously observed (Bootkul *et al.*, 2014).

In this experiment, the aluminium concentration of the DLC films was as low as 4.77–5.05 at.%. As a consequence, the hardness and mechanical qualities deteriorate. The interaction between the Al and N in ta–C:Al:N, on the other hand, maintains the σ and H, which are required for adhesion and wear resistance. This is most likely due to the fact that the majority of the N atoms form sp^3 C–N bonds. This involves Al_2O_3 in ta–C:Al:N, with the exception of ta–C:Al, which is unbonded (sp^3 C–N), but contains a combination of AlO_x and Al_2O_3.

4.1.3 Local bonding configuration

The local bonding structures and sp^2 proportion of all the DLC films were evaluated using NEXAFS spectroscopy, as illustrated in **Figure 4.5 – 4.7**. The normalized C *K*–edge NEXAFS spectra generated for all the films are shown in **Figure 4.5**, with 2 energy edges at 285.4 eV corresponding to the transitions from C 1*s* to the unoccupied π^* and σ^* state of the sp^2–hybridized C=C site and the sp–hybridized C≡C site, if present, and 288–335 eV corresponding to the overlapping C 1*s* transitions to the unoccupied π^* transitions at 285.1, 285.9, 286.3, 287.6, 287.7, 288.5, 289.6, and 293.7 eV which corresponded to transitions of the following states: (C=C), π^* (C=N), π^* (C=OH), σ^* (C–H), σ^* (C–N), π^* (C=O) or π^* (C≡C), σ^* (C–C), and σ^* (C=C), respectively. As shown in **Figure 4.5** for the ta–C, ta–C:N, ta–C:Al, and ta–C:Al:N, the sp^2 fraction was 0.345, 0.394, 0.538, and 0.348, respectively. Single dopants, such as N–doped or Al–doped DLC films, boosted graphitization as measured by an increase in the sp^2 fraction, but Al–N co–doping only slightly enhanced graphitization, and these findings matched the XPS result.
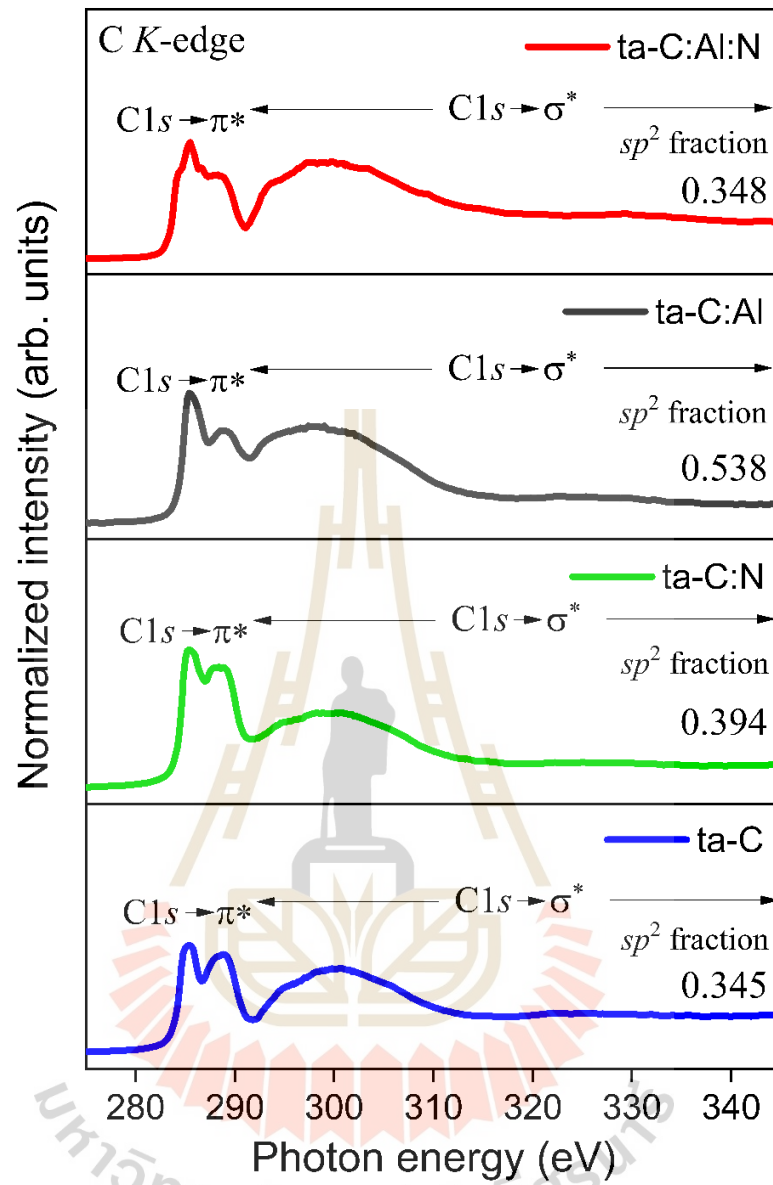
Figure 4.5 The C *K*–edge NEXAFS spectra generated for ta–C, ta–C:N, ta–C:Al, and ta–C:Al:N before the corrosion tests (Wongpanya *et al.*, 2022)

A comparison of the DLC films' O *K*–edge NEXAFS spectra shows that the O 1*s*→ π* transitions from the carbonyl and carboxyl groups of the O atoms double–bonded to the C atom (C=O) at photon energies of 531.2, 533.6, 536.0, and 540.0 eV, and the O 1*s*→ π* (C–O), σ* –OH, and the O 1*s* core–level electrons to the σ* C–O and C=O states, respectively, are shown in **Figure 4.6** (Wongpanya,

Pintitraratibodee, Thumanu, & Euaruksakul, 2021; Kim *et al.*, 2018; Lee *et al.*, 2012). For the Al–doped DLC films (ta–C:Al and ta–C:Al:N), the wide peak at 540.0 eV, which corresponds to Al_2O_3 with C=O, was clearly visible, but the intensity of C=O (at 531.2 eV) in the Al_2O_3 that was seen was consistent with the findings from Al 2p XPS (Abaffy *et al.*, 2011).
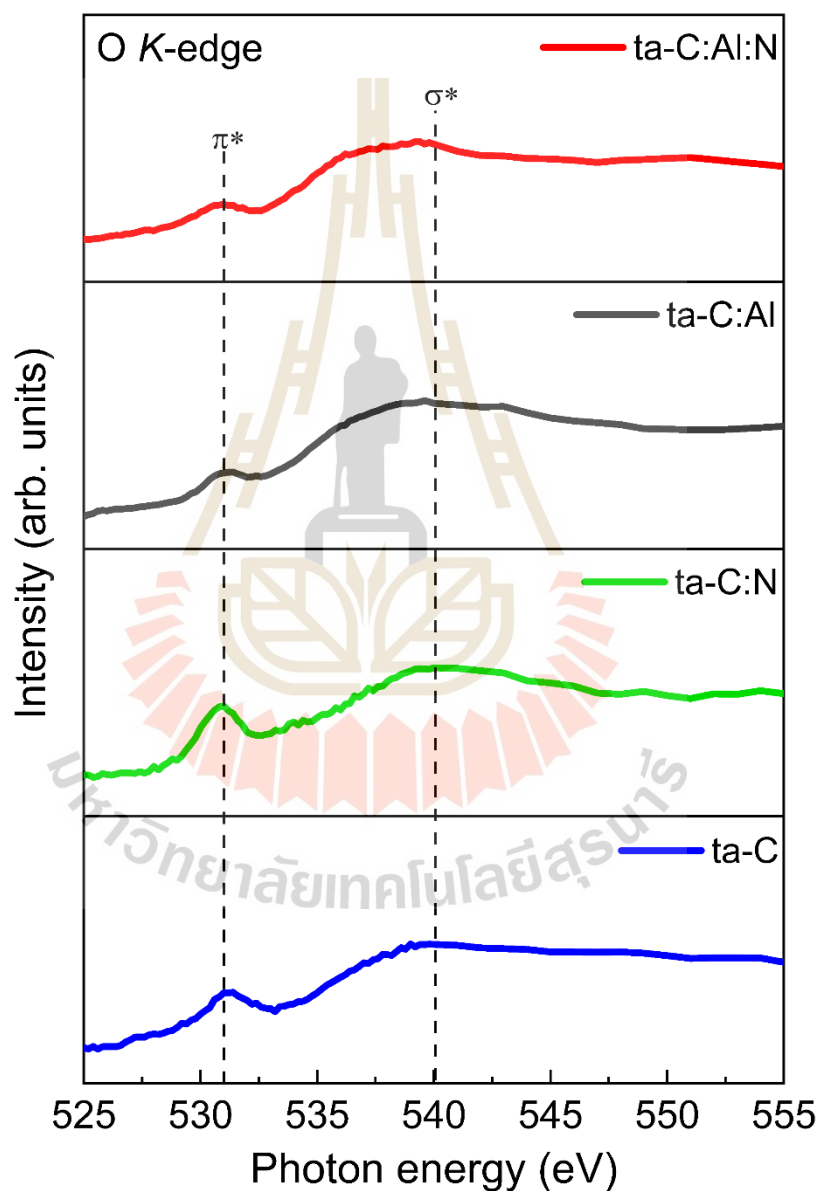
Figure 4.6 The O *K*–edge NEXAFS spectra generated for ta–C, ta–C:N, ta–C:Al, and ta–C:Al:N before the corrosion tests (Wongpanya *et al.*, 2022)

The NEXAFS spectra of N–doped DLC films: ta–C:N and ta–C:Al:N, showed that N was successfully added to the DLC films. In the hexagonal graphitic structure, there were 3 different peaks at 398.40, 399.50, and 401.50 eV, which were ascribed to sp^3–hybridized C–N (N1), sp^2–hybridized C=N (N2), and substitution nitrogen in graphite or graphite like (N3), respectively (Roy *et. al.*, 2005). There were moderately high and low intensity peaks for N1, N2, and N3 at 399.30, 400.81 and 401.50 eV, respectively, in ta–C:N, while ta–C:Al:N had strong and moderately intense peaks for N1, but no sign of N3 in the spectrum. Only N1 and N2 were found in ta–C:Al:N, whereas N3 was not identified in an XPS scan, showing the presence of sp^3–hybridized C–N at 81.99 at.% and sp^2–hybridized at 11.33 at.%. The NEXAFS findings were found to be identical to the XPS results.
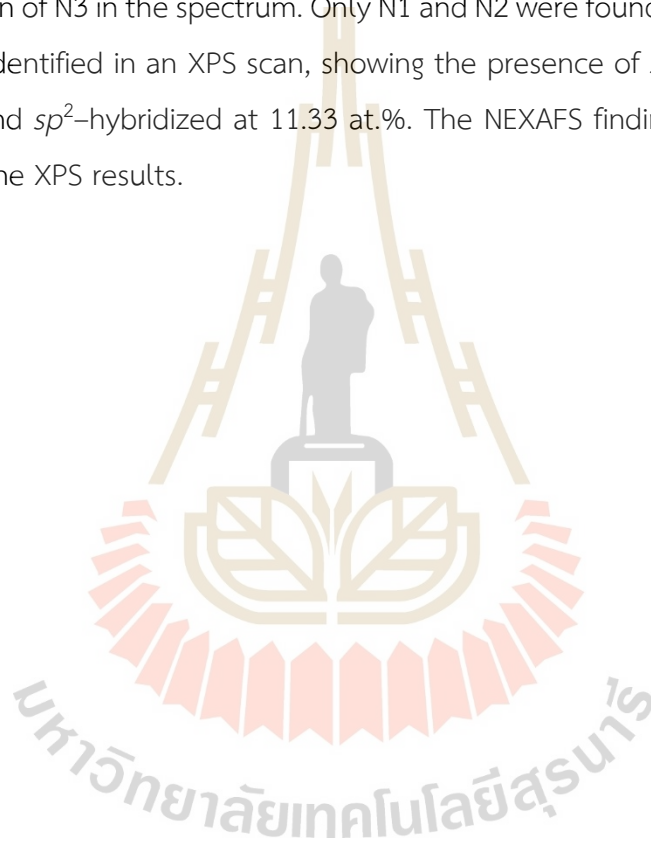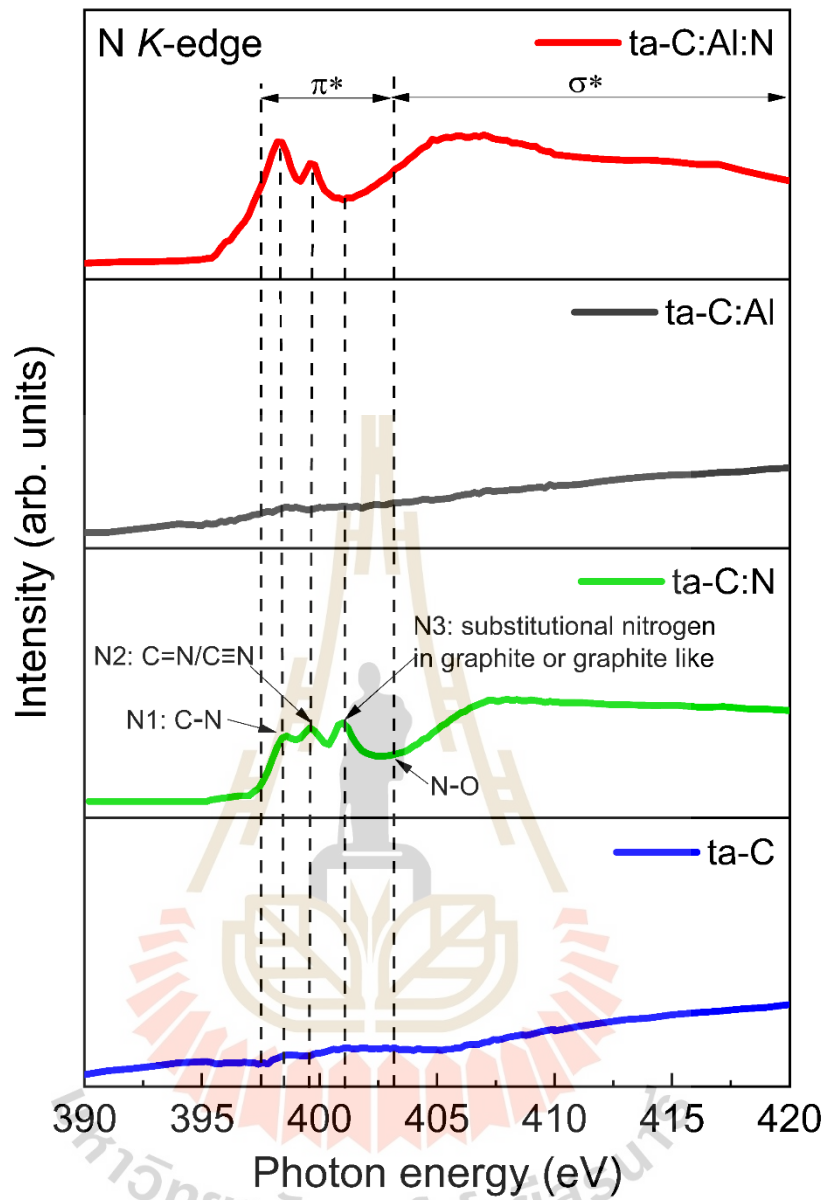
Figure 4.7 The N *K*–edge NEXAFS spectra generated for ta–C, ta–C:N, ta–C:Al, and ta–C:Al:N before the corrosion tests (Wongpanya *et al.,* 2022)

The investigation to evaluate the structure of the 2 coated DLC layers revealed that the I_D/I_G ratio, relative fraction of sp^3, and sp^2 fraction values for both sets were comparable, as shown in **Table 4.3**. The I_D/I_G ratio of the DLC films ta–C, ta–C:N, ta–C:Al, ta–C:Al:N are in the range 0.196–0.210, 0.998–0.873, 3.277–3.233, and 0.761–0.685, respectively, while the relative fraction of sp^3 values of the ta–C, ta–C:N,

ta–C:Al, ta–C:Al:N films are in the range 0.81, 0.49–0.50, 0.48–0.49, and 0.77, respectively, and the sp^2 fraction values of the ta–C, ta–C:N, ta–C:Al, ta–C:Al:N films are in the range 0.340–0.345, 0.390–0.394, 0.550–0.538, and 0.360–0.348, respectively. The mechanical properties, density, thermal stability, and corrosion resistance properties depend on the structure of the DLC film's layer. A high content of sp^3 (or low sp^2 fraction and I_D/I_G), gives high density, good thermal stability, good corrosion resistance, and good mechanical properties (Konkhunthot *et al.*, 2018, 2019; Bootkul *et al.*, 2014). As a result, both sets of specimens were produced using the FCVA technique, which indicated that the film's layer structure is the same.

Table 4.3 The summary of the I_D/I_G ratio, relative fraction of sp^3, and sp^2 fraction of ta–C, ta–C:N, ta–C:Al, and ta–C:Al:N in both sets.

Sample	I_D/I_G ratio		relative fraction of sp^3		sp^2 fraction	
	set I	set II	set I	set II	set I	set II
ta–C	0.196	0.210	0.81	0.81	0.340	0.345
ta–C:N	0.998	0.873	0.49	0.50	0.390	0.394
ta–C:Al	3.277	3.233	0.48	0.49	0.550	0.538
ta–C:Al:N	0.761	0.685	0.77	0.77	0.360	0.348

    4.1.4   Thickness, roughness, and density of the DLC films

        The cross–sectional images of all the DLC films and the continuous amorphous film layer were observed using FIB–SEM in the thickness range of 100–250 nm and the films were arranged from thickest to thinnest, as shown in **Figure 4.8**, with ta–C:N (230 nm) > ta–C (180.9 nm) > ta–C:Al:N (154.1 nm) > ta–C: Al, respectively.
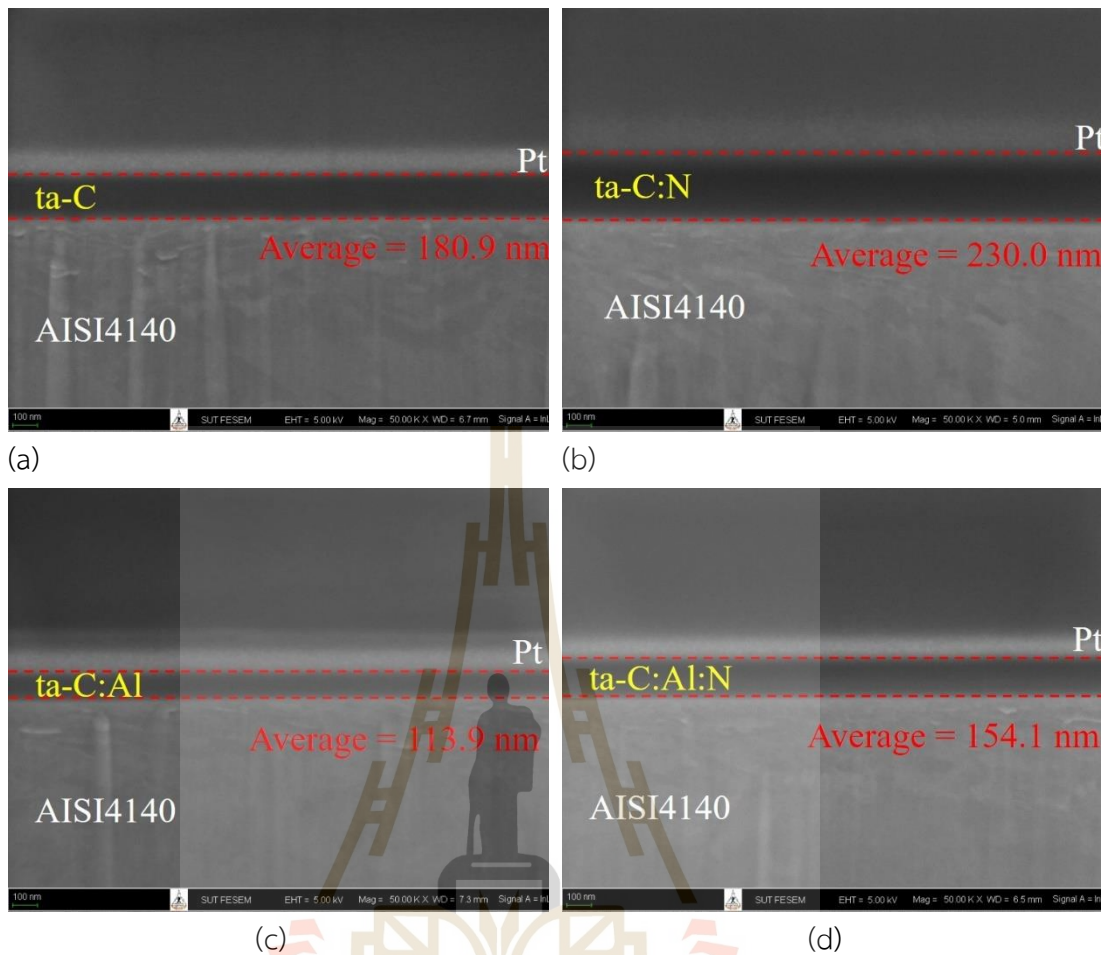
Figure 4.8 The FIB–SEM images of (a) ta–C, (b) ta–C:N, (c) ta–C:Al, and (d) ta–C:Al:N (Wongpanya, Silawong, & Photongkam, 2021)

Although the coating conditions, pressure, duty cycle, and time are the same for all the films, a film's thickness is not consistent, because the bonding structure and arrangement often influence the thickness of the DLC film. The DLC film's chains and aromatic rings contain impurities and carbon atoms (Bootkul *et al.*, 2014; Konkhunthot *et al.*, 2018; Pu *et al.*, 2015; Liu *et al.*, 2009; Modabberasl *et al.*, 2015; Sikora *et al.*, 2010). The compressive residual stress generated during lamination determines the overall film thickness. As demonstrated in the Raman results, film thickness rises as residual stress from compression increases in ta–C:N/ta–C:Al:N, and decreases as residual stress from compressive stress increases in ta–C:Al. The maximum value of the G peak moved to a higher wavenumber when the thickness of the DLC

film rose in tandem with the rise in compressive stress. This is in line with prior observations that film thickness and Raman spectra data are related (Liu *et. al.*, 2009). The doping causes a change in the thickness of the DLC film, which may be defined as follows. Due to the reacting N atoms functioning as additional deposition components in the coating chamber, the ta–C:N films' thickness may be enhanced. Because of the high concentration of N_2 in the plasma during deposition, the ta–C:N films have a high internal compressive stress (Bootkul *et al.*, 2014; Zarei Moghadam *et al.*, 2019). The tension stress and thickness of ta–C:Al are correspondingly the lowest and thinnest. This might be due to collisions between the C and Al ions during the coating process. Because Al does not mix with C to make aluminium carbide, fewer C ions have enough energy to coat and form sp^3 hybridized carbon bonds on the film layer later (Xu *et al.*, 2018; Chen *et al.*, 2005). The greatest I_D/I_G and L_a values, as well as the lowest hardness values, support this acceptable explanation; however, Al– and N–co–doped DLC (ta–C:Al:N) films do not. Although it is 26 nm thinner than undoped DLC, ta–C:Al:N has a relative compressive stress of 0.102 GPa when compared to DLC. This might be because the N_2 pressure in the coating chamber was raised from the base to 3×10^{-2} Pa during the film's formation and the combined addition of Al and N (Zarei Moghadam *et al.*, 2019; Son *et al.*, 2017), which resulted in a lower collision rate between the C and Al ions. Because N ions facilitate a film's deposition, ta–C:Al:N films are somewhat thinner than undiluted DLC films, as previously explained for ta–C:N.

The DLC film thicknesses obtained by FE–FEM for the second specimen set (set II), as shown in **Figure 4.9**, were 118.0, 118.3, 115.3, and 119.7 nm, with deposition times varying at 19, 15, 30, and 22 minutes for ta–C, ta–C:N, ta–C:Al, and ta–C:Al:N, respectively. Even if the coating factors for each of the films, such as the deposition rate, are different, it is clear that each DLC film has a different deposition time. Due to the arrangement of carbon atoms in the DLC film chain and the aromatic ring impacted by the doped composition and bond structure, the pressure, bias voltage, and duty cycle are all the same (Wongpanya, Silawong, & Photongkam, 2021; Bootkul *et al.*, 2014; Konkhunthot *et al.*, 2018; Liu *et al.*, 2009). Additionally, the stress–effect of the two sets of DLC films was similar to that seen in **Table 4.1**, where the ta–C:N and ta–C:Al:N specimens were the compressive stress while ta–C:Al is the tensile

stress. Because high–energy N atoms with adequate flow rates may be incorporated into the DLC film (Bootkul *et al.*, 2014), the ta–C:N film's thickness is reached in the lowest deposition time, while the ta–C:Al film requires more time. Because of the collision of C and Al ions during the coating, the thickness is the same (Wongpanya, Silawong, & Photongkam, 2021; Xu *et al.*, 2018); as a consequence, the film layer has less C ion coating and carbon bonding.
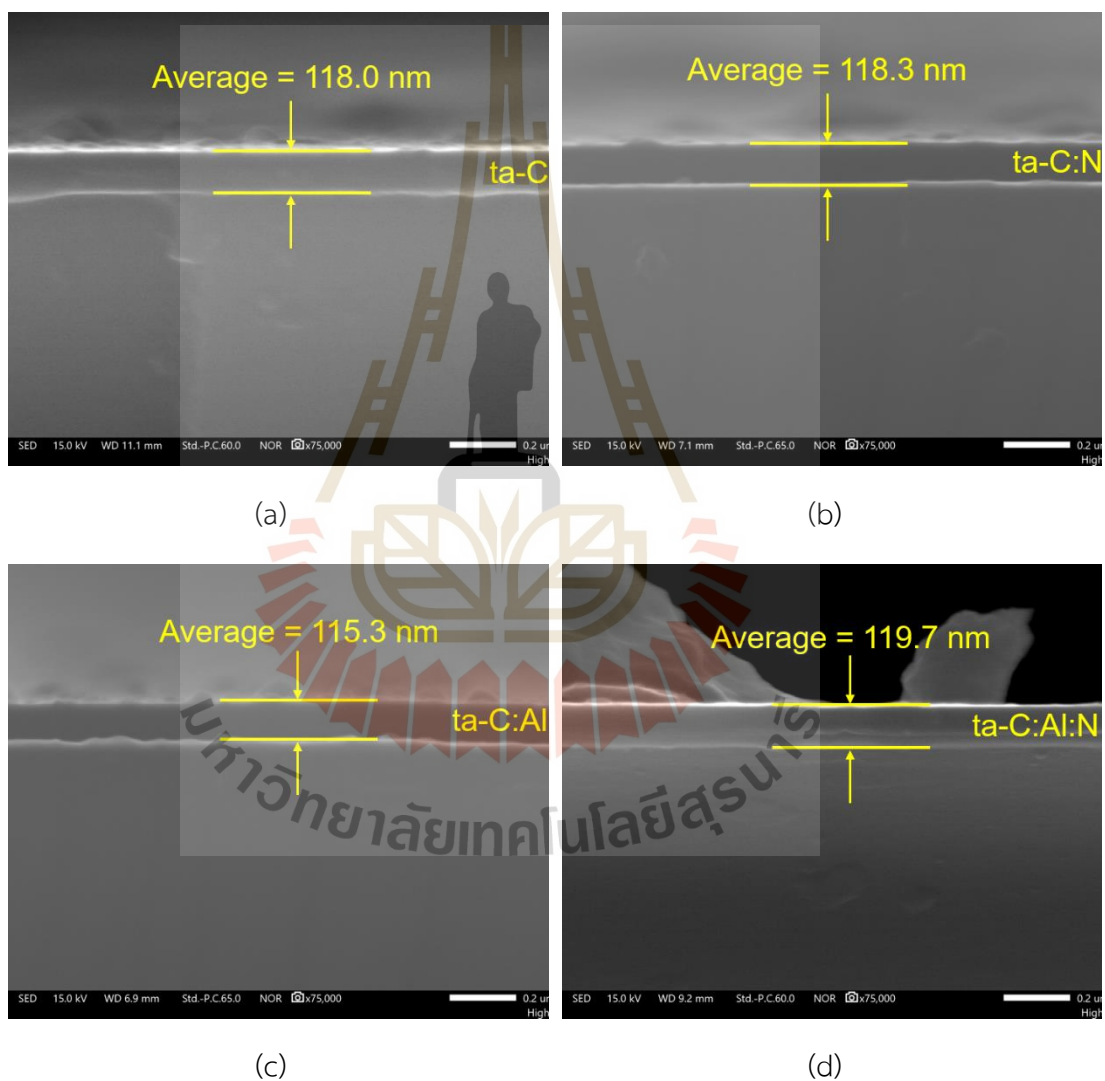
Figure 4.9 The FE–SEM images of (a) ta–C, (b) ta–C:N, (c) ta–C:Al, and (d) ta–C:Al:N
(Wongpanya *et al.*, 2022)

The surface roughness of the AISI 4140 substrate before and after polishing, as well as the AFM measurements of all the DLC layers, are shown in **Table 4.4**. Due to the treatment of the surface, there is no SiC remaining from the SiC paper imbedded on the surface. AISI 4140 has a surface roughness (Ra) of 8.8 nm, which is less than the ASTM Standard for block roughness (ASTM, E2546–07, 2007). The reference blocks should be constructed in such a way that the test is easily finished and the surface smoothed to the greatest extent possible. Additionally, the allowable mean surface roughness Ra measured on a 10 μm trace is Ra ≤ 10 nm for many applications.

This study had no effect on the nanoscale mechanical properties. Each sample exhibited a similar surface roughness (Ra 6.4–8.8 nm), with the DLC films having a roughness of 8.4, 8.0, 8.8, and 6.4 nm for the ta–C, ta–C:N, ta–C:Al, and ta–C:Al:N films, respectively. The surface roughness (Ra) of the second set of specimens for AISI 4140 (pre–DLC coating) was 8.16, whereas the roughness of the ta–C, ta–C:N, ta–C:Al, and ta–C:Al:N films was 8.16, 5.94, 7.48, and 6.14 nm, respectively. Additionally, larger particles were identified in ta–C but not in ta–C:N, ta–C:Al, or ta–C:Al:N, suggesting that N and Al impurities considerably reduce the number of large particles on the DLC surface. Collisions between the dopant and the larger particles result in a reduction in the size of the larger particles. The large particles are subsequently deposited on the ground and filtered by a copper filter coil.

Table 4.4 AFM topographies of AISI 4140, ta–C, ta–C:N, ta–C:Al, and ta–C:Al:N. (modified from Wongpanya, Silawong, & Photongkam, 2021; Wongpanya *et al*., 2022)

Sample	(set I)	(set II)
AISI4140	Ra = 8.80 nm	Ra = 8.16 nm
ta–C	Ra = 8.40 nm	Ra = 8.16 nm
ta–C:N	Ra = 8.00 nm	Ra = 5.94 nm
ta–C:Al	Ra = 8.80 nm	Ra = 7.48 nm
ta–C:Al:N	Ra = 6.40 nm	Ra = 6.14 nm
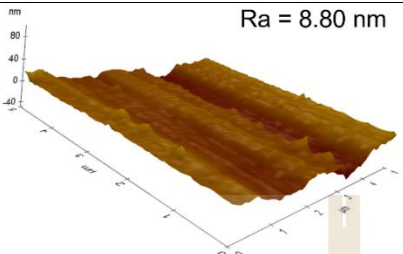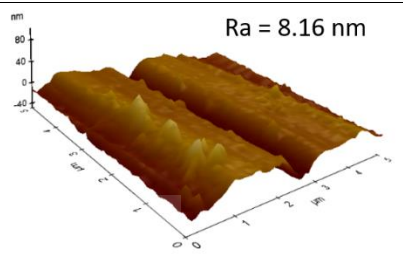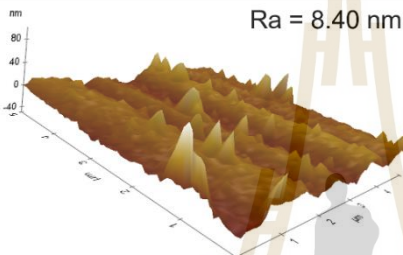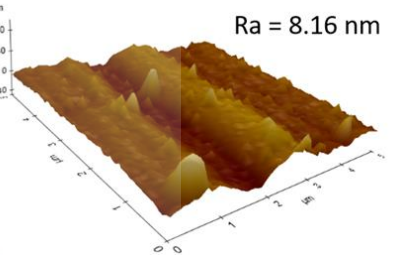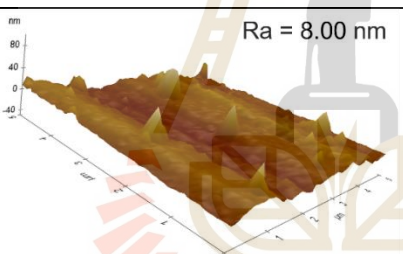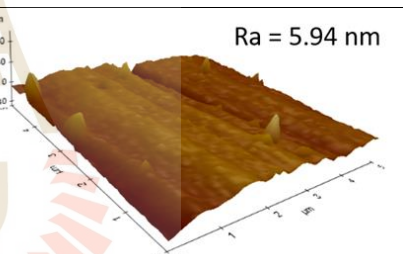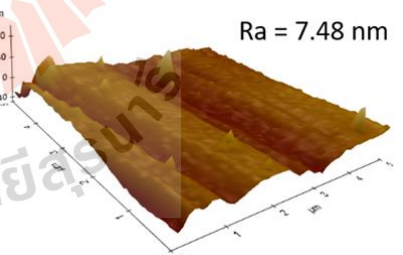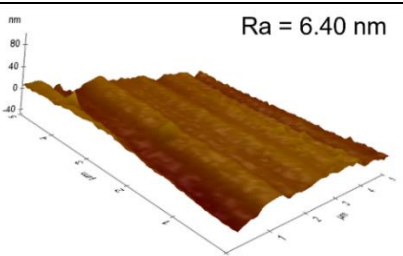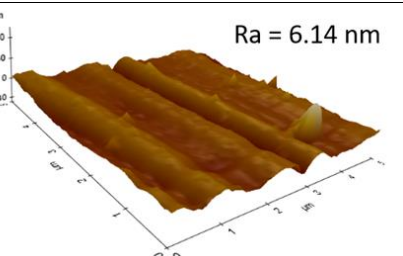
Experimental and simulation results of DLC films at different angles of incidence in the 0.01 to 2.5° range with a 0.005° scanning step are shown in **Figure 4.10** (black and red curves represent the experimental and simulated profiles of the DLC films' XRR profiles, respectively): 2.52, 2.22, 2.17, and 2.32 g cm^{-3} for ta–C, ta–C:N, ta–C:Al, and ta–C:Al:N, respectively. Adding dopant components to the DLC films resulted in a drop in the relative fraction of sp^3 in the XPS result (Konkhunthot *et al.*, 2018).
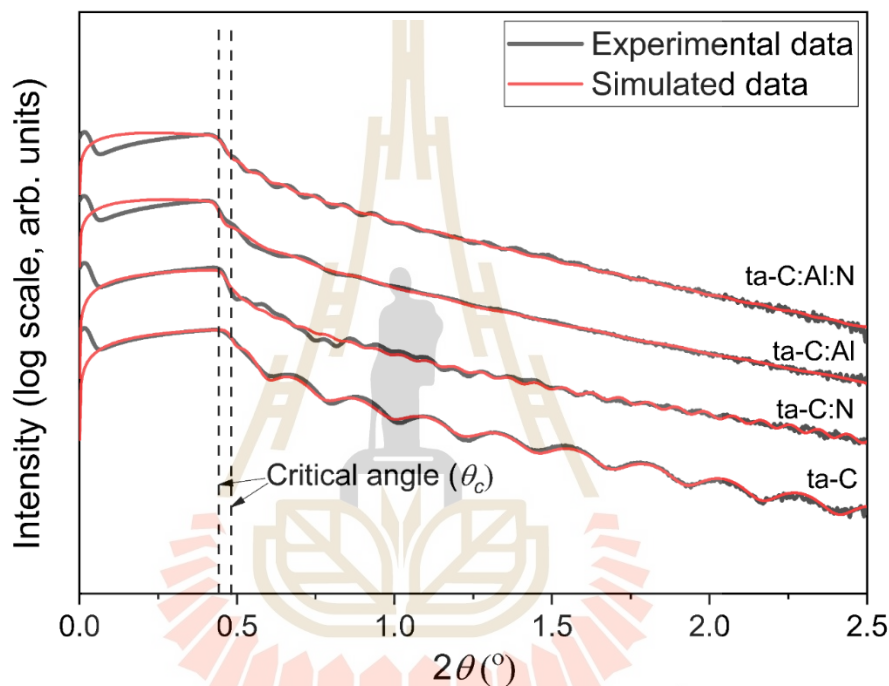
Figure 4.10 XRR profile of ta–C, ta–C:N, ta–C:Al, and ta–C:Al:N. (Wongpanya *et al.*, 2022)

4.2 The nanomechanical, adhesion strength, thermal stability, and corrosion resistance of the DLC films deposited on AISI 4140 by Al and N co–doping.

4.2.1 Nanomechanical property and adhesion strength analysis

The high elastic recovery (%ER) due to the elastic–to–plastic deformation transition, as reported in Page *et al.* (1992), and plastic deformation bands which are typically parallel to the indentation edges at the low–load indentations were

depicted in this study by non–smooth load–displacement curve discontinuities. The load–displacement curves of all the DLC films are shown in **Figure 4.11**.
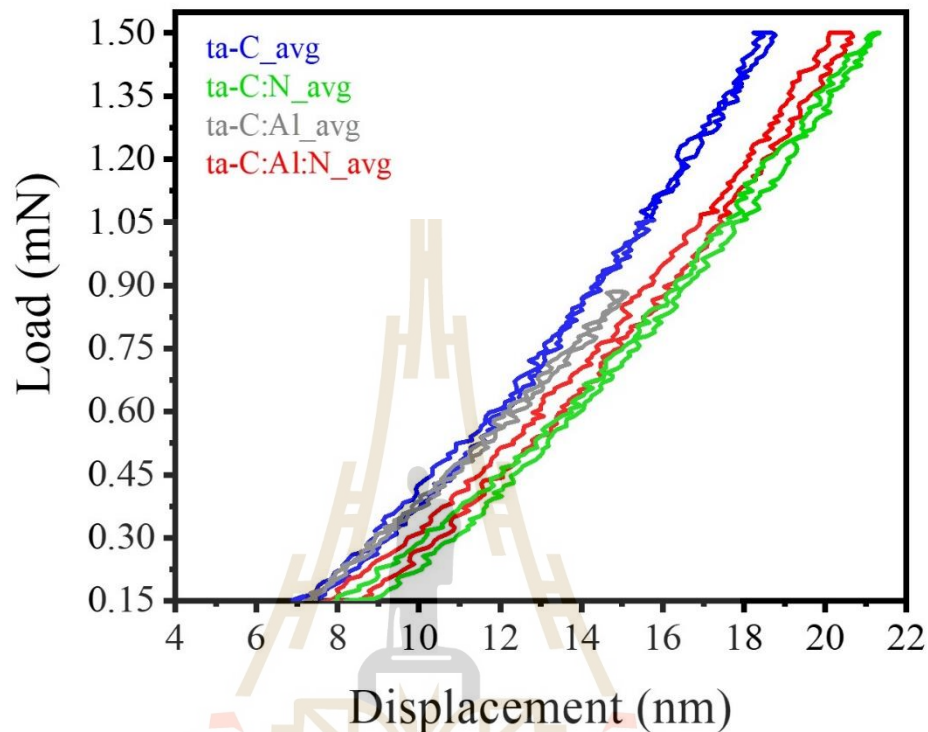
Figure 4.11 Load–displacement curves of ta–C, ta–C:N, ta–C:Al, and ta–C:Al:N
(Wongpanya, Silawong, & Photongkam, 2021)

Nanoindentation testing was used to evaluate the nanomechanical characteristics of the DLC films, including hardness (H), elastic modulus (E), plastic index parameter, the ratio of hardness to elastic modulus, H/E, and elastic recovery (%ER). The elastic recovery (%ER) obtained from the load–displacement curves displayed in **Figure 4.11** has been used to determine the elasticity of the DLC films, which has been computed using the following equation:

$$\%ER = \left(\frac{d_{\max} - d_{\mathrm{res}}}{d_{\max}}\right) \times 100,$$

(4.3)

where $d_{\mathbf{max}}$ and $d_{\mathbf{res}}$ are the displacement at the maximum load and the residual displacement after load removal, respectively.

Table 4.5 Mechanical properties of ta–C, ta–C:N, ta–C:Al, and ta–C:Al:N (test from set I) (from Wongpanya, Silawong, & Photongkam, 2021)

Sample	Mechanical properties			
	Hardness, *H* (GPa)	Elastic modulus, *E* (GPa)	Plastic index parameter, *H/E*	Elastic recovery (%*ER*)
ta–C	51.12 ± 1.08	302.29 ± 6.35	0.169 ± 0.005	60.06 ± 1.93
ta–C:N	47.32 ± 1.91	210.51 ± 4.82	0.225 ± 0.010	57.92 ± 1.35
ta–C:Al	38.84 ± 1.78	159.65 ± 3.94	0.243 ± 0.013	50.47 ± 1.53
ta–C:Al:N	49.04 ± 1.33	251.09 ± 6.57	0.195 ± 0.007	58.43 ± 1.73

Table 4.5 shows that the H and E of ta–C:N, ta–C:Al, and ta–C:Al:N were 47.32 ± 1.91 and 210.51 ± 4.82, 38.84 ± 1.78 and 159.65 ± 3.94, and 49.04 ± 1.33 and 251.09 ± 6.57 GPa, respectively, and were lower than those of the non–doped DLC (51.12 ± 1.08 and 302.29 ± 6.35 GPa). The XPS spectra show that the lower H and E correlate to greater I_D/I_G and La ascribed to an increased sp^2–hybridized carbon bond concentration and reduced sp^3/sp^2.

As a result of the higher dopant concentration, the nanomechanical characteristics of the DLC films revealed greater graphitization and bigger graphite clusters (L_a). Furthermore, the mechanical characteristics of the DLC films, particularly the ta–C film, were dramatically impacted by the sp^3–hybridized carbon bond concentration, and with a decreasing sp^3–hybridized carbon bond concentration, the mechanical characteristics of the ta–C film, such as hardness, surface smoothness, atomic density, and Young's modulus, all reduced (Bootkul *et al.*, 2014). Because of the NC diamond phase (Singha *et. al.*, 2006) that had developed in the co–doped DLC film, the H of the ta–C:Al:N became lower than that of the non–doped DLC, as demonstrated by the peak at ~1248.17 cm^{-1} in the Raman result from **Figure 4.1**.

These findings suggest that doping the DLC film with Al and N increased the film's hardness. Nevertheless, all the DLC films improved the hardness of the AISI 4140 steel bare substrate, as shown by the increased hardness of 38.84 ± 1.78, 47.32 ± 1.91, and 49.04 ± 1.33 GPa for ta–C:Al, ta–C:N, and ta–C:Al:N–coated 4140 steel, respectively, from 3.3 GPa for AISI 4140 (Ochoa *et al.*, 2006). Furthermore, as compared to genuine diamond (56–102 and 1050 GPa, respectively), the DLC nanomechanical characteristics (H and E) were above 38 and 150 GPa, suggesting the deposition of high–quality DLC films. Using these values, the coatings could successfully protect substrate surfaces from scratches and wear (Savvides and Bell, 1993; Robertson, 2002). The H/E and %ER were used to evaluate the DLC films' elastic–plastic behavior and wear resistance (Savvides and Bell, 1993). Materials with high elastic strain–to–failure are ranked according to their H/E ratio. A high H/E indicates that a DLC film has a high wear resistance, making it acceptable for use on vehicle components (Ishpal *et al.*, 2012).

The DLC film's hardness is reduced by Al and N–doping even though the elastic strain to failure is increased (**Table 4.5** shows that the H/E values of the ta–C:N, ta–C:Al, and ta–C:Al:N films are 0.225 ± 0.010, 0.243 ± 0.013, and 0.195 ± 0.007, respectively), while the ta–C film is only 0.169 ± 0.005. The relaxation of the elastic strain inside the DLC structure is well–known to result in high elasticity and recovery in typical hard and adherent DLC films (Ankit *et al.*, 2017; Coll *et al.*, 1996). Elastic recovery is also greatly influenced by the amount of sp^3–hybridized carbon bonds in the film (Ishpal *et al.*, 2012). As a result, as shown by the %ER data in **Table 4.5**, the elastic recovery of the DLC films dropped as the dopant concentration increased. According to the XPS study, %ER has been classified in decreasing order as follows: ta–C>ta–C:Al:N>ta–C:N>ta–C:Al, which corresponds to the sp^3–hybridized carbon bond concentration in the films.

The following sections go through important aspects including local bonding structure and thermal stability to see whether doping and co–doping are acceptable for DLC films used as protective coatings for wear and tribological applications, particularly for automotive components. Adhesion strength, scratch test data and SEM pictures were utilized to assess and compare the adhesion failure of all

the DLC films in **Figiure 4.12**. There are 2 distinct phases of critical load (L_c), the first of which is loaded and utilized to initiate the DLC film's initial failure, such as plastic deformation. The first term (L_{c1}) represents edge cracks and fine cracks, while the second term (L_{c2}) represents the critical normal load that identifies the reason for film adhesion failure. The L_{c1} and L_{c2} occurred at 126.57, 87.75, 65.16, and 99.60 mN and 195.29, 191.62, 199.46, and 221.96 mN for ta–C, ta–C:N, ta–C:Al, and ta–C:Al:N, respectively. It is obvious that for L_{c1} ta–C has the greatest value and the films may be ranked in decreasing order as ta–C, ta–C:Al:N, ta–C:N, and ta C:Al, respectively, while for L_{c2}, the Al–doped film layers, ta–C:Al and ta–C:Al:N had greater second–stage critical load values than ta–C and ta–C:N. It was discovered that only L_{c1} tended to correlate with the film hardness (H) and elastic recovery (%ER) of the DLC films in a previous work (Wongpanya, Silawong, & Photongkam, 2021) in which these properties depend on the quantity of sp^3 C—C in the DLC corresponding to the relative proportion of sp^3. The maximum L_{c1} can be seen in ta–C, as evidenced by the high %ER, which was due to elastic strain relaxation inside the film. As a result, ta–C could recover without deformation and had a greater cohesive strength (L_{c1}) than the other DLC films (Ankit *et al.*, 2017; Coll *et al.*, 1996).

Interestingly, increasing L_{c2} can be seen when the non–doped DLC film (ta–C) has been doped with Al and Al–N. That effect reduces internal stress and increases the graphite cluster size of the sp^2 sites (L_a), resulting in a high content of sp^3–hybridized C–N bonds (ta–C:Al:N only) (Zhou *et al.*, 2019; Dai and Wang, 2011), and the Al doping in DLC film can reduce the friction coefficient as reported. On the other hand, the ta–C:N had the highest stress in the DLC film, resulting in the lowest L_{c2} in this study. Typically, the plastic index parameter (H/E) is a critical attribute for assessing a coating surface that has been heavily deformed during elastic strain to failure in order to determine wear resistance (Konkhunthot *et al.*, 2019; Wongpanya, Silawong, & Photongkam, 2021; Ishpal *et al.*, 2012). Conversely, the toughness of the film should be proportional to the product of the lower critical load and the difference between the high (L_{c2}) and low (L_{c1}) critical loads, that was defined as scratch crack propagation

resistance (CPRs) = L_{c1} (L_{c2} − L_{c1}), calculated by Equation (4.4) (Zhou *et al.*, 2019; Zhang et al., 2004):

$$\text{CPRs} = L_{c1} (L_{c2} - L_{c1}) \tag{4.4}$$

The ta–C:Al:N, ta–C:N, ta–C:Al, and ta–C films had CPRs values of 12187.06, 9114.59, 8750.99, and 8697.89 mN^2, respectively. As a result, the CPRs values of the Al– and N–doped DLC films were elevated much higher than those of the other films, indicating that ta–C:Al:N exhibited the maximum toughness and adhesion strength in this experiment.

The SEM morphologies of scratch tracks for all the DLC films at L_{c2}, which are heavily damaged and peeled off the substrate, thus showing the failure of the adhesion strength of the DLC films to the substrate, are shown in the insets in **Figure 4.12** (a)–(d).
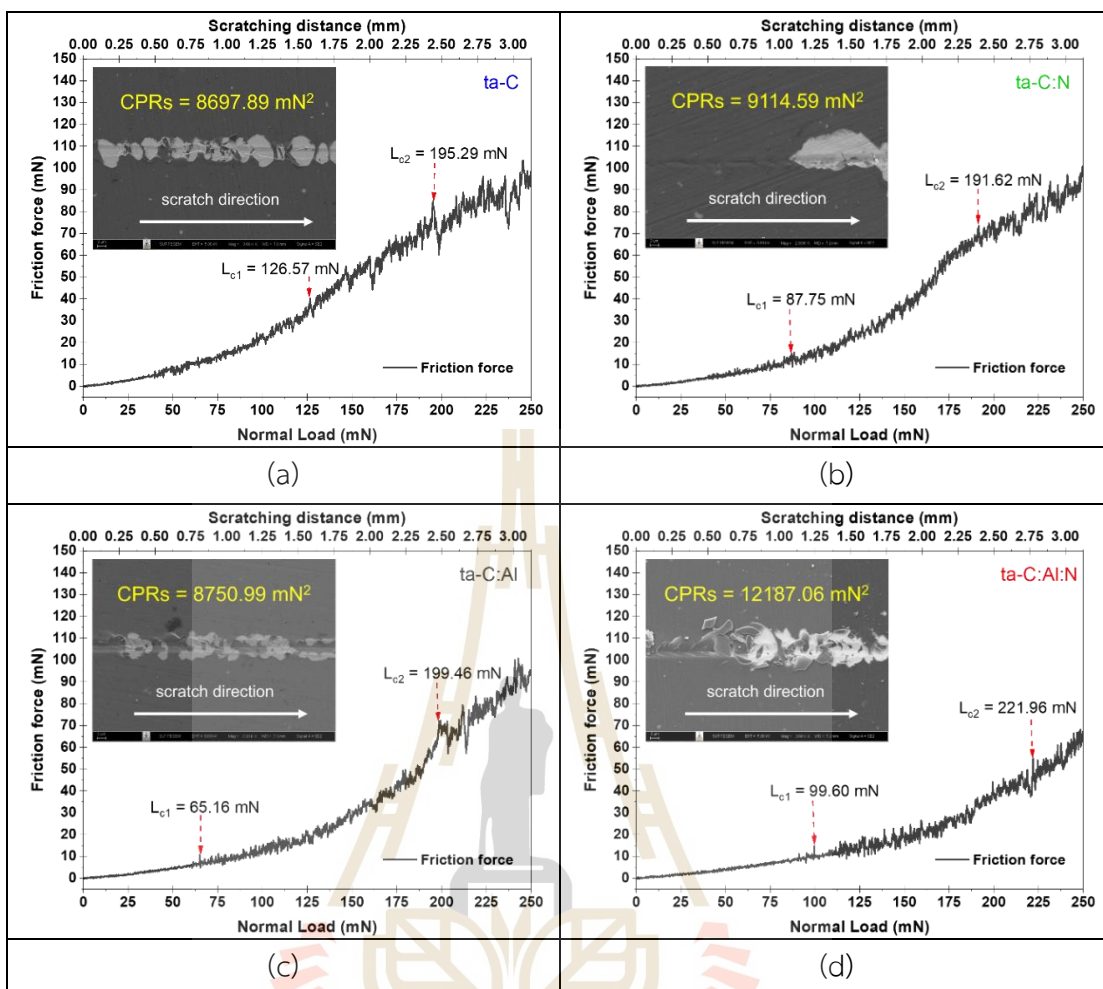
Figure 4.12 Scratch curves and the SEM micrographs of the corresponding scratch tracks at L_{c2} for (a) ta–C, (b) ta–C:N, (c) ta–C:Al, and (d) ta–C:Al:N, respectively (Wongpanya *et al.*, 2022)

There are segment fractures and breaks along both sides of the scratch track for ta–C as evidence of brittle fracture, but for ta-C:N, ta-C:Al, and ta-C:Al:N doping the wear tracks are deeper and wider demonstrating the enhancement of the adhesion strength. As shown by the Raman findings in **Table 4.1**, the compressive stress of the film on ta–C:N was 1.193 GPa, while the compressive stress of the films on ta–C:Al and ta–C:Al:N was –2.886 GPa and 0.127 GPa, respectively; the decreases in residual stress in the DLC films have been linked to an improvement in adhesion strength for N–doped, Al–doped, and Al–N co–doped films. Consequently, a higher residual stress

equals a high amount of stored elastic energy in the films. DLC films have a high stored elastic energy, which leads them to delaminate from the substrate if the adhesion energy between the DLC films and the substrates is inadequate (Konkhunthot *et al.*, 2019). Furthermore, higher sp^3–hybridized C–N bonds for ta–C:N and ta–C:Al:N, as well as Al_2O_3 which has substantially better toughness relative to ta–C for ta–C:Al and ta–C:Al:N, contribute to improved lubrication performance or friction–reducing properties (Bootkul *et al.*, 2014; Bouabibsa *et al.*, 2018; Dai and Wang, 2011). This is because, during the scratch test, the temperature in the region of the test contact increases, resulting in film surface oxidation and the creation of a thicker Al_2O_3 film layer, which slows the plastic deformation and the scratch resistance and allows the DLC film layer to maintain its lubricating properties (Zhou *et al*, 2019; Wang *et al.*, 2018; Ye *et al.*, 2017).

4.2.2 Thermal stability analysis by in–situ NEXAFS

Analyses of the thermal stability of the DLC films at RT and thermally annealed between 200 and 700°C in 100°C increments were carried out utilizing high–temperature NEXAFS spectroscopy of the local atomic structures of ta–C, ta–C:N, ta–C:Al, and ta–C:Al:N. The C *K*–edge NEXAFS spectrum produced for ta–C:Al:N at RT is shown in **Figure 4.13**. Subtraction and deconvolution of the spectrum resulted in several peaks. When the sp^2–hybridized C=C site is present, it may have contributed also to the pre–edge resonance at 285.4 eV, which has been determined to be a transition from the unoccupied π^* state (Konkhunthot *et al.*, 2019; Lenardi *et al.*, 1999; Tagawa *et al.*, 2010).

At the high–energy edge, overlapping C 1*s* transitions to unoccupied σ^* states at *sp*, sp^2, and sp^3–hybridized sites in DLC films generated the broadband zone between 288 and 335 eV (Lenardi *et al.*, 1999). The intermediate area identified between the π^* and σ^* states corresponds to transitions between the states at 285.1, 285.9, 286.3, 287.6, 287.7, 288.5, 289.6, and 293.7 eV (Ashtijoo *et al.*, 2016; Soin *et al.*, 2012). Other high resonances observed at 297.8 and 304.3 eV (Lenardi *et al.*, 1999; Soin *et al.*, 2012) were attributed to C 1*s* $\longrightarrow$ π^* (C=C), π^* (C=N), π^* (C=OH), σ^* (C–H), σ^* (C–N), π^* (C=O) or π^* (C≡C), σ^* (C–C), and σ^* (C=C). Because hydrogen was not present during the FCVA deposition, the hydrogen saturation of the surface–carbon

dangling bonds (i.e., nonpaired electrons) was assigned to **σ*** (C–H) states, while carbon that had been oxidized by air exposure was assigned to **σ*** (C=O) states (Lenardi *et al.*, 1999; Ashtijoo *et al.*, 2016; Soin *et al.*, 2012).
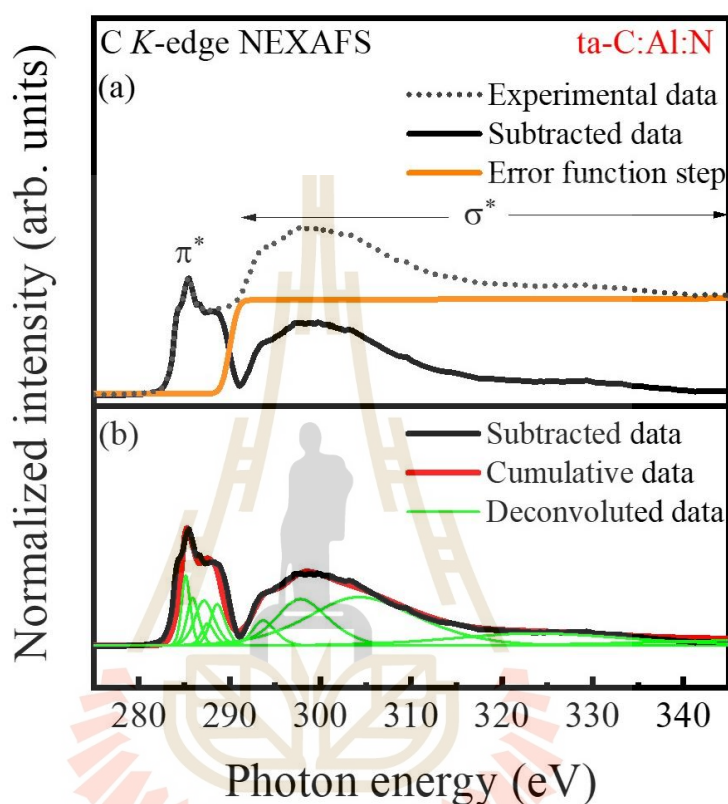
Figure 4.13 In–situ high–temperature NEXAFS C *K*–edge spectra were generated before (a) and after (b) data subtraction (Wongpanya, Silawong, & Photongkam, 2021)

The peak area corresponding to the C 1*s* ⟶ **π*** transition at 285.4 eV must be normalized with C 1*s* ⟶ **σ*** transitions in the range 288–335 eV to estimate the *sp*[2]–hybridized bond content in a sample. The following equation (Lenardi *et al.*, 1999; Tagawa *et al.*, 2010; Yoshitake *et al.*, 2009) may therefore be used to compute the *sp*[2]–hybridized bond fraction:

$$f_{sp^2} = \frac{I_{sam}^{\pi*}/I_{sam}^{total}}{I_{ref}^{\pi*}/I_{ref}^{total}},$$

(4.5)

where $\pi*$ is the position of the C $1s \longrightarrow \pi*$ transitions in C=C bonds, total is the integration areas calculated under the spectrum for binding energies in the range 288–335 eV, and sam and ref define the deconvoluted peaks for a sample thin film and a reference sample (highly oriented pyrolytic graphite (HOPG)), respectively.

The in–situ C *K–edge* NEXAFS spectra of ta–C, ta–C:N, ta–C:Al, and ta–C:Al:N at RT and thermally annealed up to 700°C are shown in **Figure 4.14**. As demonstrated by the spectrum characteristics, the chemical bonding configuration displayed minor heterogeneities, indicating that the atomic bonding structure altered gradually when the dopant concentration (Al and N) was low. As illustrated in **Figure 4.14** and **Figure 4.15**, the sp^2–hybridized bond fractions of the ta–C, ta–C:N, ta–C:Al, and ta–C:Al:N films were 0.34, 0.39, 0.55, and 0.36 at RT, respectively. Doping with simply N or Al obviously caused the production of graphitic sp^2–hybridized bonds known as "graphitization," as demonstrated by the sp^2–hybridized bond fractions, but co–doping with both Al and N induced very minimal graphitization. Because graphitization converted sp^3–hybridized ($\sigma*$) states in the amorphous carbon film into sp^2–hybridized ($\pi*$), the percentage sp^2–hybridized bond fraction rose with increasing the annealing temperature (Grierson *et al.*, 2010). The NEXAFS spectra of ta–C:N, ta–C, and ta–C:Al indicated that sp^3–hybridized ($\sigma*$) states had considerably converted into sp^2–hybridized ($\pi*$) ones in the amorphous carbon films at 400, 500, and 600°C, respectively, which meant that they had already graphitized; this is similar to results in earlier research (Fu *et al.*, 2005; Zhang *et al.*, 2002; Tallant *et al.*, 1995). In ta–C:Al:N, on the other hand, the percentage sp^2–hybridized bond fraction grew steadily from 0.36 at room temperature to 0.39 at 300°C.
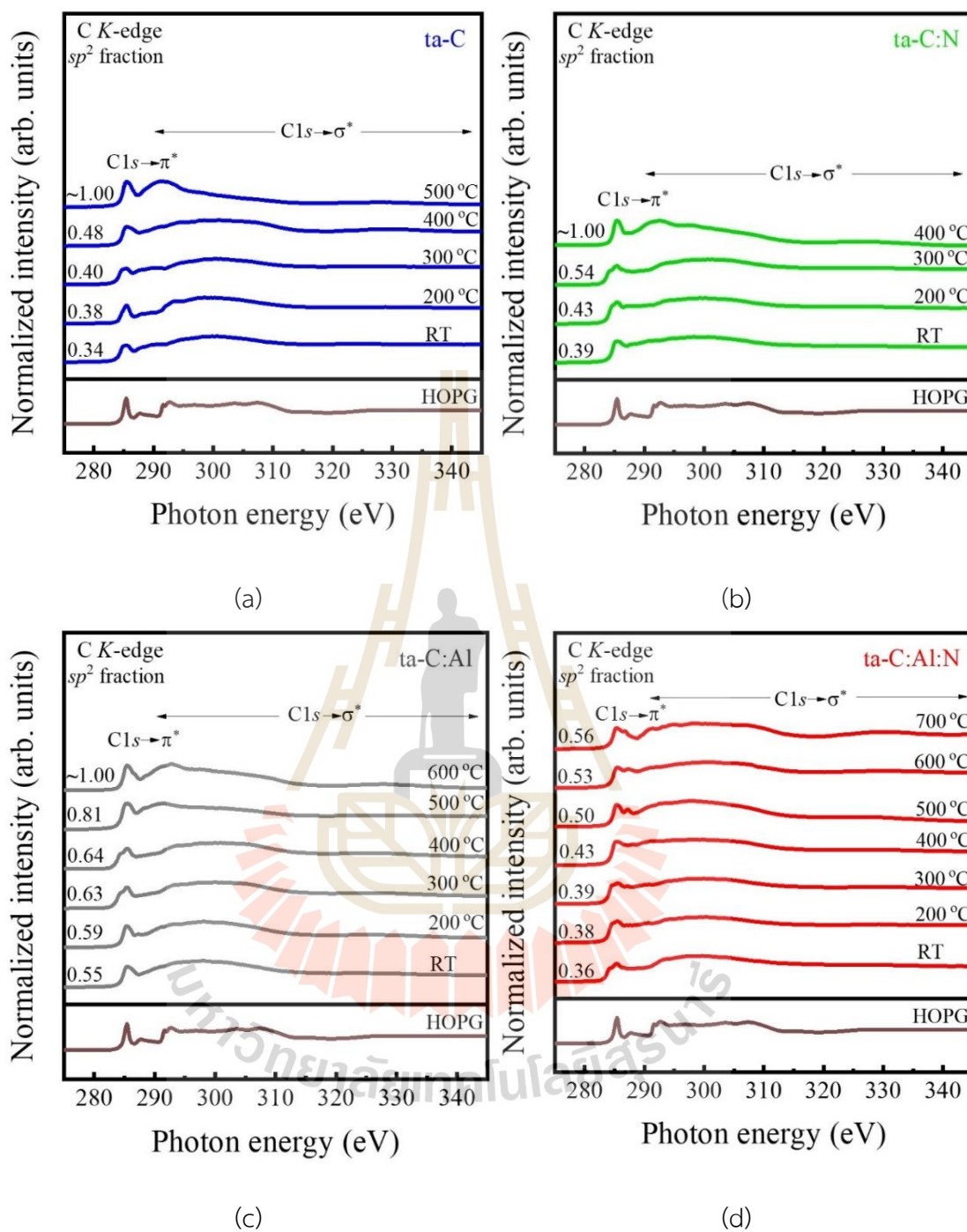
Figure 4.14 The C K–edge NEXAFS spectra obtained at room temperature (RT) and thermally annealed to graphitization temperature for (a) ta–C, (b) ta–C:N, (c) ta–C:Al, and (d) ta–C:Al:N (Wongpanya, Silawong, & Photongkam, 2021)

The relative sp^2–hybridized bond ratio in ta–C changed from 0.34 to 0.40 in the same temperature range, which was just slightly different. From 400 to 700 °C, the relative sp^2–hybridized bond fraction of ta–C:Al:N increased dramatically from 0.43 to 0.56. As seen in **Figure 4.15**, the carbon in the ta–C:Al:N film remained amorphous, meaning that ta–C:Al:N graphitized more slowly and at a higher annealing temperature than ta–C:N, ta–C, and ta–C:Al, because the diamond structure had transformed to graphite at 400-700 °C, as indicated by sp^2 fractions up to 1. The great thermal stability of ta–C:Al:N is indeed owing to the synergistic synthesis of stable Al_2O_3 oxide and sp^3–hybridized N–C bonds, as evidenced by the XPS result in section 4.1, respectively, during in–situ high–temperature annealing of amorphous ta–C:Al:N, this greatly delayed graphitization, stabilizing the DLC structure (B. Zhou, 2019, Y. Zhou, 2019, V. Podgursky, 2020)
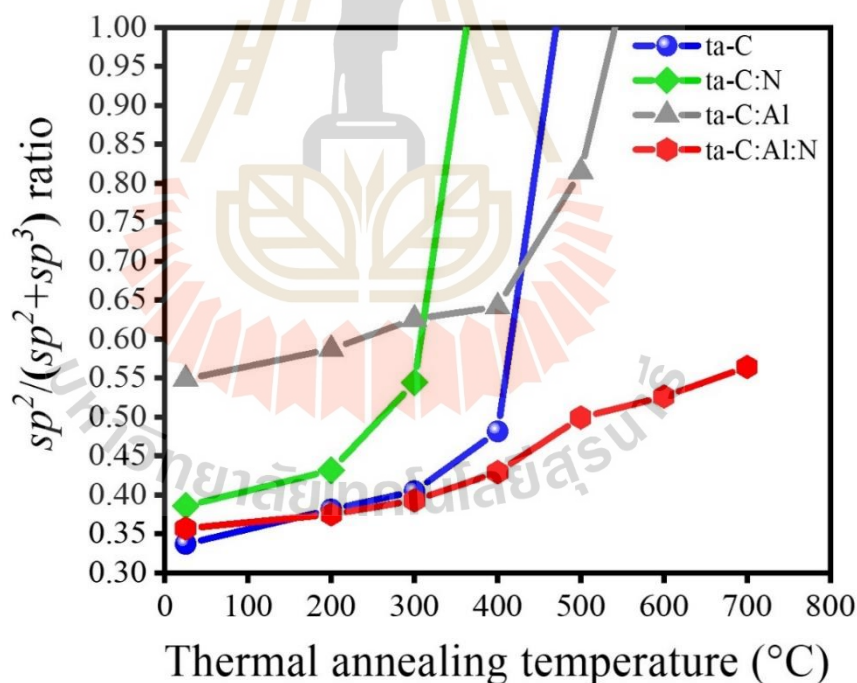
Figure 4.15 The sp^2–hybridized bond fractions of ta–C, ta–C:N, ta–C:Al, and ta–C:Al:N as a function of thermal annealing temperature from room temperature (RT) to graphitization temperature. (Wongpanya, Silawong, & Photongkam, 2021)

4.2.3   Electrochemical corrosion analysis by potentiodynamic
polarization technique

The polarization curves for AISI 4140 steel and all the DLC films, ta–C, ta–C:N, ta–C:Al, and ta–C:Al:N, electrochemically evaluated in 3.5 wt% NaCl solution (pH ~6.6) at 27±0.5 °C are shown in **Figure 4.16**. The E_{corr}, i_{corr}, the anodic and cathodic Tafel constants (b_a and b_c), E_{pit}, i_p, R_p, CR, P, and P_i, as well as other important corrosion parameters, were determined and are presented in **Table 4.6**. The DLC–coated steels had 3 separate zones, the active, passive, and transpassive zones, while the 4140 steel had no passive area and no pitting resistance, suggesting inferior corrosion resistance. When compared to the 4140 steel, all the DLC coatings significantly improved corrosion resistance, with increases in E_{corr}, E_{pit}, and R_p, but decreases in i_{corr} and CR. All of the DLC films had similar i_{corr} and CR values and were 3 orders of magnitude less than the 4140 steel. The E_{corr} moved from –443.31 and –442.69 mV to –425.08 and –382.93 mV for ta–C and ta–C:N, and ta–C:Al and ta–C:Al:N, respectively, indicating that Al–doped and Al–N–co–doped DLC films are slightly more stable than non–doped and N–doped DLC films. Furthermore, due to the synergy of Al oxide and sp^3 C–N bonds generated in the DLC films, ta–C:Al and ta–C:Al:N showed the second and highest corrosion resistance, respectively, as shown by the high R_p (3890.89 and 4237.02 Ω cm^2), high P_i (77.77 and 79.22 %) and low P (2.09×10^{-4} and 3.49×10^{-5}) demonstrated by XPS, which behaves as the primary barrier against the corrosive environment's penetration and destruction (Konkhunthot *et al.*, 2019; Wongpanya *et al.*, 2022; Xu *et al.*, 2018; Zhou *et al.*, 2019).
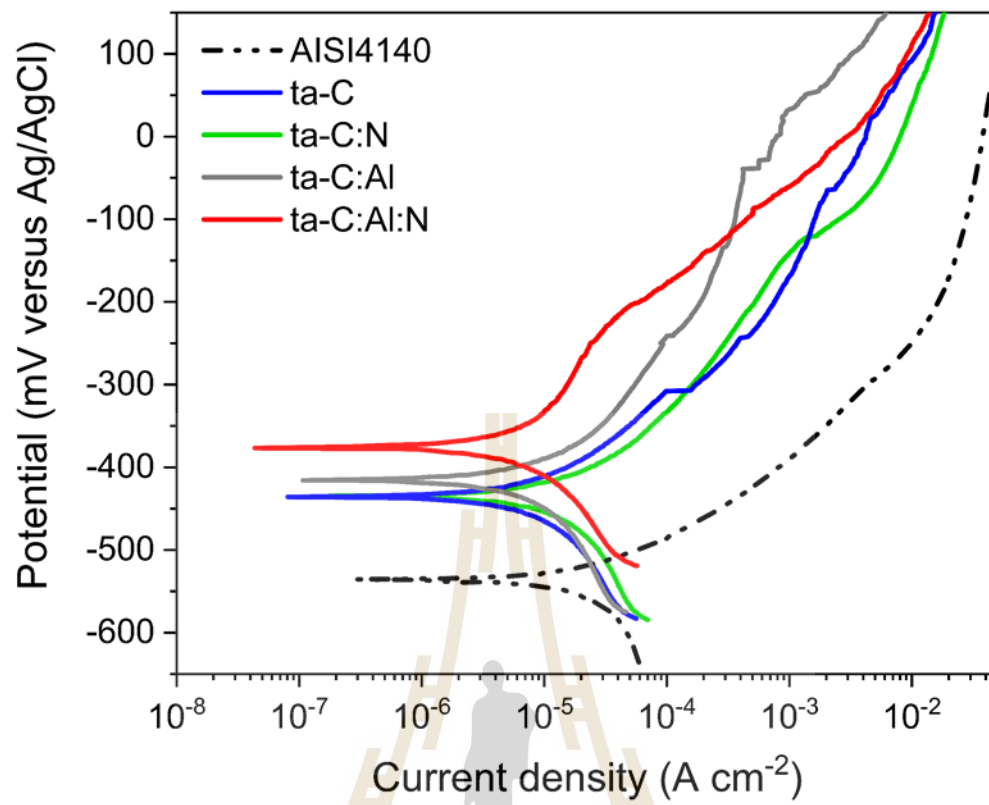
Figure 4.16 The polarization curves of AISI 4140, ta–C, ta–C:N, ta–C:Al, and ta–C:Al:N

in 3.5 wt% NaCl solution, respectively (Wongpanya *et al.*, 2022)

Table 4.6 Corrosion results for 4140 and ta–C, ta–C:N, ta–C:Al, and ta–C:Al:N electrochemically tested in 3.5 wt% NaCl solution (Wongpanya *et al.*, 2022)

Sample	E_{corr} (mV)	i_{corr} (µA cm^{-2})	b_a (mV dec^{-1})	b_c (mV dec^{-1})	E_{pit} (mV)	i_p (µA cm^{-2})	R_p (Ω cm^2)	CR (mm yr^{-1})	P	P_i (%)
AISI 4140	−547.44 (± 8.079)	10.30 (± 0.226)	40.38 (± 1.146)	53.13 (± 0.956)	–	–	967.20	1.22×10^{-1}	–	–
ta–C	−443.31 (± 6.072)	2.39 (± 0.050)	44.76 (± 1.596)	46.79 (± 1.220)	−310.06 (± 4.247)	46.50 (± 0.973)	4156.17	1.01×10^{-4}	1.09×10^{-3}	76.79
ta–C:N	−442.69 (± 7.949)	4.54 (± 0.143)	39.53 (± 1.429)	43.47 (± 1.133)	−126.66 (± 2.274)	354.00 (± 11.150)	1980.11	2.14×10^{-4}	1.09×10^{-3}	55.92
ta–C:Al	−425.08 (± 6.837)	2.29 (± 0.064)	39.80 (± 1.201)	42.36 (± 0.629)	−44.23 (± 0.711)	184.00 (± 5.140)	3890.89	1.28×10^{-4}	2.09×10^{-4}	77.77
ta–C:Al:N	−382.93 (± 5.883)	2.14 (± 0.042)	43.12 (± 1.118)	40.49 (± 0.602)	−201.13 (± 3.090)	22.20 (± 0.436)	4237.02	1.17×10^{-4}	3.49×10^{-5}	79.22
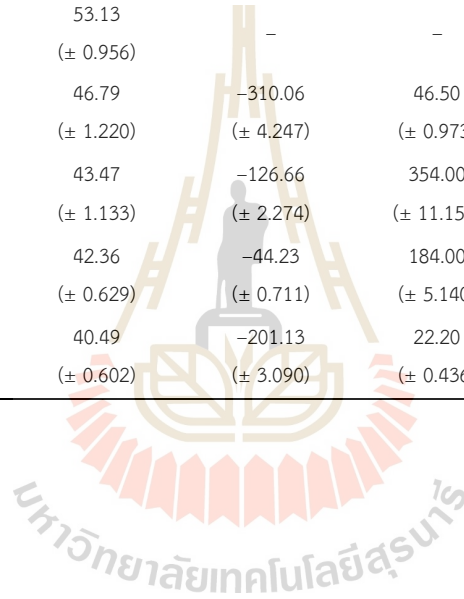
4.2.4 The structural and local bonding configuration analysis after the corrosion tests

The chemical bond structure was studied using XPS and NEXAFS methods once all the DLC films' corrosion experiments were completed. The observation of chemical elements C, N, and Al, as well as Fe (i.e., corrosion of the metal surface substrate), have been associated with the deterioration of the DLC films, with the exception of O due to contamination. This suggests that following corrosion testing, the DLC films' degradation was greatly decreased, as seen by the films' characteristics, such as sp^3 C–C, sp^3/sp^2 ratio, and the sp^3 relative fraction. The sp^3 C–C bond was obviously diminished in the DLC films, as evidenced by C 1s in **Table 4.8**, suggesting the corrosion degradation of the sp^3

C–C bond to the sp^2 C=C bond (Wongpanya, Pintitraratibodee, Thumanu, & Euaruksakul, 2021). The addition of Al and N to the DLC films reduced the deterioration of the DLC properties, as shown in the difference of the diamond structure (sp^3 C–C) quantity before and after the corrosion test, (11.85, 18.70, and 26.06 at.% declines for ta–C:Al:N, ta–C:Al, and ta–C:N, respectively), showing that the addition of Al and N to the DLC films hindered the degradation of the DLC properties (Konkhunthot et $al.$, 2019; Wongpanya, Silawong, & Photongkam, 2021). The slowing of all elements of the doped DLC films might be attributed to nitrides (sp^3–hybridized C–N for ta–C:N and ta–C:Al:N) and aluminium oxide (Al_2O_3 for ta–C: Al and ta–C:Al:N), as shown in **Tables 4.7** and **4.8**, respectively. Before corrosion testing, for example, ta–C:Al:N was discovered. After corrosion degradation, sp^3–hybridized C–N bond to the high Al_2O_3 content (81.99 and 100 at.%, respectively, in **Table 4.7**), and these bonds include the converted oxide to sp^2–hybridized C=N mixed with AlO_x (82.95 and 100 at.%, respectively, in **Table 4.8**).

Table 4.7 Type of bonding, sp^3/sp^2 ratio, and relative fraction of sp^3 of all the DLC films before the corrosion tests (Wongpanya *et al.*, 2022)

XPS spectra	Sample	Type of bonding (at.%)								Total	sp^3/sp^2 ratio	relative fraction of sp^3
		sp^3 C—C	sp^2 C=C	sp^3 C—N	sp^2 C=N	C—OH	C—O	C=O	Al—C—O			
C 1s	ta–C	68.95	16.12			2.41		12.52		100.00	4.28	0.81
	ta–C:N	40.52	17.74	2.97	26.61		12.16			100.00	0.98	0.50
	ta–C:Al	38.81	40.99			11.09	6.94		2.17	100.00	0.95	0.49
	ta–C:Al:N	50.65	21.20	21.19	0.24	6.64			0.08	100.00	3.35	0.77
		C—O	C—OH	C=O	N—O	O=C—OH						
O 1s	ta–C		10.90	89.10						100.00		
	ta–C:N	81.19			18.81					100.00		
	ta–C:Al	35.38	59.40			5.22				100.00		
	ta–C:Al:N	55.13	41.42		3.45					100.00		
		sp^3 C—N	sp^2 C=N	N—O								
N 1s	ta–C:N	25.59	67.77	6.64						100.00		
	ta–C:Al:N	81.99	11.33	6.68						100.00		
		AlO$_x$	Al$_2$O$_3$									
Al 2p	ta–C:Al	23.40	76.60							100.00		
	ta–C:Al:N		100.00							100.00		

Table 4.8 Type of bonding, sp^3/sp^2 ratio, and relative fraction of sp^3 of all the DLC films after the corrosion tests (Wongpanya *et al.*, 2022)

XPS spectra	Sample	Type of bonding (at.%)								Total	sp^3/sp^2 ratio	relative fraction of sp^3
		sp^3 C—C	sp^2 C=C	sp^3 C—N	sp^2 C=N	C—OH/C—O—C	C—O	C=O/COOH	Al—C—O			
C 1s	ta–C	24.77	50.12			19.39		5.72		100.00	0.49	0.33
	ta–C:N	14.46	50.98	1.51	21.99		3.24	7.82		100.00	0.22	0.18
	ta–C:Al	20.11	50.42			18.56	2.40	6.61	1.90	100.00	0.40	0.29
	ta–C:Al:N	38.80	42.78	1.52	9.43	0.71		6.59	0.17	100.00	0.77	0.44
		C—O/Al—OH	C—OH	C=O	N—O	O=C—OH	Fe₃O₄	FeO/Fe₂O₃	Metal carbonates	Al₂O₃		
O 1s	ta–C		1.16	6.32			39.57	47.42	5.53		100.00	
	ta–C:N	2.60			3.00		18.15	71.21	5.04		100.00	
	ta–C:Al	3.74	3.70			3.54	25.45	35.79		27.78	100.00	
	ta–C:Al:N	2.65	5.74		1.62		22.54	31.24		36.21	100.00	
		sp^3 C—N	sp^2 C=N	N—O								
N 1s	ta–C:N	8.92	88.23	2.85							100.00	
	ta–C:Al:N	13.54	82.95	3.51							100.00	
		AlOₓ	Al₂O₃	Al(OH)₃	Al–OH							
Al 2p	ta–C:Al	0.56	90.63	4.63	4.18						100.00	
	ta–C:Al:N	100.00									100.00	
		Fe (Me)	Fe (II)	Fe (III)								Fe (II)/Fe (III) ratio
Fe 2p	ta–C	13.93	51.59	34.48							100.00	1.496
	ta–C:N	6.53	63.10	30.37							100.00	2.078
	ta–C:Al	27.13	44.73	28.14							100.00	1.589
	ta–C:Al:N	26.59	31.37	42.04							100.00	0.746

This means that during corrosion, sp^3–hybridized C–N coupled with Al_2O_3 sacrificed itself. Thus, although ta–C:Al or ta–C:N deteriorates and sacrifices itself during corrosion, the deterioration of the sp^3 C–C bonds may be slowed. Both Al_2O_3 (76.60 at.%) and AlO_x (23.40 at.%) were used to determine this, as well as the low content of sp^3–hybridized C–N (25.59 at.%), which evaluated corrosion resistance performance. After corrosion, the quantity of the remaining sp^3 C–C bond was smaller than that for ta–C:Al:N (20.11, 14.46, and 38.80 at.% for ta–C:Al, ta–C:N, and ta–C:Al:N, respectively, in **Table 4.8**). As a result, the corrosion resistance of the DLC films degrading in NaCl solution may be graded as follows: slow decrease in sp^3–hybridized C–N and Al_2O_3 > Al_2O_3 > sp^3–hybridized C–N was established based on the synergistic impact of the 2 materials. The sp^3–hybridized C–N and Al_2O_3 are remarkable not only for the gradual deterioration of the DLC film in corrosive solutions, but also for the suppression of the DLC film degradation at high temperatures, and they are effective in preventing DLC films from corroding in water. However, there are drawbacks to preventing the DLC films' deterioration at high temperatures (Wongpanya, Silawong, & Photongkam, 2021), but the creation of a single bond sp^3–hybridized C–N structure might inhibit the process. At high temperatures, the film becomes graphitized; while it is not quite up to par in terms of corrosion resistance, Fe $2p$ confirmed that the DLC film had deteriorated. A wide range of Fe (metal and compound) XPS measurements were made, including Fe (II) (Fe_2O_3, Fe_3O_4), Fe (III) (Fe_2O_3, Fe_3O_4), and Fe (III) (FeOOH) at roughly 707.0, 709.6, 710.8, and 711.8 eV, respectively (Fredriksson et $al.$, 2012; Guo et $al.$, 2014). Degradation of all the DLC films occurred until the metal (Fe) surface was found. The oxidation of Fe into Fe^{2+} ions generates oxides of Fe (II), which are further oxidized to create oxides of Fe (III) (Jones, 1996) in a corrosive environment rich in water and oxygen. All films included a combination of Fe (II) and Fe (III) molecules. The Fe (II)/Fe (III) ratio is used to measure the stability of Fe oxides, and it is graded as follows: deterioration of the DLC film structure may be seen in the decrease in ta–C:Al:N < ta–C:Al < ta–C:N. This investigation confirmed the interaction between the O and C or metals (Al and Fe in this work) during corrosion, as well as the O 1s measurement findings in the XPS and peaks compatible with Al and/or Fe oxides (O^{2-}) at around 530.3 eV. In Konkhunthot et $al.$, 2019, Wongpanya, Pintitraratibodee,

Thumanu, & Euaruksakul, 2021, Wang *et al.*, 2001, Hanawa *et al.*, 2002, and Marcelin *et al.*, 2013, the N–O/O=C–OH bonds and the C–O, C–OH, and C=O at 530.50 eV and 532.0–533.4 eV peaks which existed before corrosion (Konkhunthot *et al.*, 2019; Jiménez *et al.*, 2001) resembled what was discovered. A combination of X–PEEM and NEXAFS was used to investigate the effects of corrosion on the structural bonding of the DLC films in various locations, including the mildly corroded zone (Area 1) and the severely corroded zone (Area 2), as seen in **Figure 4.17**. The NEXAFS C *K*–edge spectra for all the DLC films in **Figure 4.17** show distinct characteristics for Area 1 and Area 2. According to Area 2, it is clear that the C 1*s* transition to the unoccupied π^* and σ^* states at the sp^2–hybridized site was detected by the peaks at 285.4 and 292.0eV, respectively (Konkhunthot *et al.*, 2019; Wongpanya, Silawong, & Photongkam, 2021; Soin *et al.*, 2012). Due to severe corrosion, the sp^2–hybridized bond percentage of all the DLC films before corrosion in **Figure 4.5** rose from 0.345, 0.394, 0.538, and 0.348 for ta–C, ta–C:N, ta–C:Al, and ta–C:Al:N, respectively, to 1.00. However, in Area 1 these transitions, notably at 292.0 eV, were almost undetectable owing to the minor rise in the sp^2–hybridized bond fraction to 0.491 for ta–C, 0.615 for ta–C:Al, 0.455 for ta–C:Al, and 0.640 for ta–C:N, due to mild corrosion. The graphitization of the DLC films due to corrosion can be seen in these data, which are in agreement with the XPS results.
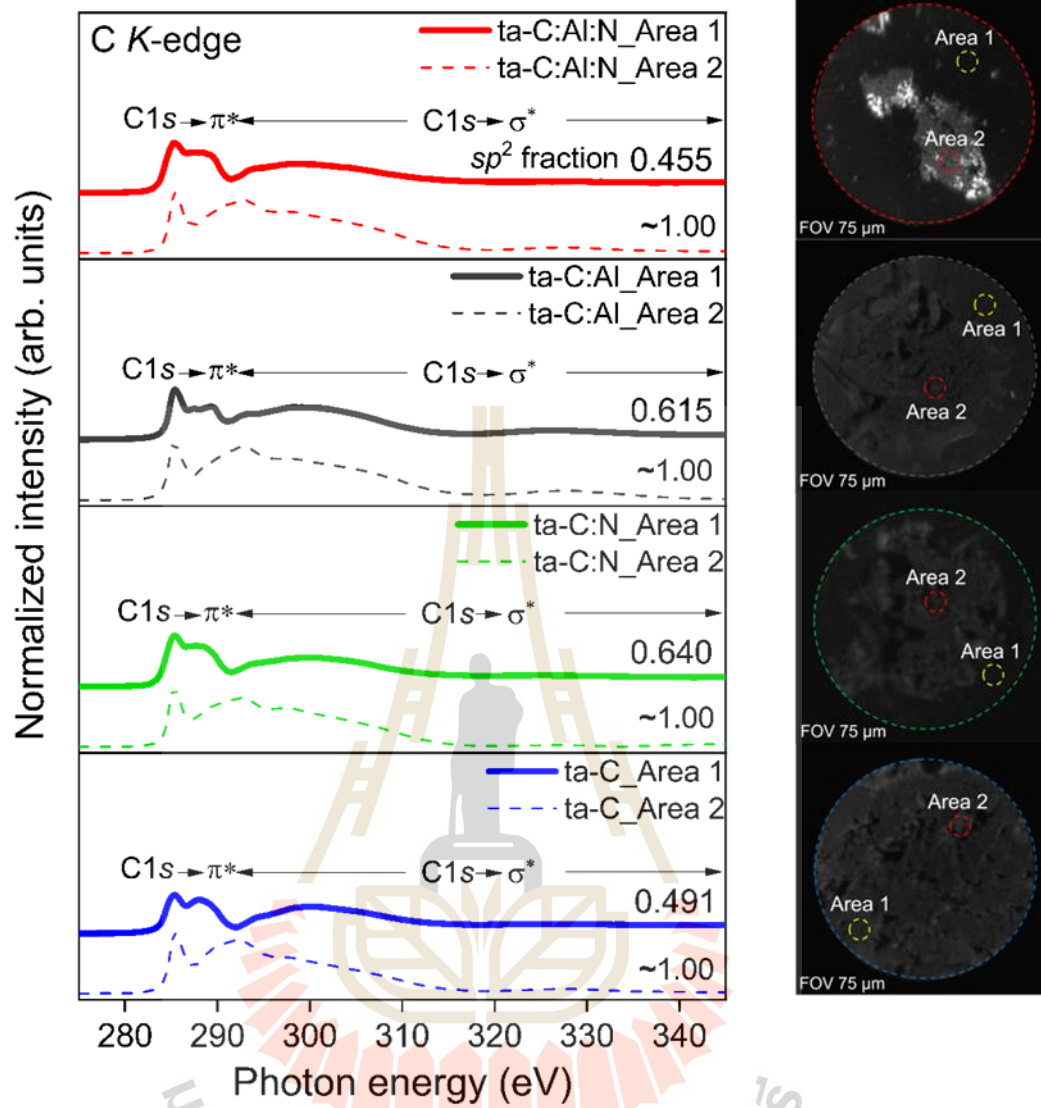
Figure 4.17 The C *K*–edge NEXAFS spectra generated for ta–C, ta–C:N, ta–C:Al, and ta–C:Al:N after the corrosion tests (Wongpanya *et al.,* 2022)
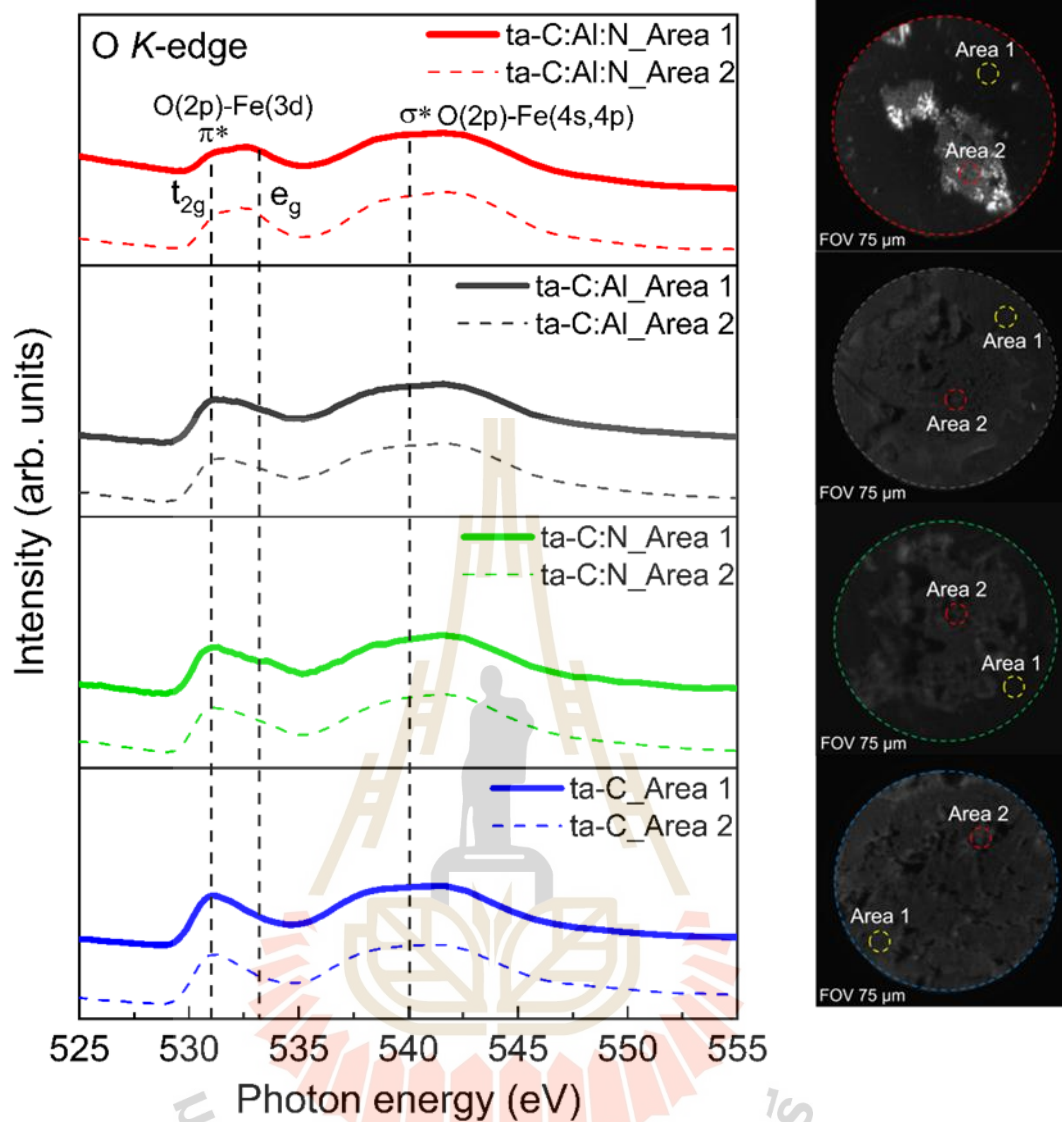
Figure 4.18 The O *K*–edge NEXAFS spectra generated for ta–C, ta–C:N, ta–C:Al, and ta–C:Al:N after the corrosion tests (Wongpanya *et al.*, 2022)

Although the NEXAFS O *K*–edge spectra (**Figure 4.18**) of all the DLC films before corrosion were comparable, extra strong peaks at ~533.0 and 540.0 eV, which correspond to O 2*p* hybridization with 3*d* and 4*s* and 4*p* metals, respectively, were seen. Area 1 and Area 2 DLC films had similar O *K*–edge spectra before corrosion, however the increased predominant peaks at ~533.0 and 540.0 eV, which correspond to O 2*p* had become hybridized with 3*d*, 4*s*, and 4*p* metals, respectively, including the O 1*s* $\longrightarrow$ **σ*** (C–O and C=O) transitions (at 540.0 eV), clearly indicating the degradation

of the DLC films and the evolution of Fe oxides from corrosion, respectively (de Groot *et al.*, 1989; Kim *et al.*, 2018).
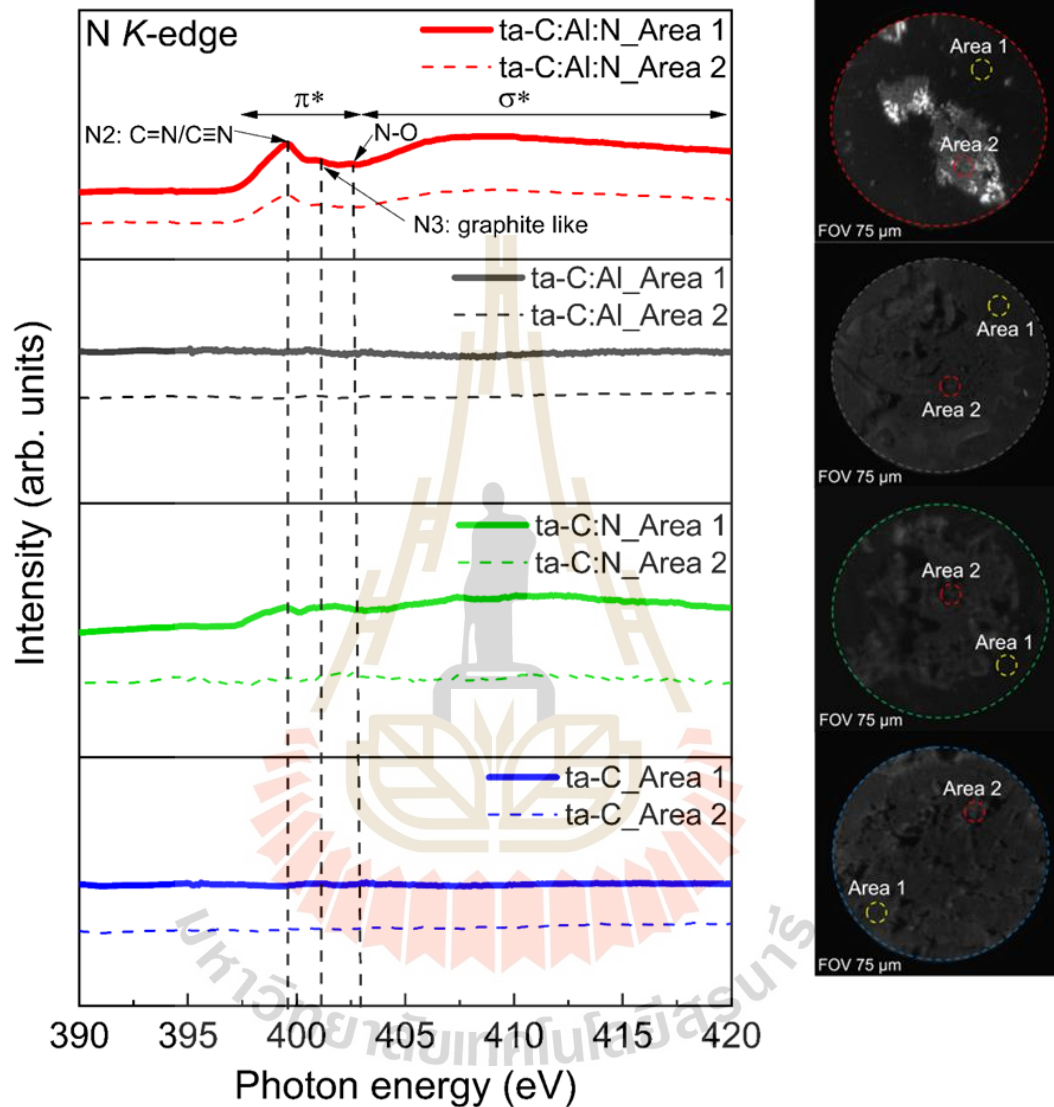
Figure 4.19 The N *K*–edge NEXAFS spectra generated for ta–C, ta–C:N, ta–C:Al, and ta–C:Al:N after the corrosion tests (Wongpanya *et al.*, 2022)

Following the corrosion tests, all the specimens' N *K*–edge NEXAFS spectra (**Figure 4.19**) were analyzed. The ta–C:Al:N specimen, which has N2, N3, and N—O peaks at around 399.5, 401.5–402.4, and 403.2 eV, respectively, demonstrates the

N *K*–edge NEXAFS spectral features. In the Area 1 spectral peak, the ta–C:N specimen contains a C=N bond and/or a C≡N link, graphite–like molecules, and nitrogen molecules (Iyer and Maguire, 2011; Roy *et al.*, 2005). The spectrum is obscured and undetectable in Area 2 due to significant corrosion on the material. The N *K*–edge NEXAFS spectrum was not identified in the ta–C or ta–C:Al specimens, which is consistent with the absence of N—O before the corrosion tests in the elemental doped materials. The specimens may be exposed to air or natural contaminants after the corrosion test, which react with the coating layer. In circumstances when a post–test NEXAFS analysis is necessary, the surface cannot be cleaned using the sputtering technique prior to testing. This is because it prevents corrosion products or the corroded film layer from being removed, which may result in inaccurate results.

Fe (metal), Fe (II) (FeO and Fe_3O_4), and Fe (III) (Fe_2O_3, Fe_3O_4, and FeOOH), respectively, were found in the NEXAFS Fe $L_{3,2}$–edge spectra for all the DLC films at 708, 710.1, and 711 eV (Leveneur *et al.*, 2011; Everett *et al.*, 2014). Fe metal, Fe (II), and Fe (III) were detected in all the DLC layers following corrosion (III), except for ta–C:Al:N, which correlates to the XPS findings; the Fe (II) peak was much more intense than the Fe (III) peak, particularly for ta–C, ta–C:N, and ta–C:Al.
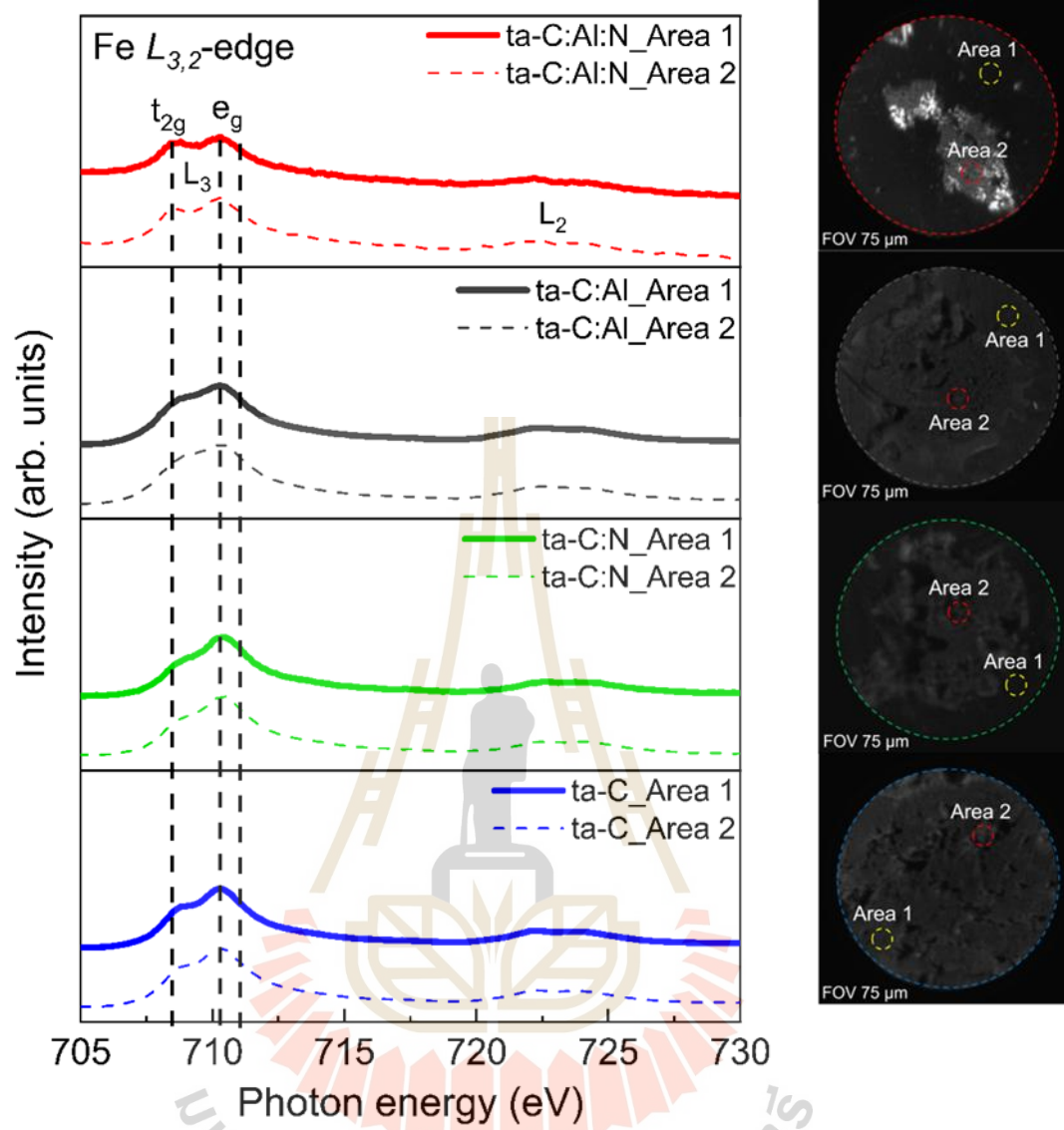
Figure 4.20 The Fe $L_{3,2}$–edge NEXAFS spectra generated for ta–C, ta–C:N, ta–C:Al, and ta–C:Al:N after the corrosion tests (Wongpanya *et al.*, 2022)

Following the corrosion tests, structural analysis using XPS and NEXAFS was performed, as shown, and the results discussed in section 4.2.4. When all the AISI 4140 steel specimens and specimens coated with the DLC film layer were evaluated for corrosion in 3.5 wt% NaCl solution, the surfaces were analyzed using SEM, as shown in **Figure 4.21**. Corrosion surface damage was observed to be greater in the AISI 4140 steel than in the DLC film layers. The appearances of the corrosion surfaces indicate that the corrosion behavior of AISI 4140 is general corrosion. For the DLC coating, the appearance of cracks in the film, delamination, and corrosion at certain spots may be due to a defect or droplet, including cracks in the film layer owing to the high film stress or the ability to have low adhesion between the DLC films and the substrate material. When the solution passes through the film layer, it causes severe corrosion with behavior comparable to crevice corrosion or localized corrosion. The DLC coatings and substrate materials have different chemical compositions that are not all equally resistant to corrosion, and it can be said that between these areas there are different electrochemical potentials. Whereas the substrate material has a lower electrochemical potential than the DLC films and, thus, the substrate material loses its metal, the DLC films act as an electron acceptor. This is known as galvanic corrosion. The severity of this form of corrosion is determined by the difference in electrochemical potential. The larger the difference, the greater the degree of corrosion. As a result, specimens with the DLC coating are prone to surface degradation and there was such a severe loss of metal that some film sites ruptured and collapsed following corrosion, as shown in the SEM images, consistent with the research by Liu *et al.*, 2006.
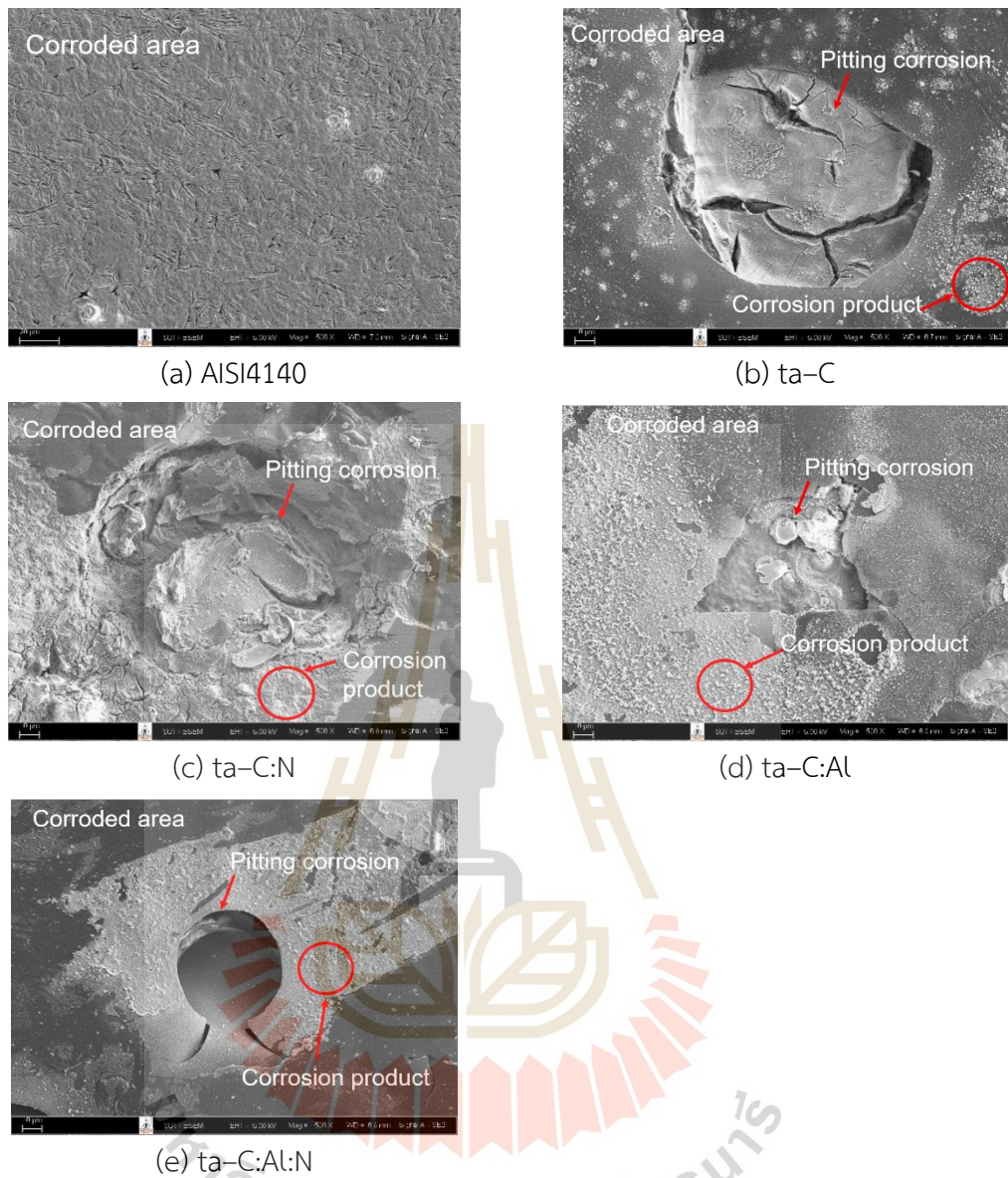
Figure 4.21 Surface appearance of specimens after corrosion testing: (a) AISI4140, (b) ta–C, (c) ta–C:N, (d) ta–C:Al, and (e) ta–C:Al:N, respectively, at 500X

For AISI 4140 steels contacted to a 3.5 wt% NaCl (pH ~6.6) solution, a significant amount of hydroxyl [OH⁻] ion was dissolved as a consequence of the NaCl solution dissociating, resulting in surface corrosion. For the portion of the surface that comes into touch with the solution, corrosion will develop on a regular basis across the surface. This is often seen in metals when a protective coating cannot develop

quickly enough, resulting in extensive corrosion and significant surface damage. To begin, the oxidation processes that results in the formation of iron ions during corrosion are shown in Equation (4.6) below. When the solution is exposed to air or includes oxygen and water vapor, it begins to decompose. When iron ions react quickly with [OH$^-$] Equation (4.7) below, ferrous hydroxide is formed and precipitates on the surface, as shown in Equation (4.8) below, and when ferrous hydroxide reacts with oxygen, ferric oxide or hematite compounds are formed. When the very stable oxide coating (Fe$_2$O$_3$) on the steel surface interacts with water, only iron rust in the form of Fe$_2$O$_3$ remains, which has a reddish–brown color, as in Equation (4.9) below. As a consequence of the dissolved oxygen in the solution forming water molecules, as shown in Equation (4.10) below, the corrosion process continues. All of these processes, starting with Equations (4.6) through (4.10), regulate the corrosion of AISI4140 steel (Datta $et\ al.$, 2021).

$$Fe_{(s)} \longrightarrow Fe^{2+}_{(aq)} + 2e^- \qquad (4.6)$$

$$O_2 + 2H_2O + 4e^- \longrightarrow 4OH^-_{(aq)} \qquad (4.7)$$

$$Fe^{2+}_{(aq)} + 4OH^- \longrightarrow 2Fe(OH)_{2\ (s)} \qquad (4.8)$$

$$2Fe(OH)_{2\ (s)} + (1/2)O_{2\ (g)} \longrightarrow Fe_2O_3 \cdot 3H_2O_{(s)} + H_2O_{(l)} \qquad (4.9)$$

$$O_{2\ (g)} + 4H^+_{(aq)} + e^- \longrightarrow 2H_2O \qquad (4.10)$$
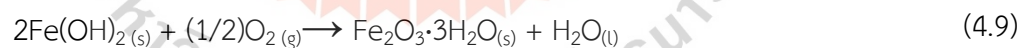
Moreover, iron oxide deposits (FeOOH, Fe$_2$O$_3$, Fe$_3$O$_4$) on the substrate have an effect on these surface film formation processes. The cathodic and anodic reactions, Equations (4.6) and (4.7), may occur underneath the FeOOH and Fe$_3$O$_4$– covered specimens. The following reactions took place on the steel substrate while the FeOOH deposit was present (Kim and Kim, 2017). Raises in the FeOOH reduction process demand more Fe^{2+} ions, which increases the solubility of Equation (4.6)'s

anode. Under deposition of FeOOH, these reactions may result in the production of Fe_3O_4, as shown in Equations (4.11) and (4.12):

$$2FeOOH + Fe^{2+}_{(aq)} \longrightarrow Fe_3O_4 + 2H^+ \tag{4.11}$$

$$Fe^{2+} + 8FeOOH + 2e^- \longrightarrow 3Fe_3O_4 + 4H_2O \tag{4.12}$$
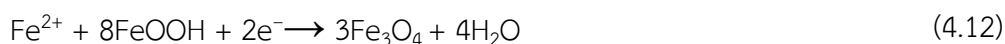
Corrosion of the whole DLC film layer occurs when the film layer is dissolved and ionized in the electrolyte solution upon contact with the 3.5 wt% NaCl solution. The reaction produces electrons that flow through the film's lowest resistance area to the cathodic reaction zone. Thus, the most significant reactions occur when the liberated electrons reduce the dissolved oxygen, water molecules, and hydrogen ions in the electrolyte, where O^{2-} denotes oxygen in its reduced state as H_2O, OH^-, and/or Me–O (Khun et $al.$, 2009; Elam et $al.$, 2021). As a result, for the film electrochemical reaction, DLC follows Equations (4.13) to (4.18).

$$2H^+ + 2e^- \longrightarrow H_2 \tag{4.13}$$

$$2H_2O + 2e^- \longrightarrow H_{2(g)} + 2OH^- \tag{4.14}$$

$$2H_2O + O_2 + 4e^- \longrightarrow 4OH^- \tag{4.15}$$

$$C + 6OH^- \longrightarrow CO_3^{2-} + 3H_2O + 4e^- \tag{4.16}$$

$$C + (O^{2-}) \longrightarrow CO + 2e^- \tag{4.17}$$

$$CO + (O^{2-}) \longrightarrow CO_2 + 2e^- \tag{4.18}$$

Similarly, the reaction occurs in the nitrogen–doped DLC film. This is because nitrogen doped in the film's layer is capable of dissolving and forming a bind with the film's carbon. The dissolving and ionization of the film layer in the electrolyte solution are induced by the conversion of sp^3 to the sp^2 structure (Khun *et al.*, 2009), which indicates if the film layer has degraded or generated graphitization during corrosion.

When the aluminium–doped film layer in the DLC film comes into contact with a 3.5 wt% NaCl solution, both anodic and cathodic reaction corrosion of the aluminium occurs. This results in an increase in the solubility of the aluminium and a decrease in dissolved oxygen. Finally, the aluminium hydroxide, $Al(OH)_{3(ads)}$ (Singh *et al.*, 2014), then develops a transformation to aluminium oxide as demonstrated in Equations (4.19) to (4.22):

$$Al_{(ads)} \longrightarrow Al^{3+} + 3e^- \tag{4.19}$$

$$(1/2)O_2 + 2H_2O + 3e^- \longrightarrow 3OH^- + (1/2)H_2 \tag{4.20}$$

$$Al^{3+} + 3OH^- \longrightarrow Al(OH)_{3\,(ads)} \tag{4.21}$$

$$2Al(OH)_{3\,(ads)} \longrightarrow Al_2O_3 \cdot 3H_2O \tag{4.22}$$
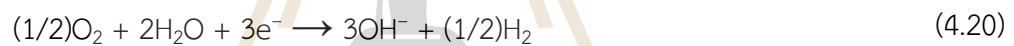
For the Al–doped and Al and N co–doped DLC, the corrosion resistance is provided by the Al_2O_3 that develops on the workpiece's surface. Due to the fact that it is a very chemical inert compound in an aquatic environment, as long as oxygen is available, this Al_2O_3 oxide develops with an increased thickness. If a fault arises, this oxide will return to its initial condition. However, in a 3.5 wt% NaCl solution, breakdown of the passive film occurs and repairs to it are hampered because of the strong environment corrosion (Singh *et al.*, 2014).

CHAPTER 5

CONCLUSION AND SUGGESSTION

5.1   Conclusion

As stated in Chapter 4, the qualities of the synthesized film were evaluated before and after the tests for mechanical properties, thermal stability, and corrosion resistance, which can be summarized in the thesis as follows:

5.1.1   The optimal conditions for all DLC films on the AISI4140 substrate by FCVA deposition are:

- V_{arc} of C is 800V and V_{arc} of Al is 400V.

- V_{bias} of sample is -1000V.

- Duty cycle and Frequency are 0.003% and 6.0 Hz, respectively.

- Base pressure is 8.5×10^{-4} Pa.

- UHP N_2 flow rate is 2.5 SCCM for ta-C:N and ta-C:Al:N, respectively.

5.1.2   The thermal stability test using in-situ NEXAFS spectroscopy, the heat resistance of Al-N co-doped film was up to 600°C because the sp^3 C–N and Al_2O_3 bonding in the film are promoted the thermal stability of the film. The maximum temperature resistances of the Al-doped, N-doped, and pure DLC are RT, 280, and 400°C, respectively (the sp^2–fraction of up to 0.50).

5.1.3   The nanomechanical properties, adhesion strength, and corrosion resistance of the all DLC films are:

5.1.3.1 The nanomechanical properties of the DLC films with N doping and Al–N co–doping dropped slightly when compared to the pure DLC, while the Al–doped films decreased considerably. Reduced H and E correspond with higher I_D/I_G, whereas L_a is related to an increase in the concentration of sp^2–hybridized carbon bonds and a decrease in sp^3/sp^2. The quantity of sp^3–hybridized carbon bonds in the film significantly affects the nanomechanical characteristics.

5.1.3.2 The adhesion strength of all DLC films, as the dopant

concentration was raised, the elastic recovery of the DLC films decreased. When the undoped DLC film (ta–C) is doped with Al and Al–N, a rising L_{c2} is seen. This decreases internal stress and increases the size of the graphite clusters at the sp^2 sites (L_a). This phenomenon results in a large proportion of sp^3–hybridized C–N bonds in ta–C:N and Al_2O_3 in ta–C:Al and ta–C:Al:N. These films (ta–C:Al:N > ta–C:N > ta–C:Al > ta–C) had CPRs of 12187.06, 9114.59, 8750.99, and 8697.89 mN^2, respectively, with ta–C:Al:N having the highest toughness and adhesion strength.

5.1.3.3 The all DLC coatings improved corrosion resistance while decreasing i_{corr} and CR as compared to the AISI 4140 steels. The i_{corr} and CR values for all DLC films were identical. E_{corr} shifted from –443.31 to –442.69 mV for ta–C and ta–C:N, and –425.08 to –382.93 mV for ta–C:Al and ta–C:Al:N, respectively. DLC films with Al–doped and Al–N–co–doped are marginally more stable than pure DLC and DLC with N–doped. Due to the synergy of Al oxide and sp^3 C – N bonds in the DLC films (referred to in the XPS result), ta–C: Al and ta–C:Al:N are also exceptionally resistant to corrosion (the second and highest, respectively). The high R_p (3890.89 and 4237.02 cm^2) and high P_i (77.77 and 79.22 %), as well as the low P, demonstrate this (2.09x10^{-4} and 3.49x10^{-5}), respectively. Because of co–doping DLC, the DLC film additives including Al and N preserve both remarkable nanomechanical characteristics and great thermal stability. Along with its excellent corrosion resistance and strong adhesion strength, the Al–N co–doped DLC is very attractive and is ideal as an alternative for surface coating applications to be utilized in wear and tribological applications, particularly at high temperatures or in corrosive environments.

5.2   Suggestions

The nanoscale mechanical characteristics, film adhesion, oxidation resistance, and corrosion resistance of AISI 4140 steel coated with non–doped, N–doped, Al–doped, and co–doped Al–N diamond–like carbon films by the FCVA process should be investigated. As seen in the preceding chapter, this PhD thesis includes research and experimentation. It is anticipated that the information gathered in this research will be beneficial and can contribute significantly to the advancement of knowledge useful for future development or practical application. As a result, more research

should be conducted under that section on particular facets. As a result, the following suggestions are given for further research:

5.2.1   Experiments should be conducted to determine the appropriate quantities of aluminium alloy and nitrogen and to investigate or measure the Al which may react with N to produce an AlN layer in the film layer.

5.2.2   The thermal annealing should be cyclically tested in range of RT to 700 °C for investigation the thermal stability of DLC film nearly the apply condition.
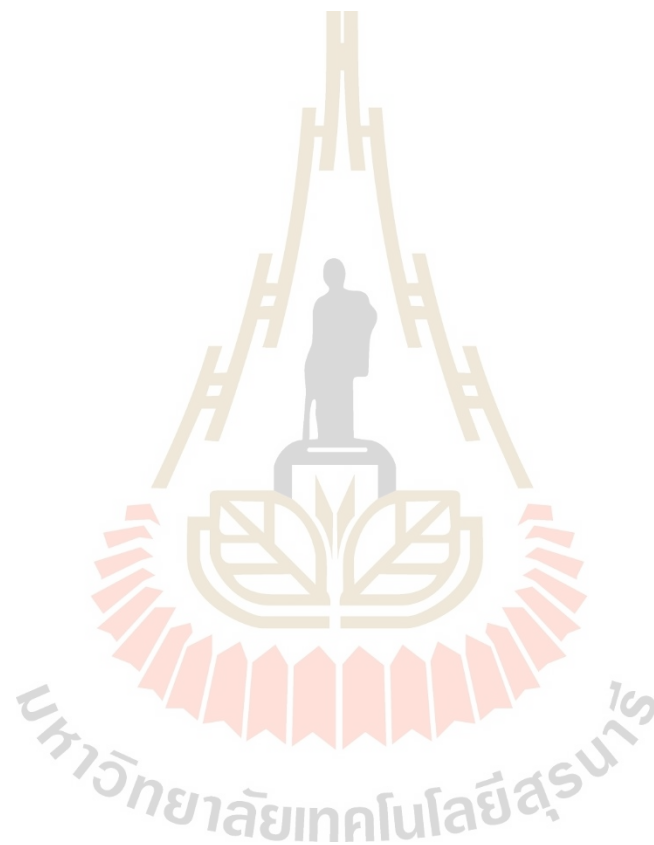
REFERENCES

Al Mahmud, K. A. H., Kalam, M. A., Masjuki, H. H., Mobarak, H. M., & Zulkifli, N. W. M. (2015). An updated overview of diamond-like carbon coating in tribology. **Critical Reviews in Solid State and Materials Sciences**, 40(2), 90-118. doi:10.1080/10408436.2014.940441

Anders, A. (2008a). *Case study: Tetrahedral amorphous carbon (ta–c) in cathodic arcs, from fractal spots to energetic condensation*. New York: Springer Science+Business Media. LLC, 394–399.

------. (2008b). *Cathodic arcs: From fractal spots to energetic condensation*. New York

------. (2008c). *Tetrahedral amorphous carbon (ta–c) in cathodic arcs, from fractal spots to energetic condensation*. New York: Springer Science+Business Media. LLC, 445–447.

Aperador, W., Delgado, A., & Duque, J. (2013). Corrosion resistanne of the [tin/crn]n coatings deposited on steel aisi 4140. **International Journal of Electrochemical Science**, 8, 10711-10719.

Ashtijoo, P. (2016). *Fabrication and characterization of adherent diamond–like carbon based thin films on polyethylene terephthalate by end hall ion beam deposition.* Master of Science, University of Saskatchewan, Saskatoon, Canada.

ASTM-102–89. (2015). Standard practice for calculation of corrosion rates and related information from electrochemical measurements. *ASTM Int* (89), 1-7. doi:10.1520/G0102–89R15E01

ASTM-E2546-07. (2007). Standard practice for instrumented indentation testing. *ASTM B Stand 1* (03.01), 1-23. doi:10.1520/E2546-15

ASTM-G3–89. (2006). Standard practice for conventions applicable to electrochemical measurements in corrosion testing. *ASTM Int* (3.02), 1-9.

ASTM-G59–97. (2014). Standard test method for conducting potentiodynamic polarization resistance measurements. *ASTM Int* (97), 1-4. doi:10.1520/G0059–97R14

Beake, B. D., Ogwu, A. A., & Wagner, T. (2006). Influence of experimental factors and film thickness on the measured critical load in the nanoscratch test. **Materials Science and Engineering: A**, 423(1), 70-73. doi.org/10.1016/j.msea.2005.09.121

Beake, B. D., Vishnyakov, V. M., Valizadeh, R., & Colligon, J. S. (2006). Influence of mechanical properties on the nanoscratch behaviour of hard nanocomposite tin/si3n4coatings on si. **Journal of Physics D: Applied Physics**, 39(7), 1392-1397. doi:10.1088/0022-3727/39/7/009

Bhandari, H., Kumar, S. A., & Dhawan, S. K. (2012). Conducting polymer nanocomposites for anticorrosive and antistatic applications *Nanocomposites - new trends and developments*.

Biluš Abaffy, N., McCulloch, D. G., Partridge, J. G., Evans, P. J., & Triani, G. (2011). Engineering titanium and aluminum oxide composites using atomic layer deposition. **Journal of Applied Physics**, 110(12), 123514. doi:10. 1063 /1.3667134

Bootkul, D., Supsermpol, B., Saenphinit, N., Aramwit, C., & Intarasiri, S. (2014). Nitrogen doping for adhesion improvement of dlc film deposited on si substrate by filtered cathodic vacuum arc (fcva) technique. **Applied Surface Science**, 310, 284-292. doi:10.1016/j.apsusc.2014.03.059

Bouabibsa, I., Lamri, S., Alhussein, A., Minea, T., & Sanchette, F. (2018). Plasma investigations and deposition of me-dlc (me = al, ti or nb) obtained by a magnetron sputtering-rfpecvd hybrid process. **Surface and Coatings Technology**, 354, 351-359. https://doi.org/10.1016/j.surfcoat.2018.09.033

Chen, C.-C., & Hong, F. C.-N. (2005). Structure and properties of diamond-like carbon nanocomposite films containing copper nanoparticles. **Applied Surface Science**, 242(3), 261-269. https://doi.org/10.1016/j.apsusc.2004.08.036

Chu, P. K., & Li, L. (2006). Characterization of amorphous and nanocrystalline carbon films. **Materials Chemistry and Physics**, 96(2), 253-277. doi.org/ 10.1016/j.matchemphys.2005.07.048

Coll, B. F., & Chhowalla, M. (1996). Amorphous diamond film by enhanced arc deposition. **Surface and Coatings Technology**, 79(1), 76-86. doi.org /10.1016 /0257-8972(95)02444-1

Constantinou, M., Pervolaraki, M., Koutsokeras, L., Prouskas, C., Patsalas, P., Kelires, P., Constantinides, G. (2017). Enhancing the nanoscratch resistance of pulsed laser deposited dlc films through molybdenum-doping. **Surface and Coatings Technology**, 330(C), 185-195. doi:10.1016/j.surfcoat.2017.09.048

Cui, X.-J., Ning, C.-M., Shang, L.-L., Zhang, G.-A., & Liu, X.-Q. (2019). Structure and anticorrosion, friction, and wear characteristics of pure diamond-like carbon (dlc), cr-dlc, and cr-h-dlc films on az91d mg alloy. **Journal of Materials Engineering and Performance**, 28(2), 1213-1225. doi:10.1007/s11665-019-3854-8

Da Silva, D. S., Côrtes, A. D. S., Oliveira, M. H., Motta, E. F., Viana, G. A., Mei, P. R., & Marques, F. C. (2011). Application of amorphous carbon based materials as antireflective coatings on crystalline silicon solar cells. **Journal of Applied Physics**, 110(4), 043510. doi:10.1063/1.3622515

Dai, W., Gao, X., Liu, J., Kwon, S.-H., & Wang, Q. (2017). Compositionally modulated multilayer diamond-like carbon coatings with altisi multi-doping by reactive high power impulse magnetron sputtering. **Applied Surface Science**, 425, 855-861. doi.org/10.1016/j.apsusc.2017.07.080

Dai, W., Gao, X., Liu, J., & Wang, Q. (2016). Microstructure, mechanical property and thermal stability of diamond-like carbon coatings with al, cr and si multi-doping. **Diamond and Related Materials**, 70, 98-104. doi.org/10.1016 /j.diamond. 2016.10.017

Dai, W., & Wang, A. (2011). Deposition and properties of al-containing diamond-like carbon films by a hybrid ion beam sources. **Journal of Alloys and Compounds**, 509(13), 4626-4631. doi:10.1016/j.jallcom.2011.01.132

Datta, T., Pathak, A. D., Basak, S., Gollapudi, S., & Sahu, K. K. (2021). Fractal behavior of surface oxide crack patterns on aisi 4140 high-strength low-alloy steel exposed to the simulated offshore environment. **Applied Surface Science Advances**, 5, 100110. doi.org/10.1016/j.apsadv.2021.100110

De Groot, F. M. F., Grioni, M., Fuggle, J. C., Ghijsen, J., Sawatzky, G. A., & Petersen, H. (1989). Oxygen 1s x-ray-absorption edges of transition-metal oxides. **Physical Review B**, 40(8), 5715-5723. doi:10.1103/PhysRevB.40.5715

De Moerlooze, K., Al-Bender, F., & Van Brussel, H. (2011). An experimental study of ball-on-flat wear on a newly developed rotational tribometer. **Wear***, 271(7), 1005-1016. doi.org/10.1016/j.wear.2011.01.027

Deng, X., Kousaka, H., Tokoroyama, T., & Umehara, N. (2013). Thermal stability and high-temperature tribological properties of a-c:H and si-dlc deposited by microwave sheath voltage combination plasma. **Tribology Online***, 8(4), 257-264. doi:10.2474/trol.8.257

Derradji, N. E., Mahdjoubi, M. L., Belkhir, H., Mumumbila, N., Angleraud, B., & Tessier, P.-Y. (2005). Nitrogen effect on the electrical properties of cnx thin films deposited by reactive magnetron sputtering. **Thin Solid Films***, 482, 258-263. doi:10.1016/j.tsf.2004.11.137

Ding, J. C., Mei, H., Jeong, S., Zheng, J., Wang, Q. M., & Kim, K. H. (2021). Effect of bias voltage on the microstructure and properties of nb-dlc films prepared by a hybrid sputtering system. **Journal of Alloys and Compounds***, 861, 158505. doi.org/10.1016/j.jallcom.2020.158505

Dingemans, G., Engelhart, P., Seguin, R., Mandoc, M. M., Sanden, M. C. M., & Kessels, W. M. M. (2010). *Comparison between aluminum oxide surface passivation films deposited with thermal ald, plasma ald and pecvd*.

Donnet, C. (1998). Recent progress on the tribology of doped diamond-like and carbon alloy coatings: A review. **Surface and Coatings Technology***, 100-101, 180-186. doi.org/10.1016/S0257-8972(97)00611-7

Edlmayr, V., Moser, M., Walter, C., & Mitterer, C. (2010). Thermal stability of sputtered al2o3 coatings. **Surface and Coatings Technology***, 204, 1576-1581. doi:10.1016/j.surfcoat.2009.10.002

Eklund, P., Madanag, S., Singh, G., & Bøttiger, J. (2009). Thermal stability and phase transformations of γ-/amorphous-al2o3 thin films. **Plasma Processes and Polymers***, 6. doi:10.1002/ppap.200932301

Elam, F. M., Hsia, F.-C., van Vliet, S., Bliem, R., Yang, L., Weber, B., & Franklin, S. E. (2021). The influence of corrosion on diamond-like carbon topography and friction at the nanoscale. **Carbon***, 179, 590-599. doi.org/10.1016/j.carbon.2021.04.068

Euaruksakul, C., Jearanaikoon, N., Busayaporn, W., Kamonsutthipaijit, N., Photongkam, P., Tunmee, S., & Songsiriritthigul, P. (2013). Photoemission electron microscopy beamline at the synchrotron light research institute. **Journal of Physics: Conference Series**, 425, 182011. doi:10.1088/1742-6596/425/18/182011

Everett, J., Céspedes, E., Shelford, L. R., Exley, C., Collingwood, J. F., Dobson, J., . . . Telling, N. D. (2014). Ferrous iron formation following the co-aggregation of ferric iron and the alzheimer's disease peptide β-amyloid (1–42). **Journal of The Royal Society Interface**, 11(95), 20140165. doi:10.1098/rsif.2014.0165

Fattah, M., & Mahboubi, F. (2010). Comparison of ferritic and austenitic plasma nitriding and nitrocarburizing behavior of aisi 4140 low alloy steel. **Materials & Design**, 31(8), 3915-3921. doi.org/10.1016/j.matdes.2010.03.008

Ferrari, A. C. (2002). Determination of bonding in diamond-like carbon by raman spectroscopy. **Diamond and Related Materials**, 11(3), 1053-1061. doi.org/10.1016/S0925-9635(01)00730-0

Ferrari, A. C., Libassi, A., Tanner, B. K., Stolojan, V., Yuan, J., Brown, L. M., Robertson, J. (2000). Density, ${\mathrm{sp}^{3}}$ fraction, and cross-sectional structure of amorphous carbon films determined by x-ray reflectivity and electron energy-loss spectroscopy. **Physical Review B**, 62(16), 11089-11103. doi:10.1103/PhysRevB.62.11089

Ferrari, A. C., & Robertson, J. (2000). Interpretation of raman spectra of disordered and amorphous carbon. **Physical Review B**, 61(20), 14095-14107. doi:10.1103/PhysRevB.61.14095

----. (2001). Resonant raman spectroscopy of disordered, amorphous, and diamondlike carbon. **Physical Review B**, 64(7), 075414. doi:10.1103/PhysRevB.64.075414

Filik, J., May, P. W., Pearce, S. R. J., Wild, R. K., & Hallam, K. R. (2003). Xps and laser raman analysis of hydrogenated amorphous carbon films. **Diamond and Related Materials**, 12(3), 974-978. doi.org/10.1016/S0925-9635(02)00374-6

Fredriksson, W., Malmgren, S., Gustafsson, T., Gorgoi, M., & Edström, K. (2012). Full depth profile of passive films on 316l stainless steel based on high resolution haxpes in combination with arxps. **Applied Surface Science**, 258(15), 5790-5797. doi.org/10.1016/j.apsusc.2012.02.099

Fu, R., Mei, Y. F., Fu, M. Y., Liu, X., & Chu, P. (2005). Thermal stability of metal-doped diamond-like carbon fabricated by dual plasma deposition. **Diamond and Related Materials**, 14, 1489-1493. doi:10.1016/j.diamond.2005.03.006

Genel, K., Demirkol, M., & Guelmez, T. (2000). Corrosion fatigue behaviour of ion nitrided aisi 4140 steel. **Materials Science and Engineering A, Structural Materials: Properties, Microstructure and Processing**, 288(1), 91-100.

Gómez, I., Claver, A., Santiago, J. A., Fernandez, I., Palacio, J. F., Diaz, C., Garcia, J. A. (2021). Improved adhesion of the dlc coating using hipims with positive pulses and plasma immersion pretreatment. **Coatings**, 11(9). doi:10.3390/coatings11091070

Grierson, D. S., Sumant, A. V., Konicek, A. R., Friedmann, T. A., Sullivan, J. P., & Carpick, R. W. (2010). Thermal stability and rehybridization of carbon bonding in tetrahedral amorphous carbon. **Journal of Applied Physics**, 107(3), 033523. doi:10.1063/1.3284087

Grill, A. (1999). Diamond-like carbon: State of the art. **Diamond and Related Materials**, 8(2), 428-434. doi.org/10.1016/S0925-9635(98)00262-3

Guenther, S., Kaulich, B., Gregoratti, L., & Kiskinova, M. (2002). Photoelectron microscopy and applications in surface and materials science. **Progress in Surface Science**, 70, 187–260. doi:10.1016/S0079-6816(02)00007-2

Guo, L. Q., Lin, M. C., Qiao, L. J., & Volinsky, A. A. (2014). Duplex stainless steel passive film electrical properties studied by in situ current sensing atomic force microscopy. **Corrosion Science**, 78, 55-62. doi.org/10.1016/j.corsci.2013.08.031

Hainsworth, S. V., & Uhure, N. J. (2007). Diamond like carbon coatings for tribology: Production techniques, characterisation methods and applications. **International Materials Reviews**, 52(3), 153-174. doi:10.1179/ 174328007 X160272

Hanawa, T., Hiromoto, S., Yamamoto, A., Kuroda, D., & Asami, K. (2002). Xps characterization of the surface oxide film of 316l stainless steel samples that were located in quasi-biological environments. **MATERIALS TRANSACTIONS**, 43(12), 3088-3092. doi:10.2320/matertrans.43.3088

Hassan, M. A., Bushroa, A. R., & Mahmoodian, R. (2015). Identification of critical load for scratch adhesion strength of nitride-based thin films using wavelet analysis and a proposed analytical model. **Surface and Coatings Technology**, 277(C), 216-221. doi:10.1016/j.surfcoat.2015.07.061

Hauert, R., Glisenti, A., Metin, S., Goitia, J., Kaufman, J. H., Loosdrecht, P. H. M. V., Kellock, A. J., Hoffmann, P., White, R. L., & Hermsmeier, B. D. (1995). Influence of nitrogen doping on different properties of a-C: H. **Thin Solid Films**, 268(1-2), 22-29. doi.org/10.1016/0040-6090(95)06824-4

Heydarzadeh Sohi, M., Ebrahimi, M., Honarbakhsh-Raouf, A., & Mahboubi, F. (2010). Comparative study of the corrosion behaviour of plasma nitrocarburised aisi 4140 steel before and after post-oxidation. **Materials & Design - MATER DESIGN**, 31, 4432-4437. doi:10.1016/j.matdes.2010.04.017

Honglertkongsakul, K., May, P. W., & Paosawatyanyong, B. (2010). Electrical and optical properties of diamond-like carbon films deposited by pulsed laser ablation. **Diamond and Related Materials - DIAM RELAT MATER**, 19, 999-1002. doi:10.1016/j.diamond.2010.03.007

Ishpal, Kumar, S., Dwivedi, N., & Rauthan, C. M. S. (2012). Investigation of radio frequency plasma for the growth of diamond like carbon films. **Physics of Plasmas**, 19(3), 033515. doi:10.1063/1.3694855

Iyer, G. R. S., & Maguire, P. D. (2011). Metal free, end-opened, selective nitrogen-doped vertically aligned carbon nanotubes by a single step in situ low energy plasma process. **Journal of Materials Chemistry**, 21(40), 16162-16169. doi:10.1039/C1JM12829A

Ji, L., Wu, Y., Li, H., Song, H., Liu, X., Ye, Y., . . . Liu, L. (2015). The role of trace ti concentration on the evolution of microstructure and properties of duplex doped ti(ag)/dlc films. **Vacuum**, 115. doi:10.1016/j.vacuum.2015.01.023

Jibin, P., Zhang, G., Wan, S., & Zhang, R. (2013). Synthesis and characterization of low-friction al-dlc films with high hardness and low stress. **Journal of Composite Materials**, 49. doi:10.1177/0021998313515291

Jiménez, I., Gago, R., Albella, J. M., & Terminello, L. J. (2001). X-ray absorption studies of bonding environments in graphitic carbon nitride. **Diamond and Related Materials***, 10(3), 1170-1174. doi.org/10.1016/S0925-9635(00)00383-6

Jones, D. A. (1992). *Principles and prevention of corrosion* (2 ed.). University of Michigan, New Jersey: Macmillan Publishing Company.

Jongwannasiri, C., Li, X., & Watanabe, S. (2013). Improvement of thermal stability and tribological performance of diamond-like carbon composite thin films. **Materials Sciences and Applications***, Vol.04No.10, 7. doi:10.4236/msa.2013. 410077

K, A., Varade, A., K, N. R., Dhan, S., M, C., N, B., & Krishna, P. (2017). Synthesis of high hardness ir optical coating using diamond-like carbon by pecvd at room temperature. **Diamond and Related Materials***, 78, 39-43. doi.org/10.1016/ j.diamond.2017.07.008

Kelly, P. J., & Arnell, R. D. (2000). Magnetron sputtering: A review of recent developments and applications. **Vacuum***, 56(3), 159-172. doi.org/10.1016/ S0042-207X(99)00189-X

Khani Sanij, M. H., Ghasemi Banadkouki, S. S., Mashreghi, A. R., & Moshrefifar, M. (2012). The effect of single and double quenching and tempering heat treatments on the microstructure and mechanical properties of aisi 4140 steel. **Materials & Design***, 42, 339-346. doi.org/10.1016/j.matdes.2012.06.017

Khun, N. W., & Liu, E. (2010). Corrosion behavior of aluminum doped diamond-like carbon thin films in nacl aqueous solution. **J Nanosci Nanotechnol***, 10(7), 4767-4772. doi:10.1166/jnn.2010.1682

Khun, N. W., Liu, E., Yang, G. C., Ma, W. G., & Jiang, S. P. (2009). Structure and corrosion behavior of platinum/ruthenium/nitrogen doped diamondlike carbon thin films. **Journal of Applied Physics***, 106(1), 013506. doi:10.1063/1.3154022

Khun, N. W., Liu, E., & Zeng, X. T. (2009). Corrosion behavior of nitrogen doped diamond-like carbon thin films in nacl solutions. **Corrosion Science***, 51(9), 2158-2164. doi.org/10.1016/j.corsci.2009.05.050

Kim, H. W., Ross, M. B., Kornienko, N., Zhang, L., Guo, J., Yang, P., & McCloskey, B. D. (2018). Efficient hydrogen peroxide generation using reduced graphene oxide-based oxygen reduction electrocatalysts. **Nature Catalysis**, 1(4), 282-290. doi:10.1038/s41929-018-0044-2

Kishimoto, S., Hashiguchi, T., Ohshio, S., & Saitoh, H. (2008). Density investigation by x-ray reflectivity for thin films synthesized using atmospheric cvd. **Chemical Vapor Deposition - CHEM VAPOR DEPOSITION**, 14, 303-308. doi:10.1002/cvde.200806703

Konkhunthot, N., Photongkam, P., & Wongpanya, P. (2019). Improvement of thermal stability, adhesion strength and corrosion performance of diamond-like carbon films with titanium doping. **Applied Surface Science**, 469, 471-486. doi.org/10.1016/j.apsusc.2018.11.028

Konkhunthot, N., Tunmee, S., Zhou, X., Komatsu, K., Photongkam, P., Saitoh, H., & Wongpanya, P. (2018). The correlation between optical and mechanical properties of amorphous diamond-like carbon films prepared by pulsed filtered cathodic vacuum arc deposition. **Thin Solid Films**, 653, 317-325. doi.org/10.1016/j.tsf.2018.03.053

Kovacı, H., Baran, Ö., Yetim, A. F., Bozkurt, Y., Kara, L., & çelik, A. (2018). The friction and wear performance of dlc coatings deposited on plasma nitrided aisi 4140 steel by magnetron sputtering under air and vacuum conditions. **Surface and Coatings Technology**, 349. doi:10.1016/j.surfcoat.2018.05.084

Kvasnica, S., Schalko, J., Eisenmenger Sittner, C., Benardi, J., Vorlaufer, G., Pauschitz, A., & Roy, M. (2006). Nanotribological study of pecvd dlc and reactively sputtered ti containing carbon films. **Diamond and Related Materials**, 15, 1743-1752.

Lapteva, L., Fedoseeva, Y., Shlyakhova, E., Makarova, A., Bulusheva, L., & Okotrub, A. (2019). Nexafs spectroscopy study of lithium interaction with nitrogen incorporated in porous graphitic material. **Journal of Materials Science**, 54. doi:10.1007/s10853-019-03586-6

Lee, V., Dennis, R. V., Jaye, C., Wang, X., Fischer, D. A., Cartwright, A. N., & Banerjee, S. (2012). In situ near-edge x-ray absorption fine structure spectroscopy investigation of the thermal defunctionalization of graphene oxide. *Journal of Vacuum Science & Technology B*, 30(6), 061206. doi:10.1116/1.4766325

Lei, Y., Jiang, J., Wang, Y., Bi, T., & Zhang, L. (2019). Structure evolution and stress transition in diamond-like carbon films by glancing angle deposition. *Applied Surface Science*, 479, 12-19. doi.org/10.1016/j.apsusc.2019.02.063

Lenardi, C., Piseri, P., Briois, V., Bottani, C. E., Bassi, A. L., & Milani, P. (1999). Near-edge x-ray absorption fine structure and raman characterization of amorphous and nanostructured carbon films. *Journal of Applied Physics*, 85(10), 7159-7167. doi:10.1063/1.370527

Leveneur, J., Waterhouse, G. I. N., Kennedy, J., Metson, J. B., & Mitchell, D. R. G. (2011). Nucleation and growth of fe nanoparticles in sio2: A tem, xps, and fe l-edge xanes investigation. *The Journal of Physical Chemistry C*, 115(43), 20978-20985. doi:10.1021/jp206357c

Li, J., Yang, X., Wang, S., Wei, K., & Hu, J. (2014). A rapid d.C. Plasma nitriding technology catalyzed by pre-oxidation for aisi4140 steel. *Materials Letters*, 116, 199-202. doi.org/10.1016/j.matlet.2013.11.033

Li, Y., Liu, Z., Luo, J., Zhang, S., Qiu, J., & He, Y. (2019). Microstructure, mechanical and adhesive properties of crn/crtialsin/wcrtialn multilayer coatings deposited on nitrided aisi 4140 steel. *Materials Characterization*, 147, 353-364. doi.org/10.1016/j.matchar.2018.11.017

Li, Y., Ye, Q., Zhu, Y., Zhang, L., He, Y., Zhang, S., & Xiu, J. (2019). Microstructure, adhesion and tribological properties of crn/crtialsin/wcrtialn multilayer coatings deposited on nitrocarburized aisi 4140 steel. *Surface and Coatings Technology*, 362, 27-34. doi.org/10.1016/j.surfcoat.2019.01.091

LiBassi, A., Ferrari, A. C., Stolojan, V., Tanner, B. K., Robertson, J., & Brown, L. M. (2000). Density, sp^3 content and internal layering of dlc films by x-ray reflectivity and electron energy loss spectroscopy. *Diamond and Related Materials*, 9(3), 771-776. doi.org/10.1016/S0925-9635(99)00233-2

Lifshitz, Y., Kasi, S. R., & Rabalais, J. W. (1989). Subplantation model for film growth from hyperthermal species: Application to diamond. **Physical Review Letters**, 62(11), 1290-1293. doi:10.1103/PhysRevLett.62.1290

Liu, E., Li, L., Blanpain, B., & Celis, J. P. (2005). Residual stresses of diamond and diamondlike carbon films. **Journal of Applied Physics**, 98(7), 073515. doi:10.1063/1.2071451

Liu, F.-X., & Wang, Z.-L. (2009). Thickness dependence of the structure of diamond-like carbon films by raman spectroscopy. **Surface and Coatings Technology**, 203(13), 1829-1832. doi.org/10.1016/j.surfcoat.2009.01.008

Liu, F.-X., Yao, K.-L., & Liu, Z.-L. (2007). Substrate bias effect on structure of tetrahedral amorphous carbon films by raman spectroscopy. **Diamond and Related Materials**, 16(9), 1746-1751. doi.org/10.1016/j.diamond.2007.06.007

Liu, X., Lu, P., Wang, H., Ren, Y., Tan, X., Sun, S., & Jia, H. (2018). Morphology and structure of ti-doped diamond films prepared by microwave plasma chemical vapor deposition. **Applied Surface Science**, 442. doi:10.1016/j.apsusc.2018.02.180

Liu, Z., Cong, W., Kim, H., Ning, F., Jiang, Q., Li, T., . . . Zhou, Y. (2017). Feasibility exploration of superalloys for aisi 4140 steel repairing using laser engineered net shaping. **Procedia Manufacturing**, 10, 912-922. doi.org/10.1016/j.promfg.2017.07.080

Lu, Z., & Chung, J. (2008). Electrochemical characterization of diamond like carbon thin films. **Diamond and Related Materials - DIAM RELAT MATER**, 17, 1871-1876. doi:10.1016/j.diamond.2008.03.031

Lu, Z. G., Lo, M. F., & Chung, C. Y. (2008). Pulse laser deposition and electrochemical characterization of lifepo4–c composite thin films. **The Journal of Physical Chemistry C**, 112(17), 7069-7078. doi:10.1021/jp0744735

Lubwama, M., Corcoran, B., Rajani, K. V., Wong, C. S., Kirabira, J. B., Sebbit, A., Sayers, K. (2013). Raman analysis of dlc and si-dlc films deposited on nitrile rubber. **Surface and Coatings Technology**, 232, 521-527. doi.org/10.1016/ j.surfcoat.2013.06.013

Lung, B. H., Chiang, M. J., & Hon, M. H. (2001). Growth characterization and properties of diamond-like carbon films by electron cyclotron resonance chemical vapor deposition. **Thin Solid Films***, 392, 16-21.

Mabuchi, Y., Higuchi, T., & Weihnacht, V. (2013). Effect of sp^2/sp^3 bonding ratio and nitrogen content on friction properties of hydrogen-free dlc coatings. **Tribology International***, 62, 130–140. doi:10.1016/j.triboint.2013.02.007

Marcelin, S., Pébère, N., & Regnier, S. (2013). Electrochemical characterisation of a martensitic stainless steel in a neutral chloride solution. **Electrochimica Acta***, 87, 32–40. doi:10.1016/j.electacta.2012.09.011

Marjanovic, N., Tadic, B., Ivkovic, B., & Mitrovic, S. (2006). Design of modern concept tribometer with circular and reciprocating movement. 28, 3-8.

Marques, F. C., Lacerda, R. G., Champi, A., Stolojan, V., Cox, D. C., & Silva, S. R. P. (2003). Thermal expansion coefficient of hydrogenated amorphous carbon. **Applied Physics Letters***, 83(15), 3099-3101. doi:10.1063/1.1619557

Martin, P. M. (2015). Filtered cathodic arc deposition, guides to vacuum processing. **Executive, Vacuum and Coating Technology**.

Maruno, H., & Nishimoto, A. (2018). Adhesion and durability of multi-interlayered diamond-like carbon films deposited on aluminum alloy. **Surface and Coatings Technology***, 354, 134-144. doi.org/10.1016/j.surfcoat.2018.08.094

Maruyama, T., Naritsuka, S., & Amemiya, K. (2015). In situ high-temperature nexafs study on carbon nanotube and graphene formation by thermal decomposition of sic. **The Journal of Physical Chemistry C***, 119(47), 26698-26705. doi:10.1021/acs.jpcc.5b05854

Matlak, J., & Komvopoulos, K. (2018). Ultrathin amorphous carbon films synthesized by filtered cathodic vacuum arc used as protective overcoats of heat-assisted magnetic recording heads. **Scientific Reports***, 8(1), 9647. doi:10.1038/s41598-018-27528-5

Matthes, B., Broszeit, E., Aromaa, J., Ronkainen, H., Hannula, S. P., Leyland, A., & Matthews, A. (1991). Corrosion performance of some titanium-based hard coatings. **Surface and Coatings Technology***, 49(1), 489-495. doi.org/10.1016/0257-8972(91)90105-6

Miki, Y., Nishimoto, A., Sone, T., & Araki, Y. (2015). Residual stress measurement in dlc films deposited by pbiid method using raman microprobe spectroscopy. **Surface and Coatings Technology***, 283, 274-280. doi.org/10.1016/ j.surfcoat. 2015.10.048

Modabberasl, A., Kameli, P., Ranjbar, M., Salamati, H., & Ashiri, R. (2015). Fabrication of dlc thin films with improved diamond-like carbon character by the application of external magnetic field. **Carbon***, 94, 485-493. doi.org/10.1016/ j.carbon.2015.06.081

Moriguchi, H., Ohara, H., & Tsujioka, M. (2016). History and applications of diamond-like carbon manufacturing processes. 52-58.

Nakazawa, H., Kawabata, T., Kudo, M., & Mashita, M. (2007). Structural changes of diamond-like carbon films due to atomic hydrogen exposure during annealing. **Applied Surface Science***, 253, 4188-4196.

Narayan, J. (2005). Laser processing of diamond-like carbon–metal composites. **Applied Surface Science - APPL SURF SCI***, 245, 420-430. doi:10.1016 /j.apsusc.2004.11.026

Ochoa, E., Figueroa, C., & Alvarez, F. (2006). Nitriding of aisi 4140 steel by a low energy broad ion source. **Journal of Vacuum Science & Technology A: Vacuum, Surfaces, and Films***, 24, 2113-2116. doi:10.1116/1.2356480

Ohmagari, S., Tsuyoshi, Y., Akira, N., Al Riyami, S., Ohtani, R., Hiroyuki, S., Nagayama, K. (2009). Near-edge x-ray absorption fine structure of ultrananocrystalline diamond/hydrogenated amorphous carbon films prepared by pulsed laser deposition. **Journal of Nanomaterials***, 2009. doi:10.1155/2009/876561

Ohmagari, S., Yoshitake, T., Nagano, A., Al-Riyami, S., Ohtani, R., Setoyama, H., Nagayama, K. (2009). Near-edge x-ray absorption fine structure of ultrananocrystalline diamond/hydrogenated amorphous carbon films prepared by pulsed laser deposition. **Journal of Nanomaterials***, 2009, 876561. doi:10.1155/2009/876561

Oliver, W. C., & Pharr, G. M. (2004). Measurement of hardness and elastic modulus by instrumented indentation: Advances in understanding and refinements to methodology. **Journal of Materials Research***, 19(1), 3. doi:10.1557/ jmr.2004.19.1.3

Ozensoy, E., Szanyi, J., & Peden, C. H. F. (2005). Interaction of water with ordered θ-al2o3 ultrathin films grown on nial(100). **The Journal of Physical Chemistry B***, 109(8), 3431-3436. doi:10.1021/jp0449206

Page, T. F., Oliver, W. C., & McHargue, C. J. (2011). The deformation behavior of ceramic crystals subjected to very low load (nano)indentations. **Journal of Materials Research***, 7(2), 450-473. doi:10.1557/JMR.1992.0450

Panwar, O. S., Khan, M. A., Kumar, M., Shivaprasad, S. M., Satyanarayana, B. S., Dixit, P. N., Khan, M. Y. (2008). Effect of high substrate bias and hydrogen and nitrogen incorporation on filtered cathodic vacuum arc deposited tetrahedral amorphous carbon films. **Thin Solid Films***, 516(8), 2331-2340. doi.org/10.1016/ j.tsf.2007.09.024

Parratt, L. G. (1954). Surface studies of solids by total reflection of x-rays. **Physical Review***, 95(2), 359-369. doi:10.1103/PhysRev.95.359

Piazza, F., Golanski, A., Schulze, S., & Relihan, G. (2003). Transpolyacetylene chains in hydrogenated amorphous carbon films free of nanocrystalline diamond. **Applied Physics Letters***, 82(3), 358-360. doi:10.1063/1.1538349

Piazza, F., Grambole, D., Schneider, D., Casiraghi, C., Ferrari, A. C., & Robertson, J. (2005). Protective diamond-like carbon coatings for future optical storage disks. **Diamond and Related Materials***, 14. doi:10.1016/j.diamond.2004.12.028

Plasma-polymerized thiophene films for corrosion protection in microelectronic devices. (2002). **Journal of Materials Science Letters***, 21(12), 951-953.

Podgursky, V., Yashin, M., Jõgiaas, T., Viljus, M., Shaikh, A., Danilson, M., & Bogatov, A. (2020). High temperature tribological properties of al2o3/ncd films investigated under ambient air conditions. **Coatings***, 10, 175. doi:10.3390/coatings10020175

Polo, M. C., Andújar, J. L., Hart, A., Robertson, J., & Milne, W. I. (2000). Preparation of tetrahedral amorphous carbon films by filtered cathodic vacuum arc deposition. **Diamond and Related Materials**, 9(3), 663-667. doi.org/10.1016 /S0925-9635(99)00339-8

Qiang, L., Gao, K., Zhang, L., Wang, J., Zhang, B., & Zhang, J. (2015). Further improving the mechanical and tribological properties of low content ti-doped dlc film by w incorporating. **Applied Surface Science**, 353, 522-529. doi.org/10.1016/ j.apsusc.2015.06.040

Qiang, L., Zhang, B., Zhou, Y., & Zhang, J. (2013). Improving the internal stress and wear resistance of dlc film by low content ti doping. **Solid State Sciences**, 20, 17-22. doi.org/10.1016/j.solidstatesciences.2013.03.003

Rao, X., Yang, J., Chen, Z., Yuan, Y., Chen, Q., Feng, X., Zhang, Y. (2020). Tuning c–c sp^2/sp^3 ratio of dlc films in fcva system for biomedical application. **Bioactive Materials**, 5(2), 192-200. doi.org/10.1016/j.bioactmat.2020.02.009

Ray, S., Pong, W.-F., & Papakonstantinou, P. (2016). Iron, nitrogen and silicon doped diamond like carbon (dlc) thin films: A comparative study. **Thin Solid Films**, 610. doi:10.1016/j.tsf.2016.04.048

Robertson, J. (1996). Amorphous carbon. **Current Opinion in Solid State and Materials Science**, 1(4), 557-561. doi.org/10.1016/S1359-0286(96)80072-6

Robertson, J. (2002). Diamond-like amorphous carbon. **Materials Science and Engineering: R: Reports**, 37(4), 129-281. doi.org/10.1016/S0927-796X(02)00005-0

Roy, S., McCann, R., Papakonstantinou, P., Maguire, P., & McLaughlin, J. (2005). The structure of amorphous carbon nitride films using a combined study of nexafs, xps and raman spectroscopies. **Thin Solid Films**, 482, 145-150. doi:10.1016 /j.tsf.2004.11.132

Ruden, A., Restrepo-Parra, E., Paladines, A. U., & Sequeda, F. (2013). Corrosion resistance of crn thin films produced by dc magnetron sputtering. **Applied Surface Science**, 270, 150-156. doi.org/10.1016/j.apsusc.2012.12.148

Ryu, H., Kim, J., Kim, J., Kim, D. H., Kang, Y.-J., Jang, Y.-J., & Jeong, J. H. (2020). Enhancement of a heat transfer performance on the al6061 surface using microstructures and fluorine-doped diamond-like carbon (f-dlc) coating. **International Journal of Heat and Mass Transfer***, 148, 119108. doi.org/ 10.1016/j.ijheatmasstransfer.2019.119108

Safaie, P., Eshaghi, A., & Bakhshi, S. R. (2017). Oxygen doping effect on the wettability of diamond-like carbon thin films. **Journal of Non Crystalline Solids***, 471, 410-414. doi:10.1016/j.jnoncrysol.2017.06.034

Savvides, N., & Bell, T. J. (1993). Hardness and elastic modulus of diamond and diamond-like carbon films. **Thin Solid Films***, 228(1), 289-292. doi.org /10.1016/0040-6090(93)90618-Y

Sayuti, M., Sarhan, A., & Faheem, S. (2014). Novel uses of sio2 nano-lubrication system in hard turning process of hardened steel aisi4140 for less tool wear, surface roughness and oil consumption. **Journal of Cleaner Production***, 67, 265–276. doi:10.1016/j.jclepro.2013.12.052

Schwan, J., Ulrich, S., Batori, V., Ehrhardt, H., & Silva, S. R. P. (1996). Raman spectroscopy on amorphous carbon films. **Journal of Applied Physics***, 80(1), 440-447. doi:10.1063/1.362745

Sharifahmadian, O., Mahboubi, F., & Yazdani, S. (2019). Comparison between corrosion behaviour of dlc and n-dlc coatings deposited by dc-pulsed pacvd technique. **Diamond and Related Materials***, 95, 60-70. doi.org/10.1016 /j.diamond. 2019.04.007

Sheeja, D., Tay, B. K., Lau, S. P., Shi, X., & Ding, X. (2000). Structural and tribological characterization of multilayer ta-c films prepared by filtered cathodic vacuum arc with substrate pulse biasing. **Surface and Coatings Technology***, 132(2), 228-232. doi.org/10.1016/S0257-8972(00)00848-3

Sheeja, D., Tay, B. K., Leong, K. W., & Lee, C. H. (2002). Effect of film thickness on the stress and adhesion of diamond-like carbon coatings. **Diamond and Related Materials***, 11(9), 1643-1647. doi.org/10.1016/S0925-9635(02)00109-7

Shi, J. R. (2006). Study on nitrogenated amorphous carbon films prepared by unbalanced magnetron sputtering. **Journal of Applied Physics**, 99(3), 033505. doi:10.1063/1.2168027

Shi, X., Tay, B. K., Flynn, D. I., Ye, Q., & Sun, Z. (1997). Characterization of filtered cathodic vacuum arc system. **Surface and Coatings Technology**, 94-95, 195-200. doi.org/10.1016/S0257-8972(97)00347-2

Sikora, A., Garrelie, F., Donnet, C., Loir, A. S., Fontaine, J., Sanchez-Lopez, J. C., & Rojas, T. C. (2010). Structure of diamondlike carbon films deposited by femtosecond and nanosecond pulsed laser ablation. **Journal of Applied Physics**, 108(11), 113516. doi:10.1063/1.3510483

Singh, A., Lin, Y., Liu, W., Yu, S., Jie, P., Ren, C., & Kuanhai, D. (2014). Plant derived cationic dye as an effective corrosion inhibitor for 7075 aluminum alloy in 3.5% nacl solution. **Journal of Industrial and Engineering Chemistry**, 20, 4276-4285. doi:10.1016/j.jiec.2014.01.033

Singha, A., Ghosh, A., Roy, A., & Ray, N. R. (2006). Quantitative analysis of hydrogenated diamondlike carbon films by visible raman spectroscopy. **Journal of Applied Physics**, 100(4), 044910. doi:10.1063/1.2219983

Soin, N., Roy, S., Ray, S., Lemoine, P., Rahman, M. A., Maguire, P., McLaughlin, J. (2011). Thickness dependent electronic structure of ultra-thin tetrahedral amorphous carbon (ta-c) films. **Thin Solid Films**, 520. doi:10.1016/ j.tsf.2011.12.039

Son, M., Zhang, T. F., Jo, Y. J., & Kim, K. (2017). Enhanced electrochemical properties of the dlc films with an arc interlayer, nitrogen doping and annealing. **Surface and Coatings Technology**, 329. doi:10.1016/j.surfcoat.2017.09.025

Srisang, C., Asanithi, P., Siangchaew, K., Limsuwan, S., Pokaipisit, A., & Limsuwan, P. (2012). Raman spectroscopy of dlc/a-si bilayer film prepared by pulsed filtered cathodic arc. **Journal of Nanomaterials**, 2012, 745126. doi:10.1155/2012/ 745126

Sun, L., Guo, P., Ke, P., Li, X., & Wang, A. (2016). Synergistic effect of cu/cr co-doping on the wettability and mechanical properties of diamond-like carbon films. **Diamond and Related Materials**, 68, 1-9. doi.org/10.1016/ j.diamond. 2016.05.006

Suryo, S., Bayuseno, A., Jamari, J., & Ramadhan, M. (2018). *Analysis of aisi material power of aisi 4140 bucket teeth excavator using influence of abrasive wear* (Vol. 1977).

Tagawa, M., Yokota, K., Kitamura, A., Matsumoto, K., Yoshigoe, A., Teraoka, Y., Niibe, M. (2010). Synchrotron radiation photoelectron spectroscopy and near-edge x-ray absorption fine structure study on oxidative etching of diamond-like carbon films by hyperthermal atomic oxygen. **Applied Surface Science***, 256(24), 7678-7683. doi.org/10.1016/j.apsusc.2010.06.030

Tallant, D. R., Parmeter, J. E., Siegal, M. P., & Simpson, R. L. (1995). The thermal stability of diamond-like carbon. **Diamond and Related Materials***, 4(3), 191-199. doi.org/10.1016/0925-9635(94)00243-6

Tay, B. K., Sheeja, D., Choong, Y. S., Lau, S. P., & Shi, X. (2000). Pin-on-disk characterization of amorphous carbon films prepared by filtered cathodic vacuum arc technique. **Diamond and Related Materials***, 9(3), 819-824. doi.org/10.1016/S0925-9635(99)00226-5

Totik, Y. (2006). The corrosion behaviour of manganese phosphate coatings applied to aisi 4140 steel subjected to different heat treatments. **Surface and Coatings Technology***, 200(8), 2711-2717. doi.org/10.1016/j.surfcoat.2004.10.004

Toya, T., Jotaki, R., & A., K. (1986). Specimen preparations in epma and sem. **JEOL Training Center EP Section**.

Tucker, M. D., Ganesan, R., McCulloch, D. G., Partridge, J. G., Stueber, M., Ulrich, S., . . . Marks, N. A. (2016). Mixed-mode high-power impulse magnetron sputter deposition of tetrahedral amorphous carbon with pulse-length control of ionization. **Journal of Applied Physics***, 119(15), 155303. doi:10.1063/1.4946841

Tunmee, S., Photongkam, P., Euaruksakul, C., Takamatsu, H., Zhou, X., Wongpanya, P., . . . Saitoh, H. (2016). Investigation of pitting corrosion of diamond-like carbon films using synchrotron-based spectromicroscopy. **Journal of Applied Physics***, 120, 195303. doi:10.1063/1.4967799

Vasudev, M. C., Anderson, K. D., Bunning, T. J., Tsukruk, V. V., & Naik, R. R. (2013). Exploration of plasma-enhanced chemical vapor deposition as a method for thin-film fabrication with biological applications. **ACS Applied Materials & Interfaces**, 5(10), 3983-3994. doi:10.1021/am302989x

Vetter, J. (2014). 60years of dlc coatings: Historical highlights and technical review of cathodic arc processes to synthesize various dlc types, and their evolution for industrial applications. **Surface and Coatings Technology**, 257, 213-240. doi.org/10.1016/j.surfcoat.2014.08.017

Wachesk, C. C., Trava-Airoldi, V. J., Da-Silva, N. S., Lobo, A. O., & Marciano, F. R. (2016). The influence of titanium dioxide on diamond-like carbon biocompatibility for dental applications. **Journal of Nanomaterials**, 2016, 8194516. doi:10.1155/2016/8194516

Wang, J., Zhang, K., Wang, F., & Zheng, W. (2018). Improving frictional properties of dlc films by surface energy manipulation. **RSC Advances**, 8(21), 11388-11394. doi:10.1039/C8RA00580J

Wang, Q. N., Li, S., & Wan, S. (2012). Investigation of field emission characteristics and microstructure of nickel-doped dlc nanocomposite films by electrochemical deposition. **Physica E-low-dimensional Systems & Nanostructures**, 46, 89-96.

Wang, S., Zhu, J., Wang, J., Yin, X., & Han, X. (2011). Raman spectroscopy and mechanical properties of multilayer tetrahedral amorphous carbon films. **Thin Solid Films**, 519(15), 4906-4909. doi:10.1016/j.tsf.2011.01.051

Wang, X., Yu, Z., Wu, Y., & Zhang, L. (2001). Atomic force microscopy and x-ray photoelectron spectroscopy study on the passive film for type 316l stainless steel. **Corrosion**, 57. doi:10.5006/1.3290380

Wang, Y., Alsmeyer, D. C., & McCreery, R. L. (1990). Raman spectroscopy of carbon materials: Structural basis of observed spectra. **Chemistry of Materials**, 2(5), 557-563. doi:10.1021/cm00011a018

Wang, Z., Wang, X., Xu, T., Liu, W., & Zhang, J. (2007). Comparing internal stress in diamond-like carbon films with different structure. **Thin Solid Films**, 515, 6899-6903. doi:10.1016/j.tsf.2007.02.069

Wei, C., & Yen, J.-Y. (2007). Effect of film thickness and interlayer on the adhesion strength of diamond like carbon films on different substrates. **Diamond and Related Materials - DIAM RELAT MATER**, 16, 1325-1330. doi:10.1016/j.diamond.2007.02.003

Weng, K.-W., Han, S., Chen, Y.-C., & Wang, D.-Y. (2008). Characteristics of diamond-like carbon film deposited by filter arc deposition. **Journal of Materials Processing Technology - J MATER PROCESS TECHNOL**, 203, 117-120. doi:10.1016/j.jmatprotec.2007.09.061

Wiesing, M., to Baben, M., Schneider, J. M., de los Arcos, T., & Grundmeier, G. (2016). Combined electrochemical and electron spectroscopic investigations of the surface oxidation of tialn hppms hard coatings. **Electrochimica Acta**, 208, 120-128. doi.org/10.1016/j.electacta.2016.05.011

Woehrl, N., Ochedowski, O., Gottlieb, S., Shibasaki, K., & Schulz, S. (2014). Plasma-enhanced chemical vapor deposition of graphene on copper substrates. **AIP Advances**, 4(4), 047128. doi:10.1063/1.4873157

Wongpanya, P., Pintitraratibodee, N., Thumanu, K., & Euaruksakul, C. (2021). Improvement of corrosion resistance and biocompatibility of 316l stainless steel for joint replacement application by ti-doped and ti-interlayered dlc films. **Surface and Coatings Technology**, 425, 127734. doi.org/10.1016/j.surfcoat.2021.127734

Wongpanya, P., Silawong, P., & Photongkam, P. (2021). Nanomechanical properties and thermal stability of al–n-co-doped dlc films prepared by filtered cathodic vacuum arc deposition. **Surface and Coatings Technology**, 424, 127655. doi.org/10.1016/j.surfcoat.2021.127655

Wongpanya, P., Silawong, P., & Photongkam, P. (2022). Adhesion and corrosion of diamond–like carbon films with Al–N–co–doping prepared by filtered cathodic vacuum arc deposition, **Ceramics International**, 48, 20743-20759. doi.org/10.1016/j.ceramint.2022.04.055

Wu, J.-b., Chang, J.-J., Li, M.-Y., Leu, M.-S., & Li, A.-K. (2007). Characterization of diamond-like carbon coatings prepared by pulsed bias cathodic vacuum arc deposition. **Thin Solid Films**, 516, 243-247. doi:10.1016/j.tsf.2007.06.134

Xu, N., Tsang, S. H., Teo, E. H. T., Wang, X., Ng, C. M., & Tay, B. k. (2012). Effect of initial sp^3 content on bonding structure evolution of amorphous carbon upon pulsed laser annealing. **Diamond and Related Materials**, 30, 48-52. doi.org/10.1016/ j.diamond.2012.09.008

Xu, W., Zhou, K., Lin, S., Dai, M., Shi, Q., & Wei, C. (2018). Structural properties of hydrogenated al-doped diamond-like carbon films fabricated by a hybrid plasma system. **Diamond and Related Materials**, 87, 177-185. doi.org/10.1016 /j.diamond.2018.06.012

Xu, X., Zhou, Y., Liu, L., Guo, P., Li, X., Lee, K.-R., . . . Wang, A. (2020). Corrosion behavior of diamond-like carbon film induced by al/ti co-doping. **Applied Surface Science**, 509, 144877. https://doi.org/10.1016/j.apsusc.2019.144877

Xu, Z., Zheng, Y. J., Jiang, F., Leng, Y. X., Sun, H., & Huang, N. (2013). The microstructure and mechanical properties of multilayer diamond-like carbon films with different modulation ratios. **Applied Surface Science**, 264, 207-212. doi.org/10.1016/j.apsusc.2012.10.003

Xu, Z. Y., Zheng, Y. J., Sun, H., Leng, Y., & Huang, N. (2012). Numerical and experimental study of residual stress of multilayer diamond-like carbon films prepared by filtered cathodic vacuum arc deposition. **IEEE Transactions on Plasma Science**, 40(9), 2261-2266. doi:10.1109/TPS.2012.2204068

Yan, X., Xu, T., Chen, G., Yang, S., & Liu, H. (2004). Study of structure, tribological properties and growth mechanism of dlc and nitrogen-doped dlc films deposited by electrochemical technique. **Applied Surface Science**, 236, 328-335. doi:10.1016/j.apsusc.2004.05.005

Yang, B., Zheng, Y., Zhang, B., Wei, L., & Zhang, J. (2012). The high-temperature tribological properties of si-dlc films. **Surface and Interface Analysis**, 44(13), 1601-1605. doi.org/10.1002/sia.5094

Ye, Y., Kapilashrami, M., Chuang, C.-H., Liu, Y.-s., Glans, P.-A., & Guo, J. (2017). X-ray spectroscopies studies of the 3d transition metal oxides and applications of photocatalysis. **MRS Communications**, 7(1), 53-66. doi:10.1557/mrc.2017.6

Zarei Moghadam, R., Rezagholipour Dizaji, H., & Ehsani, M. H. (2019). Modification of optical and mechanical properties of nitrogen doped diamond-like carbon layers. **Journal of Materials Science: Materials in Electronics**, 30(22), 19770-19781. doi:10.1007/s10854-019-02343-4

Zhang, C., & Fujii, M. (2015). Influence of wettability and mechanical properties on tribological performance of dlc coatings under water lubrication. **Journal of Surface Engineered Materials and Advanced Technology**, 05(03), 110-123. doi:10.4236/jsemat.2015.53013

Zhang, H. S., & Komvopoulos, K. (2009). Synthesis of ultrathin carbon films by direct current filtered cathodic vacuum arc. **Journal of Applied Physics**, 105(8), 083305. doi:10.1063/1.3098254

Zhang, L. H., Gong, H., & Wang, J. P. (2002). Kinetics and mechanisms of the thermal degradation of amorphous carbon films. **Journal of Applied Physics**, 91(12), 9646-9651. doi:10.1063/1.1478133

Zhang, S., Sun, D., Fu, Y. Q., Du, H., & Zhang, Q. (2005). Effect of sputtering target power on preferred orientation in nc-tin/a-sinx nanocomposite thin films. **Journal of Metastable and Nanocrystalline Materials**, 23, 175-178. doi:10.4028/ www. scientific.net/JMNM.23.175

Zhang, T. F., Deng, Q. Y., Liu, B., Wu, B. J., Jing, F. J., Leng, Y. X., & Huang, N. (2015). Wear and corrosion properties of diamond like carbon (dlc) coating on stainless steel, cocrmo and ti6al4v substrates. **Surface and Coatings Technology**, 273, 12-19. doi.org/10.1016/j.surfcoat.2015.03.031

Zhou, B., Xu, B., Xu, Y., Yu, S., Wu, Y., Wu, Y., & Liu, Z. (2018). Selective bonding effect on microstructure and mechanical properties of (al,n)-dlc composite films by ion beam-assisted cathode arc evaporation. **Applied Physics A**, 125, 1-15.

Zhou, Y., Guo, P., Sun, L., Linlin, L., Xu, X., Li, W., . . . Wang, A. (2019). Microstructure and property evolution of diamond-like carbon films co-doped by al and ti with different ratios. **Surface and Coatings Technology**, 361. doi:10.1016/ j.surfcoat.2019.01.049

Zou, Y. S., Zhou, K., Wu, Y. F., Yang, H., Cang, K., & Song, G. H. (2012). Structure, mechanical and tribological properties of diamond-like carbon films on aluminum alloy by arc ion plating. **Vacuum**, 86(8), 1141-1146. doi.org/10.1016/ j.vacuum.2011.10.019

[Online], Available : http://lalithvarun.blogspot.com/2013/02/what–is thermogravimetric – analysis.html.

[Online], Available : http://www.parkafm.com/index.php/products/small–sample–afm/ park– nx10/ technical–info.

[Online], Available : https://cellularphysiology.wikispaces.com.

[Online], Available : https://groups.oist.jp/fsu/leem–peem.

[Online], Available : https://pharm.virginia.edu/facilities/atomic–force–microscope–afm/.

[Online], Available : https://www.uj.ac.za/faculties/science/physics /research/Pages/ Electronic–Structure–studies–at–UJ–Physics.aspx.

[Online], Available : https://www3.nd.edu/~kamatlab/facilities_spectroscopy.html.

[Online], Available: [http://www.pvdadvancedtech.com/dlc/] Aug 17, 2017.

[Online], Available: http://bwtek.com/Raman–theory–of–Raman–scattering/ (27/08/2017).

[Online], Available: http://jes.ecsdl.org/content/159/4/D181.abstract

[Online], Available: http://www.substech.com/dokuwiki/doku.php?id=adhesion_tests.

[Online], Available: https://www.bruker.com/fileadmin/user_upload/8–PDF–Docs/ SurfaceAnalysis/ TMT/Webinars/Advanced–Scratch–Testing–for–Evaluation–of– Coatings–Slides.pdf.

[Online], Available: [http://www.pvdadvancedtech.com/dlc/] Dec 30, 2021

[Online], Available: https://www.theworldmaterial.com/astm–sae–aisi–4140–steel/)

[Online], Available: http://nptel.ac.in/courses/115103038/28,

[Online], Available: http://www.indiamart.com/devraj–engineering/job–work.html,

[Online], Available: http://www.caperay.com/blog/index.php/2013/i–guarantee–this– device–wont–fail/,

[Online], Available: http://www.intechopen.com/books/arthroplasty–update/the–evolution –of–modern–total–knee–prostheses,

[Online], Available: https://watchessiam.com/2019/10/30/panerai-luminor-titanium-dlc-bucherer-blue-pam01021/).

[Online], Available: http://jes.ecsdl.org/content/159/4/D181.abstract.

[Online], Available: https://groups.oist.jp/fsu/leem-peem.

[Online], Available : http : //www.phi.com/images/products/quantera/scanning-xray. jpg 18/13

APPENDIX A

THE XPS SPECTRA OF BEFORE AND AFTER CORROSION TESTING
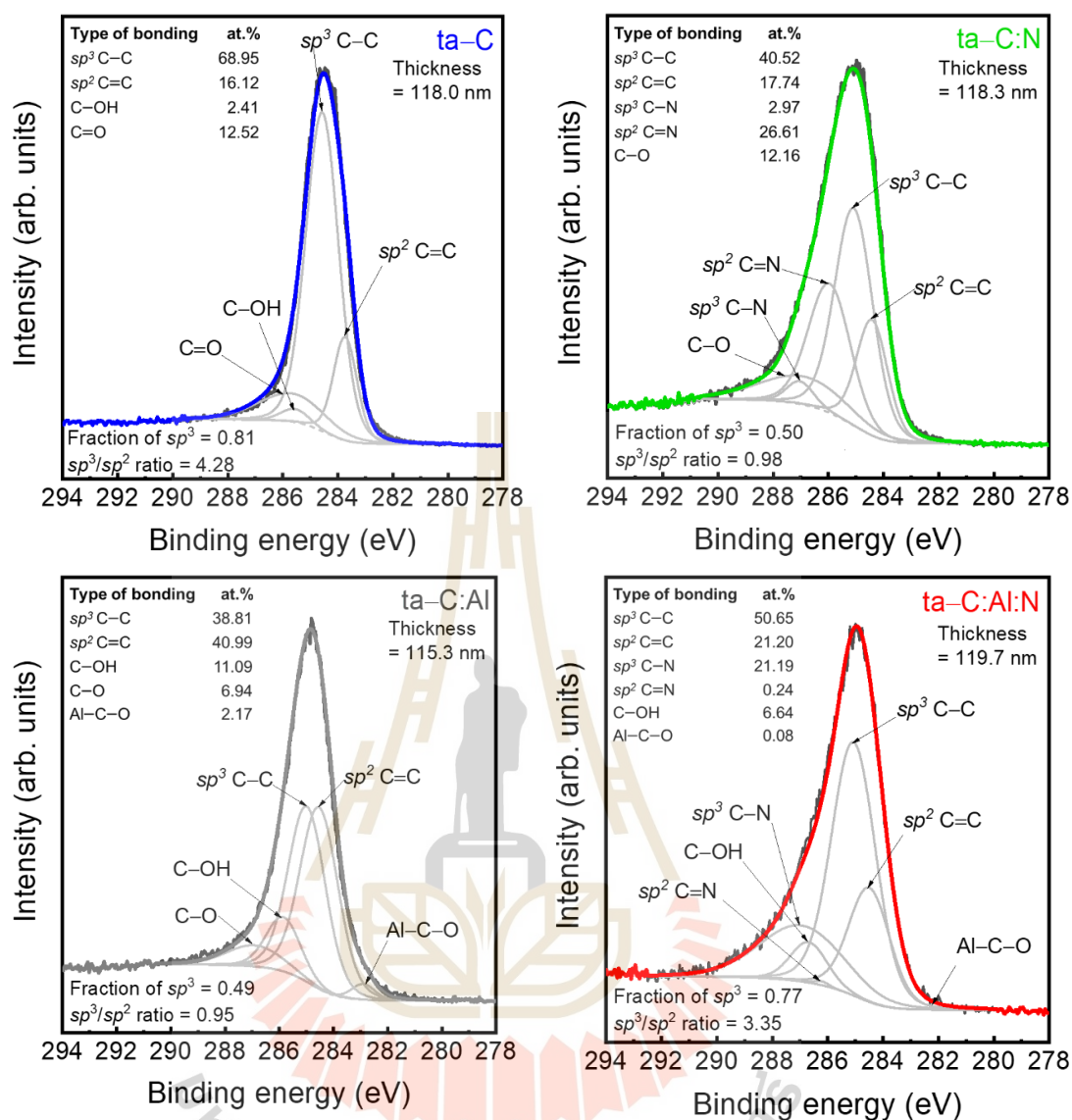
Figure A1. The C 1*s* XPS spectra and the corresponding deconvoluted Gaussian peaks of the films before the corrosion tests (Wongpanya *et al.*, 2022)
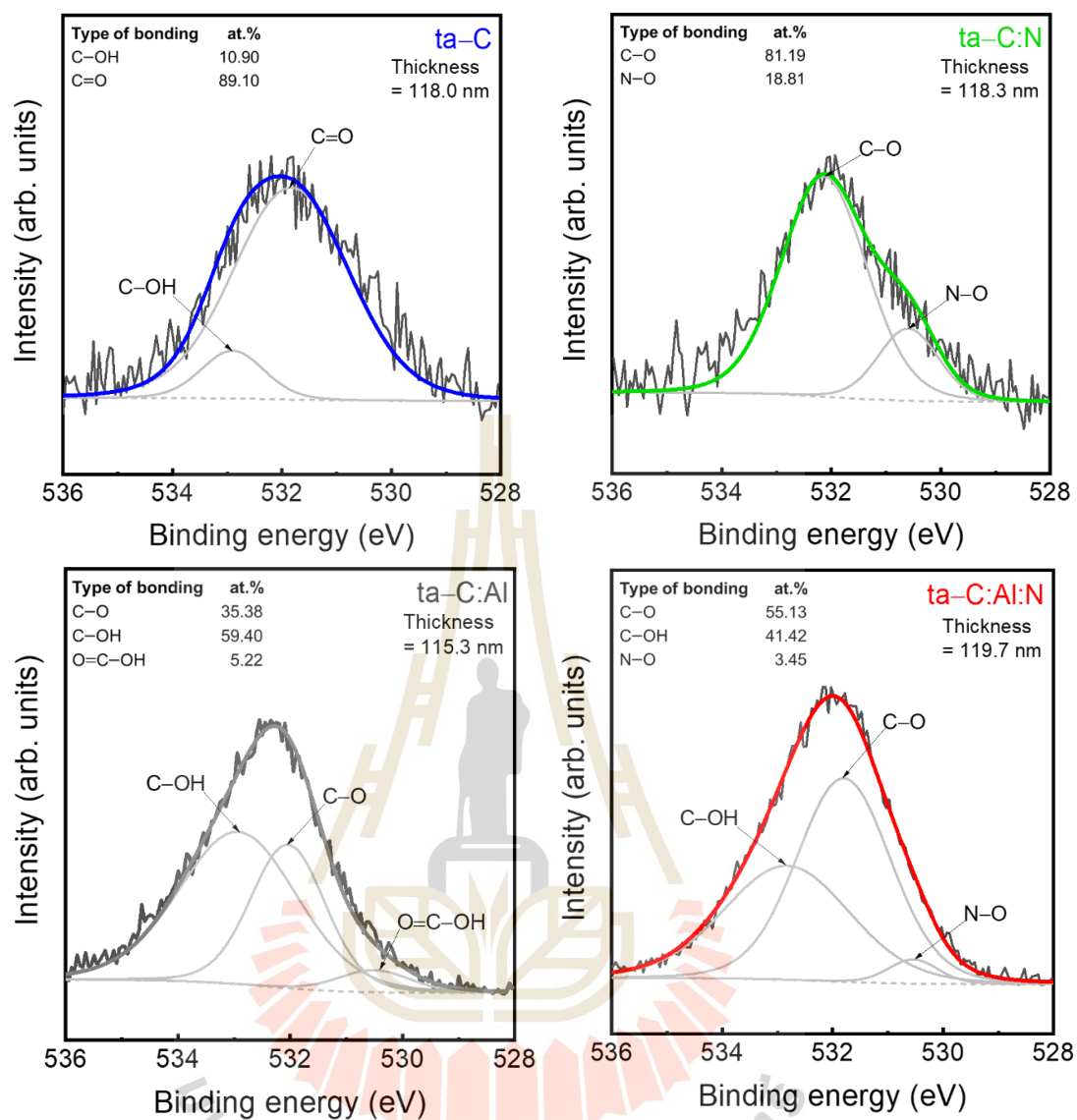
Figure A2. The O 1*s* XPS spectra and the corresponding deconvoluted Gaussian peaks of the films before the corrosion tests (Wongpanya *et al.*, 2022)
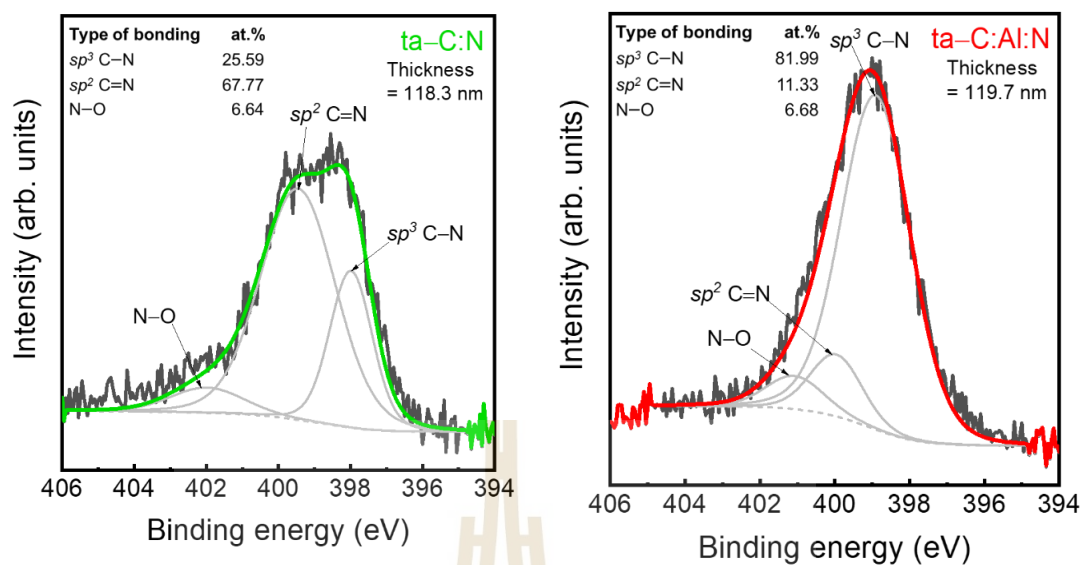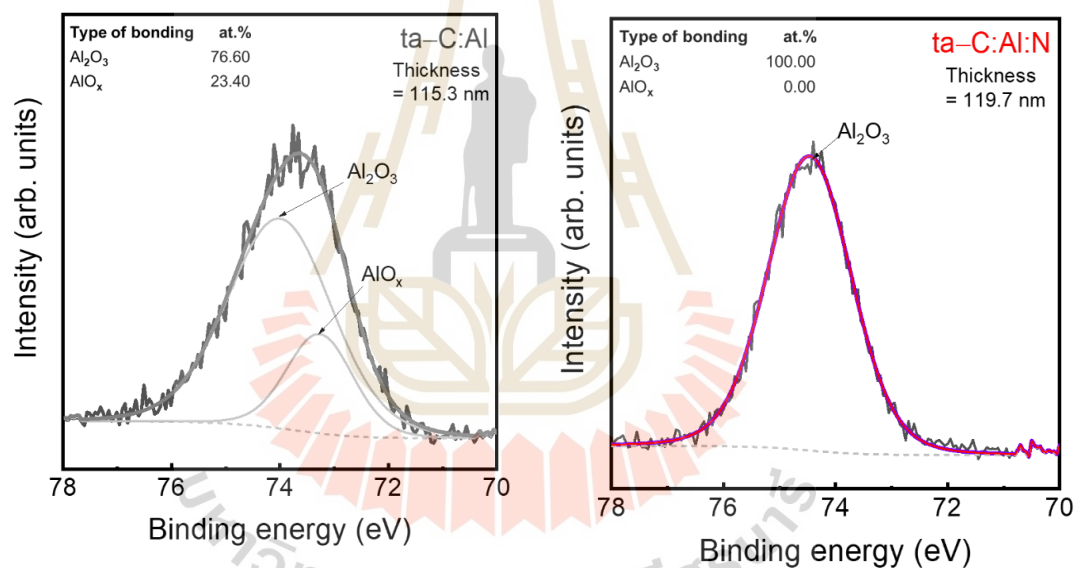
(a) N 1*s* spectra

(b) Al 2*p* spectra

Figure A3. XPS spectra and the corresponding deconvoluted Gaussian peaks of the films before the corrosion tests: (a) N 1*s*, and (b) Al 2*p* (Wongpanya *et al.*, 2022)
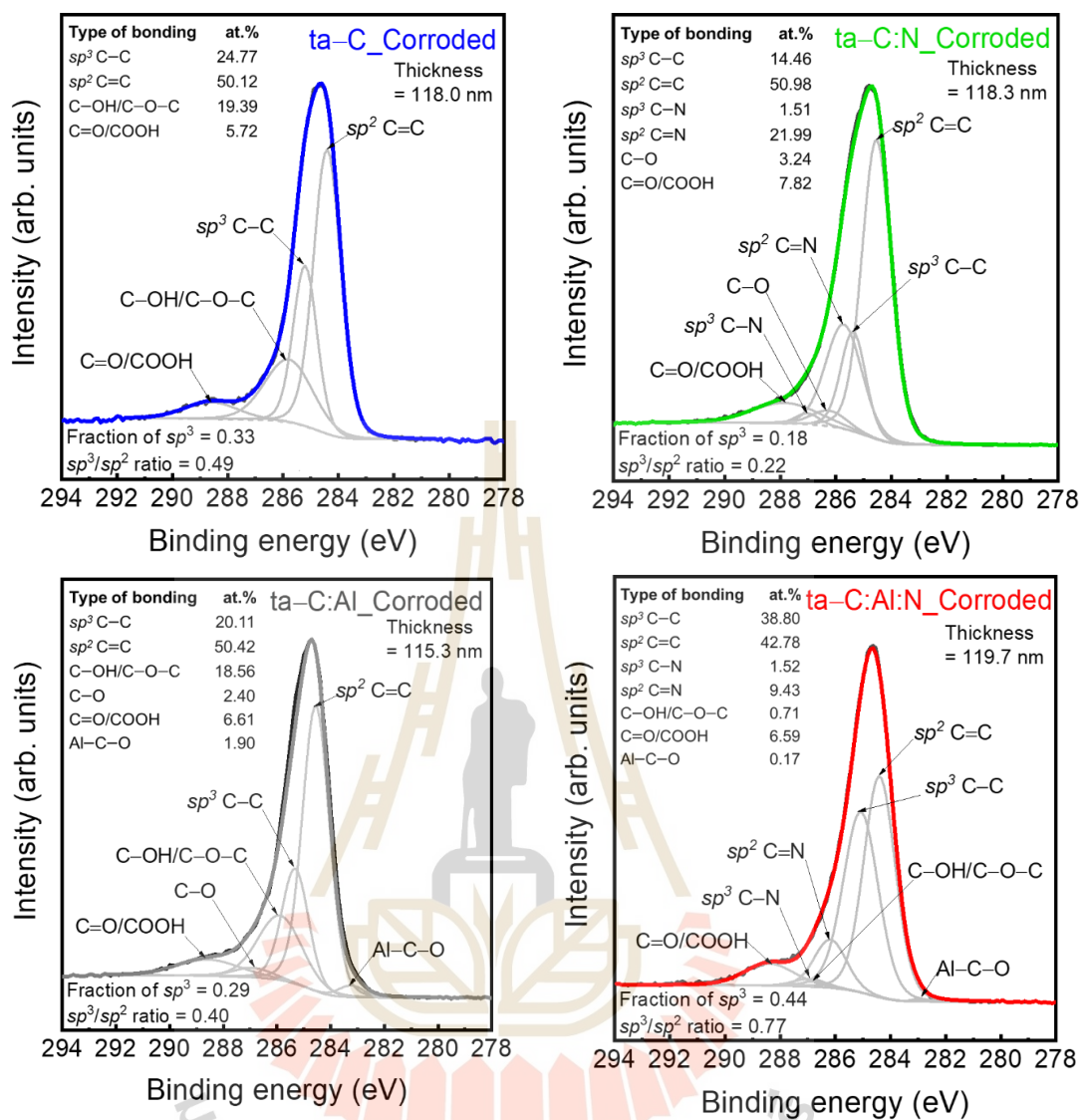
Figure A4. The C 1*s* XPS spectra and the corresponding deconvoluted Gaussian peaks of the films after the corrosion tests (Wongpanya *et al.*, 2022)
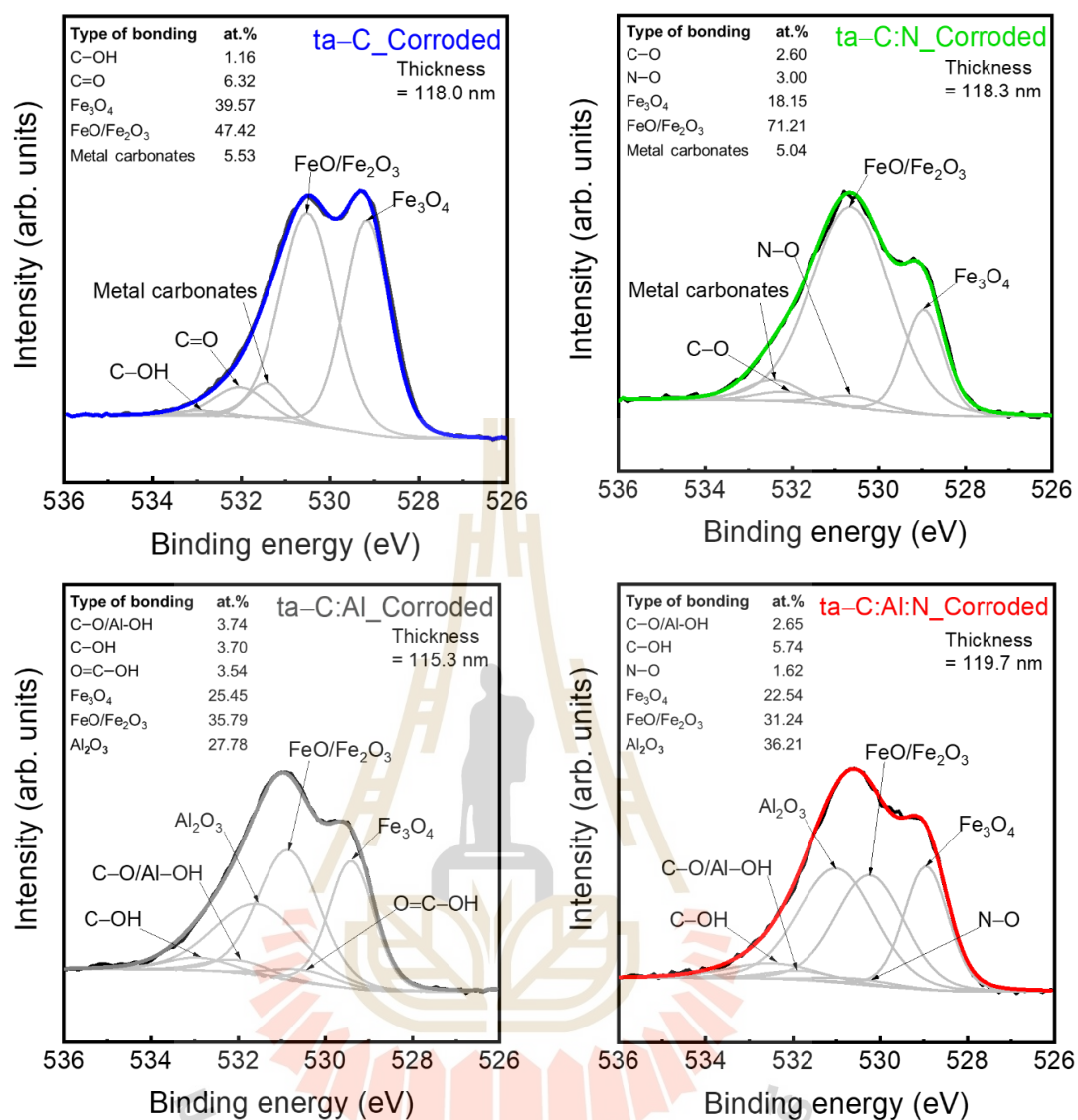
Figure A5. The O 1*s* XPS spectra and the corresponding deconvoluted Gaussian peaks of the films after the corrosion tests (Wongpanya *et al.*, 2022)
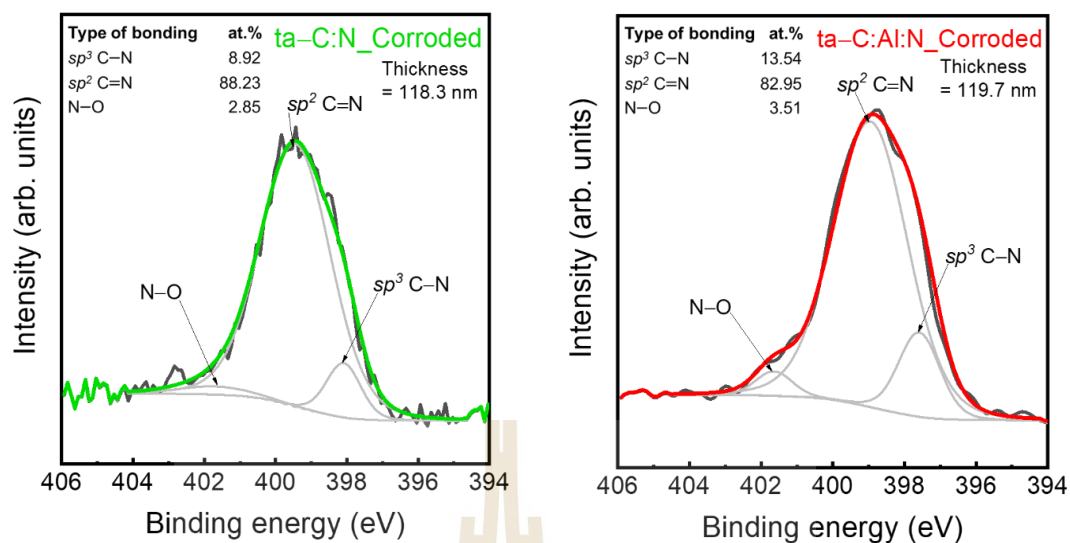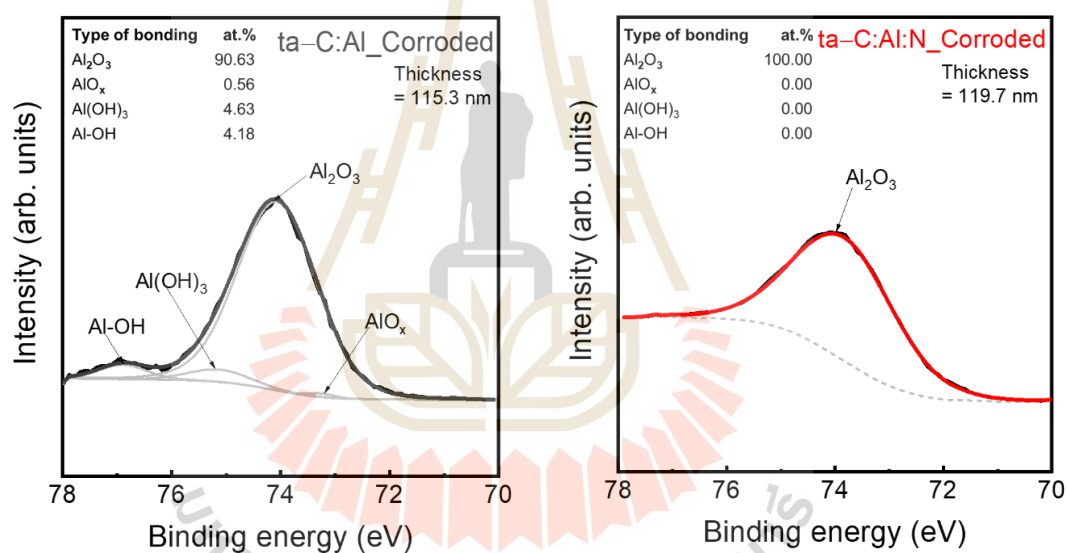
(a) N 1*s* spectra

(b) Al 2*p* spectra

Figure A6. XPS spectra and the corresponding deconvoluted Gaussian peaks of the films after the corrosion tests: (a) N 1*s*, and (b) Al 2*p* (Wongpanya *et al.*, 2022)
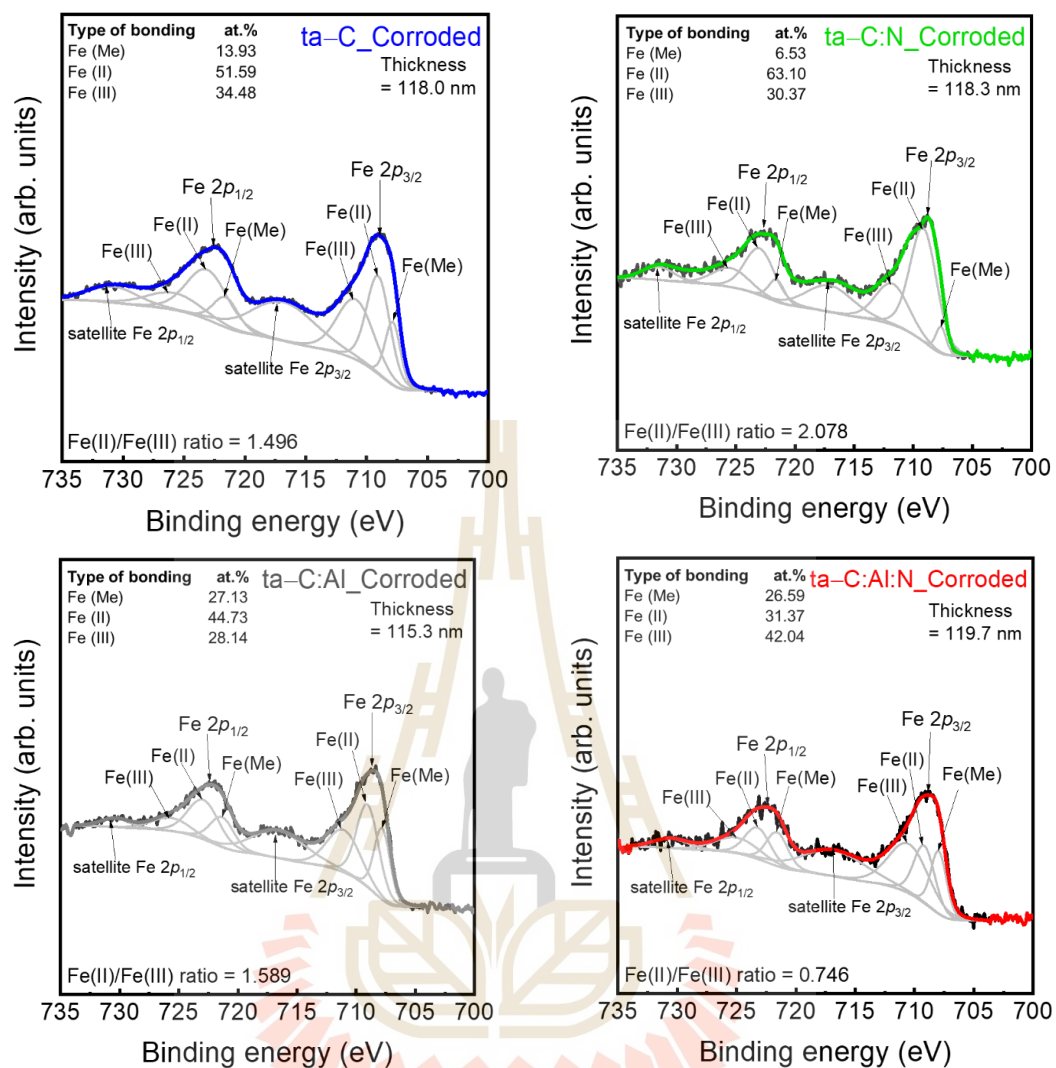
Figure A7. The Fe 2*p* XPS spectra and the corresponding deconvoluted Gaussian peaks of the films after the corrosion tests (Wongpanya *et al.*, 2022)

APPENDIX B
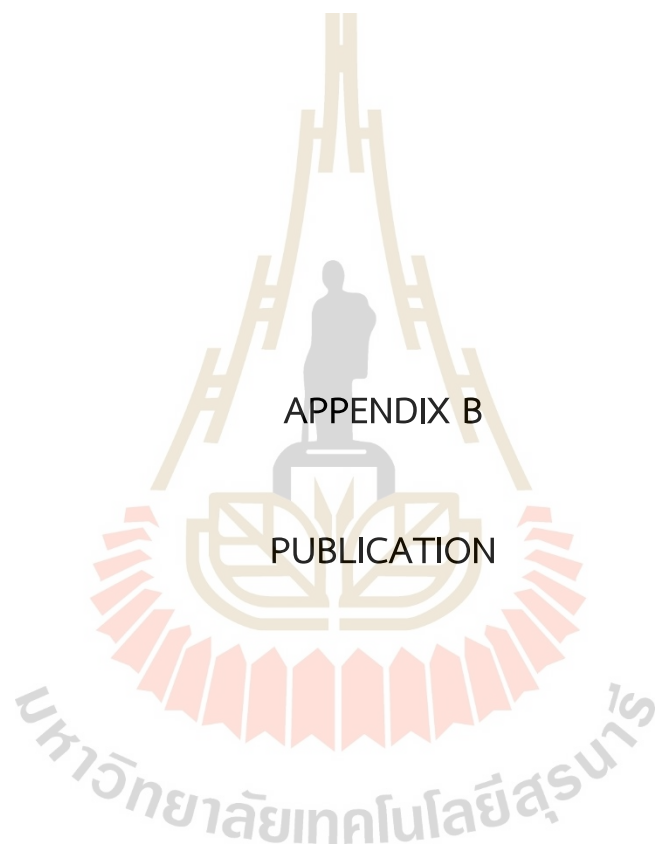
PUBLICATION

List Of Publication

Wongpanya, P., Silawong, P., & Photongkam, P. (2021). Nanomechanical properties and thermal stability of al–n-co-doped dlc films prepared by filtered cathodic vacuum arc deposition. **Surface and Coatings Technology**, 424, 127655. doi.org/10.1016/j.surfcoat.2021.127655

Wongpanya, P., Silawong, P., & Photongkam, P. (2022). Adhesion and corrosion of diamond–like carbon films with Al–N–co–doping prepared by filtered cathodic vacuum arc deposition, **Ceramics International**, 48, 20743-20759. doi.org/10.1016/j.ceramint.2022.04.055

Nanomechanical properties and thermal stability of Al–N-co-doped DLC films prepared by filtered cathodic vacuum arc deposition

Pornwasa Wongpanya [a,*], Praphaphon Silawong [a,b], Pat Photongkam [b]

[a] School of Metallurgical Engineering, Institute of Engineering, Suranaree University of Technology, Nakhon Ratchasima 30000, Thailand
[b] Synchrotron Light Research Institute (Public Organization), 111 University Avenue, Muang District, Nakhon Ratchasima 30000, Thailand

ARTICLE INFO

Keywords:
Co-doped diamond-like carbon
Filtered cathodic vacuum arc
Nanomechanical property
Thermal stability
In-situ near edge X-ray absorption fine structure
X-ray photoelectron spectroscopy

ABSTRACT

Al and N were incorporated into diamond-like carbon (DLC) films deposited using a filtered cathodic vacuum arc on AISI 4140 low-alloy steel. The structure, nanomechanical properties, local bonding, and thermal stability of non-doped DLC (ta-C), Al- and N-doped (ta-C:Al, and ta-C:N), and Al- and N-co-doped (ta-C:Al:N) films were thoroughly investigated. The thermal stability of the deposited films was measured using radiative heating and electron beam bombardment under a vacuum during thermal annealing. In-situ near-edge X-ray absorption fine structure spectroscopy was performed to characterize the surface nanostructures at different temperatures. ta-C:Al:N exhibited not only high hardness (49.04 GPa) and high (58.45%) elastic recovery (ER)—approximately equal to those of non-doped DLC films: 51.12 GPa and 60.06% ER, respectively)—but also higher thermal stability than ta-C at ~600 °C owing to the synergy of Al₂O₃ and sp² N-C bonds formed in the DLC films, as confirmed by X-ray photoelectron spectroscopy. ta-C:Al:N, therefore, is a suitable coating for wear and tribological applications, especially at high temperatures.

1. Introduction

AISI 4140 low-alloy carbon steel is widely used in engineering applications—especially in automotive parts—owing to its reasonable price, superior mechanical properties (strength, hardness, and ductility), and formability. The wear and corrosion resistance of AISI 4140 steel is enhanced by conventional thermal annealing and surface treatments such as quenching and tempering, carburizing, nitriding, nitrocarburizing, and plasma nitriding [1–4]. Automotive parts degrade mainly owing to exposure to humidity, chemical substances, friction, and temperature [2,5]. Although conventional thermal annealing and surface treatments have been developed continuously for four decades and have been extensively used to prevent steel-surface wear, corrosion, and oxidation [6–9], such treated steels might be unsuitable for application at high temperatures, which degrade mechanical properties and destabilize microstructures. To avoid such problems and enhance steel lifetimes, hard films such as CrN, TiC, TiN, TiCN, TiAlN, and diamond-like carbon (DLC) have been increasingly applied to machines, tools, and automobiles [10–14]. Owing to their outstanding mechanical and chemical properties including high hardness, low friction, wear resistance, chemical inertness, and thermal stability, DLC films are an attractive choice for engineering applications—especially automotive ones in which exposure to high temperatures, oxidation, corrosion, tribology, and wear all degrade metal surfaces. The prominent DLC mechanical and chemical properties originate from the amorphous DLC structure, which exhibits both diamond (sp^3 tetrahedral hybridized) and graphite (sp^2 trigonal hybridized) bonding [12–14]. The essential methods of synthesizing DLC films are ion deposition, sputtering, plasma deposition, pulsed laser deposition, and cathodic vacuum arc deposition [15–18].

Although cathodic vacuum arcs have been widely used to deposit DLC films, macroparticles usually form during arc deposition, thereby diminishing the quality of synthesized DLC films. A magnetic-filtered coil is usually employed to eliminate the macroparticles, and the resulting technique is known as filtered cathodic vacuum arc (FCVA) deposition [19–21], which can synthesize an sp^3-bond-rich DLC film in which 80–90% of the bonds are sp^3 tetrahedral hybridized [15,19–23]. However, the challenge facing DLC films is the high internal stress that increases with increasing film thickness. In addition, decreasing the DLC-film sp^2/sp^3 ratio at high temperatures, called graphitization, results in low hardness. To avoid degrading DLC properties, nonmetallic and metallic elements (including N, Si, Ti, Al, Cu, W, Cr, Ni, and Ag) have been incorporated into DLC structures to enhance adhesion,

friction coefficient, corrosion resistance, and thermal stability properties; however, this practice also decreases the sp^3-tetrahedral-hybridized carbon content in DLC films because dopants increase the fraction of sp^2-hybridized carbon bonds/atoms [24–26]. Because each dopant affects the DLC-film bonding structure and properties differently, co-dopants—especially nitrogen (N) and aluminum (Al)—are attractive for rectifying both the high internal stress and low adhesion of DLC films [27–29]. Although nitrogen notably improves the adhesion of synthesized tetrahedral amorphous carbon (ta-C) DLC films by approximately 20–90%, it reduces the hardness by approximately 2–10% [27]. Aluminum, on the other hand, remarkably reduces residual stress and does not form Al_4C_3 in DLC films because Al atoms dissolve in the carbon-film matrix without bonding with C atoms [28]. In addition, synthesizing Al–N-co-doped DLC films [30] by direct current (DC)- and pulsed cathode arcing deposition at a high target current and low pulse frequency promotes the formation of C–N and sp^3-N–C bonds owing to the high N-atom and Al–N-bond contents in DLC films, thereby enhancing hardness and toughness.

To the best of our knowledge, there are no reports in the literature on the role of Al–N co-doping on the correlation between the thermal stability and the structure and hardness of DLC films. Elucidating the role of such co-doped elements may improve the predictability of DLC-film lifetime and performance to meet the requirements of high-performance protective coatings. Therefore, Al- and N-doped, Al–N-co-doped, and non-doped DLC films were synthesized on AISI 4140 steel using pulsed two-FCVA deposition to elucidate the correlation between the structure, mechanical properties, and thermal stability of the films. The geometric structure and thermal stability of the films were studied using in-situ near-edge X-ray absorption fine structure (NEXAFS) spectroscopy. The Al- and N-doped, Al–N-co-doped, and non-doped DLC films were investigated using radiative heating and electron beam bombardment under vacuum at room temperature and during thermal annealing to 700 °C. The cross-section and thickness of the DLC films were determined using field emission–scanning electron microscopy (FE–SEM) and focused ion-beam milling combined with scanning electron microscopy (FIB–SEM). Vital structural information including the I_G/I_D ratio, D and G peaks, full width at half maximum of the G peak (FWHM (G)), compressive residual stress (σ), and graphite cluster size of the sp^2 sites (L_a), was determined using Raman spectroscopy, while the dopant content and sp^3/sp^2 ratio were evaluated using X-ray photoelectron spectroscopy (XPS).

2. Experimental procedures

AISI 4140 steel was cut into 10×10-mm squares to prepare coated samples. All the samples were ground using silicon carbide paper of consecutively finer grits up to 1500, and the ground samples were ultrasonically rinsed with acetone and ethanol for 20 min to eliminate surface contamination and were then dried with N_2 gas (99.99% pure). Fig. 1 shows the schematic of the FCVA deposition system having two vacuum arc plasma sources. Each vacuum arc plasma source has its own macroparticle magnetic-filtered coil and is independently controlled

Fig. 1. The schematic of the FCVA deposition system.

using the arc power supply controller operating two sources concurrently. The precleaned substrates were loaded into an FCVA chamber to deposit the non-doped, doped, and co-doped DLC coatings, and the chamber was evacuated to a controlled base pressure of 8.0×10^{-4} Pa. A graphite cathode (99.99% pure) and an aluminum cathode (99.00% pure) with an ø8-mm rod were installed separately on each cathodic source. Targets and ceramic insulators were placed between the anode and cathode and marked with a graphite pencil to form a conduction path used to initiate the spot arc and generate the plasma arc discharge during DLC deposition. The source-generated plasma moved through the 90° curved magnetic-filter coil connected to the arc-system electrical supply during DLC deposition. The distance between the magnetic-filter coil outlet and substrate was 30 mm, and the deposition time was 30 min under all the conditions. The bias voltage (V_{bias}) of -1000 V was applied to drive the arc current with pulse repetition rates of 6.0 Hz and a duty cycle of 0.003% (the percentage of the ratio of the pulse duration to the total period of the waveform) for both the graphite and aluminum cathodes to maintain the balance between the cathode consumption and arc stability during deposition, as shown in Table 1. Both aluminum and graphite cathodes were arced for 5 min at V_{bias} of -1500 V prior to remove any surface contaminations of cathodes [31,32]. The substrate was bombarded with carbon ion at V_{bias} of -1500 V, which is higher than the bias used for the deposition process, to remove any surface oxides and create an active surface for DLC films. The film coating process had begun after vacuum pressure reduces to base pressure of 8.5 $\times 10^{-4}$ Pa. For N doping, ultrahigh purity (UHP) N_2 gas was continuously flowed into the chamber such that vacuum pressure raise from base pressure to 3×10^{-2} Pa and waits for 5 min to ensure N_2 gas flowing stably inside the chamber [27] before deposition process. The sample was set in deposited position (cross area between C and Al) on the jig (fixed), and applied V_{bias} directly. Table 1 shows the conditions for preparing non-doped DLC (ta-C), nitrogen-doped DLC (ta-C:N), aluminum-doped DLC (ta-C:Al), and aluminum- and nitrogen-co-doped DLC (ta-C:Al:N) films using FCVA deposition.

The bonding structures of the ta-C, ta-C:N, ta-C:Al, and ta-C:Al:N films were investigated using a dispersive Raman microscope (SENTERRA; OPUS; BRUKER, Germany) operating in backscattering mode, and an Ar^+ laser ($\lambda = 532$ nm; power: 25 mW) was used as the excitation source. The focused-spot size and spectral resolution for the scanned Raman range (800–2000 cm^{-1}) were 3 μm and 3 cm^{-1}, respectively. The Raman spectra were fitted to three Gaussian line shapes using OriginPro software, Version 2018. From the fitted Raman spectra, the positions of the D (disordered) and G (graphite) bands were indicated by peaks at approximately 1360 and 1540 cm^{-1}, respectively, and the full width at half maximum (FWHM) was used to calculate the D–G-band intensity ratio (I_D/I_G) [27,30,33–35]. The elemental composition of the DLC films was evaluated using XPS (PHI5000; VersaProbe™; ULVAC-PHI, Japan) operating with an Al K_α radiation source (1486.6 eV) under ultrahigh vacuum (UHV; ~10^{-7} Pa) at the SUT-NANOTEC-SLRI joint research facility, beamline 5.3: SUT-NANOTEC-SLRI XPS, SLRI, Nakhon Ratchasima, Thailand. Prior to analysis, the sample surfaces were sputtered with Ar^+ ions accelerated at 1000 V for 1 min to eliminate any natural oxides. The pass energy and scanning step were 46.95 and 0.1 eV, respectively, at a 100-μm spot. XPS spectra and CasaXPS software were used to quantitatively analyze the film bonding states, and elemental atomic concentrations were calculated using MultiPak Spectrum ESCA software. In addition, the thicknesses of DLC-film cross-sections were measured using FIB–SEM (AURIGA®; Carl Zeiss, Germany) operating at 50,000× magnification and FE–SEM operating at 5-kV acceleration. Surface roughness of the AISI 4140 substrate and all the DLC films was measured using Atomic Force Microscope (AFM) (Park Systems AFM XE-120, South Korea) operating at non-contact mode with 5×5 μm of area, and scan rate 0.3 Hz.

DLC-film hardness and elastic moduli were evaluated using nano-indentation testing with a NanoTest Instrument (Vantage; Micro Materials, UK) equipped with a Berkovich indenter under the maximum load,
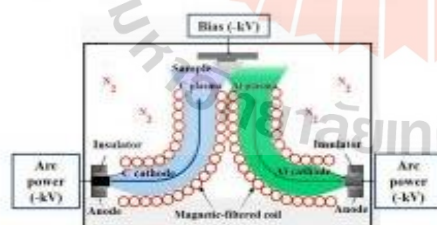
Table 1
FCVA deposition conditions for ta-C, ta-C:N, ta-C:Al, and ta-C:Al:N.

Sample	Pressure (Pa)		Voltage (V)			%Duty cycle		Frequency (Hz)		UHP N_2 gas	Time
	Base	N_2	V_{arc-C}	V_{arc-Al}	V_{bias}	C	Al	C	Al	N_2 flow rate (SCCM)[a]	(min)
ta-C	8.5×10^{-4}	–	800	–	–1000	0.003	–	6.0	6.0	–	30
ta-C:N	8.5×10^{-4}	3×10^{-2}	800	–	–1000	0.003	–	6.0	6.0	2.5	30
ta-C:Al	8.5×10^{-4}	–	800	400	–1000	0.003	0.003	6.0	6.0	–	30
ta-C:Al:N	8.5×10^{-4}	3×10^{-2}	800	400	–1000	0.003	0.003	6.0	6.0	2.5	30

[a] SCCM denotes standard cubic centimeters per minute at standard temperature and pressure (STP).

according to the ASTM E2546-07 standard [36]. Nanoindentation technique is used to detect depth-sensing by a pendulum-based method and is an extensively reliable method for mechanical measuring amorphous carbon thin films. The specimens were measured ten repeated and choose for six-point average value to statistical reliability for the report. Each sample measurements were carried out using a Berkovich type of indenter, and the maximum penetration depth for the films was in the range of 10–15% of the film thickness to avoid the substrate effect [32]. Moreover, the maximum penetration depth of each film followed the ASTM E2546-07 standard [36]. Therefore, the nanomechanical properties in this study followed the international criteria, although their thickness was different. Loading and unloading curves were measured at the rate of 0.1 mN s^{-1} with a dwell time of 10 s.

ta-C, ta-C:N, ta-C:Al, and ta-C:Al:N thermal stabilities were sequentially investigated using in-situ high-temperature NEXAFS spectroscopy in a UHV system from room temperature (RT) to 700 °C at 10 °C min^{-1} while holding the films for 20 min at each annealing temperature. The films were then cooled to 300 °C at each step, and the local bonding configuration was measured using in-situ NEXAFS spectroscopy coupled with spectroscopic photoemission and low-energy electron microscopy (SPELEEM; ELMITEC Elektronenmikroskopie GmbH, Germany) at beamline 3.2Ub: PEEM, SLRI, Nakhon Ratchasima, Thailand. The monochromatic photon energy of the beamline was operated in the range 40–1040 eV, in which synchrotron radiation was dispersed at 17° incident to the film surface under UHV (~3 × 10^{-8} Pa). NEXAFS spectra were measured in partial-electron-yield (PEY) mode by setting the bias to –20 kV, which is equal to the pass energy of the hemispherical energy analyzer. Therefore, only low-energy electrons (near the photoelectron threshold) were utilized as the NEXAFS intensity. NEXAFS C K-edge spectra were measured using photons in the range 270–350 eV and were scanned in 0.1-eV steps.

The absorption signals of all the DLC films were normalized using the NEXAFS intensity (in the same photon-energy range) of a flashed-Si wafer and highly oriented pyrolytic graphite (HOPG) as the reference material. The normalized C K-edge spectrum was deconvoluted using IGOR Pro 6.3 software to calculate the sp^2-bonding fraction of the films. The thermal stability of the non-doped, doped, and co-doped DLC films was evaluated based on the change in the sp^2-bonding fraction, and correlations between thermal stability and the other film properties were established.

3. Results and discussion

3.1. Structural analysis and film thickness

Raman spectroscopy, a well-known non-destructive analysis technique, is usually used to examine the bonding structure of amorphous carbon or DLC films [34,35,37–39]. Fig. 2 shows the Raman spectra of the non-doped, doped, and co-doped DLC films measured in the range 800–2000 cm^{-1}. The Raman spectra were fitted to the main Gaussian curves and were deconvoluted into G and D peaks and bands centered in the range ~ 1140–1260 cm^{-1} [40]. The G and D peaks and FWHM were used to calculate I$_D$/I$_G$ and evaluate the content of hybridized carbon bonds, respectively. Usually, the D peak (i.e., breathing mode) at ~1360 cm^{-1} corresponds to aromatic-ring vibrations (i.e., the disordered structure in six-fold aromatic rings), and the G peak (i.e., stretching mode) at

Fig. 2. Raman spectra of ta-C, ta-C:N, ta-C:Al, and ta-C:Al:N.

~1540 cm^{-1} corresponds to the stretching of all the pairs of sp^2-hybridized carbon atoms in aromatic rings and to carbon-chain vibrations [31,41]. The bands centered in the range ~1140–1260 cm^{-1} were assigned to the trans-polyacetylene (trans-PA) structure and were associated with hydrogen atoms bonded with sp^2-hybridized carbon atoms in the chain [42,43]. In addition, the peak at ~1260 cm^{-1} was attributed to the nanocrystalline (NC) diamond structure [40], indicating sp^3-hybridized carbon and H contents. Nevertheless, D and G peaks can be detected in various ranges; for example, the D and G peaks were detected in ranges ~1350–1370 and ~1500–1650 cm^{-1}, respectively, for the DLC films in this study [27,33,34,37,44]. The G peaks for ta-C, ta-C:N, ta-C:Al, and ta-C:Al:N were detected at ~1544.5, ~1552.5, ~1532.3, and ~1545.1 cm^{-1}, respectively, as listed in Table 2. Notably, doping noticeably changed the DLC-film structure, as indicated by the shifting G peak. The G peak shifted to higher wavenumbers for ta-C:N and ta-C:Al:N and a lower wavenumber when DLC was doped with Al (ta-C:Al). Extensive research has shown that G-peak shifting is related to changes in L$_a$ and σ for DLC films [45,46]. The vital Raman parameters (i.e., G and D peaks, I$_D$/I$_G$, and FWHM (G)) were determined from the area under the G- and D-peak Gaussian curves, while σ and L$_a$ were respectively estimated using the following equations [33,47,50]

$$\frac{I_D}{I_G} = C'(\lambda)L_a^2, \tag{1}$$

Table 2
Vital parameters obtained from Raman analysis: D and G peaks, FWHM (D), FWHM (G), I_D/I_G ratio, L_a and σ of ta-C, ta-C:N, ta-C:Al, and ta-C:Al:N.

Sample	Raman analysis						
	G Peak (cm^{-1})	D Peak (cm^{-1})	FWHM of G peak (cm^{-1})	FWHM of D peak (cm^{-1})	I_D/I_G ratio	L_a (nm)	σ (GPa)
ta-C	1544.54	1379.77	226.91	285.44	0.196	5.965	0.000
ta-C:N	1552.49	1386.85	189.17	250.05	0.998	13.469	1.339
ta-C:Al	1532.33	1387.15	156.16	257.53	3.277	24.489	−2.056
ta-C:Al:N	1545.14	1384.34	195.66	219.15	0.761	11.785	0.102

where $C'(514 \text{ nm}) \approx 0.0055$.

$$\sigma = 2G\left[\frac{1+\upsilon}{1-\upsilon}\right]\left[\frac{\Delta\omega}{\omega_0}\right].\tag{2}$$

where G is the shear modulus (70 GPa), υ is Poisson's ratio (≈ 0.3), $\Delta\omega$ is the shift in the G-peak Raman wavenumber, and ω_0 is the Raman wavenumber of the DLC sample, which is the (not necessarily stress-free) reference material.

Table 2 lists the Raman parameters obtained for ta-C, ta-C:N, ta-C:Al, and ta-C:Al:N, clearly indicating that doping had shifted the G peak to lower or higher wavenumbers, significantly increased I_D/I_G, and drastically decreased FWHM (G). The decrease in G corresponded to larger graphite clusters at sp^2-hybridized carbon sites because L_a (calculated using Eq. (1)) was consistent with those found in previous studies [31,34,48]. Remarkably, the L_a values of the N-doped/co-doped and Al-doped DLC films (i.e., ta-C:N/ta-C:Al:N and ta-C:Al) were double and approximately quintuple that of the non-doped DLC film, respectively. The increased L_a of the doped and co-doped DLC films depends on increased I_D/I_G and decreased FWHM (G) [45,51]. The increased I_D/I_G was mainly attributed to the increased sp^2-hybridized carbon content in the aromatic-ring structure, thereby reducing the sp^3-hybridized carbon content. The decreased I_D/I_G, on the other hand, was correlated with the sp^2-hybridized carbon-bonding cluster arranged in the chain structure [47]. These results indicate that high-L_a doped and co-doped DLC films (i.e., ta-C:Al, ta-C:Al:N, ta-C:N) exhibited lower sp^3-hybridized carbon contents than non-doped DLC, indicating progressive transformation toward the graphitic sp^2-hybridized carbon structure in DLC films doped and co-doped with Al and N.

Raman spectroscopy is employed to quantify the internal stress of materials because stress-strain-dependent properties are directly related to atomic-vibration frequencies. Moreover, because the wavenumber obtained using Raman spectroscopy is proportional to vibrational frequencies, it was applied to estimate the internal stress of the DLC films. When the load was applied to DLC films, the constituent atoms reversibly changed. Therefore, the interatomic-force constants, which determine the atomic vibrational frequencies, also changed because they are related to the interatomic separation. For example, with increasing DLC-film tensile load, bond lengths increased and force constants and vibrational frequencies both decreased, and the opposites happened when the material was subjected to compressive loads [52–54]. The Raman spectra clearly showed that doping DLC films with only N or Al-N shifted the G peak to higher wavenumbers ($\sim$1552.49 and $\sim$1545.14 cm^{-1}) while doping with only Al shifted the G peak to lower wavenumber ($\sim$1532.33 cm^{-1}). Relative to the internal compressive residual stress of DLC, those of ta-C:N, ta-C:Al, and ta-C:Al:N (calculated using Eq. (2)) were 1.339, −2.056, and 0.102 GPa, respectively. From the estimated σ, G peaks shifted to higher and lower wavenumbers, clearly indicating increased and decreased compressive stress in DLC films, respectively [52–54]. Furthermore, the XPS spectra presented in Section 3.3 indicate that increasing the compressive stress (σ) in ta-C:N and C:Al:N induced the carbon-bonding structure to transition from sp^3- to sp^2-hybridized carbon less than decreasing compressive stress in ta-C:Al, in which the carbon bonding structural transition from sp^3- to sp^2-hybridized carbon was crucial. These results are in good agreement with those published in previous studies [28,53]. The ta-C:Al G peak shifted toward the lower wavenumber might be affected by the Al-induced increased content of disordered graphite (i.e., sp^2-hybridized carbon) in the DLC structure and the low Al/aluminum oxide content generated and incorporated into the DLC-film matrix [28]. In addition, the Al crystal structure is face-centered cubic (FCC), which hinders carbide formation in DLC films, thereby allowing nanocrystal growth in the DLC matrix [51].

Fig. 3 shows a smooth and continuous amorphous film layer coated on the AISI 4140 surface. All the DLC-film cross-sections observed using FIB–FEM were in the range 100–250-nm thick, and the films are arranged from thickest to thinnest as follows: ta-C:N (230 nm) > ta-C (180.9 nm) > ta-C:Al:N (154.1 nm) > ta-C:Al (113.9 nm). Although the coating conditions (i.e., pressure, voltage, duty cycle, and time) were identical for all the films, as listed in Table 1, the film thicknesses were unequal because DLC-film thickness is regularly affected by the bonding structure and arrangement of carbon atoms in the DLC-film chain and aromatic rings and by dopant composition [27,31,44,55–57]. The thickness of all the films depends on the compressive residual stress generated during coating. Film thickness increased with increasing compressive residual stress in ta-C:N/ta-C:Al:N and film thickness decreased with decreasing compressive residual stress in ta-C:Al, as listed in Table 2 and shown in Fig. 3. DLC-film thickness increased not only with increasing compressive stress but also with the G peak shifting to a higher wavenumber, which is consistent with previous findings that film thickness was correlated with Raman spectral data [55].

The dopant-induced change in the DLC film thickness could be explained as follows. The ta-C:N film thickness could have increased because of reactive N atoms as an additional deposition element in the chamber. The high internal compressive stress of the ta-C:N film might have been due to the high N_2 plasma concentration during deposition [27,47]. In contrast, the ta-C:Al compressive stress and thickness were the lowest and thinnest, respectively, which may be because C and Al ions had collided during coating; subsequently, fewer C ions exhibited sufficient energy to coat and form sp^3-hybridized carbon bonds on the film layer and because Al does not combine with C to form aluminum carbide [28,51]. This plausible explanation is supported by the highest I_D/I_G and L_a and the lowest hardness values. Although the Al- and N-co-doped DLC film (ta-C:Al:N) was approximately 26 nm thinner than the non-doped DLC film (ta-C), the relative compressive stress of ta-C:Al:N was approximately 0.102 GPa, as compared with ta-C. This may have been due to the reduced collision rate between C and Al ions because the N_2 pressure had increased from the base to 3×10^{-2} Pa in the coating chamber during film growth and Al and N co-doping [47,58]. As previously described for ta-C:N, because N ions also promoted film deposition, the ta-C:Al:N film was slightly thinner than the non-doped DLC film.

Fig. 4 shows the surface roughness of AISI 4140 substrate (for both before and after polishing) and all the DLC films measured using AFM. There was no SiC from the SiC paper embedded on the surface as the substrate was cleaned properly. The surface roughness (Ra) of AISI 4140 was 8.8 nm, which is less than the roughness of the block standard according to the ASTM E2546-07 standard [36], mentioned that the reference blocks should be prepared in such a way that the test surface is as smooth as is possible. Moreover, an acceptable value of average surface roughness, Ra, for many applications is Ra $\leq$ 10 nm measured over a 10 μm trace. It might therefore say that the surface roughness of all samples in this study rarely affected nanomechanical properties. The surface roughness of all the samples was nearly the same (Ra 6.4–8.8

(a)   (b)

(c)   (d)
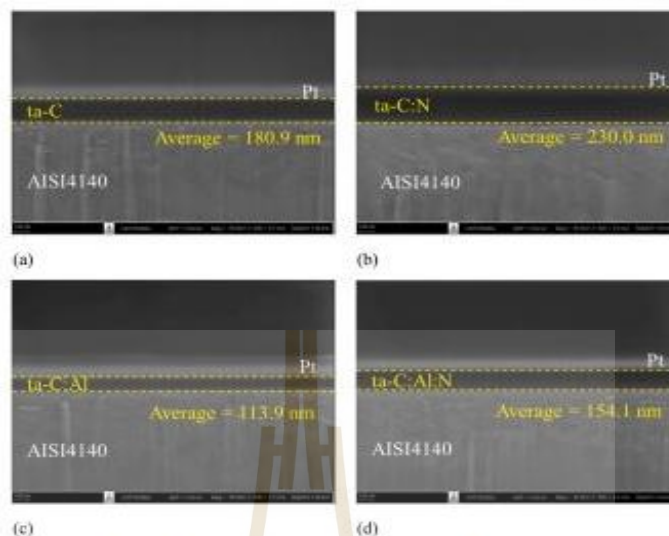
Fig. 3. FIB–SEM images of (a) ta-C, (b) ta-C:N, (c) ta-C:Al, and (d) ta-C:Al:N.

nm), and the roughness of DLC films (Ra) was 8.4, 8.0, 8.8, and 6.4 nm for ta-C, ta-C:N, ta-C:Al, and ta-C:Al:N, respectively. Moreover, macroparticles were detected on ta-C, while they were found rarely on ta-C:N, ta-C:Al, and ta-C:Al:N. It meant that N and Al dopants remarkably decreased macroparticles on the DLC surface. The decrease in the macroparticles was due to the collision between the dopants and macroparticles. Then, the macroparticles were fallen and filtered by the copper filter coil.

3.2. Nanomechanical properties

Fig. 5 shows the load-displacement curves of all the DLC films. Non-smooth load-displacement curves (discontinuities) represented the high elastic recovery (%ER) owing to the elastic-to-plastic deformation transition, as described in [59], and plastic deformation bands often parallel to the indentation edges at the low-load indentations (applied in this study).

The nanomechanical properties of the DLC films—including hardness (H), elastic modulus (E), plastic index parameter (i.e., the ratio of hardness to elastic modulus, H/E), and elastic recovery (%ER)—were evaluated using nanoindentation testing. The elasticity of the DLC films was estimated using the elastic recovery (%ER) obtained from the load–displacement curves shown in Fig. 5 and was calculated using the following equation:

$$\%ER = \left(\frac{d_{max} - d_{res}}{d_{max}}\right) \times 100.$$ (3)

where d_{max} and d_{res} are the displacement at the maximum load and the residual displacement after load removal, respectively.

As listed in Table 3, the H and E of the ta-C:N, ta-C:Al, and ta-C:Al:N were 47.32 ± 1.91 and 210.51 ± 4.82, 38.84 ± 1.78 and 159.65 ± 3.94, and 49.04 ± 1.33 and 251.09 ± 6.57 GPa, respectively, and were lower than those of non-doped DLC (51.12 ± 1.08 and 302.29 ± 6.35 GPa,

respectively). Lower H and E correspond to increased I_D/I_G and L_a attributed to increased sp^2-hybridized carbon bond content and decreased sp^3/sp^2, as confirmed by the XPS spectra (Section 3.3). Therefore, the nanomechanical properties showed that the DLC films exhibited increased graphitization and larger graphite clusters (L_a) with increasing dopant content. Moreover, the sp^3-hybridized carbon bond content significantly affected the mechanical properties of the DLC films, especially the ta-C film. The mechanical properties of the ta-C film (i.e., hardness, surface smoothness, atomic density, and Young's modulus) all degraded with decreasing sp^3-hybridized carbon bond content [27]. The H of the ta-C:Al:N was slightly lower than that of non-doped DLC possibly owing to the NC diamond phase [40] that had formed in the co-doped DLC film, as indicated by the peak at ~1248.17 cm⁻¹ in Fig. 2. These results imply that doping the DLC film with Al and N improved the hardness of the DLC film. However, all the DLC films enhanced the hardness of the bare steel (AISI 4140) substrate, as verified by the increased hardness from 3.3 GPa [60] for bare steel (AISI 4140) to 38.84 ± 1.78, 47.32 ± 1.91, and 49.04 ± 1.33 GPa for ta-C:Al, ta-C:N, and ta-C:Al:N-coated 4140 steel, respectively. In addition, DLC nanomechanical properties (H and E) were above 38 and 150 GPa, respectively, compared with those of natural diamond (56–102 and 1050 GPa, respectively), thereby implying the deposition of high-quality DLC films. These values are consistent with others published in the literature [61,62]; therefore, the films could effectively protect the substrate surface from scratches and wear.

The elastic–plastic behavior and wear resistance of the DLC films were considered through H/E and %ER [61]. H/E, an important parameter that combines both properties, is used to rank materials in which surface layers intensively deform during service, which is the so-called elastic strain to failure. Therefore, DLC films exhibiting high H/E also exhibit high wear resistance [63], and such protective coatings might be suitable for application to automobile parts. The ta-C:N, ta-C:Al, and ta-C:Al:N films exhibited H/E values of 0.225 ± 0.010, 0.243 ± 0.013, and 0.195 ± 0.007, respectively, slightly higher than that of the
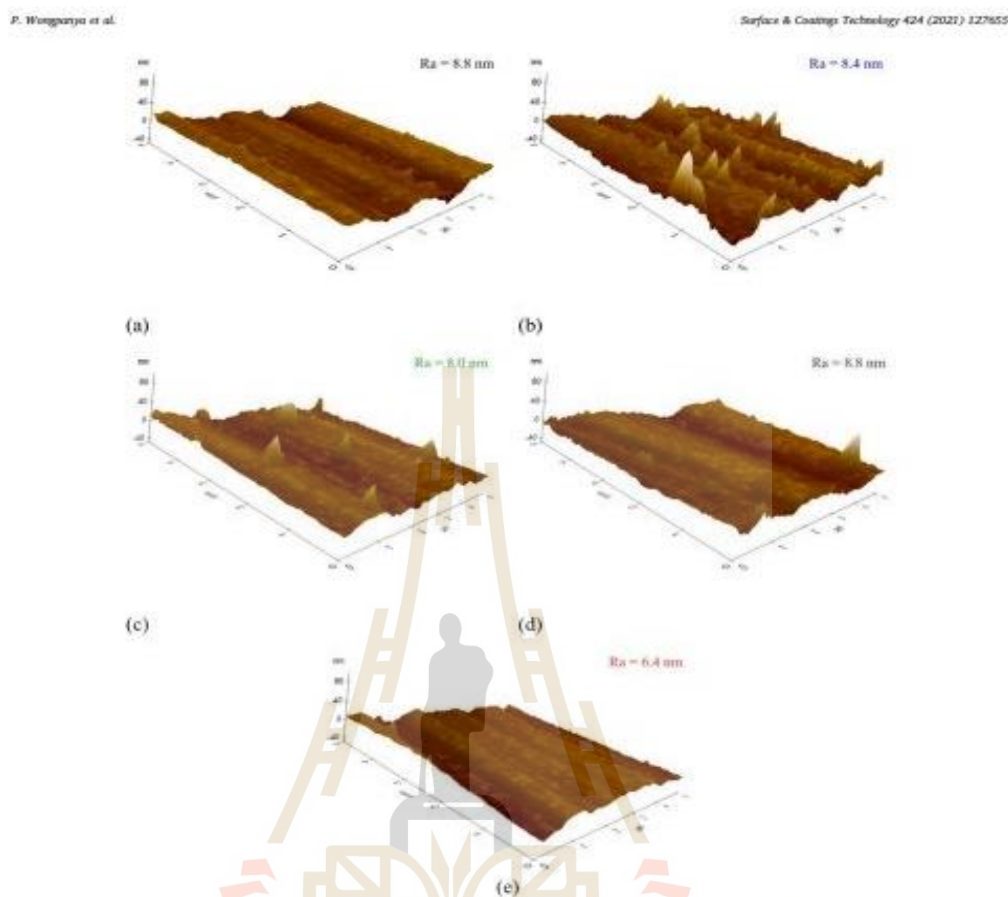
Fig. 4. AFM topographies of (a) AISI 4140, (b) ta-C, (c) ta-C:N, (d) ta-C:Al, and (e) ta-C:Al:N.

ta-C film (0.169 ± 0.005), as listed in Table 3, meaning that although Al and N doping might improve the elastic strain to failure, they also reduce DLC-film hardness. It is well known that typical hard and adherent DLC films exhibit high elasticity and recovery owing to the relaxation of the elastic strain within the DLC structure [64,65]. In addition, elastic recovery strongly depends on the sp³-hybridized carbon bond content in the film [63]. Therefore, the elastic recovery of the DLC films decreased with increasing dopant content, as indicated by %ER data listed in Table 3. Similar to the trend in H, %ER is ranked in descending order as follows: ta-C > ta-C:Al:N > ta-C:N > ta-C:Al, corresponding to the sp³-hybridized carbon bond content in the films, as confirmed by the XPS analysis in Section 3.3. Vital properties such as the local bonding structure and thermal stability are further discussed in subsequent sections to consider whether doping and co-doping are appropriate for DLC films applied as protective coatings for wear and tribological applications, especially for automobile parts.

3.3. Elemental composition and chemical bonding structure

The elemental composition and chemical bonding structure of ta-C, ta-C:N, ta-C:Al, and ta-C:Al:N were quantified using XPS. Table 4 lists the elemental compositions of the films. Clearly, doping decreased the atomic concentration (at.%) of C from 90.01 for ta-C to 79.23, 78.20, and 58.83 for ta-C:N, ta-C:Al, and ta-C:Al:N, respectively, as listed in Table 4, and decreased the sp³-hybridized C-C content of the DLC films, as shown in Fig. 6. The N content was approximately 11.21 and 14.12 at. % in ta-C:N and ta-C:Al:N, respectively, while the Al content was approximately 4.77 and 7.18 at.% in ta-C:Al and ta-C:Al:N, respectively. O content increased with increasing Al content possibly because O had adsorbed on or bonded with Al on the film surface to form an oxide layer when the films were exposed to air [29].

The chemical compositions and bonding states of the non-doped, doped, and co-doped DLC films were measured using XPS, and the essential C 1s, N 1s, and Al 2p peaks were detected in all the spectra, as

Fig. 5. Load–displacement curves of ta-C, ta-C:N, ta-C:Al, and ta-C:Al:N.

Al, and ta-C:Al:N, respectively) and sp^2-hybridized C-C bonds (at 284.92, 284.80, and 285.02 eV for ta-C:N, ta-C:Al, and ta-C:Al:N, respectively) were shifted to binding energies higher than those of their counterpart peaks in the deconvoluted spectrum for DLC, and all the peak positions corresponded almost exactly to those previously reported in the literature [15,29,69]. The percentage of sp^3-hybridized C-C bonds in the DLC films decreased remarkably from 68.01% for ta-C to 40.20 and 38.58% for ta-C:N and ta-C:Al, respectively, because the DLC films had been doped with only one element. In contrast, the Al and N co-dopant synergy was obvious; that is, the percentage of sp^3-hybridized C-C bonds only slightly decreased compared to that in the single-doped films, from 68.01 to 50.41% for ta-C and ta-C:Al:N, respectively (Fig. 6). These results indicated that the percentage of sp^3-hybridized C-C bonds decreased with increasing alloying contents. Furthermore, the decreased percentage of sp^3-hybridized C-C bonds corresponded to reduced hardness (H) in the doped and co-doped DLC films (i.e., ta-C:N, ta-C:Al, and ta-C:Al:N), as listed in Table 3. Although the deconvoluted spectra obtained for ta-C:N and ta-C:Al:N exhibited high-resolution deconvoluted C 1s peaks in ranges 285.50–286.54 and 285.20–287.45 eV (corresponding to sp^2-hybridized C–N and sp^3-hybridized C-N bonds, respectively), the spectra did not exhibit any peaks corresponding to sp-

Table 3
Mechanical properties of ta-C, ta-C:N, ta-C:Al, and ta-C:Al:N.

Sample	Mechanical properties			
	Hardness, H (GPa)	Elastic modulus, E (GPa)	Plastic index parameter, H/E	Elastic recovery (%ER)
ta-C	51.12 ± 1.08	302.29 ± 6.35	0.169 ± 0.005	60.06 ± 1.93
ta-C:N	47.32 ± 1.91	210.51 ± 4.82	0.225 ± 0.010	57.92 ± 1.35
ta-C:Al	38.84 ± 1.78	159.65 ± 3.94	0.243 ± 0.013	50.47 ± 1.53
ta-C:Al:N	49.04 ± 1.33	251.09 ± 6.57	0.195 ± 0.007	58.43 ± 1.73

Table 4
ta-C, ta-C:N, ta-C:Al, and ta-C:Al:N elemental compositions (at.%) quantitively measured using XPS.

Sample	Atomic Concentration[a] (at.%)			
	C 1s	N 1s	O 1s	Al 2p
ta-C	90.01	–	9.99	–
ta-C:N	79.23	11.21	9.56	–
ta-C:Al	78.20	–	17.03	4.77
ta-C:Al:N	58.83	14.12	19.87	7.18

[a] Atomic concentration was calculated using MultiPak Spectrum ESCA software.

shown in Figs. 6–8. The C 1s XPS spectra were deconvoluted into distinct Gaussian–Lorentzian peaks using Shirley backgrounds to estimate the percentage of sp^3-hybridized C-C bonds in the DLC films [56,66]. Fig. 6 shows peaks obtained for the deconvoluted C 1s spectra of ta-C, ta-C:N, ta-C:Al, and ta-C:Al:N. In the deconvoluted spectrum for DLC, peaks corresponding to pure carbon–carbon bonds at 283.5 and 284.19 eV were assigned to C–C bonds (i.e., sp^3-hybridized carbon atoms) and C-C bonds (i.e., C sp^2-hybridized carbon atoms), while another peak in the binding energy range 286–288 eV was matched to C–OH, C–O, or C–O bonds, indicating bonding between the carbon and hydrogen atoms and air-exposure-induced environmental oxygen contamination in the local DLC-film bonding structure [15,31,39,47,48,67,68]. The deconvoluted C 1s peaks for sp^3-hybridized C-C and sp^2-hybridized C–C bonds were slightly shifted because double bonds are slightly shorter than single ones; therefore, the charge density (around the C atom) moved closer to the carbon nucleus and the valence electrons contracted in the sp^2-hybridized C–C bonds, thereby decreasing the binding energy of the C 1s core level [15]. In the deconvoluted spectra for ta-C:N, ta-C:Al, and ta-C:Al:N, the deconvoluted C 1s peaks obtained for sp^3-hybridized C–C bonds (at 284.54, 284.38, and 284.42 eV for ta-C:N, ta-C:

hybridized C≡N bonds (i.e., nitrile groups) at 286.70 eV [38,39,66,70]. When DLC films are doped with N during coating, N significantly forms various bonds with local carbon atoms to generate an amorphous structure consisting of pyridine (sp^2-hybridized C~N bonds), urotropine (sp^3-hybridized C-N bonds), and nitrile groups (sp-hybridized C≡N bonds) [29,38,39,66,71]. Therefore, the sp^3 and ($sp^2 + sp^3$) C-bond ratios changed from 0.81 for ta-C to 0.49, 0.48, and 0.77 for ta-C:N, ta-C:Al, and ta-C:Al:N, respectively. The C 1s spectra showed that the fraction of sp^3-hybridized C atoms decreased with increasing N and Al contents, corresponding to decreased H (Table 3). Furthermore, the decreased relative fraction of sp^3-bonded C and N atoms corresponded to more and larger sp^2-bonded clusters (L_a) [72] and increasing I_D/I_G, as listed in Table 2. The XPS results showed good agreement with the Raman analysis (Section 3.1) and hardness tests (Section 3.2).

Likewise, the deconvoluted N 1s spectra for ta-C:N and ta-C:Al:N, shown in Fig. 7, exhibited three peaks in ranges 397.50–399.40, 399.10–400.60, and 401.5–402.9 eV corresponding to sp^3-hybridized N-C, sp^2-hybridized N–C, and N-O bonds, respectively [29,39,66]. These peaks are consistent with organic nitrogen-containing polymers pyridine (which exhibits sp^2-hybridized C~N bonds and C 1s and N 1s peaks at 285.50 and 400.16 eV, respectively) and urotropine (which exhibits sp^3-hybridized C-N bonds and C 1s and N 1s peaks at 286.9 and 399.40 eV, respectively) [66]. In ta-C:N and ta-C:Al:N, N atoms are mainly bonded to sp^2- and sp^3-hybridized carbon atoms (i.e., N-C and N-C bonds), respectively, because the relative fraction of sp^3-bonded N and C atoms: (sp^3-hybridized N-C bonds)/(sp^3-hybridized N-C bonds + sp^2-hybridized N-C bonds) changed from 0.28 to 0.89, as shown in Fig. 7. More sp^2-hybridized N-C bonds in DLC films, especially ta-C:N, significantly reduced the relative fraction of sp^3-bonded N and C atoms because N doping reduced the number of dangling bonds in the aromatic ring [39]. In addition, the weak peak at 282.2 eV in the C 1s spectra for ta-C:Al and ta-C:Al:N corresponded to Al–O–C bonds, which might be due to air-exposure-induced contamination and oxygen [73].
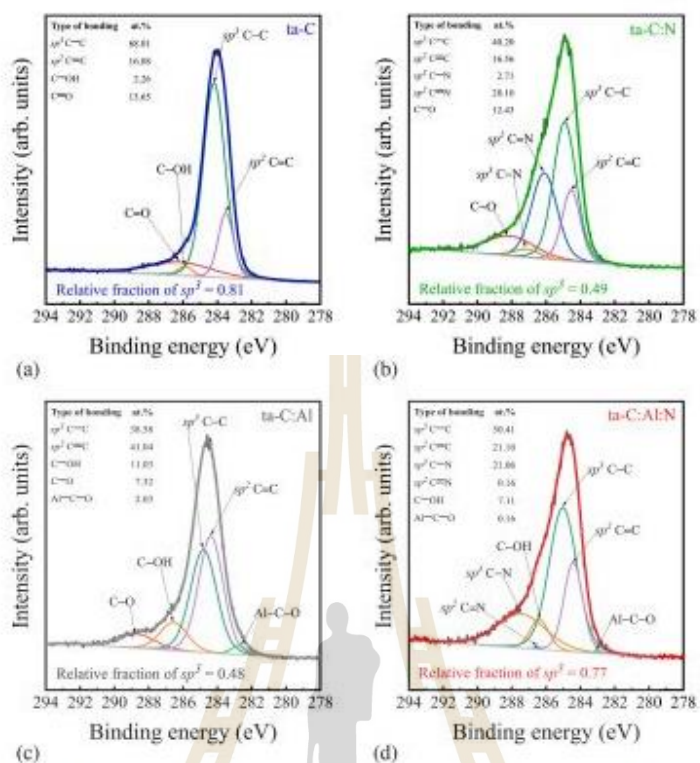
Fig. 6. C 1s XPS spectra and corresponding deconvoluted Gaussian peaks of (a) ta-C, (b) ta-C:N, (c) ta-C:Al, and (d) ta-C:Al:N.
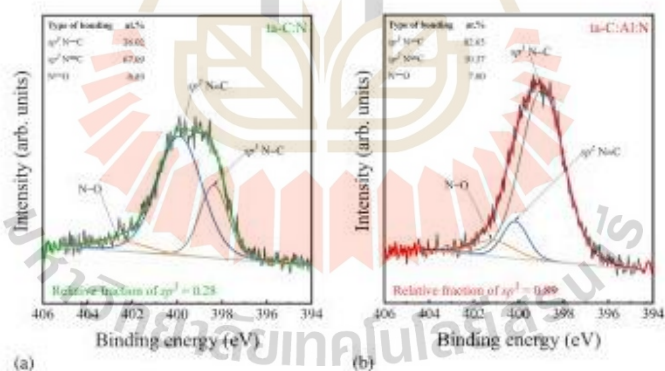
Fig. 7. N 1s XPS spectra and corresponding deconvoluted Gaussian peaks of (a) ta-C:N and (b) ta-C:Al:N.
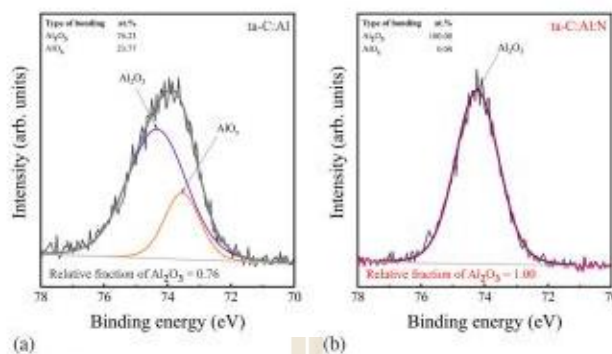
Fig. 8. Al 2p XPS spectra and corresponding deconvoluted Gaussian peaks of (a) ta-C:Al and (b) ta-C:Al:N.

Fig. 8 shows the peaks in the deconvoluted Al 2p spectra for ta-C:Al and ta-C:Al:N. In the spectrum for ta-C:Al, peaks at 73.54 and 74.24 eV were assigned to AlO_x and Al_2O_3, respectively, while the spectrum for ta-C:Al:N exhibited only one peak at 74.24 eV. The relative fraction of Al_2O_3: $Al_2O_3/(Al_2O_3 + AlO_x)$ was 0.76 and 1.00 for ta-C:Al and ta-C:Al:N, respectively, as shown in Fig. 8. Noticeably, the most stable aluminum oxide (Al_2O_3) [74] was present in ta-C:Al:N, whereas aluminum suboxides (AlO_x) coexisted with Al_2O_3 in ta-C:Al [29,73,75]. Al_2O_3 has been widely used to manufacture machining tools and solar cells and in other high-temperature applications because of its excellent properties including wear resistance, thermal stability, and corrosion resistance [76,77]. However, doping DLC with only Al degraded the compressive stress (σ) and hardness (H), which are vital properties for tribological applications such as adhesion and wear resistance, owing to the presence of significantly fewer sp^3-hybridized C-C bonds (without any sp^3-hybridized N-C bonds) in the films, as reported in a previous study [27]. This result suggested that single-doping DLC films with only a low aluminum content (e.g., 4.77 at.% in this experiment) decreased hardness and degraded the mechanical properties. In contrast, the synergy between Al and N in ta-C:Al:N maintained σ and H—both necessary for adhesion and wear resistance—which might be because N atoms mainly formed sp^3-hybridized N-C bonds associated with Al_2O_3 in ta-C:Al:N, except for ta-C:Al, which does not contain any sp^3-hybridized N-C bonds but does contain a mixture of AlO_x and Al_2O_3. Therefore, altering the DLC-film bonding structures, especially carbon–carbon bonds, and the thermal stability changes when DLC films are co-doped with Al and N will be further investigated in Section 3.4.

3.4. Thermal stability

The local atomic structures of ta-C, ta-C:N, ta-C:Al, and ta-C:Al:N were evaluated using in-situ high-temperature NEXAFS spectroscopy to assess the thermal stability of DLC films at RT and thermally annealed in the range 200–700 °C in 100 °C increments. Fig. 9 shows the C K-edge NEXAFS spectrum generated for ta-C:Al:N at RT. Multiple peaks were obtained by subtracting and deconvoluting the spectrum. Evidently, the pre-edge resonance at ~285.4 eV was assigned to transitions from C 1s to the unoccupied π^* state of the sp^2-hybridized C=C site, including the contribution of the sp-hybridized C≡C site if present [32,78,79]. For the high-energy edge, the broadband region between 288 and 335 eV originated from overlapping C 1s transitions to unoccupied σ^* states at sp-, sp^2-, and sp^3-hybridized sites in the DLC films [78]. The intermediate region distinguished between the π^* and σ^* states at ~285.1, 285.9, 286.3, 287.6, 287.7, 288.5, 289.6, and 293.7 eV corresponded to
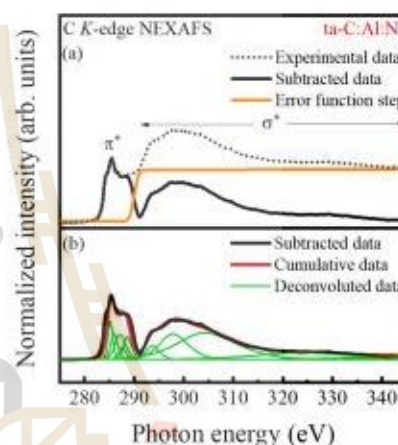
Fig. 9. In-situ high-temperature NEXAFS C K-edge spectrum generated for ta-C:Al:N (a) prior to data subtraction (where error function step was applied to fit edge jumping at ionization potential, as indicated in orange) and (b) after data subtraction (where spectrum was deconvoluted into multiple Gaussian peaks).

transitions between the following states: C 1s → π^* (C=C), π^* (C=N), π^* (C-OH), σ^* (C-H), σ^* (C-N), π^* (C=O) or π^* (C≡C), σ^* (C-C), and σ^* (C-C), respectively [80,81]. Other high resonances detected at ~297.8 and ~304.3 eV were attributed to C 1s transitions to the σ^* (C-O) and σ^* (C=C) states, respectively [78,81]. Because hydrogen was absent during FCVA deposition, σ^* (C-H) states were related to the hydrogen saturation of the surface-carbon dangling bonds (i.e., nonpaired electrons), while carbon oxidized owing to air exposure was assigned to π^* (C=O) states [78,80,81].

To evaluate the sp^2-hybridized bond content in a sample, the peak area corresponding to the C 1s → π^* transition at ~285.4 eV must be normalized with C 1s → σ^* transitions in the range 288–335 eV. The sp^2-hybridized bond fraction can then be calculated using the following equation [78,70,82]:

$$f_{sp^2} = \frac{I_{sam}^{\pi^*}/I_{sam}^{total}}{I_{ref}^{\pi^*}/I_{ref}^{total}} \qquad (4)$$

where "π^*" denotes the position of the C $1s \rightarrow \pi^*$ transitions (i.e., C=C bonds), "total" assigns integration areas calculated under the spectrum to binding energies in the range 288–335 eV, and "sam" and "ref" define deconvoluted peaks for a sample thin film and a reference sample (highly oriented pyrolytic graphite (HOPG)), respectively.

Fig. 10 shows the in-situ C K-edge NEXAFS spectra for ta-C, ta-C:N, ta-C:Al, and ta-C:Al:N at RT and thermally annealed up to 700 °C. The chemical bonding configuration exhibited slight heterogeneities, as indicated by the spectral features, meaning that the atomic bonding structure changed gently when the dopant content (Al and N) was low. At RT, the sp^2-hybridized bond fractions of the ta-C, ta-C:N, ta-C:Al, and ta-C:Al:N films were 0.34, 0.39, 0.55, and 0.36, respectively, as shown in Figs. 10 and 11. Doping with only N or Al clearly induced the formation of graphitic (i.e., sp^2-hybridized) bonds (called "graphitization"), as indicated by the sp^2-hybridized bond fractions, while co-doping with

both Al and N only slightly induced graphitization. The relative sp^2-hybridized bond fraction increased with increasing annealing temperature because graphitization transformed sp^3-hybridized (σ^*) states into sp^2-hybridized (π^*) ones in the amorphous carbon film, thereby resulting in fewer-carbon dangling bonds [83]. Remarkably, the NEXAFS spectra of ta-C:N, ta-C, and ta-C:Al showed that sp^3-hybridized (σ^*) states had significantly transformed into sp^2-hybridized (π^*) ones in the amorphous carbon films, thereby increasing the relative sp^2-hybridized bond fraction to 1.00 (i.e., 100% sp^2-hybridized bond content) at 400, 500, and 600 °C, respectively, which is consistent with findings in previous studies [84–86]. In contrast, the relative sp^2-hybridized bond fraction in ta-C:Al:N increased gradually from 0.36 at RT to 0.39 at 300 °C, which was only slightly different from the change in the relative sp^2-hybridized bond ratio in ta-C (i.e., from 0.34 to 0.40) in the same temperature range. Although the relative sp^2-hybridized bond fraction of ta-C:Al:N rose abruptly from 0.43 to 0.56 from 400 to 700 °C, the carbon remained amorphous in the ta-C:Al:N film, implying that ta-C:Al:N graphitized more slowly and at a higher annealing temperature than
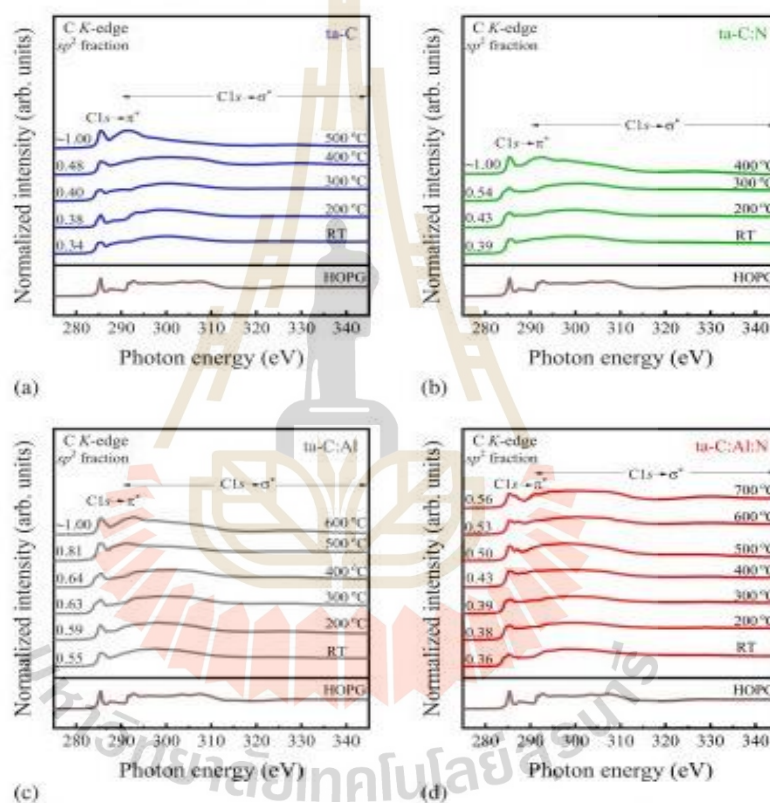

Fig. 10. C K-edge NEXAFS spectra generated for (a) ta-C, (b) ta-C:N, (c) ta-C:Al, and (d) ta-C:Al:N at room temperature (RT) and thermally annealed to graphitization temperature.
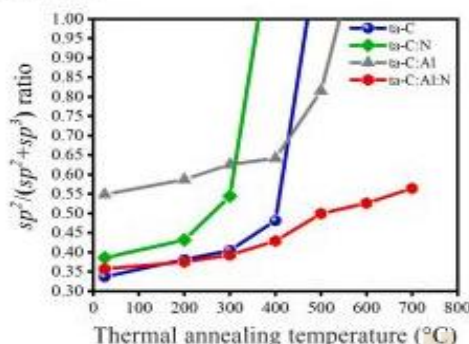
Fig. 11. ta-C, ta-C:N, ta-C:Al, and ta-C:Al:N sp^2-hybridized bond fractions plotted as functions of thermal annealing temperature from room temperature (RT) to graphitization temperature.

ta-C:N, ta-C, and ta-C:Al, as shown in Fig. 11. The high thermal stability of ta-C:Al:N might be due to the synergistic formation of stable oxide (Al_2O_3) and nitride (i.e., sp^3-hybridized) N-C bonds, as confirmed by the XPS results shown in Figs. 7 and 8, respectively, which significantly slowed graphitization in amorphous ta-C:Al:N during in-situ high-temperature annealing, thereby stabilizing the DLC structure [29,30,87].

4. Conclusions

Al-doped (ta-C:Al), N-doped (ta-C:N), Al-N co-doped (ta-C:Al:N), and non-doped (ta-C) DLC films were synthesized on AISI 4140 steel using FCVA deposition, and their nanomechanical properties and thermal stability were thoroughly investigated. Raman analysis showed that compressive stress/thickness increased with increasing N and Al—N contents (ta-C:N and ta-C:Al:N) and decreased with increasing Al content (ta-C:Al). Nanomechanical properties including hardness, elastic modulus, and elastic recovery (%ER), all decreased significantly in ta-C:Al, except in ta-C:N and ta-C:Al:N —which exhibited relatively high hardness (47.32 and 49.04 GPa) and high ER (57.92 and 58.43%) compared to ta-C (51.12 GPa and 60.06%), respectively. Moreover, based on sp^2-hybridized carbon bonding fraction, not more than 0.50, ta-C:Al:N exhibited outstanding thermal stability up to ~600 °C compared to ta-C:Al, ta-C:N, and ta-C tolerating the maximum temperature up to ~RT, ~280, and ~ 400 °C, respectively, as determined using in-situ high-temperature NEXAFS spectroscopy. The ta-C:Al:N thermal stability was enhanced by the formation of Al_2O_3 and sp^3-hybridized N-C bonds, as confirmed using X-ray photoelectron spectroscopy (XPS). Therefore, because co-doping DLC films with Al and N maintained both outstanding nanomechanical properties and high thermal stability, ta-C:Al:N was the preferred candidate for wear and tribological applications, particularly at high temperatures.

CRediT authorship contribution statement

Pornwasa Wongpanya: Conceptualization, Methodology, Validation, Formal analysis, Writing – original draft, Writing – review & editing, Supervision, Project administration, Resources, Funding acquisition. **Praphaphon Silawong:** Formal analysis, Investigation, Visualization, Writing – original draft. **Pat Photongkam:** Conceptualization, Writing – review & editing, Supervision.

References

[1] M.H. Khani Sanij, S.S. Ghasemi Banadkouki, A.R. Mashreghi, M. Moshrefifar, The effect of single and double quenching and tempering heat treatments on the microstructure and mechanical properties of AISI 4140 steel, Mater. Des. 42 (2012) 339–346, https://doi.org/10.1016/j.matdes.2012.06.017.

[2] J. Li, X. Yang, S. Wang, K. Wei, J. Hu, A rapid D.C. plasma nitriding technology catalyzed by pre-oxidation for AISI4140 steel, Mater. Lett. 116 (2014) 199–202, https://doi.org/10.1016/j.matlet.2013.11.033.

[3] D.S. Silva, A.D.S. Côrtes, M.H. Oliveira, E.F. Motta, G.A. Viana, Application of amorphous carbon based materials as antireflective coatings on crystalline silicon solar cells, J. Appl. Phys. 110 (2011) 04351, https://doi.org/10.1063/1.3622525.

[4] H. Kovacı, A.F. Yetim Baran, Y.B. Bozkurt, L. Kara, A. Çelik, The friction and wear performance of DLC coatings deposited on plasma nitrided AISI 4140 steel by magnetron sputtering under air and vacuum conditions, Surf. Coat. Technol. 349 (2018) 969–979, https://doi.org/10.1016/j.surfcoat.2018.05.084.

[5] M. Sayuti, A.A.D. Sarhan, F. Salem, Novel uses of SiO₂ nano-lubrication system in hard turning process of hardened steel AISI4140 for less tool wear, surface roughness and oil consumption, J. Clean. Prod. 67 (2014) 265–276, https://doi.org/10.1016/j.jclepro.2013.12.052.

[6] Y. Totik, The corrosion behaviour of manganese phosphate coatings applied to AISI 4140 steel subjected to different heat treatments, Surf. Coat. Technol. 200 (2006) 2711–2717, https://doi.org/10.1016/j.surfcoat.2004.10.004.

[7] M. Heydarzadeh Sohi, M. Ebrahimi, A. Honarbakhsh Raouf, F. Mahboubi, Comparative study of the corrosion behaviour of plasma nitrocarburised AISI4140 steel before and after post-oxidation, Mater. Des. 31 (2010) 4432–4437, https://doi.org/10.1016/j.matdes.2010.04.017.

[8] M. Fattah, F. Mahboubi, Comparison of ferritic and austenitic plasma nitriding and nitrocarburizing behavior of AISI 4140 low alloy steel, Mater. Des. 31 (2010) 3915–3921, https://doi.org/10.1016/j.matdes.2010.03.036.

[9] K. Genel, M. Demirkol, T. Gülmez, Corrosion fatigue behaviour of ion nitrided AISI 4140 steel, Mater. Sci. Eng. A Struct. 288 (2000) 91–100, https://doi.org/10.1016/S0921-5093(00)00835-2.

[10] Y. Li, Z. Liu, J. Luo, S. Zhang, J. Qiu, Y. He, Microstructure, mechanical and adhesive properties of CrN/CrTiAlSiN/WCrTiAlN multilayer coatings deposited on nitrided AISI 4140 steel, Mater. Charact. 147 (2019) 353–364, https://doi.org/10.1016/j.matchar.2018.11.017.

[11] M. Wiesing, J.M. Schneider, T.D.L. Arcos, G. Grundmeier, Combined electrochemical and electron spectroscopic investigations of the surface oxidation of TiAlN HPPMS hard coatings, Electrochim. Acta 208 (2016) 120–128, https://doi.org/10.1016/j.electacta.2016.05.011.

[12] W. Aperador, A. Delgado, J. Duque, Corrosion resistance of the (TiN/CrN)n coatings deposited on steel AISI 4140, Int. J. Electrochem. Sc. 8 (2013) 10711–10725.

[13] A. Ruden, E. Restrepo-parra, A.U. Paladines, F. Sequeda, Corrosion resistance of CrN thin films produced by dc magnetron sputtering, Appl. Surf. Sci. 270 (2013) 150–156, https://doi.org/10.1016/j.apsusc.2013.12.146.

[14] Y. Li, Q. Ye, Y. Zhu, L. Zhang, Y. He, S. Zhang, J. Xiu, Microstructure, adhesion and tribological properties of CrN/CrTiAlSiN/WCrTiAlN multilayer coatings deposited on nitrocarburized AISI 4140 steel, Surf. Coat. Technol. 362 (2019) 27–34, https://doi.org/10.1016/j.surfcoat.2019.01.091.

[15] J.B. Wu, J.J. Chang, M.Y. Li, M.S. Leu, A.K. Li, Characterization of diamond-like carbon coatings prepared by pulsed bias cathodic vacuum arc deposition, Thin Solid Films 516 (2007) 243–247, https://doi.org/10.1016/j.tsf.2007.06.154.

[16] J. Vetter, 60 years of DLC coatings: historical highlights and technical review of cathodic arc processes to synthesize various DLC types and their evolution for industrial applications, Surf. Coat. Technol. 257 (2014) 213–240, https://doi.org/10.1016/j.surfcoat.2014.08.017.

[17] J. Filik, P.W. May, S.R.J. Pearce, R.K. Wild, K.R. Hallam, XPS and laser Raman analysis of hydrogenated amorphous carbon films, Diam. Relat. Mater. 12 (2003) 974–978, https://doi.org/10.1016/S0925-9635(02)00374-6.

[18] S.V. Hainsworth, N.J. Uhure, Diamond like carbon coatings for tribology: production techniques, characterisation methods and applications, Int. Mater. Rev. 52 (2007) 153–174, https://doi.org/10.1179/174328007X160272.

[19] M.C. Polo, J.L. Andújar, A. Hart, J. Robertson, W.I. Milne, Preparation of tetrahedral amorphous carbon films by filtered cathodic vacuum arc deposition, Diam. Relat. Mater. 9 (2000) 663–667, https://doi.org/10.1016/S0925-9635(99)00339-0.

[20] X. Shi, B.K. Tay, D.I. Flynn, Q. Ye, Characterization of filtered cathodic vacuum arc system, Surf. Coat. Technol. 94–95 (1997) 195–200, https://doi.org/10.1016/S0257-8972(97)00247-2.

[21] D.U. Sheeja, B.K. Tay, S.P. Lau, X. Shi, X. Ding, Structural and tribological characterization of multilayer ta-C films prepared by filtered cathodic vacuum arc with substrate pulse biasing, Surf. Coat. Technol. 132 (2000) 228–232, https://doi.org/10.1016/S0257-8972(00)00848-7.

[22] H.-S. Zhang, K. Komvopoulos, Synthesis of ultrathin carbon films by direct current filtered cathodic vacuum arc, J. Appl. Phys. 105 (2009) 08330, https://doi.org/10.1063/1.3098254.

[23] J. Meślak, K. Komvopoulos, Ultrathin amorphous carbon films synthesized by filtered cathodic vacuum arc used as protective overcoats of heat-assisted magnetic recording heads, Sci. Rep-UK. (2018) 1–11, https://doi.org/10.1038/s41598-018-27528-5.

[24] L. Sun, P. Guo, P. Ke, X. Li, A. Wang, Synergistic effect of Cu/Cr co-doping on the wettability and mechanical properties of diamond-like carbon films, Diam. Relat. Mater. 68 (2016) 1–9, https://doi.org/10.1016/j.diamond.2016.05.006.

[25] C. Donnet, Recent progress on the tribology of doped diamond-like carbon alloy coatings: a review, Surf. Coat. Technol. 100–101 (1998) 180–186, https://doi.org/10.1016/S0257-8972(97)00611-7.

[26] L. Ji, Y. Wu, H. Li, H. Song, X. Liu, Y. Ye, J. Chen, H. Zhou, L. Liu, The role of trace Ti concentration on the evolution of microstructure and properties of duplex doped Ti(Ag)/DLC films, Vacuum. 115 (2015) 23–30, https://doi.org/10.1016/j.vacuum.2015.01.023.

[27] D. Bootkul, B. Supsermpol, N. Saenphinit, C. Aramwit, S. Intarasiri, Nitrogen doping for adhesion improvement of DLC film deposited on Si substrate by filtered cathodic vacuum arc (FCVA) technique, Appl. Surf. Sci. 310 (2014) 284–292, https://doi.org/10.1016/j.apsusc.2014.03.059.

[28] W. Xu, K. Zhou, D. Lin, M. Dai, Q. Shi, C. Wei, Structural properties of hydrogenated Al-doped diamond-like carbon films fabricated by a hybrid plasma system, Diam. Relat. Mater. 87 (2018) 177–185, https://doi.org/10.1016/j.diamond.2018.06.012.

[29] B. Zhou, B. Xu, Y. Xu, S. Yu, Y. Wu, Z. Liu, Selective bonding effect on microstructure and mechanical properties of (Al,N)-DLC composite films by ion beam-assisted cathode arc evaporation, Appl. Phys. A-Mater. A-Mater. 125 (2019) 1–15, https://doi.org/10.1007/s00339-018-2320-z.

[30] Y. Zhou, P. Guo, L. Sun, L. Liu, X. Xu, W. Li, X. Li, K.R. Lee, A. Wang, Microstructure and property evolution of diamond-like carbon films co-doped by Al and Ti with different ratios, Surf. Coat. Technol. 361 (2019) 83–90, https://doi.org/10.1016/j.surfcoat.2019.01.049.

[31] N. Konkhunthot, S. Tunmee, X.L. Zhou, K. Komatsu, P. Photongkam, H. Saitoh, P. Wongpanya, The correlation between optical and mechanical properties of amorphous diamond-like carbon films prepared by pulsed filtered cathodic vacuum arc deposition, Thin Solid Films 653 (2018) 317–325, https://doi.org/10.1016/j.tsf.2018.03.053.

[32] N. Konkhunthot, P. Photongkam, P. Wongpanya, Improvement of thermal stability, adhesion strength and corrosion performance of diamond-like carbon films with titanium doping, Appl. Surf. Sci. 469 (2019) 471–486, https://doi.org/10.1016/j.apsusc.2018.11.026.

[33] C. Srisang, P. Asanithi, K. Siangchaew, S. Limsuwan, A. Pokaipisit, P. Limsuwan, Raman spectroscopy of DLC/a-Si bilayer film prepared by pulsed filtered cathodic arc, J. Nanomater. 2012 (2012) 1–5, https://doi.org/10.1155/2012/745126.

[34] A.C. Ferrari, Determination of bonding in diamond-like carbon by Raman spectroscopy, Diam. Relat. Mater. 11 (2002) 1053–1061, https://doi.org/10.1016/S0925-9635(01)00730-0.

[35] N. Konkhunthot, C. Eauruksakul, P. Pheungkam, P. Wongpanya, Characterisation of diamond-like carbon (DLC) films deposited by filtered cathodic vacuum arc technique, J. Mol. Mater. Miner. 23 (2013) 35–44.

[36] E2546-07, Standard practice for instrumented indentation testing, ASTM B. Stand 1 (2007) 1–23, https://doi.org/10.1520/E2546-07.2.

[37] J. Schwan, S. Ulrich, V. Batori, H. Ehrhardt, Raman spectroscopy on amorphous carbon films, J. Appl. Phys. 80 (1996) 440–447, https://doi.org/10.1063/1.362745.

[38] R. Hauert, A. Glisenti, S. Metin, J. Guzin, J.H. Kaufman, P.H.M. van Loosdrecht, A. J. Kellock, P. Hoffmann, R.L. White, B.D. Hermsmeier, Influence of nitrogen doping on different properties of a-C:H, Thin Solid Films 268 (1995) 22–29, https://doi.org/10.1016/0040-6090(95)06824-4.

[39] Y. Mabuchi, T. Higuchi, V. Weihnacht, Effect of sp^2/sp^3 bonding ratio and nitrogen content on friction properties of hydrogen-free DLC coatings, Tribol. Int. 62 (2013) 130–140, https://doi.org/10.1016/j.triboint.2013.02.007.

[40] A. Singha, A. Ghosh, A. Roy, N.R. Ray, Quantitative analysis of hydrogenated diamondlike carbon films by visible Raman spectroscopy, J. Appl. Phys. 100 (2006), https://doi.org/10.1063/1.2338126.

[41] B.H. Lung, M.J. Chiang, M.H. Hon, Growth characterization and properties of diamond-like carbon films by electron cyclotron resonance chemical vapor deposition, Thin Solid Films 392 (2001) 16–21, https://doi.org/10.1016/S0040-6090(01)01010-0.

[42] H. Nakazawa, T. Kawabata, M. Kudo, M. Mashita, Structural changes of diamond-like carbon films due to atomic hydrogen exposure during annealing, Appl. Surf. Sci. 253 (2007) 4188–4196, https://doi.org/10.1016/j.apsusc.2006.09.017.

[43] F. Piazza, A. Golanski, S. Schulze, G. Relihan, Transpolyacetylene chains in hydrogenated amorphous carbon films free of nanocrystalline diamond, Appl. Phys. Lett. 82 (2003) 358–360, https://doi.org/10.1063/1.1538349.

[44] J. Pu, G. Zhang, S. Wan, R. Zhang, Synthesis and characterization of low-friction Al-DLC films with high hardness and low stress, J. Compos. Mater. 49 (2015) 199–207, https://doi.org/10.1177/0021998313515291.

[45] E. Liu, L. Li, B. Blanpain, J.P. Celis, Residual stresses of diamond and diamondlike carbon films, J. Appl. Phys. 98 (2005), https://doi.org/10.1063/1.2073451 (0–5).

[46] X. Rao, J. Yang, Z. Chen, Y. Yuan, Q. Chen, X. Feng, L. Qin, F. Zhang, Tuning C–C sp^2/sp^3 ratio of DLC films in FCVA system for biomedical application, Bioact. Mater. 5 (2020) 192–200, https://doi.org/10.1016/j.bioactmat.2020.02.005.

[47] R. Zarei Moghadam, H. Rezagholipour Dizaji, M.H. Ehsani, Modification of optical and mechanical properties of nitrogen doped diamond-like carbon layers, J. Mater. Sci-Mater. El. 30 (2019) 19770–19781, https://doi.org/10.1007/s10854-019-02343-1.

[48] S. Tunmee, P. Photongkam, C. Euaruksakul, H. Takamatsu, X.L. Zhou, P. Wongpanya, K. Komatsu, K. Kanda, H. Ito, H. Saitoh, Investigation of pitting corrosion of diamond-like carbon films using synchrotron-based spectromicroscopy, J. Appl. Phys. 120 (2016), https://doi.org/10.1063/1.4967799.

[49] A.C. Ferrari, J. Robertson, Resonant Raman spectroscopy of disordered, amorphous, and diamondlike carbon, Phys. Rev. B 64 (2001) 1–13, https://doi.org/10.1103/PhysRevB.64.075414.

[50] Y. Lifshitz, S.R. Kasi, J.W. Rabalais, Subplantation model for film growth from hyperthermal species: application to diamond, Phys. Rev. Lett. 62 (1989) 1290–1293, https://doi.org/10.1103/PhysRevLett.62.1290.

[51] C.C. Chen, F.C.N. Hong, Structure and properties of diamond-like carbon nanocomposite films containing copper nanoparticles, Appl. Surf. Sci. 242 (2005) 261–269, https://doi.org/10.1016/j.apsusc.2004.08.036.

[52] Y. Miki, A. Nishimoto, T. Sone, Y. Araki, Residual stress measurement in DLC films deposited by PBIID method using Raman microprobe spectroscopy, Surf. Coat. Technol. 285 (2015) 274–280, https://doi.org/10.1016/j.surfcoat.2015.10.046.

[53] R.J. Narayan, Laser processing of diamond-like carbon-metal composites, Appl. Surf. Sci. 245 (2005) 420–430, https://doi.org/10.1016/j.apsusc.2004.11.026.

[54] M. Lubwama, B. Corcoran, K.V. Rajani, C.S. Wong, J.B. Kirabira, A. Sebbit, K. A. McDonnell, D. Dowling, K. Sayers, Raman analysis of DLC and Si-DLC films deposited on nitrile rubber, Surf. Coat. Technol. 232 (2013) 521–527, https://doi.org/10.1016/j.surfcoat.2013.06.013.

[55] F.X. Liu, Z.L. Wang, Thickness dependence of the structure of diamond-like carbon films by Raman spectroscopy, Surf. Coat. Technol. 203 (2009) 1829–1832, https://doi.org/10.1016/j.surfcoat.2009.01.008.

[56] A. Modabberasl, P. Kameli, M. Ranjbar, H. Salamati, R. Ashiri, Fabrication of DLC thin films with improved diamond-like carbon character by the application of external magnetic field, Carbon 94 (2015) 485–493, https://doi.org/10.1016/j.carbon.2015.06.081.

[57] A. Sikora, F. Garrelie, C. Donnet, A.S. Loir, J. Fontaine, J.C. Sanchez-Lopez, T. C. Rojas, Structure of diamondlike carbon films deposited by femtosecond and nanosecond pulsed laser ablation, J. Appl. Phys. 108 113516 (2010) 1–9, https://doi.org/10.1063/1.3510485.

[58] M.J. Son, T.F. Zhang, Y.J. Jo, K.H. Kim, Enhanced electrochemical property of the DLC films with an arc interlayer, nitrogen doping and annealing, Surf. Coat. Technol. 329 (2017) 77–85, https://doi.org/10.1016/j.surfcoat.2017.09.025.

[59] T.F. Page, W.C. Oliver, C.J. McHargue, The deformation behavior of ceramic crystals subjected to very low load (nano) indentations, J. Mater. Res. 7 (1992) 450–473, https://doi.org/10.1557/JMR.1992.0450.

[60] E.A. Ochoa, C.A. Figueroa, F. Alvarez, Nitriding of AISI 4140 steel by a low energy broad ion source, J. Vac. Sci. Technol. A 24 (2006) 2113–2116, https://doi.org/10.1116/1.2356480.

[61] N. Savvides, T.J. Bell, Hardness and elastic modulus of diamond and diamond-like carbon films, Thin Solid Films 228 (1993) 289–292, https://doi.org/10.1016/0040-6090(93)90615-7.

[62] J. Robertson, Diamond-like amorphous carbon, Mater. Sci. Eng. R 37 (2002) 129–281, https://doi.org/10.1016/S0927-796X(02)00005-0.

[63] S. Kumar Ishpal, N. Dwivedi, C.M.S. Rauthan, Investigation of radio frequency plasma for the growth of diamond like carbon films, Phys. Plasmas 19 (2012), https://doi.org/10.1063/1.3694855 (033515-1–033515-14).

[64] K. Askir, A. Vacade, K. Niranjan Reddy, S. Dhan, M. Chellamalai, N. Balashunmugam, P. Krishna, Synthesis of high hardness IR optical coating using diamond-like carbon by PECVD at room temperature, Diam. Relat. Mater. 78 (2017) 39–43, https://doi.org/10.1016/j.diamond.2017.07.003.

[65] B.F. Coll, M. Chhowalla, Amorphous diamond film by enhanced arc deposition, Surf. Coat. Technol. 79 (1996) 76–86, https://doi.org/10.1016/0257-8972(95)02444-1.

[66] X. Yan, T. Xu, G. Chen, S. Yang, H. Liu, Study of structure, tribological properties and growth mechanism of DLC and nitrogen-doped DLC films deposited by electrochemical technique, Appl. Surf. Sci. 236 (2004) 328–335, https://doi.org/10.1016/j.apsusc.2004.05.005.

[67] K. Boonkerdkongma, P.W. May, B. Paosawatyanyong, Electrical and optical properties of diamond-like carbon films deposited by pulsed laser ablation, Diam. Relat. Mater. 19 (2010) 999–1002, https://doi.org/10.1016/j.diamond.2010.03.007.

[68] H. Maruno, A. Nishimoto, Adhesion and durability of multi-interlayered diamond-like carbon films deposited on aluminum alloy, Surf. Coat. Technol. 354 (2018) 154–144, https://doi.org/10.1016/j.surfcoat.2018.08.094.

[69] I. Bouabibsa, S. Lamri, A. Alhussein, T. Minea, F. Sanchette, Plasma investigations and deposition of Me-DLC (Me = Al, Ti or Nb) obtained by a magnetron sputtering-RFPECVD hybrid process, Surf. Coat. Technol. 354 (2018) 351–359, https://doi.org/10.1016/j.surfcoat.2018.09.033.

[70] J.R. Shi, Study on nitrogenated amorphous carbon films prepared by unbalanced magnetron sputtering, J. Appl. Phys. 99 (2006), 033505, https://doi.org/10.1063/1.2168027.

[71] N.E. Derradji, M.L. Mahdjoubi, H. Belkhir, N. Mumumbila, B. Angleraud, P. Y. Tessier, Nitrogen effect on the electrical properties of CN$_x$ thin films deposited by reactive magnetron sputtering, Thin Solid Films 482 (2005) 258–263, https://doi.org/10.1016/j.tsf.2004.11.137.

[72] A.C. Ferrari, J. Robertson, Interpretation of Raman spectra of disordered and amorphous carbon, Phys. Rev. B 61 (2000) 14095–14107, https://doi.org/10.1103/PhysRevB.61.14095.

[73] W. Dai, A. Wang, Deposition and properties of Al-containing diamond-like carbon films by a hybrid ion beam source, J. Alloys Compd. 509 (2011) 4626–4631, https://doi.org/10.1016/j.jallcom.2011.01.132.

[74] V. Edlmayr, M. Moser, C. Walter, C. Mitterer, Thermal stability of sputtered Al$_2$O$_3$ coatings, Surf. Coat. Technol. 204 (2010) 1576–1581, https://doi.org/10.1016/j.surfcoat.2009.10.002.

[75] E. Ozensoy, J. Szanyi, C.H.F. Peden, Interaction of water with ordered θ-Al$_2$O$_3$ ultrathin films grown on NiAl(100), J. Phys. Chem. B 109 (2005) 3431–3436, https://doi.org/10.1021/jp049920n.

[76] G. Dingemans, P. Engelhart, R. Seguin, M.M. Mandoc, M.C.M. Van De Sanden, W. M.M. Kessels, Comparison between aluminum oxide surface passivation films deposited with thermal ALD, plasma ALD and PECVD, Conf. Rec. IEEE Photovolt. Spec. Conf. (2010) 3118–3121, https://doi.org/10.1109/PVSC.2010.5614504.

[77] P. Eklund, M. Sridharan, G. Singh, J. Bøttiger, Thermal stability and phase transformations of γ-/amorphous-Al$_2$O$_3$ thin films, Plasma Process. Polym. 6 (2009) 907–911, https://doi.org/10.1002/ppap.200932301.

[78] C. Lenardi, P. Piseri, V. Briois, C.E. Bottani, A. Li Bassi, P. Milani, Near-edge X-ray absorption fine structure and Raman characterization of amorphous and nanostructured carbon films, J. Appl. Phys. 85 (1999) 7159–7167, https://doi.org/10.1063/1.370527.

[79] M. Tagawa, K. Yokota, A. Kitamura, K. Matsumoto, A. Yoshigoe, Y. Teraoka, K. Kanda, M. Niibe, Synchrotron radiation photoelectron spectroscopy and near-edge X-ray absorption fine structure study on oxidative etching of diamond-like carbon films by hyperthermal atomic oxygen, Appl. Surf. Sci. 256 (2010) 7678–7683, https://doi.org/10.1016/j.apsusc.2010.06.030.

[80] P. Ashtijoo, S. Bhattacherjee, R. Sutarto, Y. Hu, Q. Yang, Fabrication and characterization of adherent diamond-like carbon based thin films on polyethylene terephthalate by end hall ion beam deposition, Surf. Coat. Technol. (2016) 1–8, https://doi.org/10.1016/j.surfcoat.2016.06.090.

[81] N. Soin, S.S. Roy, S.C. Ray, P. Lemoine, M.A. Rahman, P.D. Maguire, S.K. Mitra, J. A. McLaughlin, Thickness dependent electronic structure of ultra-thin tetrahedral amorphous carbon (ta-C) films, Thin Solid Films 520 (2012) 2909–2915, https://doi.org/10.1016/j.tsf.2011.12.036.

[82] T. Yoshitake, S. Ohmagari, A. Nagano, S. Al-Riyami, R. Ohtani, H. Setoyama, E. Kobayashi, K. Nagayama, Near-edge x-ray absorption fine structure of ultrananocrystalline diamond/hydrogenated amorphous carbon films prepared by pulsed laser deposition, J. Nanomater. 2009 (2009) 1–5, https://doi.org/10.1155/2009/876561.

[83] D.S. Grierson, A.V. Sumant, A.R. Konicek, T.A. Friedmann, J.P. Sullivan, R. W. Carpick, Thermal stability and rehybridization of carbon bonding in tetrahedral amorphous carbon, J. Appl. Phys. 107 (2010), https://doi.org/10.1063/1.3284087.

[84] R.K.Y. Fu, Y.F. Mei, M.Y. Fu, X.Y. Liu, P.K. Chu, Thermal stability of metal-doped diamond-like carbon fabricated by dual plasma deposition, Diam. Relat. Mater. 14 (2005) 1489–1493, https://doi.org/10.1016/j.diamond.2005.03.006.

[85] L.H. Zhang, H. Gong, J.P. Wang, Kinetics and mechanisms of the thermal degradation of amorphous carbon films, J. Appl. Phys. 91 (2002) 9646–9651, https://doi.org/10.1063/1.1478131.

[86] D.R. Tallant, J.E. Parmeter, M.P. Siegal, R.L. Simpson, The thermal stability of diamond-like carbon, Diam. Relat. Mater. 4 (1995) 191–199, https://doi.org/10.1016/0925-9635(94)00243-6.

[87] V. Podgursky, M. Yashin, T. Jõgiaas, M. Viljus, A. Alamgir, M. Danilson, A. Bogatov, High temperature tribological properties of Al$_2$O$_3$/NCD films investigated under ambient air conditions, Coatings 10 (2020) 1–13, https://doi.org/10.3390/coatings10020175.

BIOGRAPHY

Acting Sub. Lt. Praphaphon Silawong was born on October 20, 1983 in Bangkok, Thailand. She graduated a Bachelor's Degree in Metallurgical Engineering, Institute of Engineering at Suranaree University of Technology (SUT). After completing her graduation, she had been started work at Thai Parkerizing Co., Ltd., (2006–2008). She enrolled in the Institute of Engineering, SUT and graduated in School of Metallurgical Engineering with a Master's Degree in 2008 – 2011. After completing her Master's Degree, she had been started work at Thai Parkerizing Co., Ltd again in the Department of Thai Technical Center for 5 years. During her studying, she worked as a research assistant at the BL3.2Ub: PEEM at the SLRI where she learned and developed her experiences and skills in a vacuum system, FCVA system, and synchrotron–based analytical technique. She continued for research on the incorporation of Al–N atoms into DLC structure and published a paper in the Journal of Surface and Coating technology is the Journal indexed in the ISI Web of Science database. She completed her Doctoral Degree in 2022. Her expertise includes the development of the pulsed two–FCVA system, as well as the deposition and characterization of carbon–based materials, most notably amorphous DLC films. She will use DLC films as protective coatings in thermal stability and corrosion resistance applications in her current research and is interested in studying and synthesizing the features of gas and metal–doped DLC films.